

Mesoporous Silica Nanoparticle for Drug Delivery of Cancer Therapeutics

Dissertation

Zur Erlangung des Grades

“Doktor der Naturwissenschaften”

im Promotionsfach Chemie

am Fachbereich Chemie, Pharmazie und Geowissenschaften der

Johannes Gutenberg-Universität

in Mainz



vorgelegt von

Sven Andreas Kurch

geboren in Wolfenbüttel

Mainz, Mai 2015

Dekan:

[REDACTED]

Gutachter/in: 1.

[REDACTED]

2.

[REDACTED]

Datum der mündlichen Prüfung: 28.06.2018

The work for this thesis was carried out at the Johannes Gutenberg-Universität Mainz during the period between 1st May 2015 and 30th April 2018 under the guidance of

████████████████████.

I hereby declare that I wrote the submitted dissertation without any unauthorized external assistance and I used only sources acknowledged in the work. All textual passages, which are appropriated verbatim or paraphrased from published and unpublished texts, as well as all information obtained from oral sources are duly indicated and listed in accordance with bibliographical rules. In carrying out this research, I complied with the rules of standard scientific practice as formulated in the statutes of the Johannes Gutenberg-Universität Mainz to insure standard scientific practice.

Mainz, 23.05.2018

Sven Kurch

Acknowledgments

Diese Arbeit entstand im Zeitraum von Mai 2015 bis Mai 2018 in Zusammenarbeit mit der Universitätsmedizin Mainz und Kooperationen mit Bielefeld und Brisbane (Australien). Viele Menschen habe mich im Laufe der letzte drei Jahre unterstützt und Ihnen möchte ich an dieser Stelle danken. In erster Linie gilt mein Dank [REDACTED] [REDACTED], welcher mir die ursprüngliche Idee von „löchrigem Sand“ mit allen Freiheiten überlassen hat. Ein großer Dank gebührt auch [REDACTED] dafür, dass sie mit ihrer unaufgeregten Art und Hilfsbereitschaft für einen reibungslosen organisatorischen [REDACTED].

Weiterer Dank geht an die medizinische Seite dieser Arbeit und somit an die Arbeitsgruppen [REDACTED], wobei [REDACTED] als zweiter Betreuer im Rahmen des Sonderforschungsbereich 1066 mir die Möglichkeit eröffnete mit einem echten Krebstherapeutikum Forschung zu betreiben. Ich möchte [REDACTED] [REDACTED] für die intensive und lustige Zusammenarbeit danken, welche durch die Hilfe von [REDACTED] auch ein gemeinsames Projekt möglich machte. Die Arbeitsgruppe [REDACTED] war immer ein lustiger Haufen und durch die Kooperation mit Brisbane in der Arbeitsgruppe [REDACTED] konnte spannende und eindrucksvolle Biodaten erzeugt werden. [REDACTED] gilt mein Dank, da wir gemeinsam über fast zwei Jahre den Wirkstoff von [REDACTED] aus Bielefeld untersucht, verflucht aber auch spannende Ergebnisse erzeugen konnten. Viele Dank an euch beide, dass ihr durchgehalten habt.

In dieser Arbeit sind viele analytische Methoden zum Einsatz gekommen, um die viele Facette des Wirkstofftransportes zu beleuchten. Ich möchte vor allem [REDACTED] und [REDACTED] für die Analyse der Partikel durch Streuprozesse danken, ein schwieriges und zeitintensives Thema. Weiterhin [REDACTED] zum Thema Röntgenbeugung, sowie [REDACTED] für die aufschlussreichen Titrations danken. Auch möchte ich [REDACTED] recht herzlich für seine stets unkomplizierte und engagierte Art danken, Festkörper MR so einfach aussehen zu lassen. Der [REDACTED] ([REDACTED] [REDACTED]) gebührt der Dank für die zahlreichen Proben, die in den drei Jahren gemessen wurden. Zusammen mit [REDACTED] konnten wir das lästige TEM Problem an der Universität angehen und teilweise verbessern. Meinem Platzpartner [REDACTED] möchte ich für die hilfreichen Diskussionen und Unmengen an Chemikalien/Laboraausstattung danken. Wenn man was brauchte, wusste man wo es zu finden ist!

[REDACTED]

Table of Content

1. Introduction and Scope	15
1.1 Overview Drug-Delivery Systems.....	17
1.2 Core-Shell Particles	18
1.3 Surface Modification	19
1.4 Biodistribution and Functionalization of the DDS.....	19
1.5 Endocytose	20
1.6 Bio-Nano Interface	22
1.7 Protein Corona	25
1.8 Tumor Microenvironment.....	28
1.9 Passive and Active Targeting.....	30
1.10 Gatekeeper.....	34
1.11 Biorelated Degradation of the DDS.....	37
1.12 Limitation of the DDS	37
1.13 Cancer Immunotherapy	42
2. Dendritic Mesoporous Silica Nanocarrier	45
2.1 Nanocarrier Synthesis	46
2.1.1 Gas Adsorption.....	47
2.2 Pore Size and Particle Diameter.....	49
2.3 Influence of Organic Base and Temperature	51
2.4 Hydrotropes in Mixed Micelles	52
2.5 Siloxane Network Functionalization	58
2.6 Organosilane Bridging	59
2.7 Fe ₃ O ₄ Core Shell System.....	61
3. Dendritic Mesoporous Silica Nanoparticles for pH-Stimuli-Responsive Drug Delivery of TNF-Alpha.....	65
3.1 Motivation and Objective	65
3.2 Results and Discussion	68
4. Controlled Surface Functionalization of Dendritic Mesoporous Silica Nanoparticle for Drug Delivery of Small Molecule Drugs	89
4.1 Introduction	89
4.2 Results and Discussion	92
5. Summary and Outlook.....	109
A Appendix	111
A.1 Material and Methods Chapter 2.....	111
A.2 Material and Methods Chapter 3.....	115

A.3	Figures, Tables and Equations Chapter 3	124
A.4	Material and Methods Chapter 4.....	129
A.5	Instruments Chapter 4	133
A.6	Figures, Tables and Equations Chapter 4	137
A.7	Authorship Contributions.....	148
A.8	List of Figures.....	151
A.9	List of Tables.....	155
A.10	List of Abbreviations.....	155
6.	References.....	158
	Curriculum Vitae	180

Zusammenfassung

Das Ziel der vorliegenden Arbeit war es, ein Wirkstofftransportsystem (WTS) auf Basis von mesoporösem Siliziumdioxid zu entwickeln, welches den Einsatz eines hoch toxischen Zytokine (TNF- α) und eines potenten Chemotherapeutika (Dinuklearer Kupferkomplex) für die Krebstherapie möglich macht. Dabei war eine systematische Untersuchung des WTS über *in vitro* Test bis hin zu *in vivo* Versuchen in Zusammenarbeit mit der Universitätsmedizin in Mainz und dem Sonderforschungsbereich 1066 ein Kernbereich dieser Arbeit. Neben dem Transport dieser Wirkstoffe war die Entwicklung eines Schutzsystems für die lokale Freisetzung der Beladung in der Zelle Forschungsthema, wobei unter Berücksichtigung von Wirkstoffspezifischen Eigenschaften (Stabilität, Ladung, Größe) die Schutzsysteme problembezogen entwickelt wurden.

Der erste Teil dieser Arbeit beschäftigt sich mit der Synthese von mesoporösen Silica Nanopartikeln, wobei durch systematische Untersuchungen der Reaktionsbedingungen Poren- und Partikelgröße über einen breiten Bereich kontrolliert werden konnten. Hierbei wird neben der Kontrolle von Reaktionsparametern auch der Einsatz von zwei Tensiden für die Porenerweiterung analysiert. Des Weiteren wird die Funktionalisierung der Silanol- Oberfläche und Kern der Nanopartikel vorgestellt, wobei Ankergruppen für das Schutzsystem, Fluoreszenzfarbstoffe für *in vitro* Zell Lokalisierung und intrapartikuläre Brückenmoleküle eingebaut werden konnten. Einbau von Disulfid -und Tetrasulfid Funktionalitäten im Siliziumdioxid Netzwerk während der Synthese konnte die intrazelluläre Bioabbaubarkeit der Trägersysteme modifizieren. Zusätzliche konnte ein Kern Schale Modell aus Fe₃O₄ eingebettet in eine mesoporöse Silica Schale synthetisiert werden, welche die magnetische Abtrennung dieser Partikel aus einer Proteinreichen Matrix möglich macht. Vollständige Charakterisierung aller Funktionalisierung, der Partikel selbst und deren Langzeit Stabilität waren Grundlagen für den anschließenden Einsatz im medizinischen Kontext.

Zweiter Teil der Arbeit beschäftigt sich mit der Einkapslung, dem Transport und der Freisetzung des natürlichen Zytokins TNF- α *in vitro* und *in vivo*. Hierbei konnten die MSN als WTS etabliert werden und deren unbedenklicher Einsatz an verschiedene Zelllinien und Immunzellen dosisabhängig bewiesen werden. Des Weiteren konnte durch eine Synthese eines polymerbasierten Schutzsystems das Zytokin eingekapselt werden und somit seine direkte Zelltoxizität abgeschwächt werden.

Unter Erhalt seines Wirkmechanismus und somit seiner hohen Zelltoxizität konnten dessen Freisetzung *in vitro* und *in vivo* bewiesen werden. Hierbei konnte vor allem multizelluläre Sphäroide in 3D Zellkulturen als *in vivo* Simulationsmodell die Entwicklung des WTS steuern und anpassen. Abschließende Untersuchungen in einem transgenen Mausmodell mit nicht invasiver optischer Bildgebung konnten die Bioverteilung des Zytokins nach subkutaner Gabe untersuchen.

Der letzte Teil dieser Arbeit zeigt die Modifizierung des Porensystems und der Schutzhülle für den Transport eines zweikernigen Cu(II)-Komplex und Doxorubicin für die Krebstherapie. Hierbei war die Aufgabe die kleinen Wirkstoffe sicher zu verpacken und intrazellulär freizusetzen. Analog zu Kapitel zwei konnte die zeitverzögerte Wirkung der Wirkstoffe durch das Verpacken gezeigt werden. Die vollständige Quantifizierung des Schutzsystems in allen Funktionalisierungsschritten optimiert den Einkapselungsprozess und machte den kontrollierbaren Einschluss möglich.

Abstract

The aim of the present work was to develop a drug delivery system (DDS) based on mesoporous silica, which enabled the transport and release of a highly toxic cytokine (TNF- α) and small molecule drugs for cancer therapy. In cooperation with the University Medical Center in Mainz and the Collaborative Research Center 1066, a systematic investigation of the WTS via *in vitro* test up to *in vivo* experiments was possible. In addition to the transport of these active ingredients, the development of a protective system (gatekeeper) for the local release of the respective cargo inside cell was a research topic. Taking into account the drug-specific properties (stability, charge and size), the protective systems and the intracellular release mechanism were adapted accordingly.

The first part of this work presents the establishment of mesoporous silica as carrier platform. The synthesis of the dendritic mesoporous silica nanoparticles (DMSN) with various pore size and particle diameter was possible through systematic analysis of the surfactant-directed polycondensation. In addition to reaction parameter control, a dual surfactant method for pore expansion is presented. Core- and surface functionalization of the DMSN introduced anchor groups for the protective system, fluorescent dyes for *in vitro* cell localization and intraparticulate bridging molecules. Integration of disulfide and tetrasulfide functionalities in the silica network was able to modify the intracellular biodegradability of the carrier systems. In addition, a core shell particle - Fe₃O₄ embedded in a mesoporous silica shell - for possible magnetic separation from a protein-rich matrix is shown.

The second part of the work deals with the encapsulation and shielding of the highly toxic cytokine TNF- α (Beromun, tasonermin) *in vitro* and *in vivo* with a pH-sensitive hyperbranched polyethylenimine (PEI)-hydrophilic polyethyleneglycol (PEG) copolymer gatekeeper. First, the safe use of the DMSN on various cell lines and immune cells could be proven dose-dependent. Second, DMSN could attenuate the systemic toxicity of TNF- α while maintaining its pleiotropic anti-tumor activity *in vitro* and in a 3D cell model, which efficiently mimics tumor architecture and microenvironment. Colloidal stability of the DDS was shown with dynamic light scattering in simulated body fluid, an outstanding property for *in vivo* applications. Final *in vivo* experiments with non-invasive optical imaging were able to investigate the biological distribution of the cytokine after subcutaneous administration.

The last part of this work shows the development of a new DDS (DMSN and gatekeeper) for the transport of Doxorubicin and a novel dinuclear Cu(II)-complex cytostatic for cancer therapy. A dual responsive drug delivery system, utilizing pH and Redox trigger through a surface bound inclusion complex, blocking the pores. Imine bridged ferrocene stalks interacting with a cyclic sugar (β -CD) to restrict drug diffusion. The complete quantification of the surface modulation/inclusion complex optimized the DDS; enhanced drug encapsulation and ensures gatekeeper attachment. First *in vitro* experiments with a squamous cell carcinoma (SCC) tumor model demonstrate the particle uptake and intracellular release of both drugs.

Part I

The following content is partially taken and adapted from the book chapter “Bio-Nano: Theranostic At Cellular Level”. Taken parts are delimited by single quotation marks (“”). Details to the individual contribution of each author are listed in the Appendix.

1. Introduction and Scope

Cancer is one of the world most leading causes of death.^[1] According to the World Health Organization, cancer accounted for 8.2 million deaths in 2012, being 21.7 million the number of new cancer cases expected to be diagnosed, while 13 million cancer deaths are predicted in 2030.^[2,3] In Germany, there are approximately 480.000 new cancer cases every year and due to demographic changes an increase of at least 20% is expected by 2030.^[4] “Cancer therapy relies on surgery, radiotherapy and chemotherapy but can prolong a patient’s life span only by several months. Chemotherapy, besides surgery, is currently still the most promising therapy and known for cancer treatment for over 60 years.^[5] Because of its severe side effects with often massive burdens for the patient, researchers have concentrated on therapy improvement by delimiting chemotherapy to the tumor region, thereby improving therapeutic results and reducing systemic side effects. Drug delivery systems (DDS) using nanoparticles have evolved as a promising strategy. Their nanoscopic structures exhibit exceptional properties and characteristics, differentiating them noticeably from their bulk counterparts. The origin of most new properties in multicomponent nanoparticles is related to their small size and special morphology. Their size significantly increases the number of surface atoms by increasing the surface-to-volume ratio, which leads to new chemical and physical properties. At the same time, the surface structure, determined by the shape and morphology of the nanoparticles, plays a pronounced role for the chemical and physical behavior. Especially, DDSs have advanced as inorganic, organic or mesoporous carrier systems with a shell to encapsulate the drug and targeting ligands to target specific cell populations or tissue to release the cargo. The key functionalities protect the drug from premature degradation, stopping unwanted interaction with the biological environment and enhancing absorption of the drugs into specific tissue. Further advantages arise from the control of pharmacokinetics, improved intracellular penetration and therefore extended circulation half-life. Especially surface ligands are helpful for lowering aggregation rate and prolonging shelf life of the DDSs.^[6] The first FDA (Food and Drug Administration) approved carrier platform in 1995 was a liposome-based DDS Doxil® (Doxorubicin).^[7] Subsequently, different combinations of

liposome and drug, like Abraxane® (albumin-bound paclitaxel) and DaunoXome (daunorubicin), were introduced successfully into the market. Preclinical studies showed high potential while phase III clinical trials showed only marginal improvements over existing therapies. Doxil® showed not even statistically a significant efficiency gain and FDA approval was largely based on its reduced cardiotoxicity. Another example is the liposome-based drug carrier Abraxane® whose success was based on the linkage between toxicity reduction and elevated doses. Since then, much effort has been undertaken to develop nanosystems as anti-cancer therapeutics.”

The thesis is organized in the following way. After this short introduction (chapter 1) the theoretical background of nanosized drug delivery systems is presented. Additionally, biological concepts and obstacle to describe current development in cancer therapy are discussed. Chapter 2 described the development of the mesoporous carrier platform and it's detailed surface analysis and surface functionalization in preparation for *in vitro* applications. In chapter 3, the complete *in vitro/in vivo* study of mesoporous silica nanoparticle with a polymer-based gatekeeper is shown. Nanosized carrier were utilized to transport a highly toxic cytokine TNF- α , shielding it's toxicity and showed first *in vivo* behavior of the DDS through a fluorescence ubiquitination cell cycle indicator (FUCCI) 3D spheroid cell system and in a transgenic mice model. Chapter 4 outlines the development of a dual responsive drug delivery system, utilizing pH and Redox triggers for release of small molecule drugs. Imine bridged ferrocene stalks interacting with a cyclic sugar (β -CD) to form a pore blocking inclusion complex. *Cell* experiments with a novel cytostatic based on a dinuclear Cu(II) complex and doxorubicin show the *in vitro* application of the DDS. To ensure successful surface functionalization and drug encapsulation, the gatekeeper and each modification step were quantified in detail,

1.1 Overview Drug-Delivery Systems

“Researchers at Mobil Oil Corporation developed the silica based mesoporous material MCM-41 (Mobile Crystalline Material^[8,9]), and its application for drug delivery was first introduced in 2001.^[10] Silica nanoparticle show good biocompatibility, options for a variety of functionalizing strategies, high surface area and adjustable pore size.^[11–14] They are functionalized easily with alkine,^[15] carboxyl,^[16] amine^[17] and azido^[18] functional groups. The template-associated polycondensation of silica precursors leads to various porous structures and shapes, tailored specifically to the individual therapeutic agent size and their applications. Starting from non-porous silica particles^[19–21] made by the Stöber approach^[22] by the microemulsion technique,^[23,24] the first systematic study to biorelated degradation and biodistribution was completed. Dendritic silica nanoparticles^[25–31] and other unique pore shapes like cubic (Pm3n^[32]), yolk-shell^[33,34], fibrous (KCC-1^[35,36]), wrinkled^[37] and cylindrical (KIT-6^[31]) were developed for drug delivery and imaging. Organosilica hybrid nanoparticles, combining the organic flexible network with various functionalizing possibilities and the rigid, inorganic silica structure with adjustable pore size, are promising drug delivery systems (DDSs) as well.^[39–42] Other carrier systems deployed for drug delivery or diagnostic purposes are gold, iron oxide and CdSe quantum dots (QD). These metal-based systems combine an imaging of the tumor tissue and blood vessels with the possibilities for treatment with the encapsulated drug. Theranostic carrier systems, combining therapy and diagnostic, are utilized in various disease treatment scenarios, making *in vitro* and *in vivo* research cornerstones for translation of nanomedicines into the clinic. Liposomes and polymer based nanoparticle are another class of DDSs.^[43,44] First steps to the translation of nanocarriers were carried out in 2006, when small interfering RNA (si-RNA) was encapsulated in liposomes and delivered in non-human primates.^[45]” **Figure 1.1** illustrates major cornerstones in the field of cancer nanomedicine.

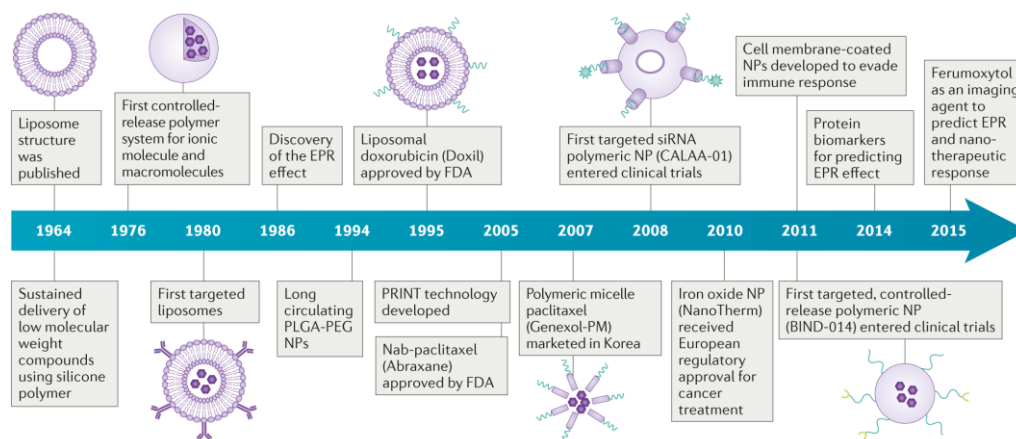


Figure 1.1. Historical timeline of major developments in the field of cancer nanomedicine. EPR, enhanced permeability and retention; FDA, US Food and Drug Administration; nab, nanoparticle albumin-bound; NP, nanoparticle; PLGA-PEG, poly(D,L-lactic-co-glycolic acid)-b-poly(ethylene glycol); PRINT, particle replication in non-wetting template; siRNA, small interfering RNA. Adapted with permission from ref.^[46]

1.2 Core-Shell Particles

“Core-shell nanoparticles, where a core material is covered by a shell of another material often with variable shell thickness, including mesoporous core-systems for drug load and shells as gate system.^[47,48] Core-shell particles are another type of heteroparticles where the second domain is present as a shell around a core material e.g. through multiple nucleation spots in a polar solvent (*vide supra*). Similarly, any organic or silica coating of inorganic nanoparticles is a wide synthetic field for core-shell nanoparticles.^[49] Core-shell nanoparticles categorization is based on their composition. A widely used type of core-shell particles includes an inorganic core combined with an inorganic shell material with silica as the most common example. Advantages of silica coatings on inorganic nanoparticles include extended suspension stability in aqueous media, various surface functionalization possibilities as well as improved biocompatibility.^[50–52]

A typical synthesis of silica uses a modified sol-gel processing (Stöber process) based on hydrolysis and polycondensation of metal/silicon alkoxides. The reaction takes place under specific reaction conditions (pH, temperature and alkoxide concentration).^[22] Particularly the pH value plays an important role for the hydrolysis of tetraalkoxy silanes under acidic as well as basic conditions. Usually a basic catalysis is used to increase the rate of condensation and to control the particle morphology by inhibiting a strong gelation to network structures.^[53,54] Another possibility to obtain monodisperse and small silica particles/coatings is the reverse microemulsion technique. A mixture of surfactant, water and oil forms a microemulsion in shape of round nanodroplets. These aqueous droplets functions as reaction containment for the formation of silica

particles/coatings. The size of the micelles determines the particle size and morphology.^[51,52] The shell thickness can be controlled by the ratio of base/tetraalkoxy and silane/number of seed particles. A template chemistry serves also for the formation of mesoporous silica structures for drug loading and triggered payload release.^[55] In chapter 2, the synthesis of Fe₃O₄ core-shell particle and its application in magnetic separation will be presented. Other valuable systems contain one or both components of the core-shell structure from organic/polymeric nature. Biocompatibility and surface functionality is facilitated through an organic shell. Common strategies include the coating of inorganic core materials with hydrophilic polymers such as polyethylene glycol (PEG)^[56-59] or polysaccharides such as dextran.^[60] Full organic core-shell structures mainly use polymers on the basis of their glass transition temperature to prepare biodegradable drug encapsulation carriers for biomedical applications.^[61]

1.3 Surface Modification

Surface modification is *a conditio sine qua non* for nanoparticle synthesis to be eligible for biomedical application. The nanoparticles are prepared either in aqueous solution or in organic solvents. In both cases, a suitable application of surfactants is required to prevent agglomeration and to provide colloidal stability. These surfactants also protect pure metal nanoparticles whose surfaces are highly reactive for oxidation. Nanoparticles prepared in nonpolar solvents disperse in organic non-polar media because of their long aliphatic chain surfactants.^[62,63] For biomedical applications, a ligand exchange is mandatory to achieve water solubility and physiological compatibility. Biomedical applications demand control on the intrinsic chemical reactivity of the particles, which may unintentionally affect reaction pathways at the cellular level. Additionally Nanoparticle interact with the immune system after injection into the bloodstream, followed by coverage with serum proteins.^[64] The latter is often referred to as the stealth effect.^[65-67] In order to understand the various tasks of surface ligands in a biological context, we have to analyze biodistribution and functionalization of the DDS.

1.4 Biodistribution and Functionalization of the DDS

FDA (Food and Drug Administration) requirement for all injected contrast agents includes, but is not limited to, full clearance from the body in a reasonable time period.^[68] Two potential ways of body excretion are relevant for the carrier systems. Renal clearance and urinary excretion covering particle and macromolecules smaller 5.5 nm, filtrating them out of the body.^[69,70] Spleen and liver, both major components of the mononuclear phagocyte system (MPS), clean the blood from particles > 10 nm, raising toxicity concerns for non-degradable carrier systems due to increased

accumulation in these organs.^[71] Kupfer cells are responsible for the phagocytic activity of the liver and represent 80-90% of the total body macrophage population.^[72] Macrophage phagocytose combined with the reduced velocity of nanomaterials passing through the liver (up to 1000 times slower than in arteries and veins) explains the increased accumulation of nanomaterials.^[73] Minimize cellular interactions, avoiding opsonization and phagocytose as well as complement activation is possible through various concepts. Opsonization is based on the formation of an opsonin corona (immunoglobulins and components of the complement system) onto foreign materials in the blood. Complemented by the phagocytose, these two mechanism are responsible for blood cleaning of materials larger than the renal threshold limit.^[74] PEGylation of the nanoparticle surface *via* adsorption or covalent binding is known to prevent opsonization and increase the blood circulation time.^[75] The “stealth effect” of PEG yielded numerous reports in the field of liposome- and inorganic nanoparticle-based drug delivery.^[76] The surface coverage with PEG alters the composition of proteins adsorbed on the surface of the materials,^[77] and these proteins (mainly clusterine) are responsible for preventing non-specific cellular uptake.^[78] Functionalization of the silica nanoparticle surface with organosilanes and PEG showed a strong correlation between the ligand density, chain length and charge to biorelated degradation and colloidal stability.^[16,79–81] Avoiding MPS recognition is essential for prolonging blood longevity and favoring passive targeting. Camouflaging of DDS through pre-formed protein or lipid shells can be a beneficial approach. Red blood cell and white blood cell membrane coating showed prolonged blood circulation time of polymeric nanoparticles due to camouflage of the nanoparticle surface.^[82,83] Platelet membrane-cloaked nanoparticles possess a unilamellar membrane coating functionalized with immunomodulatory and adhesion antigens. Lack of particle-induced complement activation resulted in decreased MPS recognition.^[84] Discher et al. utilized the membrane protein CD47 (“marker of self”) for intravenous injection of virus-sized particles, hampering phagocytosis and promoting persistent circulation.^[85]

1.5 Endocytose

The transport of chemotherapeutic drugs, proteins or fluorescent dyes into tumor cells occurs through endocytose (**Figure 1.2a**). Transport included carrier-membrane interaction followed by an engulfment and endosomal distribution to different cell compartments. Phagocytose is primarily observed in cell populations of the MPS (macrophages, dendritic cell) while pinocytosis is classified by participating endocytosis proteins. One can differentiate between a clathrin-dependent and clathrin-independent mechanism.^[86,87] For example, surface charge or particle size influences

nanoparticle uptake. Ligand density and composition are two key characteristics for carrier-cell interaction and determine the pathway for nanoparticle internalization.^[88] Simulations of nanoparticle wrapping in cell membranes showed that next to particle size and geometry, ligand density is an important factor for minimizing endocytic time^[89] (**Figure 1.2b**). Transferrin-coated gold NPs showed clathrin-mediated endocytosis,^[90] while QDs,^[91,92] silica,^[93] iron oxide^[94,95] and silver NPs^[96] showed variable endocytose mechanisms dependent on size, surface charge and functionalizing strategy.

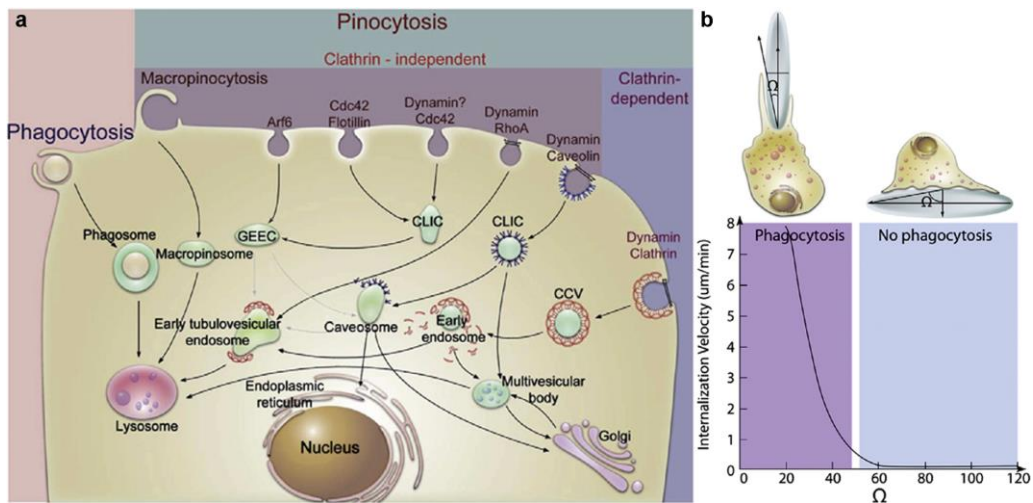


Figure 1.2. Endocytosis of particles and solutes. (a) Multiple pathways for cellular entry of particles and solutes. In all cases, the initial stage of endocytosis proceeds from the plasma membrane portals of cellular entry and involves engulfment of cargo into intracellular vesicles. The second stage involves sorting of the cargo through endosomes. It is followed by the final stage where the cargo is delivered to its final destination, recycled to the extracellular milieu or delivered across cells (not shown). Abbreviations are: CCV, clathrin coated vesicles, CLIC, clathrin-independent carriers; GEEC, GPI-anchored protein-enriched compartment; GPI, glycosylphosphatidylinositol, MVB, multivesicular body. (b) Effect of particle geometry on phagocytosis. The entry of nanoparticles inside macrophages depends on the angle between the membrane normal at the point of initial contact and the line defining the particle curvature at this point (Ω). The internalization velocity is positive at $\Omega \leq 45^\circ$, which indicates that the particle undergoes internalization. As the angle exceeds critical value ($\approx 45^\circ$) the internalization velocity is zero, the macrophages lose the ability to entrap particles and start spreading over the particle. Adapted with permission from ref.^[87].

1.6 Bio-Nano Interface

To understand the dynamic interactions of the bio-nano interface, we have to consider the nanoparticle surface and its solid-liquid contact zone with the biological environment. Physicochemical characteristics of the nanoparticle like chemical composition, surface functionalization, angle of curvature, porosity and surface crystallinity are key properties to understand the bio-nano interaction. Other quantifiable properties, such as effective surface charge (zeta potential), particle aggregation, state of dispersion, stability/biodegradability and dissolution characteristics are determined by the characteristics of the suspending media ^[64,90-94] **(Figure 1.3)**.

Possible side effects arising from uncontrolled or harmful interaction of the nanoparticle surface with the biological environment. Polymer-based spacers minimize interaction of the nanoparticle with the cell membrane. Another approach is to form an inorganic shell around the nanoparticle with accessible anchor groups for ligands, proteins and fluorescent dye labels on the surface. The interaction of the nanoparticle with cells is a sum of different contributions, ranging from traditional forces for colloids (attractive van der Waals (VDW) and repulsive electrostatic forces) to complex biomolecule interactions including receptor-ligand binding and membrane wrapping. These forces can be short-range (1-100 nm) for polymer bridging, steric and solvent interaction or long range for (up to 10^2 - 10^6 nm) for hydrodynamic interactions like Brownian diffusion and convective drag.^[71,97] Nanoparticles tend to aggregate when the energy for a single particle distribution in solution is smaller than the aggregation energy. PEG chains are able to stabilize the nanoparticles in solution sterically, resulting in a minimal particle-particle interaction. The decisive factor for stabilization is the surface concentration and chain length of the PEG spacer.^[102,103] Another approach to ensure colloidal stability is the electrokinetic stabilization of nanoparticles.

High surface charge (zeta potential of ± 20 mV) guarantees repulsion for each nanoparticle surface. The size of the carrier system is crucial for efficient cancer treatment (depth of penetration, aggregation) and is variable depending on the biological task. Nanoparticles larger than 10 nm avoid renal clearance and do not accumulate in the kidney. Sequestration by sinusoids in the spleen and fenestra of the liver filter nanoparticle from the bloodstream larger than 200 nm **(Figure 1.4)**. Gold nanoparticles have shown a size and shape dependence for uptake into mammalian cells.^[104] Ultraviolet radiation of human skin revealed deep penetration of small quantum dots, but not of TiO₂ and polystyrene nanoparticles.^[105] Sub-100 nm polymeric micelles showed a size-dependent accumulation in poorly permeable pancreatic tumors, which

increases for larger micelles when transforming growth factor- β inhibitor-affected tumor permeability.^[106] PEG-coated spherical and rod-shaped quantum dots deviate in their tumor penetration capabilities, suggesting the use of rod-shaped nanotherapeutics for efficient cancer therapy.^[107] Additionally, microfluidic systems mimicking the tumor vasculature showed a shape-dependent enhancement of the endothelial targeting of antibody-coated polystyrene nanoparticles.^[108] Real-time *in vivo* microscopic imaging was utilized to compare the extravasation of spherical quantum dots and rod-like single-walled carbon nanotubes (SWNTs) in three murine tumor models. Despite similar surface coatings, area, and charge, the nanoparticle shape and physical parameters of the tumor endothelium are responsible for increased extravasation.^[109] Multistage delivery systems utilize the tumor microenvironment (TME) in order to overcome biological barriers by subsequent degradation. Larger particle constructs aim to prolong the blood circulation and exploit passive targeting via enhanced permeability and retention effect (EPR). After TME triggered fractionation, smaller particles and molecules are capable to penetrate deeper into the tumor tissue. MSN and polymeric clustered nanoparticles showed efficient delivery of chemotherapeutics and deep penetration into cancer cells *in vivo*.^[110-112]

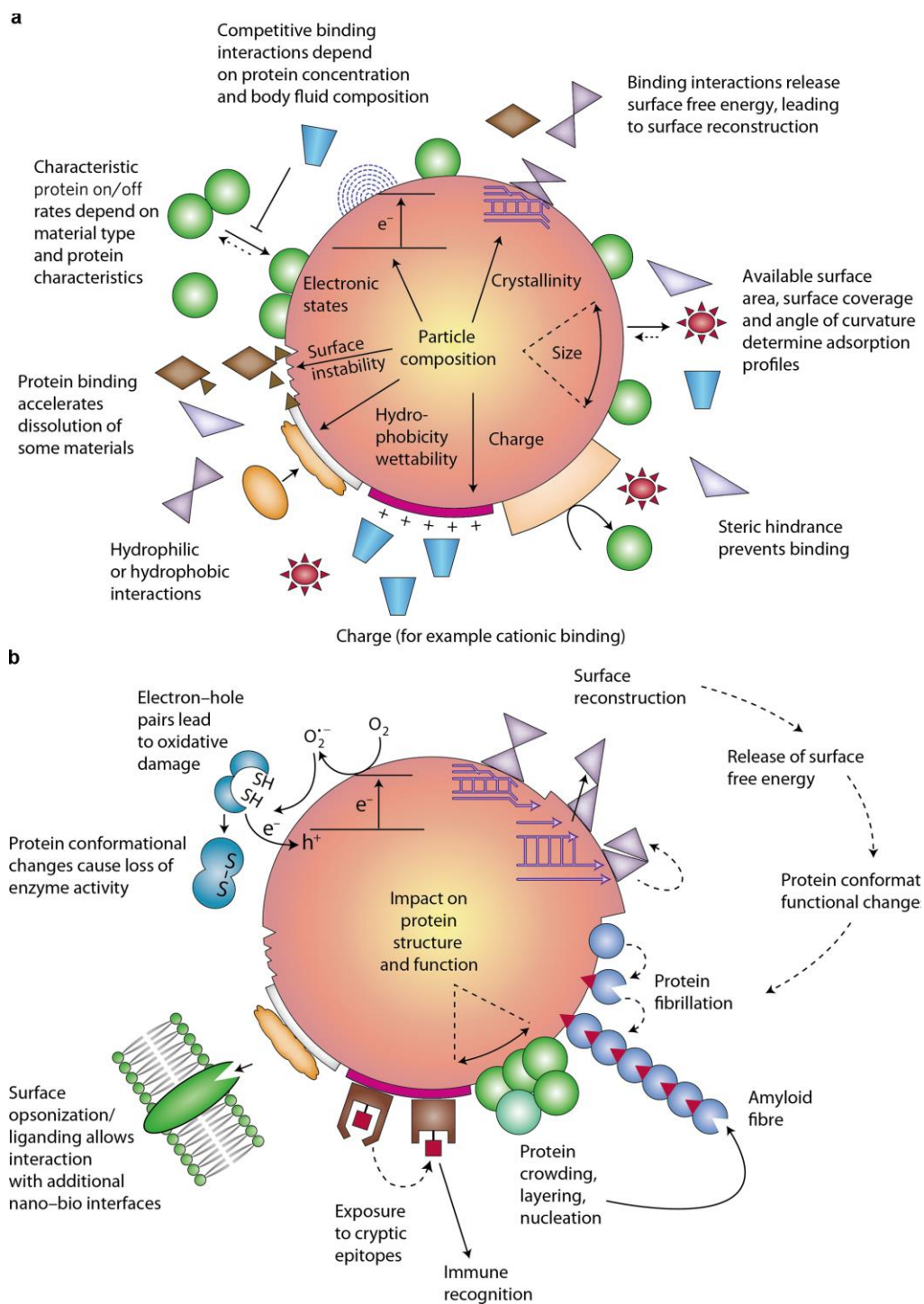


Figure 1.3. Effects of protein corona surrounding a nanoparticle. The corona constitutes a primary nano-bio interface that determines the fate of the nanoparticle and can cause deleterious effects on the interactive proteins. (a) Pre-existing or initial material characteristics contribute to the formation of the corona in a biological environment. Characteristic protein attachment/detachment rates, competitive binding interactions, steric hindrance by detergents and adsorbed polymers, and the protein profile of the body fluid lead to dynamic changes in the corona. The corona can change when particles move from one biological compartment to another. (b) Potential changes in protein structure and function as a result of interacting with the nanoparticle surface can lead to potential molecular mechanisms of injury that could contribute to disease pathogenesis. The colored symbols represent various types of proteins, including charged, lipophilic, conformationally flexible proteins, catalytic enzymes with sensitive thiol groups, and proteins that crowd together or interact to form fibrils. Adapted with permission from ref.^[97].

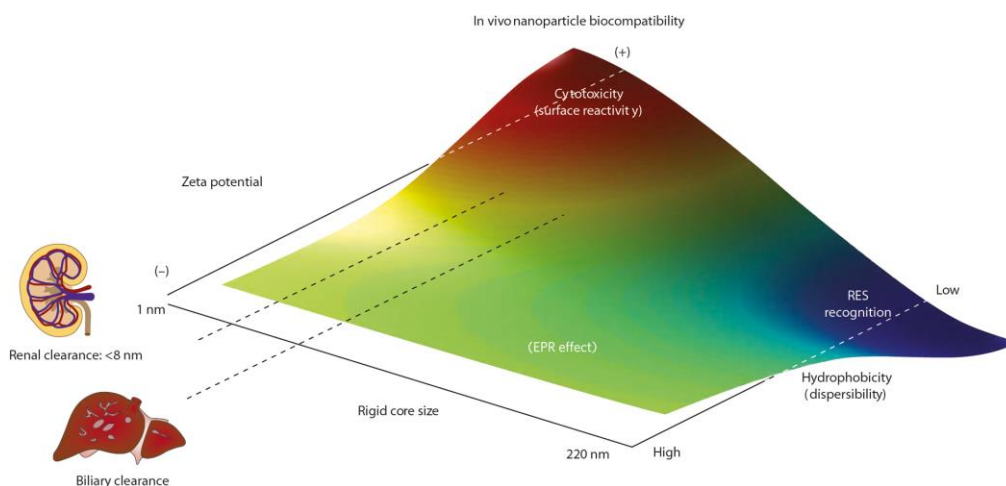


Figure 1.4. Physical characteristics of nanoparticles determine *in vivo* biocompatibility. The three-dimensional phase diagram displays the qualitative biocompatibility trends revealed after *in vivo* screening of around 130 nanoparticles intended for therapeutic use.^[113] The main independent particle variables that determine the *in vivo* biocompatibility (color spectrum) are size, zeta potential (surface charge) and dispersibility (particularly the effect of hydrophobicity). Biocompatibility is reflected in the color spectrum, with red representing likely toxicity, blue likely safety and blue–green–yellow intermediate levels of safety (in the same order). Cationic particles or particles with high surface reactivity are more likely to be toxic (red hue) than the larger relatively hydrophobic or poorly dispersed particles, which are rapidly and safely (blue hue) removed by the RES. Particles that promote EPR effects-and are therefore optimal for chemotherapeutic drug delivery to cancers-generally have mid-range sizes and relatively neutral surface charges. Reprinted with permission from ref.^[97]. Copyright Macmillan Publishers Ltd 2009.

1.7 Protein Corona

Several obstacles and barriers interfere with drug delivery after injecting DDSs into the bloodstream. They must disseminate by tissue perfusion, penetrate across microvascular walls and then distribute throughout the tumor stroma.^[114] The formation of a protein corona is a natural consequence of carrier-cell interactions *in vitro* and *in vivo*. They are caused by the adsorption of proteins on the high energy surface of the nanoparticle.^[98] NP properties like, size, composition, shape, crystallinity and conformational changes of proteins upon binding affect the composition, thermodynamics and kinetics of the protein corona.^[115] Solid and mesoporous silica nanoparticles with various sizes show a correlation of external surface area, surface curvature and porosity with the protein corona formation.^[116] Silica nanoparticles and gold nanoparticles show an aggregation and size increase due to corona formation and phagocyte interaction, which is described as their "biological identity".^[117]

Important physical properties that affect the composition of the protein corona are the surface charge of the DDS. Although surface charge is responsible for colloidal stabilization, interaction with counter charged solvent (medium) or ligands may lead to increased aggregation, e.g. *via* protein corona forming.^[117] We can distinguish between

a tightly bound monolayer of biomolecules (“hard” corona) and a more loosely associated and highly fluctuating layer (“soft” corona)^[118,119] (**Figure 1.5**). In general, proteins like apolipoprotein-1, albumins, immunoglobulins and complement proteins constitute the majority of the corona.^[120] Polystyrene NPs showed reduced clearance by the MPS *in vivo* due to a pre-coating of albumin on their surface. Additionally, the coating prevents adsorption of opsonization-active serum proteins.^[121] Mailänder and coworkers could verify apolipoprotein (Apo) assisted cellular uptake and identify ApoA4 or ApoC3 to be responsible for the decreased cellular uptake.^[122] Polystyrene and silica nanoparticles incubated with disease-specific human plasma showed a “personalized protein corona”, correlating medical conditions to plasma protein concentrations and structures.^[123]

Puntes *et al.* described protein corona formation of metal (Au, Ag) and metal oxide (Fe₃O₄, CoO, CeO₂) nanoparticles that can reduce reactive oxygen species (ROS) formation.^[124] The hydrophobicity of zwitterionic nanoparticles could be tuned to avoid hard corona forming in serum,^[125] showing the interconnection between nanoparticle surface interaction (chemical motif), cellular uptake and hemolysis. Another problem of protein corona formation is that “active targeting ligands” on the particle surface can be hidden, thereby preventing receptor mediated endocytose. Solid fluorescent silica nanoparticles conjugated with human transferrin showed a loss of targeting capabilities when a protein corona is formed on their surface.^[126] Many efforts were made to enhance cellular uptake minimize off-target drug delivery and control nanoparticle blood circulation time by tuning corona formation. Nevertheless, for successful exploiting corona formation for drug delivery application, the quantification and characterization have to be emphasize. A range of carrier compositions, particle sizes and surface charges need systemic analysis of protein corona formation to allow a better understanding of the protein corona formation in nanoparticle assisted cancer therapy. Isothermal titration calorimetry and surface plasmon resonance spectroscopy were employed to quantify the exchange rates and protein affinities on copolymer nanoparticles.^[127]

A time-dependent analysis of the protein corona on silica and polystyrene nanoparticles identified almost 300 different proteins. The rapid corona formation (< 0.5 minutes) did not show a significant change of the composition with time, yet increased amount of adsorbed protein. The fast corona formation could be correlated with different carrier-cell interaction mechanism like hemolysis, nanoparticle uptake and endothelial cell death.^[128] Chan et al. were able to analyze 105 surface functionalized gold nanoparticles with a bioinformatics approach to predict cellular interaction and biological response

through protein corona fingerprints.^[129] Mohr et al. showed sample preparation and measurement technique to be crucial for corona formation, which indicates that protein corona identification and characterization must be handled with care.^[130] To compare protein corona formation *in vitro* and *in vivo*, superparamagnetic iron oxide NPs (SPIONs) were magnetically extracted after intravenous injection in rats. Pronounced differences in the hard corona formation was detected during *ex situ* analysis, and question the validity of previous *in vitro* experiments for screening toxicity or uptake mechanism of DDS.^[131]

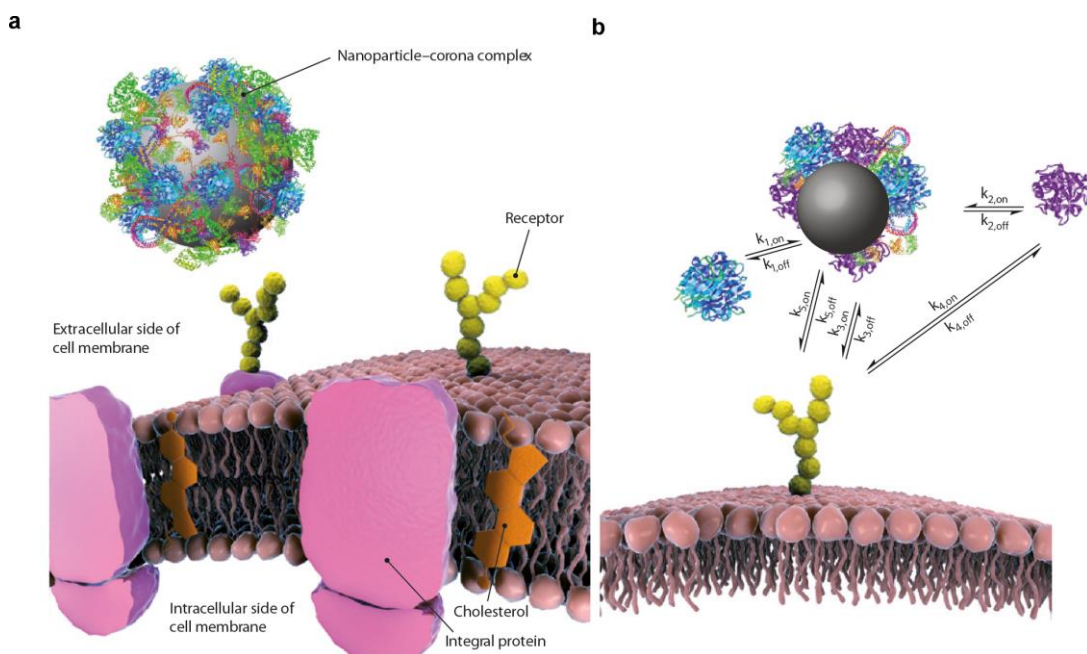


Figure 1.5. The nanoparticle–corona complex in a biological environment. (a) It is the nanoparticle–corona complex, rather than the bare nanoparticle, that interacts with biological machinery, here with a cell membrane receptor. (b) Relevant processes (arrows), in both directions (on/off), for a nanoparticle interacting with a receptor. Biomolecules in the environment adsorb strongly to the bare nanoparticle surface (k_1), forming a tightly bound layer of biomolecules, the ‘hard’ corona, in immediate contact with the nanoparticle. Other biomolecules, the ‘soft’ corona, have a residual affinity to the nanoparticle–hard-corona complex (primarily to the hard corona itself), but this is much lower, so those molecules are in rapid exchange with the environment (k_2). If sufficiently long-lived in the corona, a biomolecule may lead to recognition of the nanoparticle–corona complex as a whole by a cell-membrane receptor (k_3). The same biomolecule alone can also be recognized by the receptor (k_4). If present, the bare surface of the nanoparticle may also interact with cell surface receptors (k_5) or other constituents of the cell membrane. Reprinted with permission from ref.^[118]. Copyright Macmillan Publishers Ltd 2012.

1.8 Tumor Microenvironment

The solid tumor is composed of three basic components, that is > 50% tumor cells, 1-10% vasculature and < 35% interstitium (collagen-rich matrix).^[132] In humans, vessels range in diameter from 2.5 cm in large arteries to about 7 μm in capillaries and the volume of blood in an adult is about 4–5 L.^[133] In the TMI, uncontrolled cell growth and constant release of pro-angiogenic factors organize blood vessels more chaotically. Unlike the endothelial lining of normal vasculature, which has a turnover of approximately 1.000 days, the endothelium in tumors can double approximately every 10 days.^[134] Increased proliferation rate combined with confined space leads to an extremely high cell density, approaching or even exceeding 60%.^[132] This leads to dense areas of collagen rich vasculature, inducing enormous mechanical stress onto the cells. Spatial restriction and lack of supportive stromal structures leads to compress and collapse blood vessels, limiting blood supply, oxygen supply and resulting in hypoxic and necrotic tumor tissue.^[135]

Hypoxia, a hallmark of growing tumor tissue, is responsible for tumor properties ranging from chemoresistance and radioresistance to invasiveness, metastasis and resistance to cell death.^[136] Limited oxygen diffusion in abovementioned chaotic tumor blood vessels causes hypoxia. Especially critical is the increased intercapillary distance,^[137,138] exceeding oxygen diffusion range (up to 200 μm ^[139]), and establish a relationship between tumor vascularity and hypoxia.^[140] Hypoxia is known to aid tumor progression and metastasis (angiogenesis, inducing genetic instability, resistance to cell death by apoptosis and autophagy)^[141–143] and confers resistance against numerous cancer therapy (chemotherapies, radiation) due to the lack of oxygen.^[144,145] Optical frequency domain imaging (OFDI) as an intravital microscopy was utilized to clearly image vascular abnormality and necrotic/apoptotic areas of the tumor microenvironment *in vivo*.^[146]

In addition to visualizing necrotic/apoptotic areas and chaotic blood vessels, anti-angiogenesis therapy via vascular epidermal growth factor receptor (VEGFR) targeting showed promising results in controlling rampant tumor growth (**Figure 1.6**). In addition to hypoxia, chaotic blood vessels and necrotic/apoptotic areas, the two characteristics of interstitial fluid pressure (IFP) and ROS, define the TMI. The inability of the tumor stroma to maintain pressure gradients across the blood vessel walls increases IFP relative to the tumor periphery. Reduced or impaired ability of DDS for deep penetration and increased supply shortage of the tumor core is the result. Increasing tumor sizes lead to increased IFP in both human and animal tumors,^[147] and therefore large tumors are more difficult to treat than small ones.^[148]

Baxter and Jain investigated the therapeutic effect of monoclonal antibodies in solid tumors. They observed an inhomogeneous distribution in the tumor despite increased vascular permeability. They concluded that elevated interstitial pressure combined with heterogeneous blood perfusion, extravascular binding and hampered diffusion is responsible for the poor therapeutic outcome.^[149] By a mathematical description of these phenomena Jain et al. demonstrated for the first time an intratumoral elevated IFP, which drops abruptly to a normal level in the surrounding tissue.^[150] Besides elevated IFP, limited delivery of carrier systems to cells is linked to the high oncotic pressure (colloid osmotic pressure) in tumors.^[151] Further reduction in transport and diffusion of macromolecules and nanoparticles in the extracellular matrix (ECM) is based on the existing electrostatic interactions and collagen-derived resistance.^[152] Tissue resistance to macromolecular transport may be promoted by mucopolysaccharide in the ECM.^[153] It was suggested that maximum delivery capabilities are possible through cationic charged particle for vasculature targeting followed by change to neutral charge after exiting the bloodstream.^[154] ROS have essential functions in living organisms but display highly increased values in tumors.^[155]

They are known through metal oxide nanoparticle-induced ROS generation, inducing oxidative stress.^[156] Intracellular, mitochondria produces ROS during oxidative phosphorylation. The highly proliferating tumor microenvironment uses ROS for oxidative stress-mediated signaling, advancing energy metabolism, proliferation and cell survival.^[157] Stimulative response of different growth factors and cytokines (TNF- α , IFN- α) on the TMI induces upregulation of ROS production and increased ROS level. The adaption of tumor tissue to these harsh environmental factors is possible through multiple pathways, ranging from increased expression of anti-oxidant molecules to function alteration in cell death factors. This ROS-mediated adaptations lead to altered drug metabolism, drug resistance and chemotherapeutic resistance of the cancer tissue.^[158] To counterbalance these highly energetic and chemically reactive species, detoxification of cancer cells is achieved through increased levels of antioxidant protein (glutathione, superoxide dismutase, flavonoids and different vitamins).^[159] The vicious cycle of increased ROS levels leading to ROS induced gene mutations and consequently to additional metabolic malfunctions^[158] makes a ROS-mediated mechanism for selective therapeutic treatment plausible. One can distinguish between ROS generation,^[160-162] promoting ROS production to unsustainable levels for cell killing or ROS elimination through inhibiting redox regulatory mechanism. This approach aims to disable redox adaption and redox-sensitive survival molecules, tipping the balance in intracellular ROS level control.^[163,164]

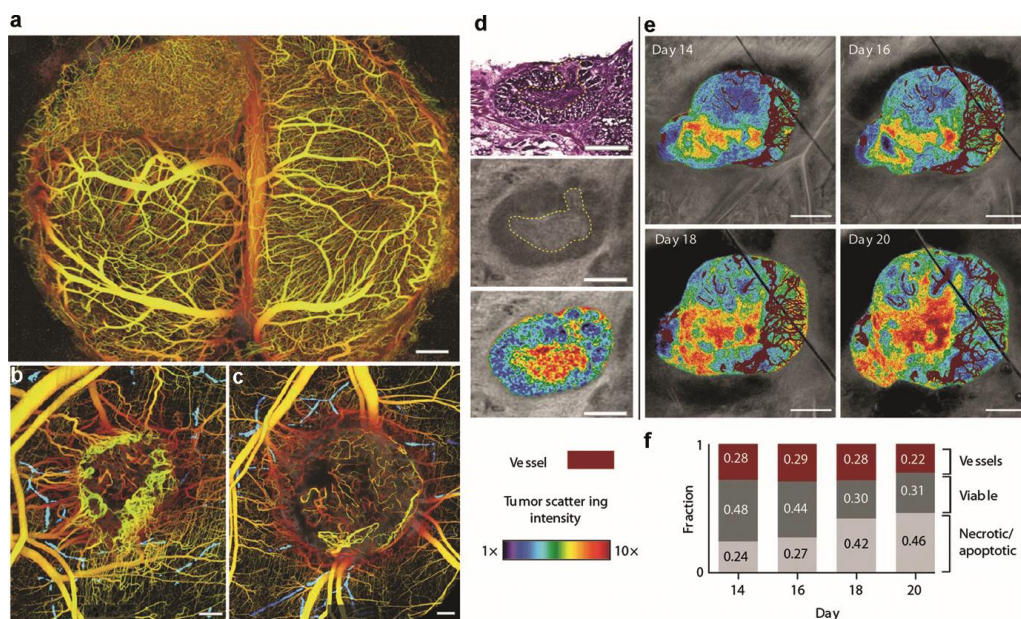


Figure 1.6. Vessel density and hypoxic/necrotic areas in developing tumors and the impact of antiangiogenic treatment onto tumor blood vessels. (a) Depth-projected vasculature within the first 2 mm of mouse brain bearing a xenotransplanted U87 human glioblastoma multiform tumor imaged with OFDI. Depth is denoted by color: yellow (superficial) to red (deep). Scale bar, 500 μm . (b) OFDI images of representative control and (c) treated tumors 5 d after initiation of antiangiogenic VEGFR-2. The lymphatic vascular networks are also presented (blue) for both tumors. Scale bars, 500 μm . (d) Comparison of standard H and E staining (top) with OFDI (middle) reveals association of tissue necrosis with highly scattering regions. Viable and necrotic regions within the same tumor are highlighted by color gradients indicating scattering intensity (bottom). (e) Scattering properties correlated with the microvasculature during tumor progression, illustrating the expansion of necrotic or apoptotic regions in areas with minimal vascular supply. (f) Quantitative analysis of tissue viability and vascular regions *in vivo*, revealing an increase in the fraction of necrotic or apoptotic tissue during tumor progression. Scale bars d, 500 μm ; e, 1 mm. Adapted with permission from ref.^[146].

1.9 Passive and Active Targeting

Passive and active targeting achieves drug delivery of chemotherapeutics to cancer cells (**Figure 1.7**). Passive targeting utilizes the abnormal vasculature formation of highly proliferated tissue. Fast tumor growth and chaotic vasculature lead to a preferred accumulation of polymers with high molecular weight and nanoparticles inside the tumor stroma (EPR effect)^[165]. Neocarzinostatin (SMANCS) conjugated with maleic acid to polystyrene in a murine tumor model was used to show the preferential accumulation at locations of increased vascular permeability (solid hepatocellular carcinoma).^[166] Jain and coworkers^[167] developed a microvascular permeability measurement technique to quantify the increased permeability and diffusivity of dextrane macromolecules in solid tumors. Passive targeting via EPR provides a higher accumulation of the transported drugs in the tumor tissue, thereby sparing healthy tissue and reducing off-target damage. One has to distinguish between the permeability of cancer blood vessels and the retention of nanoparticles or macromolecules. The

biological characteristics of blood vessels consist of well-defined smooth muscle cells and pericytes, an organized vessel architecture, a homogeneously distributed junction of endothelial cells, a functional lymphatic drainage and an underlying basement membrane.^[6,168,169]

The permeability of the tumor neovasculature develops from the necessity to maintain a sufficient supply of nutrients and oxygen (rapid tumor angiogenesis).^[170] This leads to aberrant vascular structures, adapted endothelial-cell-pericyte interactions, abnormal blood flow, increased permeability and delayed maturation, i.e. a complete change of the characteristics of normal blood vessels. An elevated microvessel density in the tumor is believed to advance the successful therapeutic outcome because of the EPR effect.^[171] Depending on the tumor type, the pores of the tumor vasculature are typically in the 100–800 nm size range.^[64] Matsumoto et al. showed that the permeability of the tumor blood vessels are based on a vigorous outward flow of fluid into the tumor interstitial space.^[172] Defect or insufficient lymphatic drainage facilitates retention of the nanoparticles or macromolecules. Increased endothelial fenestration, architectural anarchy and dysfunctional or collapsed lymph vessels lead to decreased lymphatic drainage and thus to accumulation of nanoparticles inside the tumor stroma.^[97,170,173] A major analysis of the EPR effect and the accumulation of nanomedicines in solid tumors was conducted in small animal models. In comparison, clinical data and experimental evidence for an increased accumulation *via* the EPR effect in humans are scarce. Tumor accumulation in humans was tracked with radiolabeled liposomes.^[174,175]

Local colocalization of camptothecin and CRXL101 was demonstrated, however, only by a single human gastric tumor biopsy and for human breast cancer.^[176,177] In this context, CRLX101 is a nanoparticle consisting of a cyclic oligosaccharide polymer associated with camptothecin (topoisomerase inhibitor for cancer chemotherapy). Approximately five strands self-assemble into nanoparticles with diameters of approx. 30 nm. The existence of the EPR effect has been shown conclusively only in animal models of human cancers. Recently, Davis and coworkers^[178] showed it to be efficient in humans as well. In addition to passive targeting, nanoparticles use active targeting (cell specific interaction) for guided drug delivery and release on demand at the cellular level. Targeting agents like receptor ligands (peptides, vitamins, and carbohydrates),^[179–182] proteins (mainly antibodies and their fragments)^[183–185] or nucleic acids (aptamers)^[186,187] are utilized in active targeting strategies. Examples of FDA approved antibodies for cancer therapy include rituximab^[188] (anti-CD20, B-cell surface antigen), trastuzumab^[189] (Anti-ERBB, HER2 receptor), and bevacizumab^[190] (anti-VEGF,

VEGF receptor).^[170] The ability of an antibody or protein to recognize cell specific receptors enables active targeting. First example for active targeting of nanoparticles utilized fluorescent liposome antibody construct. The heterobifunctional cross-linker N-succinimidyl 3-(2-pyridyldithio)propionate (SDPD) was used to covalently couple mouse monoclonal antibody against human β 2-microglublin to the liposomes.^[191] Overexpression of small peptide receptors has been documented for many examples of cancer.^[192] For active targeting, the receptor density should be in the range of 10^4 - 10^5 copies per cell. Lower densities in cell populations are less efficiently targeted.^[193] Tumors in the millimeter size range (1–2 mm) appear to have no vasculature.^[194]

Without the proper pathophysiological characteristics (EPR effect) active targeting in small metastases ($< 100 \text{ mm}^3$) can be a suitable treatment strategy^[195] by increasing the selectivity compared to passive targeting. The prerequisites are a strong ligand–receptor interaction (affinity) or multiple ligand-receptor interactions (avidity)^[196]. Controlled density and accessibility of the targeting ligands on the carrier is key for active targeting. With transferrin-coated gold nanoparticles the tumor accumulation was enhanced by the nanoparticle avidity, the accumulation being 5 times faster and 2-times higher compared to passive targeting.^[197] Dendrimer-bound folate molecules showed a 2.500-170.000-fold increase of the dissociation constants (KD) compared to free folate.^[198] Multivalent target binding is one approach to ensure antibody-antigen interaction, but increasing the amount of ligand on the nanoparticle surface does not necessarily increase the avidity due to steric considerations.^[199] The mode of action for antibody therapy depends on the individual targeted tumor antigen and may range from a downregulation of the cell surface receptors to an activation of the antibody-dependent cell-mediated cytotoxicity (ADCC) or the complement-dependent cytotoxicity (CDC).^[199] For active targeting strategies we may distinguish between cancer cell and tumor endothelium targeting.

These two strategies include receptor-mediated internalization of encapsulated chemotherapeutics for reduced off-target damage and direct cell killing strategies that exploit tumor angiogenesis by targeting VEGF receptors in the tumor-associated vasculature. Transferrin, folate, glycoproteins and epidermal growth factor (EGFR) are all suitable targeting receptors for active targeting of cancer cells. These receptors are highly overexpressed, they have an internalization-prone mechanism (endocytosis-prone surface receptors)^[200] and their targeting ligands can easily be conjugated to the carrier.^[201] Therapeutic targeting of the tumor microenvironment^[202,203] can be implemented in various ways, which makes the tumor stroma^[204] a viable target for

cancer therapy. Angiogenesis-associated targeting^[205,206] is effective in limiting the tumor growth. It normalizes the tumor stroma, reduces the IFP and increases oxygen flow, blood and nutrient supply. This leads to a deep penetration of the nanocarriers that avoid the chaotic tumor vasculature and the associated physiological barriers and is a suitable treatment for all cancer types.^[114,207,208] IFP reduction by 65% through collagenase-1 induced type-1 collagen depletion led to a higher accumulation and gene expression for intravenously injected lipoplexes.^[209] In addition, disrupting the growth of the blood supply cripples the metastatic capabilities of the primary tumor and reduces the secondary drug resistance due to smaller phenotypic variations in the neovascular endothelial cells.^[210] Tumor vascular targeting through a neovascular proliferation biomarker ($\alpha_v\beta_3$ -integrin) was utilized to deliver doxorubicin resulting in a reduced metastatic activity.^[211] Another approach to normalize the tumor neovasculature is to block the VEGF. VEGF-specific antibodies like bevacizumab are able to normalize the tumor vessel and to reduce the interstitial fluid pressure in animal and human models.^[212] Vascular normalization by the VEGF receptor-2 blocking antibody DC101 showed improved delivery of quantum dots in a size-dependent manner. It was suggested that 12 nm nanoparticles are optimum for deep penetration, owing to the DC101 induced reduction of the IFP.^[213] Ribal et al.^[214] demonstrated the capability of non-antibody targeting ligands with a human transferrin glycoprotein targeting ligand that induced an RNAi activity in humans *via* siRNA delivery. This study demonstrated for the first time a dose-dependent accumulation of targeted nanoparticles in human tumors. It showed the potential of active targeting to elucidate the EPR effect and the concept of passive targeting in humans.

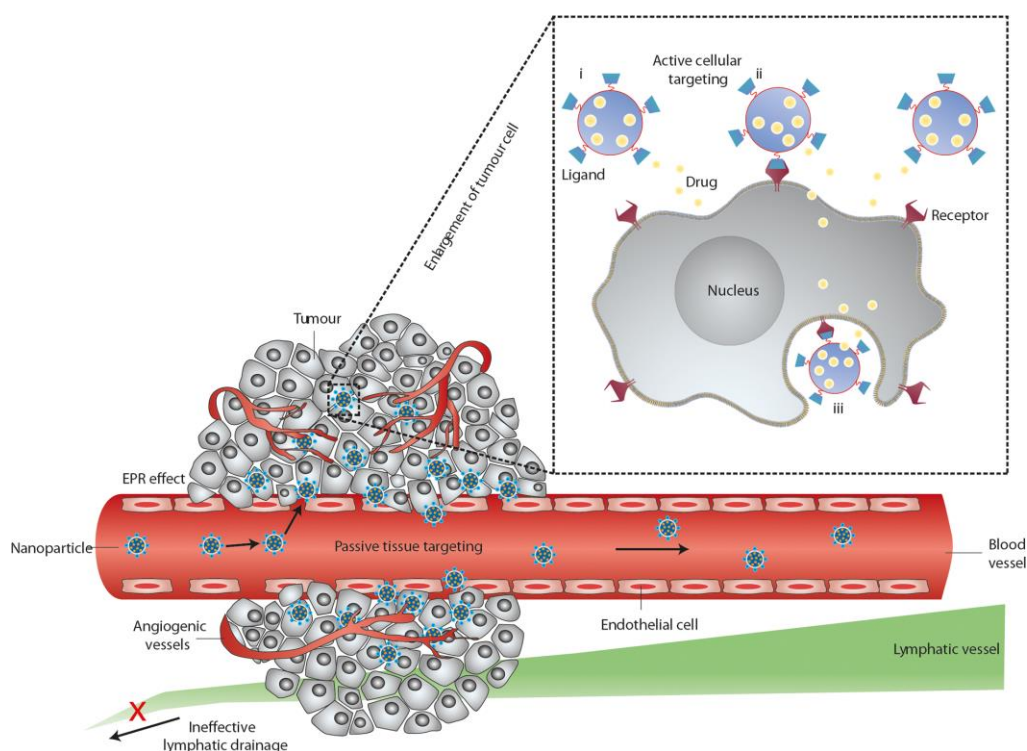


Figure 1.7. Physical characteristics of nanoparticles determine *in vivo* biocompatibility. Schematic representation of different mechanisms by which nanocarriers can deliver drugs to tumors. Nanoparticles are shown as representative nanocarriers (circles). Passive tissue targeting is achieved by extravasation of nanoparticles through increased permeability of the tumor vasculature and ineffective lymphatic drainage (EPR effect). Active cellular targeting (inset) can be achieved by functionalizing the surface of nanoparticles with ligands that promote cell-specific recognition and binding. The nanoparticles can (i) release their contents in close proximity to the target cells; (ii) attach to the membrane of the cell and act as an extracellular sustained-release drug depot; or (iii) internalize into the cell. Reprinted with permission from ref.^[6]. Copyright Macmillan Publishers Ltd 2007.

1.10 Gatekeeper

Gatekeeper prevent premature release and offside host-drug interaction of drug-loaded nanoparticle and is particularly important for biologically sensitive agents and highly toxic cargos. Insufficient shielding results in enzymatically degradation and damage to healthy tissue and organs. One example is the highly-cytotoxic tumor necrosis factor- α ^[215,216] (TNF- α Beromun), whose short half-life and acute toxicity makes it only applicable for the treatment of non-resectable tumors of the extremities *via* isolated limb perfusion (ILP).^[217] Encapsulation and transport of this protein through mesoporous silica nanoparticle could broaden its application.^[218] Important characteristics for drug delivery applications is the capability of zero premature release of the drug during storage and after incubation with a protein-rich matrix. Lin and coworkers^[219] were the first to functionalize MCM-41 mesoporous silica particles with cadmium sulfide NPs to ensure zero premature release of vancomycin and adenosine triphosphate (ATP) by physically blocking of the pore entrance. Gatekeeper systems

have to release the cargo through tumor cell specific mechanisms and triggers, utilizing the TMI and intrinsic features of the tumor phenotype. TMI properties like pH increase, oxygen deficit, elevated ROS level and intracellular glutathione concentration trigger intracellular release of the active ingredient. pH-triggered release systems depend on the low pH value within the lysosome/endosomal compartment inside tumor cells and the evaluated pH value outside the cell. A possible explanation for the increased external H^+ concentration is the high lactate production through increased glycolytic metabolism (aerobic glycolysis, Warburg effect^[220] and carbon dioxide concentration (oxidative metabolism).^[221,222]

The hypothesis that mitochondrial defects cause insufficient oxidative phosphorylation and - as a result - cancer, was modified some time ago when it was shown that the mitochondrial metabolism is reprogrammed by altered oncogenes and tumor suppressors.^[136] Increased abnormal vasculature formation of high proliferation tissue, elevated interstitial pressure and decreased lymphatic drainage lead to the observed increased of the pH value. Endosomal fusing with lysosomal vesicles after endocytose exposed the delivery system to pH values up to 4.5^[223] to trigger pH induced drug release. This pH induced gate effect was first utilized by Latorre et al.^[224] through polycondensation of amino silane onto mesoporous MCM-41 materials. pH-triggered release *via* biocompatible polycations like poly(2-vinylpyridine) (PVP)^[225,226] and poly(ethylene imine) (PEI)^[111,227-242] is an efficient method to encapsulate and deliver various small molecules, small interfering RNA (siRNA) and chemotherapeutics *in vitro* and *in vivo*. The key was to control the toxicity of high charged polycations^[243-245] onto cells and a successful release of the loaded drug into the cytosol through lysosomal escape. The proton sponge effect of aforementioned polycations is a controversial issue. It is unclear, if the large buffer capacity of PEI and other polycations is the main factor responsible for a successful endosomal/lysosomal escape.^[246-248]

Inherent problems of siRNA therapeutics are intravascular nucleotide degradation, proper tissue penetrance, immune-mediated toxicities and complete release of the siRNA into the cytosol after endocytose.^[168] The combination of modified PEI and MSN were used to co-deliver doxorubicin (inducing apoptosis) and siRNA (gene suppression of cellular anti-apoptotic defense and drug exporter) to overcome multidrug-resistant cancer cells.^[249-251] Additionally, anti-angiogenic response *in vitro* and *in vivo* was possible through knockdown of the TWIST1 transcription factor^[228] and suppression of neovascularization *via* VEGF.^[232] Numerous applications of pH gated polymer systems^[252,253] have been used in drug delivery applications, including transport of bioimaging nanosystems^[254] or delivery of anthracyclines as chemotherapy agents.^[255]

Poly(N-succinimidyl acrylate) (PSA) combined with an acid-labile acetal linker was used to encapsulate the antineoplastic antibiotic doxorubicin, functionalized with PEG (in order to decrease non-cellular uptake) and decorated with folic acid for folate receptor targeting.^[256] Redox-responsive release can be achieved by reducing unstable redox linkers (e.g. disulfide bridges) by the redox couple glutathione (GSH) / glutathione disulfide (GSSG).^[257] The intracellular glutathione concentration ranges from 0.5 to 10 mM, the corresponding extracellular values are one to three orders of magnitude lower.^[258,259] The anti-oxidative capacity of cells and the associated release potential can be utilized for surface coverage,^[260] drug encapsulation and transport^[261,262] or for an enhanced degradability of the carrier system.^[263]

Another approach to release the drug at the tumor site depends on external stimuli such as light, ultrasound and temperature. Temperature-dependent release of the loaded drug is possible through conformational change of the polymer chains by heating with light or utilizing metal-based nanocarriers for hypothermal treatment.^[264,265] Photothermal activation of the gate system via near infrared (NIR),^[15,266–268] ultra-violet (UV),^[269] red light^[270] or enzymatic degradation of a biodegradable gatekeeper are viable alternatives for drug release. Biodegradation is based on the nature of cellular proteases to degrade the gatekeeper inside the lysosome.^[169,271,272] Fukumura and coworkers^[273] were able to establish a multistage delivery system, enzymatically degradable by proteases that are highly expressed in the TMI to ensure long circulation half-life and deep tumor penetration. Tumor targeting and release triggered by the matrix metalloprotease 2 (MMP 2) is a potent concept for drug delivery.^[274,275] Supramolecular interactions of proteins enables alternative approaches to encapsulate highly toxic chemotherapeutic agents in carrier systems. The interaction between avidin or streptavidin and biotin^[276] (strong non-covalent biological interaction ($K_d = 4 \cdot 10^{-14}$ M)^[277] leads to a light-responsive protein shell, covering an MSN for successful doxorubicin delivery.^[278] Aptamers^[279] are nucleic acid ligands generated with SELEX (systematic evolution of ligands by exponential).^[280] Compared to siRNAs, where the therapeutic target is only intracellular, aptamers can be used for intracellular, extracellular^[281] or cell-surface targets^[282] and stimuli-responsive drug delivery.^[283,284]

The protocell is a unique class of nanocarrier devised by the Brinker group several years ago. It combines features of mesoporous silica particles and liposomes in a synergistic fashion. The combination of a high surface area and the rigid structure of the silica core combined with a lipid bilayer coverage for drug encapsulation and targeting moieties represented a 10^6 fold improvement in cancer cell killing over comparable liposomes.^[285] Further developments made contributions to the treatment of

neuromuscular disorders and leukemia *via* individual cell targeting.^[286,287] All strategies described above are individually capable of drug delivery and cell targeting. To ensure complete on-site drug release as well as co-delivery of different chemotherapeutics, internal and external stimulus can be linked. This combined approach is enabling site-specific drug release and the possibility for chemotherapy and photodynamic therapy.^[288] The pH/redox-responsive nanocomplexes^[289–292] and light- and pH-triggered intracellular drug release^[293,294] are examples for dual-responsive systems.

1.11 Biorelated Degradation of the DDS

Biorelated degradation of nanomaterials is a key property for DDS to prevent severe and unpredictable side effects caused by accumulating individual components in specific organs during treatment. The International Union of Pure and Applied Chemistry (IUPAC) defined biodegradation as the “degradation caused by enzymatic processes resulting from the action of cells”.^[295] In this context, most carrier systems should be addressed as “biorelated degradable” nanomaterials.^[296] We must differentiate between complete degradation of the whole carrier system or fracturing into small pieces for on-site drug release. If the shell is composed of biodegradable polymers like poly(D,L-lactide-co-glycoside) (PLGA) or poly(ϵ -caprolactone) (PCL),^[297] drug release can be achieved much faster. Typical examples for degradable inorganic nanoparticles are silicon,^{[298][299]} iron oxide,^{[300][301]} gold^[302,303] and QDs.^[68] Silica, as food additive, has been “generally recognized as safe” by the FDA for over 50 years. Mesoporous silicon is biocompatible and has received FDA approval for pharmaceutical applications for radiotherapy and implant-associated drug delivery.^[304,305] Silicon-based nanomaterials are hydrolytically unstable and dissolve in a time-dependent manner into silicic acid ($\text{Si}(\text{OH})_4$, pKa 9.6). The rate of dissolution of silicon NPs depends on the degradation medium, degree of saturation, temperature, pH, pore size, functionalization and degree and crystallinity.^[306–308] *In vivo* degradation studies of mesoporous silica in different simulated body fluid helps to support the connection between dissolution kinetics and drug release on-demand in a biological context.^[309–312]

1.12 Limitation of the DDS

Biological barriers for the delivery of chemotherapeutics to cancer cells ranging from restrictions of the carrier (blood circulation, aggregation, protein corona) to the journey in the body (influence TMI, MPS recognition) and cellular uptake. Physical barriers and the derived rules for drug delivery are complex because of the biological problem and the multicomponent system. The effects of size, shape and charge of the DDS on

diffusion and Brownian motion, particle aggregation or *in vivo* flow have to be considered.^[313] PEG stealth coating remedies MPS recognition and reduces aggregation of nanoparticle. Drawbacks of surface passivation by PEGylation are the possibility of complement activation leading to hypersensitivity reactions, toxicity of side products, degradation under stress and biodegradability. Polymer costs, FDA approval, stealth behavior, prolonged blood circulation, diminished RES uptake and EPR effect outweigh all disadvantages.^[76] Still, the immunological response and phenomena like accelerated blood clearance^[314] must be considered. 30 years after the first carrier system for cancer treatment had been approved by the FDA Chan et al. analyzed 117 publications of the past decade and concluded that only 0.7% (median) of the administered nanoparticle dose was actually delivered to solid tumors.^[315]

They concluded that a successful transfer of nanomedicines into clinical trials is only possible after re-examining of all existing DDSs to establish a simple, effective and reproducible product. The underwhelming delivery efficiency of many DDSs can be linked to an incomplete understanding of passive and active delivery strategies (**Figure 1.8**). Overestimation of the EPR effect combined with the fundamental differences (size, metabolic and development rates, tumor biology) between animal tumors (specifically murine models) and human cancers makes progress in nanomedicine sparse.^[316] Unlike artificially induced animal tumors, human tumors can take decades to develop, giving time for a more controlled angiogenic process.^[317] Additionally, human tumors are generally much smaller ranging from a few millimeters to a few centimeters at the time of diagnosis and treatment, in comparison to oversized tumors in a mouse model.^[318] Active targeting strategies are hampered through the “binding-site barrier”, resulting in decreased penetration of the carrier system due to high binding affinity.^[196] Penetration depth is essential for efficient cancer treatment, and diffusion problems arise from the size difference between DDS and cells. Thus, large molecules like a monoclonal antibody (approximately 150.000 Da) need up to several months to reach a uniform concentration in a tumor (diameter 1 cm) by diffusion.^[319] Nichols et al.^[316] interpreted the diffusion process of a nanoparticle with a reduced effectivity due to physical barriers of the ECM and tightly packed cells. Chemical interactions between the particles and tumor components further decreases diffusion range.

Despite these barriers and obstacles, multidrug resistance (MDR) is another important constraint in applied cancer therapy. MDR in cancer is defined as resistance of tumor cells to a single anticancer drug, which is accompanied by resistance to structurally and mechanistically completely unrelated drugs.^[320] We can distinguish between pre-existing (*de novo*) and (acquired) resistance developed during treatment. *De novo* drug

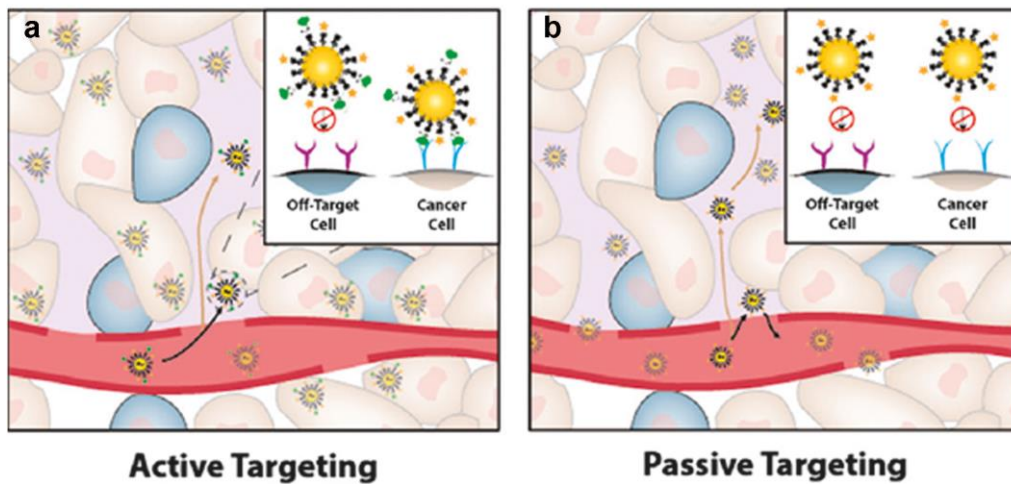
resistance like environment-mediated drug resistance (EMDR) protects cancer cells from apoptosis caused by receptor-mediated cell death, radiotherapy or chemotherapy. The cancer-specific protective mechanism is regulated by the TMI (soluble factors) and components of the ECM.^[321] Insufficient treatment of cancer leads to survival of a small subset of cancer cells (named minimal residual disease) and relapse in cancer patient is highly probable.^[322] Highly molecular and genetic heterogeneity of cancer itself combined with *de novo* drug resistance causes low response rates in cancer patients. The surviving tumor cells are now able to develop acquired resistance. Drug-mediated mutation and therapy-induced selection of a resistant subpopulation is highly probable.^[323]

It leads to a highly resistant tumor, rendered nearly immune to additional cancer therapy. Cellular mechanisms of multidrug resistance are diverse, ranging from increased efflux of hydrophobic drugs, alterations in drug metabolism and cell cycle, increased repair of DNA damage, reduced apoptosis or adaption of the tumor through survival signaling pathways and inactivation of downstream death signaling pathways.^[320,324–326] The resistance mechanism of increased drug efflux (pump resistance) is caused by the adenosine triphosphate (ATP) binding cassette (ABC) transporters such as P-glycoprotein (Pgp) or the multidrug resistance associated-protein 1 (MRP1, also known as ABCC1).^[327] They are known transmembrane proteins regulating the flux of chemotherapeutic agents across the plasma membrane,^[328,329] and valuable targets for nanoparticle-mediated delivery of ABC inhibitors to overcome pump resistance in cancer cells. Non-pump resistance is caused by activation of cellular anti-apoptotic defense (Bcl-2 protein).^[330] The simultaneous inhibition of both resistance pathways is key for successful cancer treatment^[331–333] and was utilized for the co-delivery of doxorubicin and siRNA, targeting mRNA encoding Bcl-2 protein^[249] and Pgp.^[250] Dendrimeric nanoassemblies,^[334] MSNs^[335] and gold nanoparticles^[336] were functionalized to combat physiological barriers and regulate cellular factors of multidrug resistance. Additionally, size-dependent drug efflux resistance of gold nanoparticles led to increased cancer cell killing capabilities.^[337]

The final important area in nanotechnology development and safety is the toxicity of the nanoparticle-based formula. We have to distinguish between the different ways of exposure (ingestion, injection, transdermal delivery, and inhalation)^[338] to accurately describe nanotoxicity. In the context of drug delivery, important factors are biorelated degradation byproducts of the base material, the colloidal stability of the formula and the clearance pathways from the body (MPS recognition, kidney). Additional factors to characterize nanotoxicity are the nature of the carrier system and nanoparticle properties

like size, porosity, morphology, surface coating, thermal oxidation and surface functionalization.^[339] These properties have an impact on cellular uptake, DNA synthesis and uptake, altered gene expression, immunogenicity, oxidative stress, and cell proliferation.^[225,340] Additional problems arise from interactions with red blood cells (RBCs),^[341] cellular respiration^[342] and membrane disruption.^[343] To assess nanoparticle toxicity, QDs,^[344,345] carbon nanotubes,^[346] gold^[347] and silicon^[348] nanoparticle have been analyzed *in vivo*. Wang et al. analyzed the toxicity mechanism (hemolysis mechanism at the molecular level) of difference QDs to RBCs.^[349,350] *In vitro* and *in vivo* studies of silica nanoparticles and their interactions with different parts of the body show ambiguous results. The results vary from high toxicity to general safety, probably due to differences in functionalization, size, morphology and crystallinity.^[351–353] To quantify nanoparticle-induced toxicity, different analytical methods and viability assays were used to track metabolic activity, hemolysis, apoptosis and necrosis.^[354–356] Cell viability assessment of nanomaterials is difficult due to false positive results. Particular, high surface areas, crystallinity and dye-nanomaterial interactions of silicon microparticles, carbon nanomaterials and QDs led to wrong conclusions concerning cell viabilities.^[354,357]

Expected outcome



True outcome

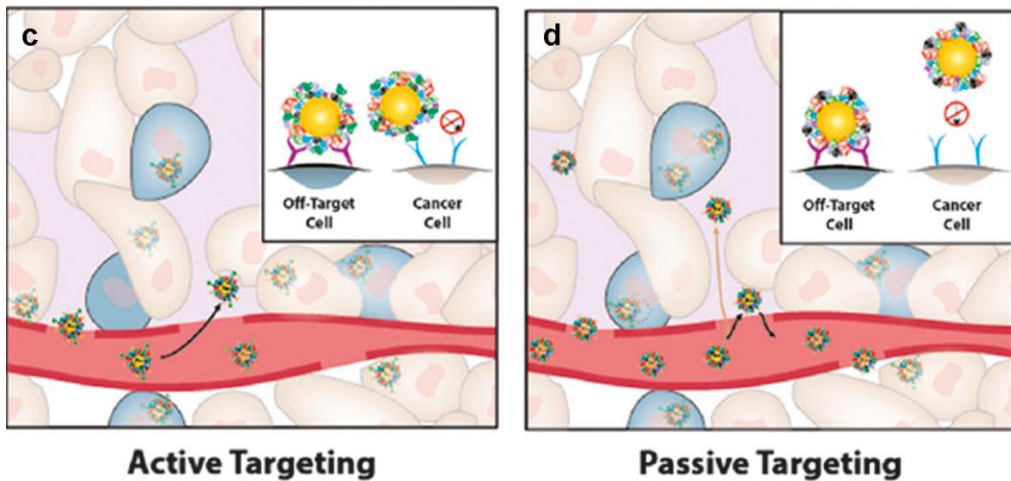


Figure 1.8. Ideal versus actual nanoparticle-tumor targeting strategies. In tumors, the unique fenestrated vasculature facilitates nanoparticle extravasation from the blood and into the interstitium. The poor lymphatic drainage and high intratumoral pressure help retain the nanoparticles within the mass. In an ideal situation without nanoparticle–blood interactions: (a) nanoparticles are surface-functionalized with ligands, bind to cell surface receptors and undergo receptor mediated endocytosis for selective entry. (b) Nanoparticles are surface-passivated with PEG to increase half-life, and provide greater opportunity to extravasate through leaky tumor endothelium and penetrate into the tumor. The true nanoparticle–blood interactions *in vivo* are very different. Protein corona formation (c) sterically hinders and masks surface bound ligands, limits cancer cell receptor-mediated interactions and supports off-target cell binding (indicated by blue cells). (d) Nanoparticles increase in the size and limits their depth of penetration into the tumor (i.e., the particles are more likely to stay near the vessel). Of note, the green and orange structures on nanoparticle surface in (a) and (b) represents a targeting ligand and cancer agent. Adapted with permission from ref.^[358].

1.13 Cancer Immunotherapy

The premise of an immune system-mediated intervention in cancer progression lies in the capacity of the immune system to distinguish between self and non-self. While highly equipped and effective in the eradication of pathogens, the ability of the immune system to effectively deal with transforming cancer cells is hampered by the fact that the cancer cell's origin is self.^[359] Despite the fact that depletion of self-antigen reactive T lymphocytes during cancer progression combined with numerous genetic alterations and loss of cellular regulatory processes should lead to immune-recognition, cancer cells evade immunosurveillance through various immunosuppressive mechanisms.^[360,361] Recognition of cancer cells is circumvented by down-regulating the expression of surface antigens, by recruiting immune suppressive cell types to the TMI and overall the cytokine-derived immunosuppressive environment.^[362,363] Cancer immunotherapy comprises several treatments in order to activate the patient's own immune system to detect and eradicate cancer cells. Promising approaches in solid tumor treatment are cancer vaccines for active immunization,^[364] antibody-based cancer therapies^[365] and immune-checkpoint blockade^[366] for rewiring the immune system to fight the growing cancer.

The activation of a tumor-associated immunosuppressive cell population (T-cells, dendritic cells^[367,368] and macrophage^[369,370]) is needed for recruiting an anti-tumor response and eradicating immunosuppression by the TMI. Nanoparticles can be utilized for the delivery of vaccines, adjuvants or immune-modulatory/stimulatory molecules, making use of advantages like passive accumulation, cell target delivery, stimuli-responsive drug release and protection of biodegradable cargos.^[371] Chemotherapy itself can help to activate the immune system, but only if the associated cell death is immunogenic. Immunogenicity describes the ability of a substance to provoke an immune response in the body.^[372] Immunogenic responses can be triggered by chemotherapy-induced cell death, release of pro-inflammatory factors and upregulation of antigen presentation.^[373] Immunogenically rendered cells can effectively stimulate the immune system and thus counteract the immune-suppressive TMI.^[374,375] Nevertheless, many cytotoxic anti-cancer agents can lead to an immunologically silent or tolerogenic immune response^[376] due to apoptosis.^[377] Apoptosis is not accompanied by the release of pro-inflammatory cytokines into the TMI, consequently preventing an adequate inflammatory response and stimulation of the immune system (silent cell death). In addition, apoptotic cells are quickly phagocytosed and do not release their cellular constituents into the tumor microenvironment.^[378] For a combination of chemo- and immunotherapy, one needs to tune the synergy of a chemotherapeutic agent and an

immunotherapeutic stimulus to achieve an effective anti-tumor response. For example, gold nanoparticle transporting siRNA to a tumor-associated macrophage (TAM^[370]) and lung cancer cells silencing the VEGF mRNA combine an immune modulation of the TMI with tumor suppressor effects *in vivo*.^[379] Gold nanoparticles for cancer immunotherapy are applied in different areas like cancer vaccines, gene therapy and adjuvant delivery.^[380] Furthermore, hollow MSN could deliver cancer antigens and showed an intrinsic immune-modulatory activity, suggesting MSN to be an efficient adjuvant for cancer immunotherapy.^[381]

Another example for a combination therapy is the synergistic effect of cisplatin and synthetic peptides (SLP) of the human papillomavirus type 16 (HPV16) that lead to increased anti-cancer activity.^[373] Still, examples of nanoparticles used for a combined chemo- and immunotherapy are scarce. Most of them focus on imaging and active targeting to a cell subpopulation.^[382] MRI imaging TAM with FDA-approved iron oxide nanoparticles (ferumoxytol or Feraheme) showed possible applications as biomarker to develop new immune-targeted therapies.^[383] Polymer-based nanoparticles were used to deliver^[384] a fluorescent platinum(IV) pro-drug^[385] and hydrazinocurcumin (HC),^[386] a synthetic analogue of curcumin, to TAM. To circumvent immunosuppression, an immune-checkpoint blockade of cytotoxic T-lymphocyte associated antigen 4 (CTLA4) and programmed death 1 (PD-1) receptors are explored in clinical trials.^[387,388] PD-1 and CTLA4 are highly expressed on T_{regs} making them valuable targets for antibody-mediated cancer treatment *via* immune-checkpoint blockade.^[366,389] Blockade of these receptors leads to an enhanced antitumor immune response by diminishing suppressive activity of intratumoral regulatory T-cells (T_{reg}).^[390] T_{reg} population in the TMI represent a major immune resistance mechanism, shielding the tumor from detection and preventing immune response of cancer patients. Examples for nanoparticle-induced elimination of T_{reg} and myeloid-derived suppressor cells (MDSCs^[391]) are the transport of a broad spectrum of anti-inflammatory triterpenoids *via* lipid-coated calcium phosphate nanoparticles.^[392] PD-L1 siRNA target delivery with PEI liposomes resulted in the formation of re-programmed tumor-associated dendritic cells.^[393]

Part II

2. Dendritic Mesoporous Silica Nanocarrier

Transport, encapsulation and administration of highly toxic cancer therapeutics through nanosized carrier is still a significant challenge.^[394] A carrier system with flexible reception volume and size is the key for a widespread application. Effective drug delivery can be possible through minimizing drug/carrier surface interaction, avoiding drug retention. One has to strike a balance between pore size/drug loading and release capabilities/drug retention to ensure effective treatment. A “zero premature release” property is especially desirable for highly-cytotoxic agents, avoiding off-target toxicity in healthy tissue. Additional obstacle arises from drug properties like hydrophobicity, hydrophilicity and size, complicating drug load, safe storage and administration of the DDS. We chose mesoporous silica nanoparticle with a unique dendritic pore structure for the transport and encapsulation of small molecules (doxorubicin, rhodamine B, dinuclear copper complex) and a large protein (tumor necrosis factor-alpha, TNF- α). Dendritic mesoporous silica nanoparticle (DMSN) show good biocompatibility, a variety of functionalizing strategies, high surface area and adjustable pore size^[64,72,395] (**Figure 2.1**). In the following chapter, the synthesis of DMSN, different strategies to adjust pore size and particle diameter, surface functionalization and core functionalization with organic moieties and the formation of Fe₃O₄ core-shell particles for magnetic separation are presented. The synthetic strategies illustrated here are the basis for the subsequent application in the biological context.

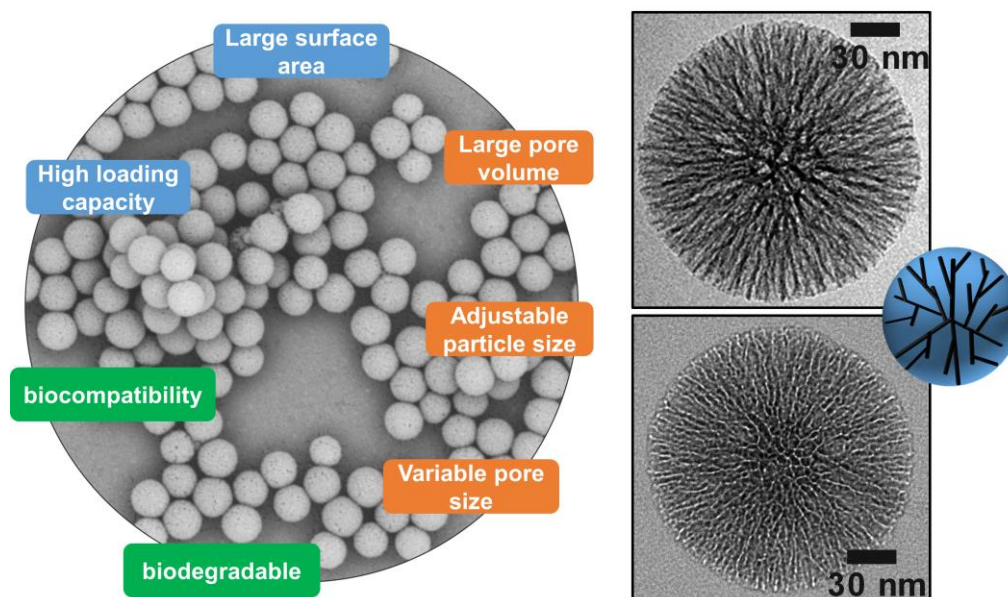


Figure 2.1. Important properties of mesoporous silica nanoparticle for drug delivery applications. (Left) Advantages of mesoporous silica for the drug delivery of cancer therapeutics. (Right) TEM images of the unique pore structure of dendritic mesoporous silica nanoparticle.

2.1 Nanocarrier Synthesis

For the loading of DMSN with different active ingredients, pore size and pore volume had to be adjustable through synthesis control. At the same time, particle size <200 nm is highly desirable for avoiding opsonization and unwanted interaction with the immune system (liver, spleen). The sol-gel chemistry of silica with structure-directing agents (SDA) leads to various pore structures. Well-known mesoporous materials like MCM-41^[10] and the highly ordered mesoporous silica structures SBA-15^[308] paved the way to develop unique pore shapes like cubic, yolk-shell and cylindrical.^[396] Supramolecular aggregates of ionic surfactant (long-chain alkyltrimethylammonium halides) direct the silica growth, and *in situ* formed cetyltrimethylammonium (CTA⁺) micelles act as template for the polycondensation of the silica.^[8] Without increasing the micelle diameter, a limited pore size of these systems restricts application for active substances of different sizes. Center-radially organized pore structures can be synthesized through micro emulsion, forming nanoparticle with fibrous, wrinkled and stellate morphologies.^[396] Utilizing large micelle templates or nanodroplets allows the adjustment of pore size over a wide range and subsequently the transport of large proteins in cancer therapy. Dendritic mesoporous silica nanoparticle with center-radial pore orientation was chosen to synthesize a carrier system with flexible reception volume and size. The particles are based on a synthesis by Zhang et al. and Yu et al.^[28,397] The authors developed an oil-water biphasic stratification approach, which utilizes an

organic layer for the storage of the silica precursor and a basic water/surfactant layer for the hydrolysis and polycondensation of the silicon alkoxides (tetraethyl orthosilicate, TEOS). Base catalyzed (triethanolamine, TEA) reaction of the silica precursor is initiated by the formation of hemispherical emulsion micelles at the oil-water interface, constituted by the shearing forces during stirring (**Figure 2.2**). Hydrolysis of the silicon source, clustering of silicate oligomers and subsequent polycondensation at small nuclei leads to the formation of nanoparticles. Penetration of the hydrophobic organic phase into the spherical CTA⁺ micelles induces an increase in the diameter. Consequently, a change of the micelle packing parameter from spherical to layered micelles occurs. These layered structures act as templates on the silica surface, directing growth of the silica oligomers and the formation of pore walls.

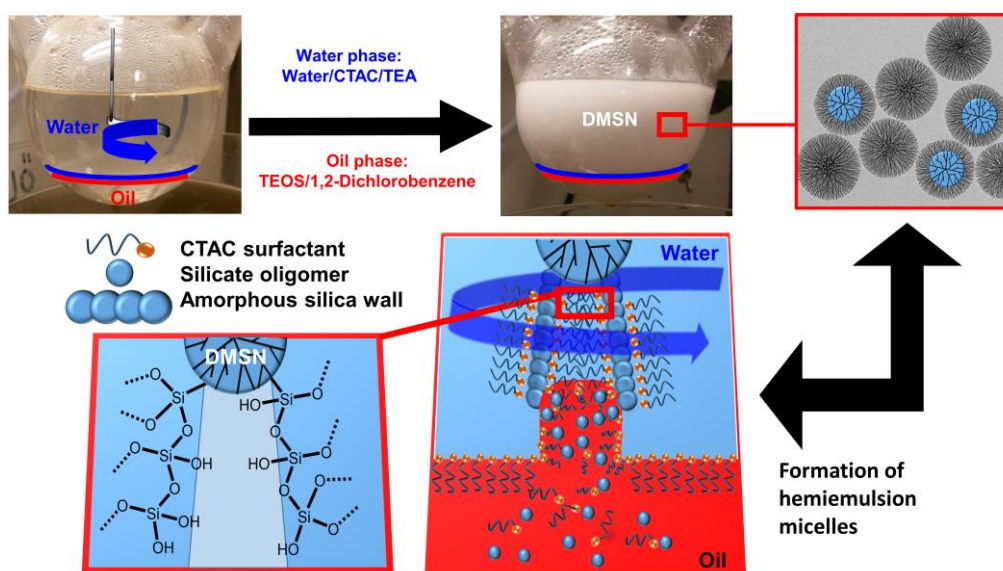


Figure 2.2. Reaction mechanism of the inverse biphasic stratification process of the DMSN. Switch of organic layer and mechanical stirring control results in a precise control of pore size and particle diameter.

2.1.1 Gas Adsorption

For the characterization of the texture of porous solids and fine powders (i.e. the adsorbent), the adsorption of gas is a well-established tool.^[398–400] Nanoporous materials are characterized through the adsorption of various subcritical fluids (i.e. adsorptive), (N₂ @ T = 77 K, Ar @ 87 K and CO₂ @ 273 K) within the relative pressure range $10^{-7} \leq p/p_0 \leq 1$. Density functional theory and molecular simulation (Monte-Carlo) procedures supports pore structure analysis. Pores are classified to their size and ranges from macropores (>50 nm), mesopores (2-50 nm) to micropores, with widths not exceeding ~2 nm. Interplay between the strength of fluid-wall and fluid-fluid interactions as well as the effect of confined pore space on the state and thermodynamic

stability of fluids defines the physisorption (physical adsorption) process.^[401] The measured adsorption-desorption isotherms can be analyzed over the complete relative pressure range, utilizing $0 \leq p/p_0 \leq 0.3$ for determination of the surface area via the BET method and $0.4 \leq p/p_0 \leq 0.9$ for pore size distribution (BJH, DFT) and accessible pore volume (**Figure 2.3**). Three stages defines adsorption of nitrogen (77K) in mesoporous structures. Monolayer adsorption (Stage 1) is followed by multilayer adsorption (Stage 2), where the adsorption space accommodates more than one layer of molecules. This accumulation results in capillary (pore) condensation (Stage 3). This first order gas-liquid phase transition in the finite pore space of the adsorptive is a unique property of mesoporous systems.^[402] The formation of the liquid-like phase inside the pores occurs at a pressure less than the saturation pressure of the bulk fluid. These three stages result in a type IVa isotherm^[398] for mesoporous systems. Capillary condensation is generally associated with hysteresis, visible in the higher-pressure range (**blue circle, Figure 2.3 top**). Hysteresis occurs when the pore width exceeds a certain critical width, dependent on adsorptive and temperature.^[402] Capillary condensation occurs during adsorption and is preceded by a metastable fluid state, while capillary evaporation during desorption occurs via a hemispherical meniscus. The separation of vapor and capillary condensed phase result in hysteresis, since pores of a specific size are filled at higher pressure and emptied at lower pressure.^[403] A shift in the hysteresis region to higher relative pressures is an indication for an increased pore size of the system.

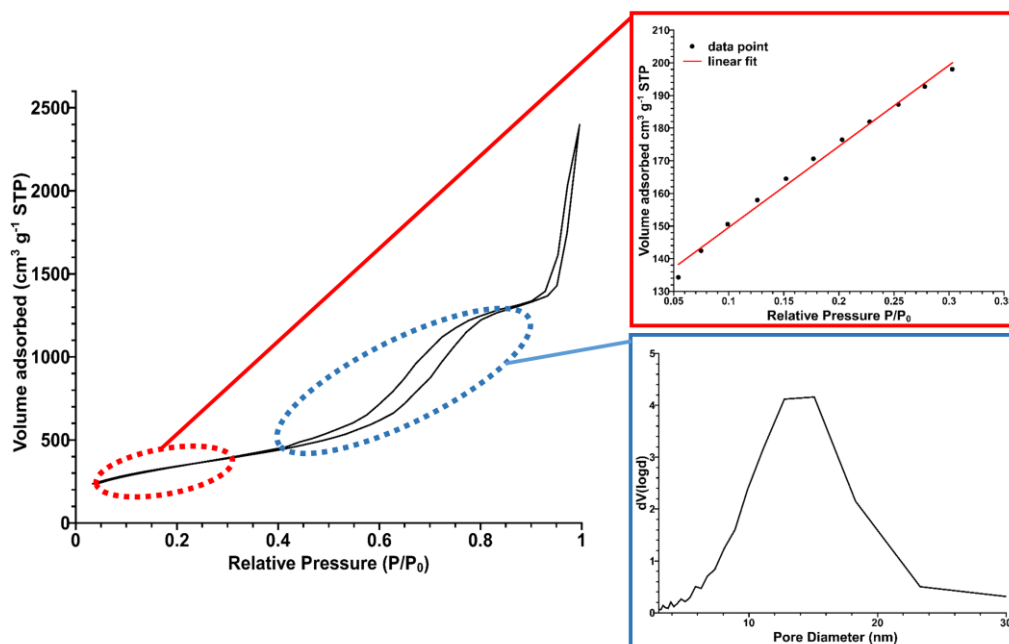


Figure 2.3. An example for the N₂ gas adsorption measurement for mesoporous silica nanoparticles. The relevant analysis areas are marked in red (BET) and blue (BJH). (B) BET fit of the pressure range 0-0.3 and (C) BJH pore size analysis for relative pressure > 0.4.

2.2 Pore Size and Particle Diameter

For precise control of particle size and pore diameter, the stirring rate and the formation of an oil-water interface are important factors. Excessive mixing of the two phases during layering leads to immediate nucleation, a result of uncontrolled hydrolysis/condensation of the silica precursor. Inadequate separation of nucleation and growth phase during nanoparticle synthesis abets broad size distributions. To solve this problem, we chose to substitute the organic layer of low density (≤ 1 , cyclohexane) for a hydrophobic solvent with high density (> 1 , dichlorobenzene, DCB). Switch of the organic layer lead to an inverse biphasic stratification approach allowing the usage of a mechanical stirrer. Control of penetration depth of the stirring blades and stirring rate minimized mixing of the water-oil phase and precise adjustment of the stirring speed controlled the formation rate, size and stability of the hemiemulsion micelle at the oil/water interface. **Figure 2.4** shows the influence of the stirring rate on the pore size and particle diameter. Faster stirring results in better mixing of the water-oil phase and faster nucleation due to TEOS hydrolysis. The formation of an increased number of seed particles results in an overall diameter decrease for a stirring rate between 100-225 rpm (**Figure 2.4A-F**). At constant TEOS concentration, more and smaller particles are formed. Faster stirring yields increased diffusion rate of the nuclei and a higher contact rate with the oil-water interface. Repeated interface contact induces a more disordered growth of the individual lamellar structures due to random directional orientation of

seed and hemiemulsion micelle. Consequently, the diameter of the pore channel increases to the outside and an overall larger pore network develops. Better mixing of the two phases increases penetration rate of the hydrophobic solvent into the CTAC micelles. As a result, the energy barrier associated with the penetration of the outer micelle shell, consisting of the ionic head group of the CTAC, can be overcome more easily. These expanded micelles are contributing to the overall increase in the pore diameter of the DMSN. **Figure 2.4G** shows the pore size changes with increasing stirring rate. The highest stirring rate yields a very broad pore size distribution with a calculated average diameter of 18 nm and a pore volume of 2.5 cc/g.

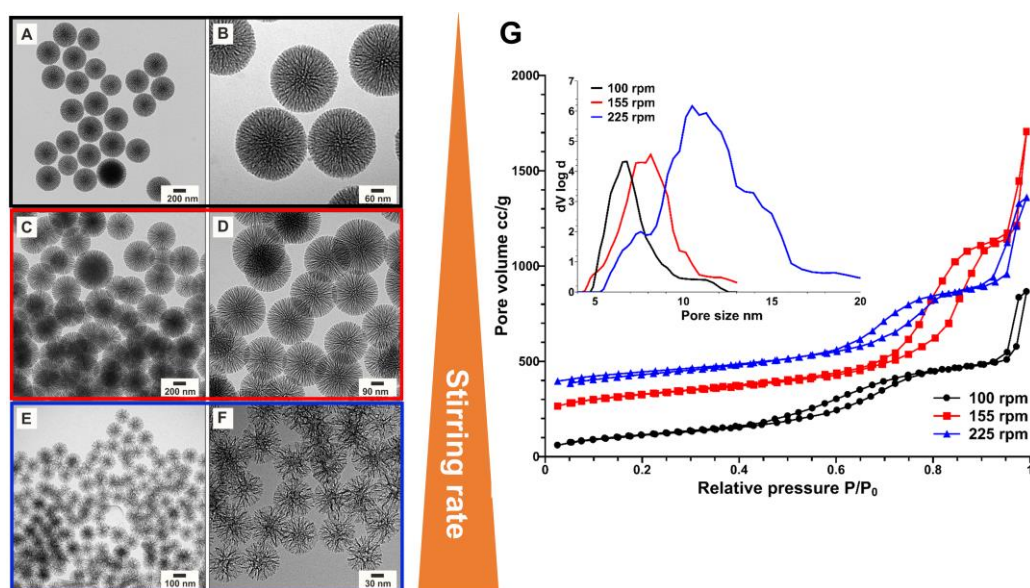


Figure 2.4. Influence of the stirring rate on the particle size and pore diameter of the DMSN. (A-F) Particle Diameter decrease of the DMSN with increasing stirring rate. The stirring rate was adjusted from 100 rpm to 225 rpm. (G) Physisorption isotherm and pore size distribution for the three different DMSN.

2.3 Influence of Organic Base and Temperature

We investigated the change of nanoparticle morphology during addition of different organic bases. TEA (pKa 7.8) as a three-armed chelating ligand interacts with silica oligomers and the positively charged CTAC micelles. The amine molecule is protonated at pH 7–10 and stabilizes *in situ* formed micelle structures through hydrogen bonding and ionic coordination. Moreover, molecules with four center hydrogen bonding favor the formation of dense networks of bridging siloxane.^[404] Reduction in hydrogen bonding capabilities (diethanolamine, ethanolamine) increases pore size and decreases particle diameter. The former is caused by a higher pH value, resulting in faster hydrolysis of TEOS, which promotes condensation of the silica oligomers and increases the number of seed particles. The latter results from the destabilization of the hemiemulsions micelles. Change in the curvature of the organic-inorganic interface enhances influx of organic solvents, swelling the template micelles **Figure 2.5**.

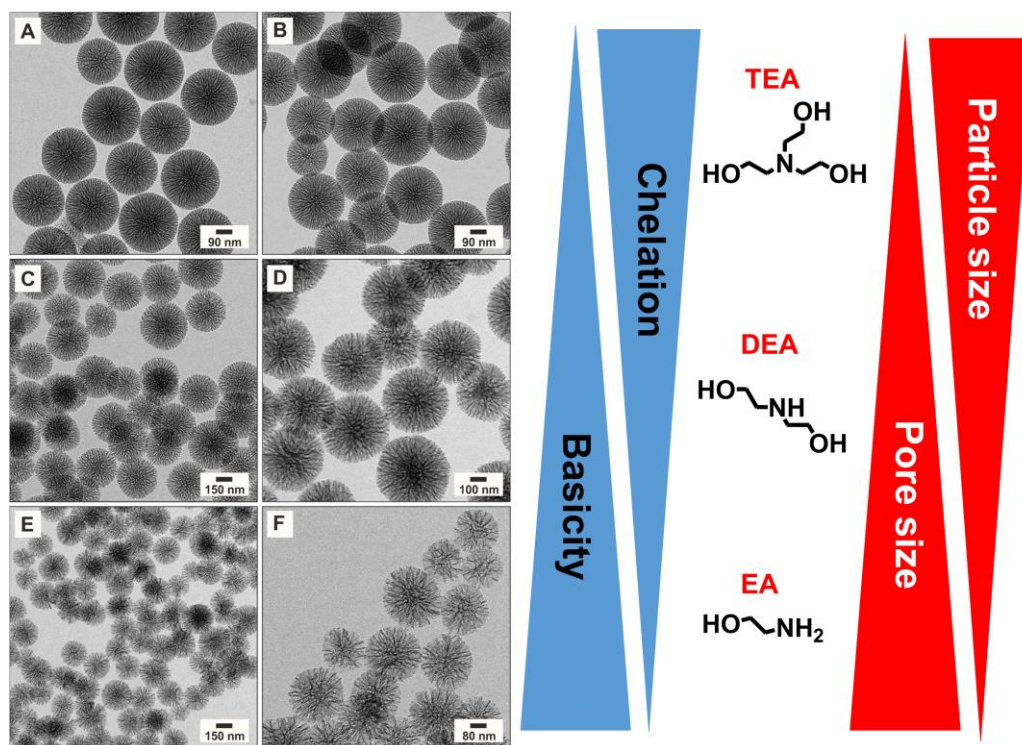


Figure 2.5. Chelation and basicity of the organic base and its influence on the particle size and pore diameter of the DMSN. TEM images of the particle diameter decrease and pore size increase of the DMSN with triethanolamine (A-B), diethanolamine (C-D) and ethanolamine (E-F).

In **Figure A.1** and **Figure A.2**, the influence of TEA concentration and temperature on the nanoparticle formation is shown. Higher TEA amount decreases the pore size of the nanoparticle by suppression the change in micelle packing parameter from spherical to layered micelles. Without layered substructures to direct siloxane network growth, a slightly swollen spherical micelle of 3-4 nm dominates pore size and pore structure

(Figure A.1). The standard synthesis was performed at 70 °C, a compromise between accelerated hydrolysis rate of the precursor and minimal influence on the water-organic interface through turbulence. Lower temperatures increase the time for orderly pore channel formation and favors heterogeneous nucleation of the silica. Consequently, larger particle diameter and bigger pores are obtained. Higher temperatures destabilize the micelle formation mechanism and the electrostatically separation of the particles, promoting interparticle agglomeration and uncontrolled pore growth **(Figure A.2)**. Additionally, the evaporation of *in situ* formed ethanol through TEOS hydrolysis increases interface mixture.

2.4 Hydrotropes in Mixed Micelles

The surfactant CTAC with the combination of hydrophobic tail and ionic head group controls the growth of silica on the nanoparticles. The unique dendritic pore structure results from the interaction of the ionic surfactant micelles with the growing siloxane framework. Coordination of chloride and ammonium ions at the respective charged interfaces introduces further stabilization. To influence the pore structure, we investigate the addition of a second structure-directing agent. Hydrotropes are amphiphilic organic compounds with hydrophilic character and used to increase solubility of organic compounds.^[405] Yu. et al. analyzed the pore extension of TEOS and 1,2-bis (triethoxysilyl) ethane (BTEE) in an aqueous system without organic solvents, utilizing the hydrotrope sodium salicylate (NaSal) for micelle swelling. NaSal combines negatively charged carboxyl group as a coordination site for the CTAC head group and a hydrophobic benzyl ring for micelle swelling in one molecule. **Figure 2.6** displays four SDA and their respective capability of interaction with the CTAC micelle (ionic interaction) and micelle swelling (hydrophobicity). In extension to single surfactant reactions, we tried to answer the questions if it is possible to influence the pore structure by using different hydrotropes instead of varying pH, temperature or reaction time. Furthermore, if the reaction at the boundary layer and the formation of the hemiemulsion micelles can still take place and how the change in micelle packing does parameter influences the pore structure development.

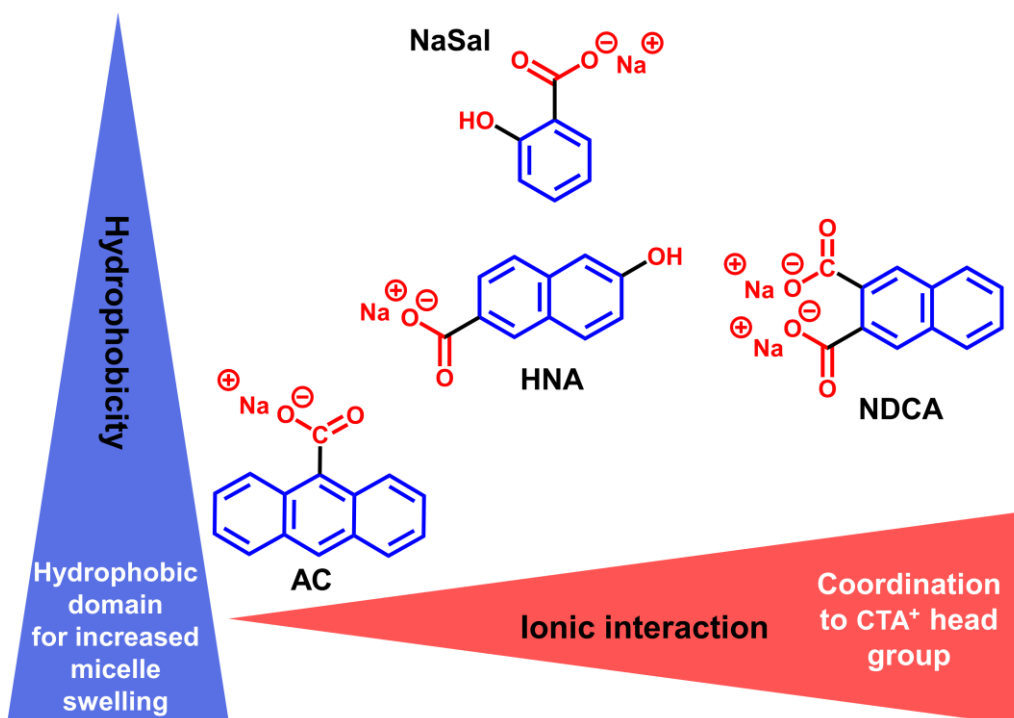


Figure 2.6. Micelle swelling and CTAC interaction capabilities of the four structure-directing agents. D

Figure 2.7 shows TEM images of the dual surfactant synthesis with anthracene-9-carboxylic acid (AC) and 6-hydroxy-naphthoic acid (HNA). The addition of AC results in a collapse of the pore structures, analog to the synthesis with increased base concentration (**Figure A.1E-F**). It is likely that the proportion of hydrophobic domain of the AC is too large to find the right balance between micelle swelling and stabilization of the layered substructures. The influence of HNA on the pore structure is dominated by the bridging interaction of the hydroxyl group in the 6-position of the ring with the siloxane network. The pore structure in **Figure 2.7C-F** appears to consist of disordered lamellae of thin silica layers, growing on a core consisting of disordered pores. The pore size of these disordered lamellae is 3-4 nm, similar to spherical CTAC micelles. HNA seems to stabilize the pore structure through interlayer bridging, likely by hydrogen bonds of the hydroxyl group between individual layers. For both surfactants, the interaction with the CTAC micelles seems too weak for a sufficient increase in pore size. It is possible, that molecular self-assembly limits the availability of hydrotropes to form cationic/anionic pairs.

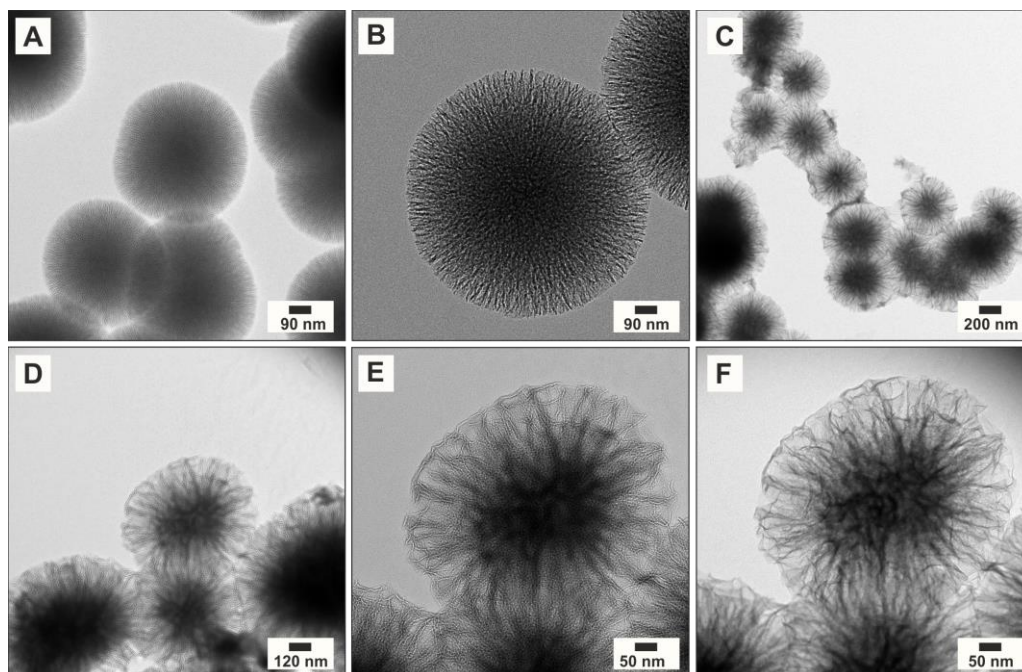


Figure 2.7. Dual surfactant synthesis of CTAC with anthracene-9-carboxylic acid (AC) and 6-hydroxy-naphthoic acid (HNA), respectively. (A-B) The hydrophobic AC leads to collapse of the pore structure and the formation of large particles. (C-F) Influence of the HNA bridging capabilities onto the pore structure formation.

Interaction with the CTAC micelles increases through addition of 2,3-naphthalenedicarboxylic acid (NDCA) with two carboxyl groups and the formed nanoparticles are illustrated in **Figure 2.8**. The strong interaction with the CTAC micelles leads to a charge neutrality on the silica surface of the individual particles. As a result, agglomeration and interparticular polycondensation of the particles takes place. Charge repulsion in aqueous media is a prerequisite for the electro kinetic stabilization of nanoparticles. High surface potential provides colloidal stability during synthesis. Increased micelle coordination facilitate agglomeration and a change in the pore structure. The original dendritic pore structure was transformed to circular shell growth. Pore size of the shell-like nanoparticles is in the range of 6-8 nm. NDCA was able to push the non-polar aromatic system into the hydrophobic micelle cores, enlarging it in the process.

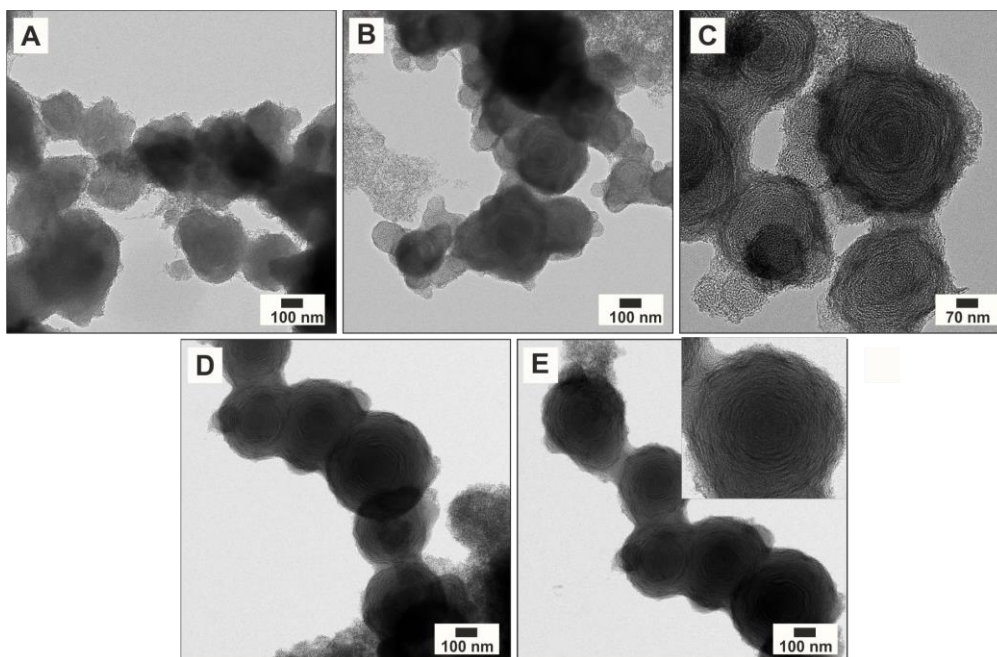


Figure 2.8. Dual surfactant synthesis with 2,3-naphthalenedicarboxylic acid (NDCA). The two carboxyl groups lead to strong interaction with the CTAC micelles and results in a charge neutrality on the silica surface. Lamellar micelle templates directing the silica growth to shell-like pore structures.

The obtained insights into the double surfactant system helped to determine the concentration range of the hydrotropes and reaction parameters such as stirring rate, temperature and pH. The hydrotrope NaSal is a well-known amphiphilic molecule, enhancing solubility of various additives. We expected that the mixture of NaSal and CTAC is capable to influence the pore forming process. First, the ionic interaction of NaSal with the CTAC micelle is weaker compared to NDCA, but the hydrophobic domain is not as rigid and large as in the other structure directing agents. Second, close proximity of the hydroxyl group to the carboxyl group provides hydrogen bonding and ionic interaction to stabilize the spherical CTAC micelles. Possible change of the micellar packing parameter into lamellar structures is favored by the close packing of the cationic/anionic pair.

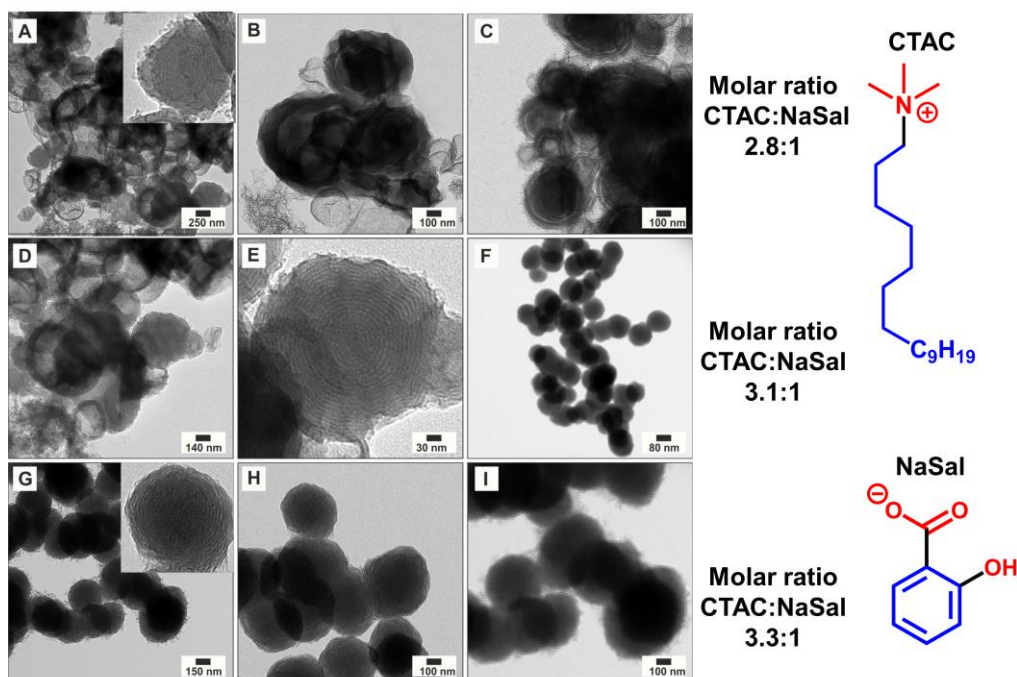


Figure 2.9. Dual surfactant synthesis with sodium salicylate (NaSal) at different molar ratio. (A-C) Molar ratio smaller than 3.3:1 show increased amounts silica agglomerates without defined pore structure and morphology. The highly ordered pore structure visible in (A, Inlet and E) is clearly a minority species. (G-I) Individual particles with an ordered shell-like structure are formed at a molar ratio CTAC:NaSal of 3.3:1.

Figure 2.9 shows the influence of various molar ratios of CTAC and NaSal. Similar to NDCA, which interacts sufficiently with the ionic head groups of the CTAC, shell-like pore structures result. The smaller non-polar domain of the NaSal can form a highly ordered pore structure through flexible arrangement and aromatic stacking. At a ratio of <3.1: 1, the formation of unmodified polycondensates and other superstructures seems to be predominant. In comparison to the single surfactant synthesis, the ratio 3.3: 1 leads to individual particles with a shell-like pore structure. Verma et. al. discussed concentration-dependent transformation of CTAB/NaSal mixtures from long micelles to flat bilayer. The authors described a formation of bilayers/disk due to the solubility mismatch between the surfactant and the hydrotrope.^[406] The shell-like pore structure shows a pore size of 5 nm with a pore volume of 0.45 cc / g (**Figure 2.10**). The spacing of the individual pore channels is also visible in the TEM image. Correlation of the gray value of the TEM image with the distance gives a height profile of the pore structure. The spacing of the individual silica layers is constant at 4.8 nm over a wide range. This ordered layer structure are a result of ionic interaction and hydrophobic swelling capabilities of the three components CTAC / NaSal / DCB.

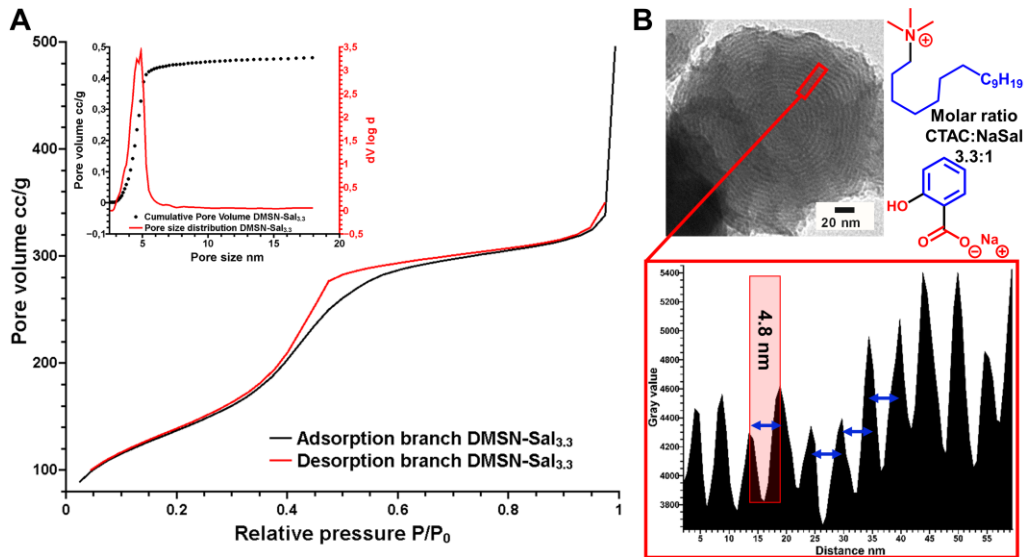


Figure 2.10. TEM height profile and gas adsorption for the ordered shell like pore structure. The pore size distribution in (A) confirms the spacing profile (B) of the individual pore channels extracted from the TEM height profile.

A model for the multicomponent system is shown in **Figure 2.11**. A densely packed layer of silica / NaSal covers the silica walls of the pore channels with small ionic molecules such as Na^+ shielding the individual charged species from one another. The distance, two CTAC molecules can physically block, is around 3 nm. In between the layered CTAC micelles, the aromatic rings (NaSal, DCB) and the hydrophobic tails of the CTAC are coordinated to form a large nonpolar separation layer.

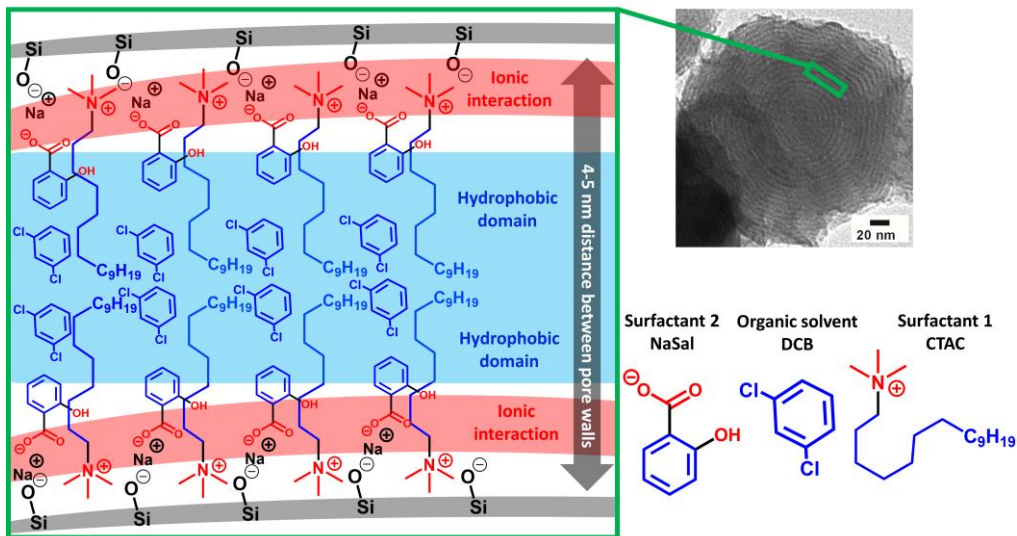


Figure 2.11. Model of the multicomponent system. The separation of ionic charged micelle layers through a hydrophobic domain of swelling agent and surfactant chains results in a shell like growth from the particle interior.

2.5 Siloxane Network Functionalization

In chapter 1, we discussed the solubility mediating property of different surface ligands, their influence on particle aggregation and interaction with the immune system. Aside from post-synthetic grafting, the customization of the silica core with organic bridging molecules or fluorescent dye is essential for multifunctional carrier systems. Detection of nanoparticles inside cells via fluorescence microscopy or flow cytometry systems requires customizable labeling. We linked various fluorescent dyes into the siloxane network of DMSN with an alkoxy silane anchor. *In situ* labelling avoids blocking of accessible pore volume that usually results from post-functionalization. We injected the activated fluorescent dye into the organic phase after water/oil interface formation within 5 minutes. Only hydrolyzed and partial charged alkoxy silane transfers into the water phase and incorporates into the already formed siloxane cluster. This ionically controlled diffusion process minimized additional seed formation, avoiding broadening of the particle size distribution.

In **Figure 2.12**, four fluorescent dyes and their structural formulas are shown. Functionalization of the activated carboxyl group with an amino alkoxy silane (3-aminopropyltriethoxysilane, APTES) serves as binding site. Transfer of unbound APTES into the DMSN synthesis during addition of the activated dye had to be avoided. Excess APTES results in elevated pH values and consequently uncontrolled polycondensation of the silica oligomers. TEOS hydrolyses faster at the oil/water interface at elevated pH values, broadening particle size distribution. We adjusted the molar ratio of APTES to dye to minimize transfer of free APTES into the DMSN synthesis. This prevents unwanted surface functionalization and minimizes pore structure distortion (**Figure 2.12C**). The hydrophobicity, size and reactive group of the fluorescent dye influences the particle diameter and pore size of the DMSN. Sulfo-Cyanine5 N-hydroxysuccinimide (Sulfo-Cy5-NHS) is highly water-soluble and interacts strongly with the silanol surface of the DMSN and the CTAC micelles. The resulting particles shows a decrease in size and slightly distorted pores. In contrast, the functionalization with hydrophobic Pacific blue and Cy5 NHS esters influenced the particle formation only minor. Fluorescein and Rhodamine B form a thiourea bond with the amino alkoxy silane.

In comparison to the NHS activated dyes, the distance between silica surface and organic dye is shorter. **Figure 2.12B** and **Figure 2.12D** show the resulting TEM images of the two activation methods. The thiourea bound dye (bottom) requires less space for the integration into the siloxane network. The amount of nucleation seed increases and particle/pore size decreases. NHS activated dyes form amid bonds between silica

surface and organic core with a flexible spacing unit between them. The high flexibility requires increased space for incorporation of the dye into the siloxane network. Larger particles with well-formed pore network could form.

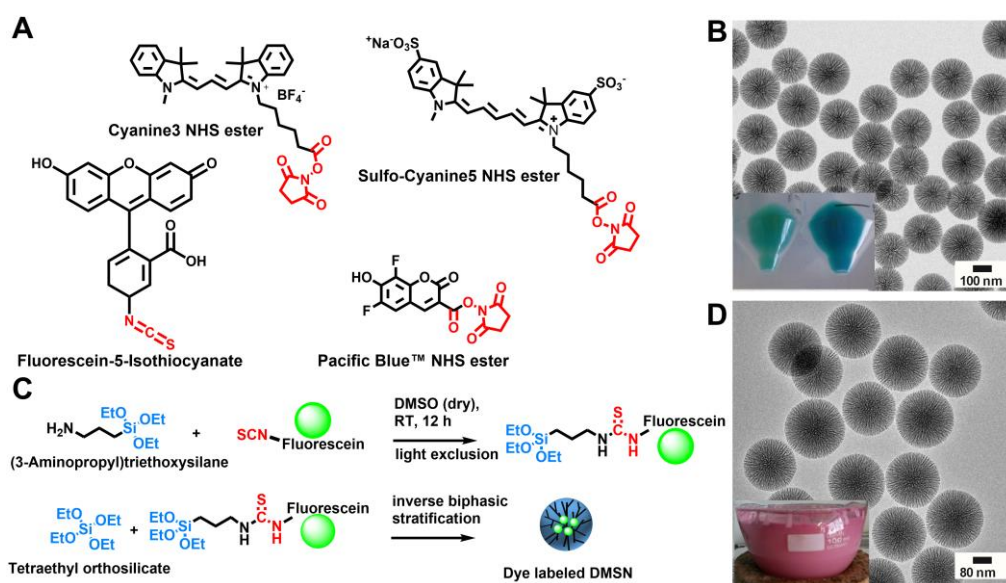


Figure 2.12. Fluorescent dyes and the silica core functionalization strategy. (A) The four carboxyl-activated fluorescent dyes with the thiocyanate and N-hydroxysuccinimide anchor. (B and D) Cy5 labeled DMSN and rhodamine B labeled DMSN. Inlets show the colored nanoparticle after the synthesis. (C) Main principle for the activation of the fluorescent dyes with an alkoxy silane anchor (APTES). The modified dyes were added into the DMSN synthesis for labeling of the silica core.

2.6 Organosilane Bridging

Organosilica hybrid nanoparticles combining an organic flexible network with various functionalizing possibilities and a rigid, inorganic silica structure with adjustable pore size. Mesoporous organosilicas are prepared by surfactant directed polycondensation of bridged organosilanes precursors and TEOS. We aimed to regulate the structural stability of the Si-O-Si framework with disulfide and tetrasulfide bridges to enhance the intracellular degradation of the particles in tumor cells. In chapter one, the important role of glutathione for the regulation of the anti-oxidative capacity inside cells was already described. Elevated level of intracellular glutathione can be utilized for redox-triggered release of active ingredients and degradation of the carrier system. Initial slow drug release (gatekeeper detachment) followed by burst release (particle disintegration) could be a valued therapeutic approach. For example, low concentrations of the endogenous cytokine tumor necrosis factor-alpha (TNF- α) can regulate vessel density and perfusion of solid tumors. Slow release manipulates the tumor microenvironment and increases penetration depth of nanosized carrier. After sufficient time, disintegration of the particles result in elevated level of cytokine inside cells, inducing apoptosis of cancer cells (Details in chapter three). Sufficient pore size and

monodisperse organosilica are key for biomedical applications. We tried to merge the biphasic stratification process with bridged silanes to form dendritic pore structures with a silsequioxane framework. **Figure 2.13A-F** show the TEM images of the synthesized particles and **Figure 2.13G** the two organosilanes bridges with the redox labile disulfide/tetrasulfide unit. We incorporate up to 5 wt. % Bis[3-(triethoxysilyl)propyl] disulfide (top, BTEPS) into the DMSN in relation to TEOS. Higher concentration of organosilica initiated additional nucleation, forming dense organosilica nanoparticle agglomerate. Faster hydrolysis/condensation of TEOS and the intramolecular interaction of the hydrophobic $-(\text{CH}_2)\text{-S}_2\text{-(CH}_2)\text{-}$ chains leads to segregation of the silica and organosilica formation. The two silica entities grow at different rates, broadening size distribution. In addition, increasing amount of organosilica decreasing particle size to 120 nm and pore size to 7 nm. Hydrophobicity of the dense silsequioxane framework restricts coordination to the charges CTA^+ micelles and limits pore formation. For a mixture of 2.5 wt. % BTEPS / 2.5 wt. % Bis[3-(triethoxysilyl)propyl] tetrasulfide (BTEPTS) and 5 wt. % BTEPS / 5 wt. % BTEPTS, we choose to speed up the hydrolysis of organosilanes through direct addition into the organic phase. We could suppress the segregation of the individual silica sources and mesoporous hybrid nanoparticles formed. However, the reduced pore size and polydispersity of the nanosized carrier restricted delivery of proteins and larger molecules.

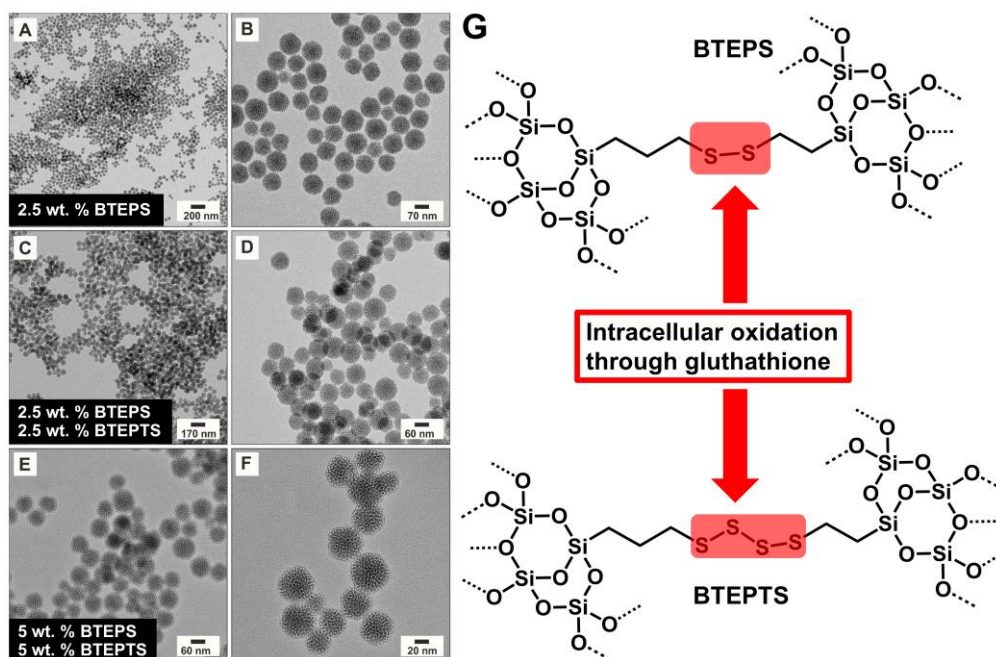


Figure 2.13. Organosilica hybrid nanoparticles for increased intracellular degradation. (A-B) Incorporation of 2.5 wt. % Bis[3-(triethoxysilyl)propyl] disulfide (BTEPS), (C-D) 2.5 wt. % BTEPS / 2.5 wt. % Bis[3-(triethoxysilyl)propyl] tetrasulfide (BTEPTS) and (E-F) 5 wt. % BTEPS / 5 wt. % BTEPTS into the silica nanoparticle. The formed particle showed a decreased particle diameter and pore size. (G) The two bridging organosilanes precursors and the red marked redox labile sulfide units.

2.7 Fe₃O₄ Core Shell System

The encapsulation of metals and metal oxide into organic/inorganic shells offers various advantages and facilitates application in the field of photo(catalysis),^[407,408] magnetic materials,^[409] bio-imaging^[410] and energy applications.^[411] Introduction of a mesoporous shell combines the aforementioned advantages with for example, the transport of small molecules or biomarker. These hybrid materials can enhance imaging capabilities and local release of active ingredients. It is highly desirable to monitor the subsequent drug release and localize the nanoparticles at once. In chapter one, we introduced the protein corona formation of nano sized carrier. Coverage of surface ligands, neutralizing of targeting capabilities and off-target interaction with healthy tissue are a consequence of corona formation. Analysis of the composition could help to identify surface-enriched proteins, a biological 'fingerprint' from the interplay between nanoparticle surface and protein matrix. We aimed to synthesis magnetic porous core shell particle with diameters between 120 nm and 200 nm. The Fe₃O₄ seed particle (15 nm diameter) were added into the water phase of the biphasic stratification reaction prior to TEOS addition. Heterogeneous nucleation leads to the encapsulation of the iron oxide core into a silica shell. Additionally, the pore structure can develop with increasing reaction time. It is important to adjust the ratio of silica precursor and Fe₃O₄ seeds, to avoid free silica

nanoparticle formation. Another obstacle arise from the limited particle size control during the synthesis. **Figure 2.14A-C** shows the mesoporous Fe_3O_4 core shell nanoparticle next to free silica formed during synthesis. The average diameter of the core-shell particles is 250 nm. The small size of the Fe_3O_4 templates lead to the incorporation of multiple nanoparticles into the mesoporous shell. To separate free silica from the magnetic type, we utilized a magnetic separation column supplied by Miltenyi Biotec. A weak magnetic field generated by the column, is amplified by 10.000-fold through a magnet, holding the core-shell nanoparticle in place. After removal of the magnet, the purified sample (**Figure 2.14D-E**) can be collected. The same principle can be applied to the isolation of protein-covered nanoparticle from the blood, making the systematic investigation of protein corona formation onto mesoporous silica nanoparticle possible. Other properties like size, porosity and surface functionalization can be screened, giving insight into the mechanism of protein corona formation.

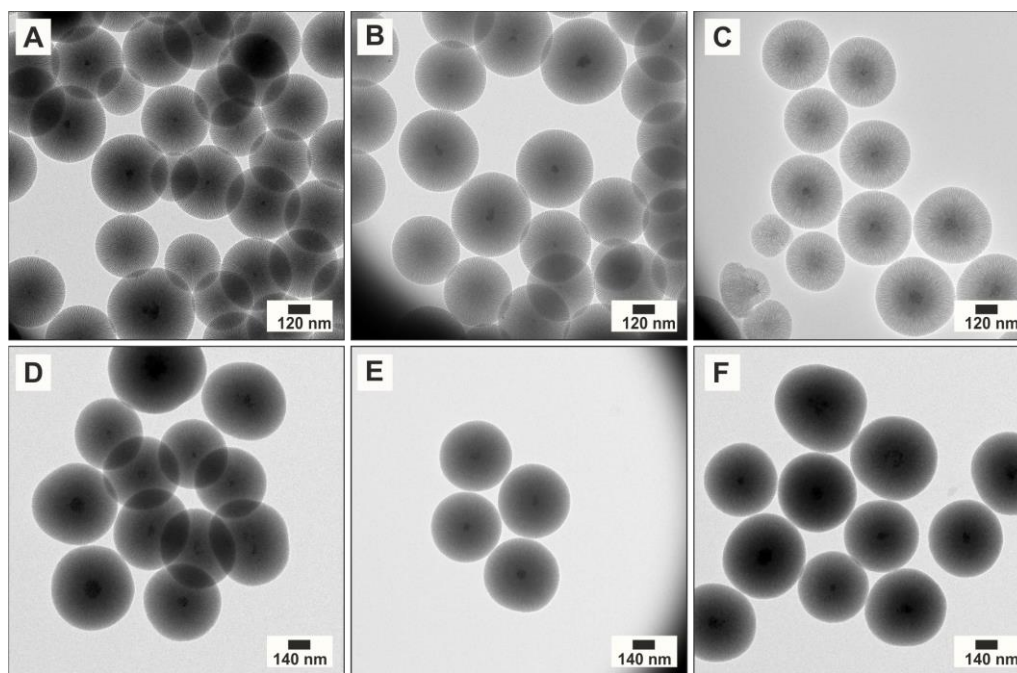


Figure 2.14. Mesoporous DMSN with magnetic core. (A-C) A mixture of free silica nanoparticles and core-shell particles is formed. The separation of these two fractions (D-F) results in magnetic DMSN with a particle diameter of 250 nm.

Conclusion

The synthesis and modification of the mesoporous carrier enables adjustment of pore size and particle diameter over a broad range. Influence through reaction parameters like pH value, temperature, stirring rate or additional surfactant makes the DDS a highly versatile tool for drug delivery. The incorporation of fluorescent dyes and the organosilica bridging gives the DMSN advantages in comparison to non-porous systems. Especially *in vitro* tracking of the DDS is an important property to monitor the drug release process. Magnetic core shell particles help for the *ex vivo* analysis of protein corona formation during incubation in the blood stream.

Part III

3. Dendritic Mesoporous Silica Nanoparticles for pH-Stimuli-Responsive Drug Delivery of TNF-Alpha

The content of the following chapter is partially taken and adapted from *Adv. Healthcare Mater.* **2017**, 6, 1700012. Taken parts are delimited by single quotation marks (“”). This project was developed in collaboration with the Translational Research Institute of the University of Queensland, (Brisbane, Australia) and the University Medical Center of the Johannes Gutenberg-University Mainz, (Mainz, Germany). Details to the individual contribution of each author are listed in the Appendix.

3.1 Motivation and Objective

“Biological barriers to the transport of drugs often hinder adequate delivery to the target organs. Despite the use of an effective drug, efficient responses are often limited in disease processes ranging from inflammation to cancer. Nonspecific distribution and inadequate accumulation of toxic therapeutics remain formidable challenges, which have been partially-addressed with nanoparticles engineered for targeted delivery of drugs or vaccines.^[394] Through spatio-temporally controlled release of their therapeutic cargo, such nanoparticles have the potential to increase drug efficacy while minimizing undesired, potentially toxic off-target effects, without changing the desired drug.^[412–414] A “zero premature release” property is especially desirable for highly cytotoxic agents such as tumor necrosis factor-alpha (TNF- α). It is a multifunctional cytokine that plays a key role in apoptosis and cell survival as well as in inflammation and immunity.^[215,216]

However, the potential utility of systemically administered TNF- α for cancer treatment is significantly limited by its acute toxic effects on normal tissues *in vivo*.^[216] In particular, depressive effects on myocardial cells may lead to a cardiogenic shock-like condition with lethal outcomes.^[415] Therefore, the current use of TNF- α in cancer is limited to the regional treatment of locally advanced soft tissue sarcomas, metastatic melanomas, and limb-salvage in otherwise unresectable tumors of the extremities.^[216,416] Beromun (tasonermin), the only clinically approved recombinant TNF- α , is used for treatment of such nonresectable tumors of the extremities via isolated limb perfusion (ILP).^[217] This treatment can only be performed in specialist clinics with surgical teams experienced with the ILP technique. During treatment, the extremity must be monitored

for any leaks using radioactive tracers, since leakage of TNF- α can lead to significant toxicities. It has been demonstrated with isolated limb perfusion that TNF- α acts synergistically with cytostatic drugs.^[417] A previous approach to encapsulate TNF- α in large lipid-based vesicles was not feasible for clinical use.^[418] Due to a size of up to 20 μm , these particles mainly accumulated in the liver, spleen, and lung - organs especially sensitive to TNF- α - within a short time period.^[418] TNF- α targets the tumor-associated vasculature by inducing hyperpermeability and destruction of the vascular lining.^[419] This results in extravasation of erythrocytes and lymphocytes, leading to hemorrhagic necrosis, as well as enhanced tumor-selective accumulation of nanoparticles and cytostatic drugs and a delayed destruction of the tumor vasculature.^[420] Through activation of dendritic cells, TNF- α drives T cell activation, enhancing immune system-dependent anti-tumor activity.^[421]

The high systemic toxicity of TNF- α , combined with its potential use in cancer treatment, makes it an ideal and relevant target to explore delivery within biodegradable dendritic mesoporous silica nanoparticles (DMSN), which have a tunable pore size, high surface area, thermal stability, chemical inertness, excellent biocompatibility and biodegradability.^[422-424] Research on porous silica-based particles has demonstrated their suitability for drug-delivery applications by their drug release profiles and high efficacy in delivering even hydrophobic drugs,^[422-424] and nano- and mesoporous silica materials have become a cornerstone for drug delivery in the expanding field of nanomedicine.^[422-424] Chemical functionalization of silica-based nanoparticles allows for the tailoring of drug binding and release properties and for the covalent immobilization of functional antibody molecules.^[103,241,251,285,425-427] Despite promising results, silica-based nanoparticle formulations have only been used for non-toxic concentrations of drugs.^[422-424] The maximum tolerated TNF- α dose for intravenous application is 150 $\mu\text{g}/\text{m}^2$.^[428] Since dosages greater than 1 mg are necessary to induce a relevant anti-tumor activity an efficient shielding of TNF- α is essential to prevent its systemic toxicity.^[216,416,428]

Other nanoparticle formulations employed TNF- α to enhance their drug delivery but surface binding cannot prevent its high systemic toxicity.^[429] The textural properties of mesoporous silica can increase the loading of drugs within the pore channels, and the silanol-containing surface can be easily functionalized, allowing for a better control over the drug diffusion kinetics.^[422-424] Biosafety research on mesoporous silica materials was conducted on different levels: from molecule, cell, blood to tissue, involving blood compatibility,^[306] cytotoxicity,^[36] biodegradability,^[81] biodistribution, and excretion.^[430] Key problem for the delivery of a highly toxic cargo to cancer cells

is to ensure complete encapsulation and shielding, therefore minimizing interaction of the cargo with healthy cells. “In this work, we utilized a pH-sensitive hyperbranched polyethylenimine (PEI)-hydrophilic polyethyleneglycol (PEG) copolymer gatekeeper for encapsulation and shielding of TNF- α homotrimer Beromun (tasonermin).” The main objective was to determine, is the protein stable during drugload and does the gatekeeper encapsulation inhibit its mechanisms of action *in vitro*? Are the coated nanoparticle stable in serum, do they penetrate cancer cells and release their cargo? Additionally, we utilized 3D fluorescent ubiquitination-based cell cycle indicator (FUCCI) spheroids in a 3D cell model to efficiently mimic tumor architecture and microenvironment.^{[431,432]”} With this setup, we were able to simulate *in vivo* conditions (vessel pressure, cell density, proteins) and gather information for the behavior of the DDS for *in vivo* applications. “DMSN penetrated these spheroids and after release from DMSN, TNF- α induced G1 cell cycle arrest and subsequently cell death in a time- and dose-dependent manner.” Last step in the analysis of the DDS was the subcutaneously application of the TNF- α loaded DMSN into NOD-scid.HLA-A2.1 transgenic mice (see chapter A1 for details). Analysis of the drug release was conducted with CLSM, monitoring the total radiation efficiency over 28 days. We gathered insight into biorelated degradation of the DMSN *in vivo* and monitored the drug release and distribution of the loaded TNF- α .

3.2 Results and Discussion

“Transport and encapsulation system: DMSN synthesis, functionalization and characterization.

For the shielding and transport of TNF- α , we synthesized three dye-labeled DMSN (Rhodamine B (DMSN-R), Fluorescein (DMSN-F) and Pacific Blue (DMSN-B)) (Details can be found in **chapter A.1**). We optimized and adjusted the biphasic stratification process through incorporating fluorescent dye during the synthesis without broadening the particle size distribution. The in situ dye labeling during synthesis led to incorporation of fluorescent dye into the silica network, sparing the necessity of post-functionalizing the DMSN after drug loading and avoiding blocking of accessible pore volume. The physicochemical properties of the DMSN are summarized in **Table 3.1**.

Table 3.1. Characterization of the dye-labeled nanocarriers DMSN-R, DMSN-B, and DMSN-F.

Sample	Dye	Diameter ^{a)}	Pore size ^{b)}	Surface area ^{c)}	Pore volume ^{d)}
		[nm]	[nm]	[m ² /g]	[cm ³ /g]
DMSN-R	Rhodamine B	168 ± 9.9	6.7	423	0.829
DMSN-B	Pacific Blue	120 ± 8.1	8.9	508	1.407
DMSN-F	Fluorescein	200 ± 9.7	12.7	614	1.602

^{a)} Average diameter by TEM; ^{b)} Calculated by BJH method; ^{c)} Calculated by BET method;

^{d)} Value at P/P₀ = 0.972 by N₂-sorption isotherm.

Dye-labeled DMSN had particle diameters between 120 nm and 205 nm as confirmed by transmission electron microscopy (TEM) (**Figure 3.1**). Surface areas (Brunauer-Emmett-Teller, BET), pore volumes and pore sizes (Barrett-Joyner-Halenda, BJH) of DMSN were determined by N₂-sorption measurements (**Figure 3.2**) and showed pore diameters in the range from 6.7 nm to 12.7 nm, pore volumes of up to 1.602 cm³/g, and surface areas of approx. 614 m²/g. Beromun (tasonermin), a clinically approved TNF- α homotrimer, has a molecular size of 52 kDa and a radius of 5.5 nm.^[433,434] Due to the radial mesopores, which significantly broaden to the outside of the nanospheres, the successful loading of the compact trimer TNF- α composed of 17.5 kDa subunits, was possible.

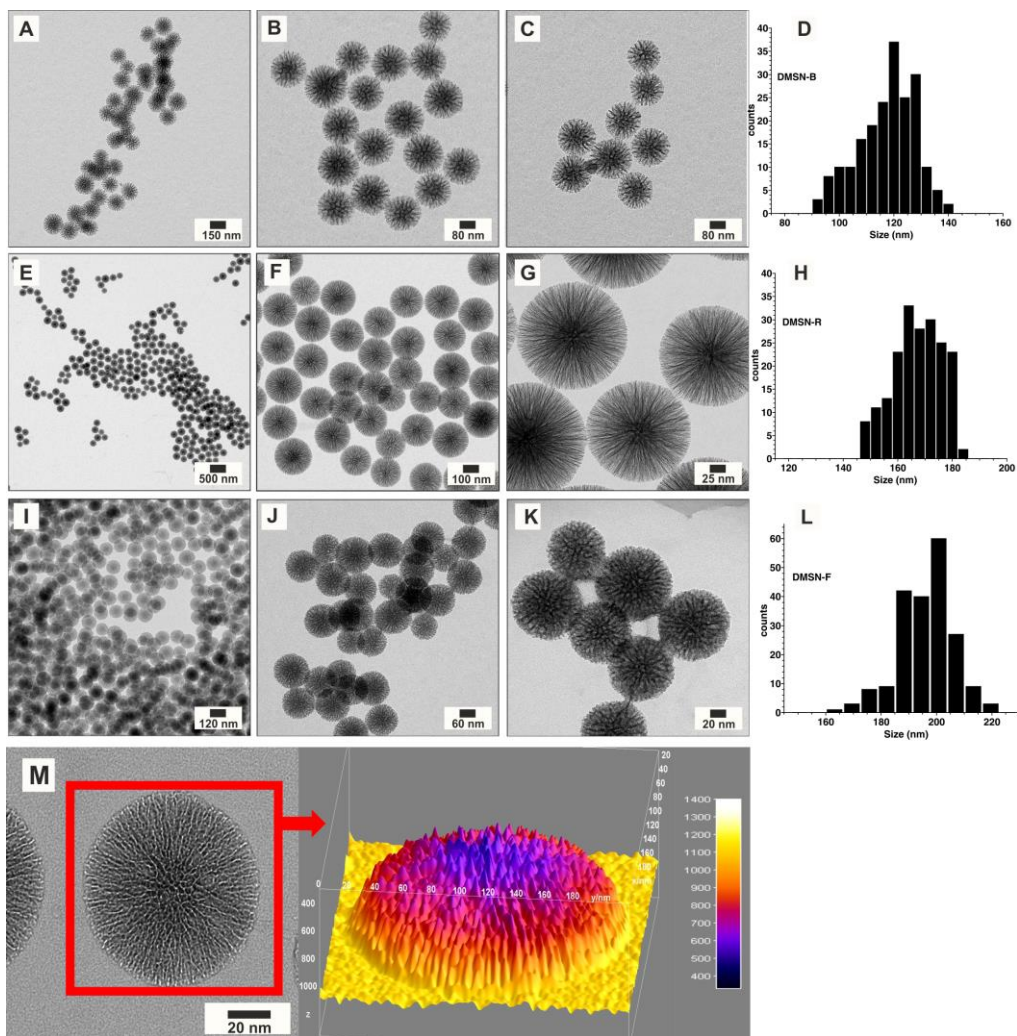


Figure 3.1. Transmission electron microscopy of the DMSN. (A-C) TEM images of DMSN-R, (E-G) DMSN-F, and (I-K) DMSN-B. (D, F, J) Size distribution of DMSN-B, DMSN-R and DMSN-F analyzed with TEM. Mean diameters were calculated using 200 particles. (L) 3D surface plot of the DMSN-F. The uncorrected gray value of the TEM area (red box) was visualized, showing dendritic channels of the mesoporous system.

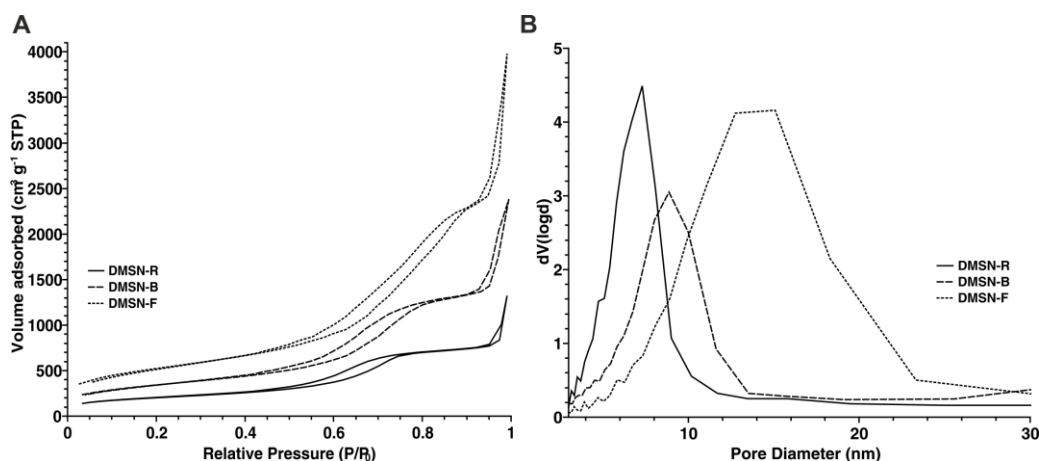


Figure 3.2. Nitrogen physisorption measurement of the mesoporous carrier. (A) Nitrogen sorption isotherm and (B) pore size distribution of DMSN-R, DMSN-B, and DMSN-F. With increasing pore size, a shift in the hysteresis region of the sorption isotherm to higher relative pressure was observed.

X-ray scattering measurements showed the amorphous character of the DMSN and confirmed the pore sizes measured by N₂-sorption (**Figure 3.3, Figure A.3**).

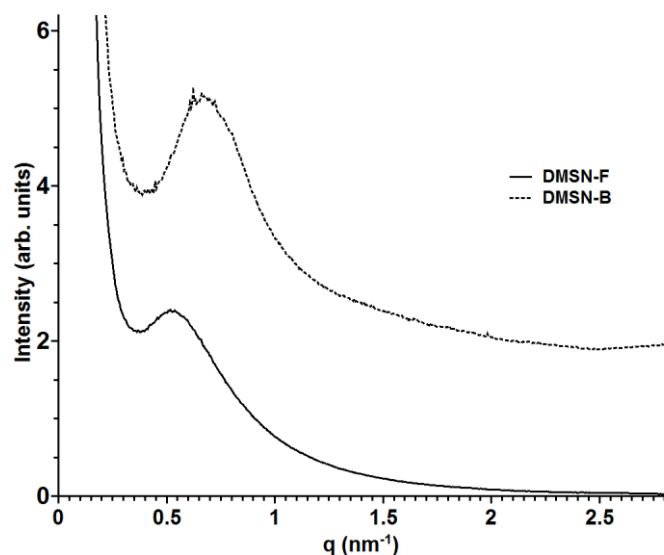


Figure 3.3. SAXS data of DMSN-F and DMSN-B. The scattering patterns show broad peaks at $q_0 = 0.51 \text{ nm}^{-1}$ and 0.54 nm^{-1} respectively. This indicates the presence of ordered mesostructures with a periodicity of approximately $d = 2\pi/q_0 = 12 \text{ nm}$. The shift of the peak maximum q_0 indicates a larger periodicity in DMSN-F compared to DMSN-B. An estimate for the pore diameter $d_p \approx 1.05 \sqrt{f} d_p = 11 \text{ nm}$ is obtained by assuming a locally hexagonal arrangement of cylindrical pores with volume fraction $f = 3/4$. This value is in good agreement with the pore size distribution obtained by BJH analysis.

²⁹Si solid-state nuclear magnetic resonance spectra (ssNMR) showed a low degree of cross-linking^[435] in the silica network and successful dye labeling of DMSN (**Figure 3.4**). ”

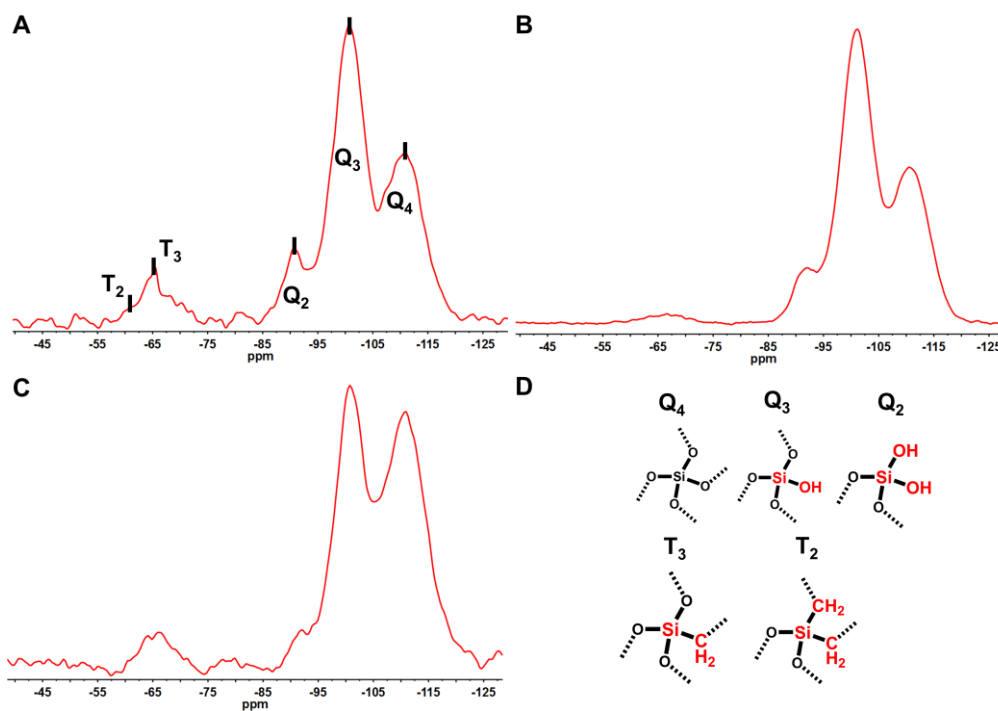


Figure 3.4. Solid-state NMR of the dye labeled DMSN. “Measurement of the ^{29}Si ssNMR spectrum of A) DMSN-R, B) DMSN-B and C) DMSN-F. The DMSN showed the resonance bands around -92, -100 and -111 ppm, which are characteristic of D) $(\text{HO})_2\text{Si}(\text{OSi})_2$ (Q_2), $(\text{HO})\text{Si}(\text{OSi})_3$ (Q_3) and $\text{Si}(\text{OSi})_4$ (Q_4) units. The resonance band at -65 ppm and -54 ppm can be attributed to the dye labeling process and shows the presence of carbon-silicon bonding $(\text{H}_2\text{C})_2\text{Si}(\text{OSi})_2$ (T_2), $(\text{H}_2\text{C})\text{Si}(\text{OSi})_3$ (T_3) inside the DMSN. The calculated degree of condensation (1.88) for DMSN-F was determined according to $(\text{Q}_2+\text{Q}_3)/\text{Q}_4$, indicating the presence of a silica network with a low degree of cross-linking.^{[435]”}“Colloidal stability of DMSN-F was evaluated in phosphate-buffered saline (PBS) buffer (150 mM, pH 7.3) and ethylenediaminetetraacetic acid (EDTA) plasma before and after functionalization with the pH-sensitive gatekeeper by dynamic light scattering (DLS) and fluorescence correlation spectroscopy (FCS) (**Figure 3.5, Figure A.4 and Table A.3**). FCS of rhodamine B-labeled PEI-PEG coated onto DMSN-F (**Figure 3.5A**) resulted in a hydrodynamic radius R_h of 115 nm for the carrier system. Multi-angle DLS demonstrated that DMSN-F functionalized with PEI-PEG coating have a slightly increased R_h of 113 nm and DMSN-F without coating a R_h of 112 nm. (**Figure 3.5B, Figure A.4A**). The minor increase in R_h for coated DMSN can largely be attributed to strong interaction of the polycation with the surface silanol groups and accumulation of PEG chains inside the mesopores.

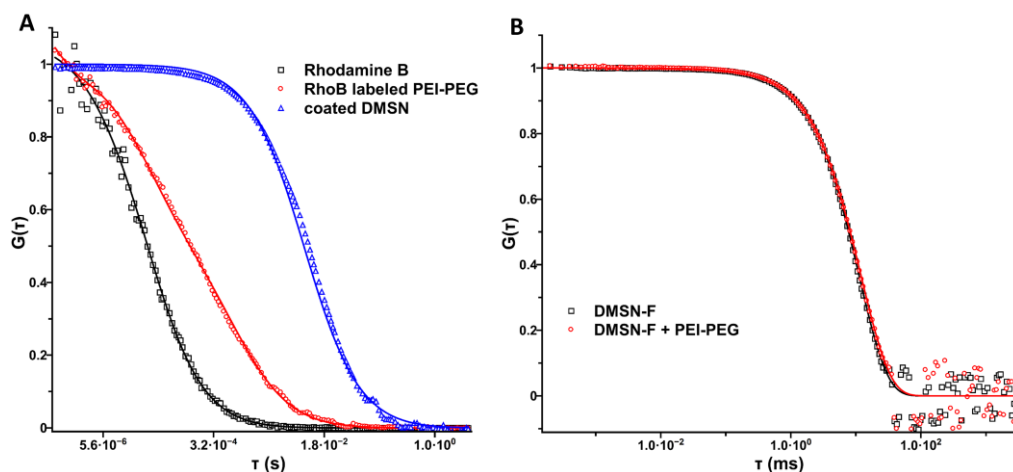


Figure 3.5. Physicochemical characterization, of DMSN. (A) FCS autocorrelation curve of the free rhodamine B (black symbols), RhoB-labeled PEI-PEG (red symbols) and the coated DMSN-F (blue symbols) in PBS. Solid lines represent the corresponding fits. The resulting hydrodynamic radius R_h of 115 nm for the coated DMSN demonstrates successful functionalization with the gatekeeper. (B) Multi-angle DLS measurement (30° scattering angle) of the drug carrier system in PBS buffer solution confirming colloidal stable nanoparticle (q -dependence shown in **Figure A.4**).

To ensure colloidal stability of the DDS for *in vivo* application, we analyzed the aggregation behavior of PEI-PEG-coated DMSN in human 90% EDTA plasma from 6 donors (details see **chapter A.2**) No aggregation for concentrations between $3 \mu\text{g/ml}$ and $300 \mu\text{g/ml}$ (**Figure 3.6**) can be observed. After measuring the autocorrelation function (ACF) of the human plasma without nanoparticle $g_1(t)_P$ and the ACF of the DMSN in PBS buffer $g_1(t)_S$, two exponential fit functions can be obtained to describe the mixture of these two compounds ($g_1(t)_{\text{mix}}$). The determined AFC of ($g_1(t)_{\text{mix}}$) is sufficient to fit the experimental data, confirming the presence of discrete and colloidal stable nanoparticles in solution and plasma. In case of aggregation formation, a third fit function ($g_1(t)_a$) needs to be added to adequately fit the autocorrelation function of the mixture.

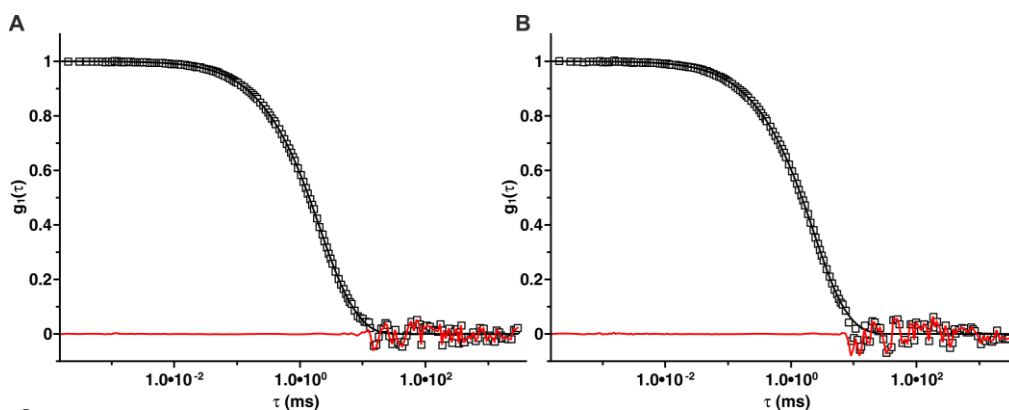


Figure 3.6. Dynamic light scattering in human plasma. Autocorrelation functions of (A) PEI-PEG coated DMSN (300 $\mu\text{g/ml}$) and (B) PEI-PEG coated DMSN (3 $\mu\text{g/ml}$) in EDTA-plasma. Back lines represent the force fits with the sum of the individual correlation functions of serum and coated DMSN according to **(Equation A.1)**. Red lines represent the fits according to **Equation A.2** accounting for the presence of aggregates; scattering angle 60° . For both concentration, no aggregation in plasma occurs.

For encapsulation of TNF- α with a pH responsive release mechanism, we synthesized a core shell block copolymer PEI(600)-PEG(1000)₃ combining cationic hyperbranched PEI block with nonionic hydrophilic PEG (**Figure 3.7A**). We were able to control the amount of PEG on the surface of PEI through the ratio of activated PEG to PEI. Longer PEG chains in comparison to PEI were chosen to prevent penetration of PEG chains into the hyperbranched PEI structure. This resulted in fully PEG-functionalized DMSN after coverage with the copolymer and ensured colloidal stability of DMSN. Pore coverage was based on electrostatic interactions of negatively charged surface silanol groups with the partially positively charged copolymer. These electrostatic differences caused the copolymer to interact with the silica nanoparticles. The partially charged PEI and the steric repulsion of the individual DMSN through the PEG chains led to successful coverage of the pores. Attenuated total reflection infrared spectroscopy (AT-IR) and ¹H, ¹³C-NMR spectroscopy monitored activation of PEG with hexamethylene di-isocyanate (HMDI), coupling with PEI polymer and the resulting disappearance of signals of the linking isocyanate groups (**Figure 3.7B**)."

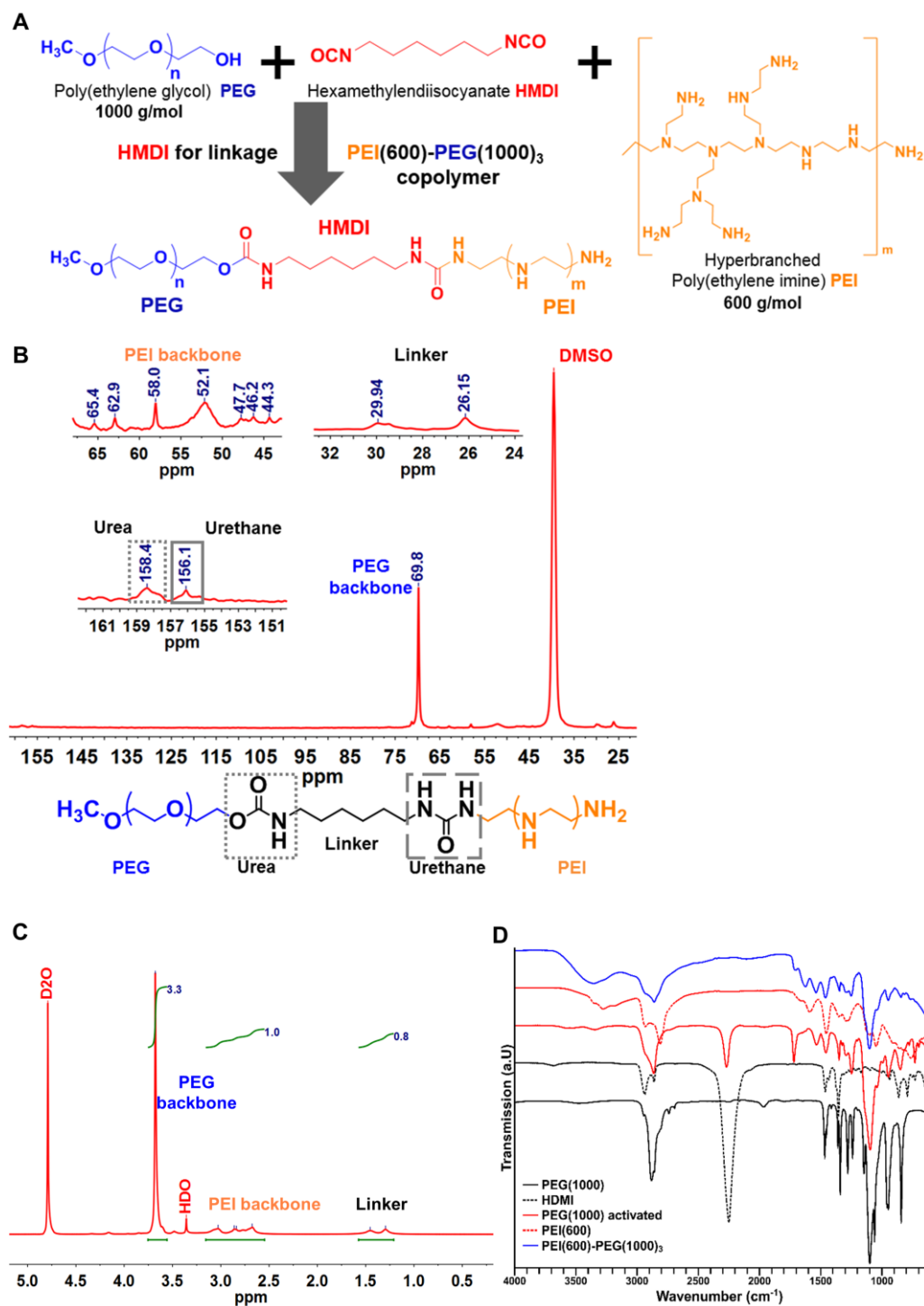


Figure 3.7. Gatekeeper synthesis and physicochemical characterization. “A) Synthesis concept of the core-shell PEI(600)-PEG(1000)₃ block copolymer “B) ¹H NMR spectroscopy of PEI-PEG copolymer. Ratio of signal intensities of the two polymer backbones for -CH₂-CH₂-O- and -CH₂-CH₂-N- results in a grafting density of three PEG chains onto the hyperbranched PEI. C) ¹³C NMR spectroscopy of the PEI-PEG copolymer. Successful linkage of the two polymers is indicated by the urea carbonyl group of the activated PEI-PEG polymer at 158 ppm and the urethane carbonyl signal at 156 ppm. D) ATR-IR spectra of PEG 1000, HMDI, activated PEG 1000, PEI 600, and block copolymer PEI-(600)-PEG(1000)₃ (from top to bottom). Disappearance of the isocyanate stretching band at 2274 cm⁻¹ and signals for the urethane bond at 1724 cm⁻¹ and the urea bond at 1620 cm⁻¹ indicated successful functionalization.^[436] Spectra are shifted for better visualization.”

“The extent of the PEG to PEI grafting was determined based on proton integration in $^1\text{H-NMR}$ spectra (**Figure 3.7C**). Ratio of signal intensities of the two polymer backbones for $-\text{CH}_2-\text{CH}_2-\text{O}-$ and $-\text{CH}_2-\text{CH}_2-\text{N}-$ results in a grafting density of three PEG chains onto the hyperbranched PEI.^[437] Due to the highly charged and hyperbranched polyelectrolyte and possible free PEG chains in the copolymer, the integration of the two backbones doesn't result in integer ratio of the two polymer backbones. The hydrodynamic radius of the unbound PEI-PEG copolymer is in the range of 6.5 nm (**Figure A.4B-C**). The resulting radius for the $\text{PEI}_{(1)}\text{-PEG}_{(3)}$ copolymer is not the sum of four homopolymer and can be attributed to crosslinked PEI chains, due to insufficient removal of the NCO-linker during copolymer synthesis. Additionally, the integration of the $^1\text{H NMR}$ (**Figure 3.7C**) showing higher values for the polymer composition, making the presence of copolymer with higher composition possible.

Negative staining TEM, isothermal titration calorimetry (ITC) (**Figure 3.8**) and differential scanning calorimetry/thermogravimetric analysis (DSC/TGA) (**Figure A.5**) were used to analyze the coating of DMSN. ITC measurement were able to analyze the energy release during the interaction of the polymers with the silanol surface and the resulting binding kinetic. PEG showed the weakest interaction with DMSN, followed by PEI-PEG copolymer. PEI showed the strongest interaction, indicating domination of the binding kinetic with DMSN. The combination of the steric repulsion of the PEG chains and the ionic interaction of the PEI polymer with the surface silanols results in a polymer, which is able to effective bind to the nanoparticle surface. Additionally, the strong interaction of the PEI segment with the carrier ensures steric stabilization of the DMSN through PEG chains, radiating outwards from the center.

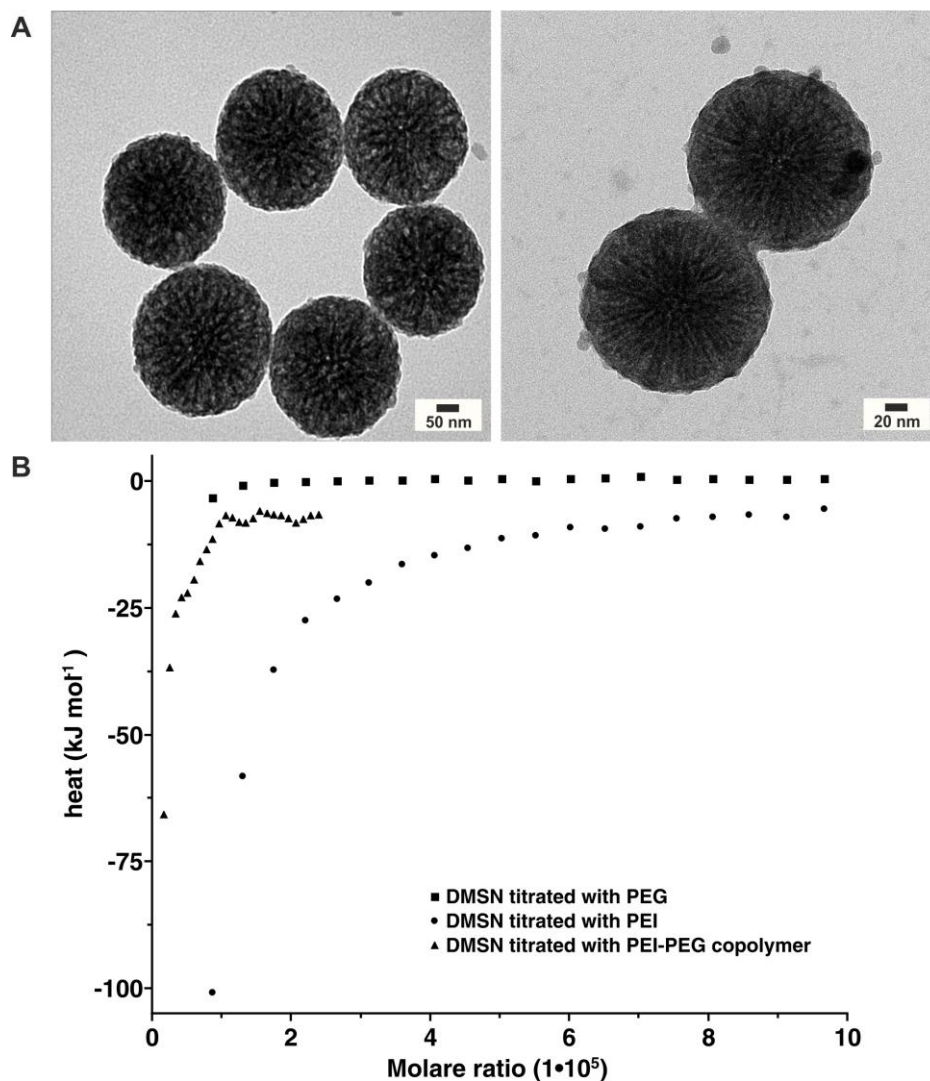


Figure 3.8. Interaction of the gatekeeper with DMSN. (A) TEM images of coated DMSN-B using phosphorous tungstic acid as negative stain for PEI-PEG confirmed full coverage of the mesoporous structure with the polymer. (B) The *in situ* coating process of DMSN-B with the gatekeeper was tracked with ITC, which demonstrated high affinity of copolymer to the silanol surface of the DMSN. Molecular weight calculations for DMSN see appendix. Mean molecular weight of the polymer was 3.600 g/mol, calculated using ^1H NMR measurements.

Effective surface charge in terms of the ζ -potential increased from -19 mV to +23 mV after functionalization of DMSN-F with PEI-PEG (**Table A.1**). Additionally, BJH and BET measurements revealed that the coating process reduced the DMSN-F surface area and the pore volume by 40% and 44%, respectively, with slightly diminished pore size distribution (**Figure A.6**). To ensure biocompatibility, biodegradability and non-toxicity, the complete removal of the surfactant was confirmed by ^{13}C ssNMR, ATR-IR and DSC/TGA measurement (**Figure 3.9**).

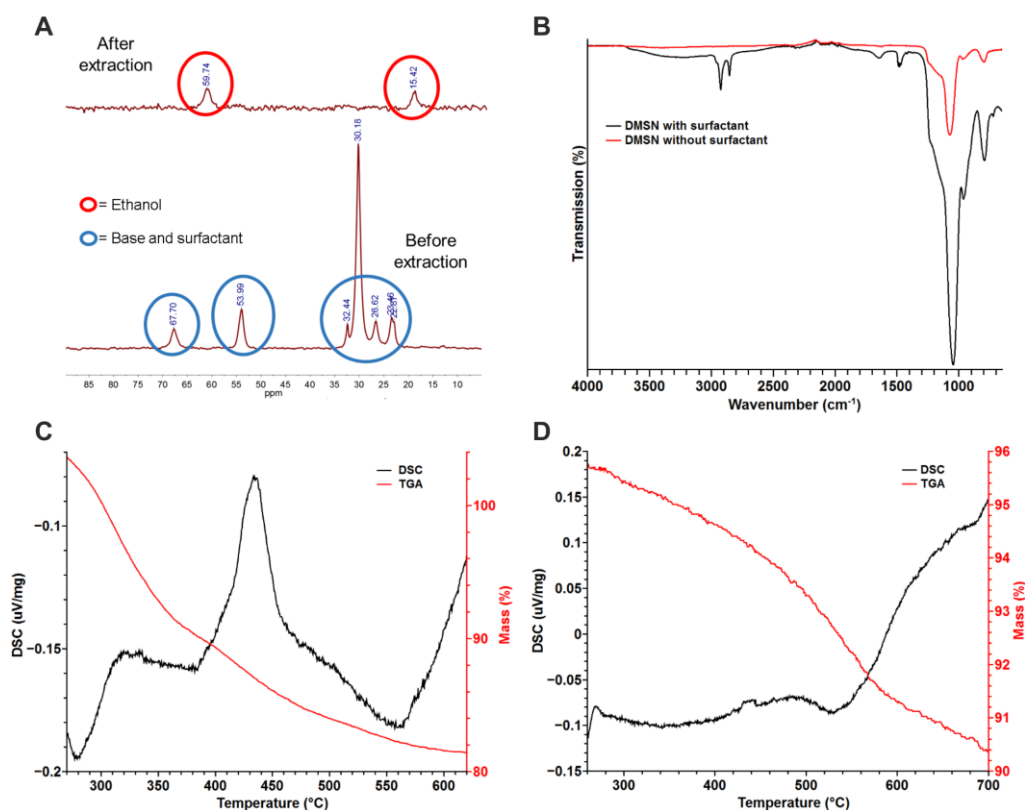


Figure 3.9. Analysis of the DMSN after surfactant extraction. (A) ^{13}C ssNMR measurements of DMSN before (bottom) and after (top) template extraction. Disappearance of surfactant- and base-related signals^[438] show successful template extraction. (B) ATR-IR spectrum of DMSN before and after surfactant removal. No vibrational signals of the surfactant alkane backbone^[439] (2850 cm^{-1} , 2920 cm^{-1} , 1470 cm^{-1}) was visible after extraction. TGA and DSC measurement of (C) non-extracted and (D) extracted DMSN shows a small mass lost and no exothermic signal at around $440\text{ }^{\circ}\text{C}$ indicating complete removal of the pore template. The small visible exothermic signal at $480\text{ }^{\circ}\text{C}$ is compatible with the decarboxylation of covalently bound fluorescent dye. The endothermic signal at higher temperature range was attributed to recrystallization of the amorphous silica network.

Furthermore, degradation of DMSN in PBS solution and Dulbecco's Modified Eagle Media (DMEM) with 10% fetal calf serum at $37\text{ }^{\circ}\text{C}$ was analyzed by TEM over time (**Figure 3.10**). After 2 d the pore structure and morphology of uncoated DMSN demonstrated significant structural degradation in both solutions, while PEI-PEG functionalization displayed delayed degradation. After 7 d, DMSN were completely degraded. MSN are biodegradable in medium due to high concentrations of divalent ions that form calcium and magnesium silicates and intercalate into DMSN. Additionally, hydrolysis of the silicon-oxygen bond by nucleophilic addition of hydroxyl ions and protonation leads to disintegration of silica-based nanoparticles after several days.^[70]

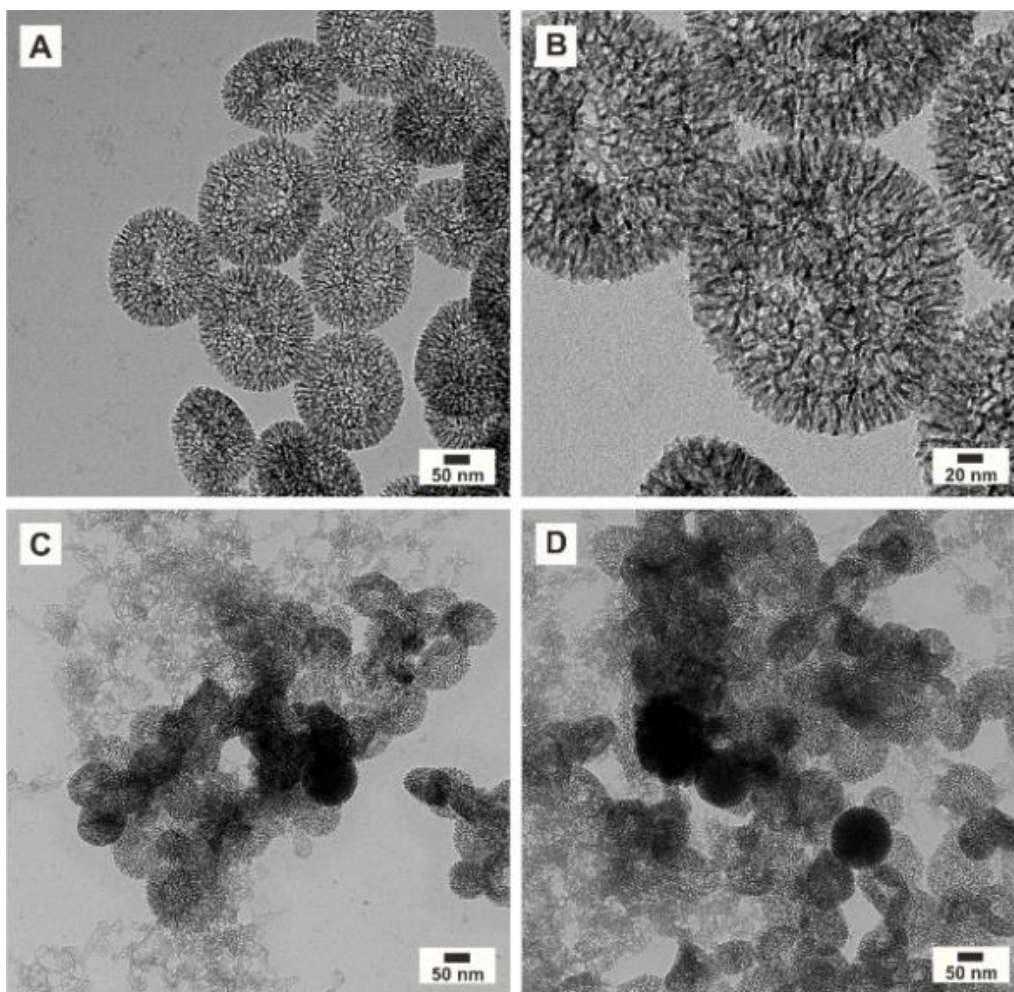


Figure 3.10. Biodegradation of the DMSN in fetal calf serum. (A, B) Biodegradability of PEI-PEG-coated DMSN in DMEM + 10% fetal calf serum at 37 °C after 48 h and (C, D) after 7 d. Pore degradation and structural deformation after 48 h was followed by complete dissolution of DMSN after 7 d.

Toxicity of nanoparticles is a key issue for safe application and dose- and nanoparticle-dependent toxicity has been reported previously.^[440–442] Toxicity of non-coated and unloaded DMSN, PEI-PEG-coated and unloaded DMSN, DMSN-F, and DMSN-R was assessed with the 3-(4,5-dimethylthiazol-2-yl)-2,5-diphenyltetrazolium bromide (MTT) assay for WeHi-164 cells. Significant toxicity was only found at 50 µg/ml for any of the tested particles. Concentrations ≤ 5 µg/ml did not lead to significant toxicity, making DMSN attractive candidates for biomedical applications. Similar results were observed for UKRV Mel15a (human melanoma cells) and A431 (human epidermoid carcinoma) cells (**Figure 3.11**, data for A431 not shown).

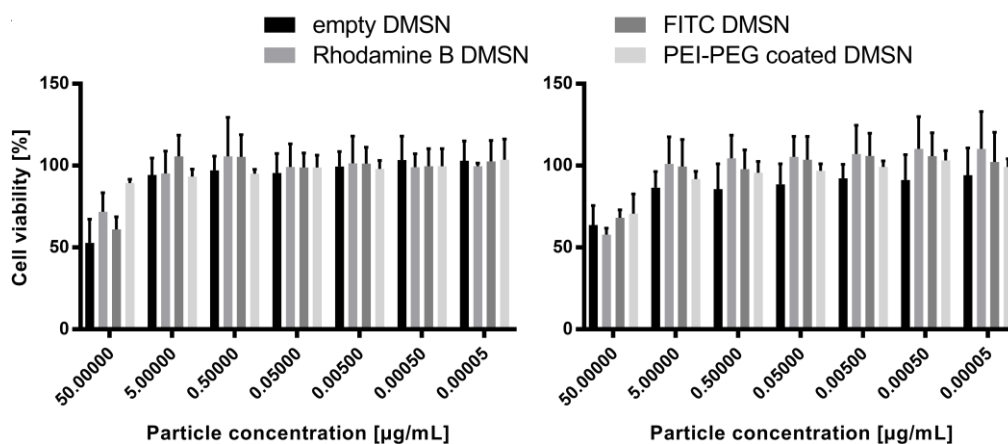


Figure 3.11. Toxicity and Uptake of DMSN. (A) After 24 h of treatment with empty, DMSN-R, DMSN-F or PEI-PEG coated DMSN at indicated concentrations, UKRV Mel15a (left) and WeHi-164 (right) cell viability was measured using MTT assay. No toxicity for concentrations below 50 µg/ml was observed. (All experiments were performed in triplicate and means \pm 1 standard deviation are shown).

Cellular uptake and cytokine release. Before TNF- α can act against tumor cells, PEI-PEG-coated DMSN must first be acidified to release their cargo. Cytokine release was made possible by utilizing the cationic charge of the hyperbranched PEI. Endosomal processing after cellular uptake involves acidification (pH 5 and lower).^[247] Upon protonation of the polymer, the osmotic influx and interactions of the cationic polymer with the anionic cell membrane can break the endosome.^[247,248] Furthermore, pH-triggered carriers are effective due to acute hypoxia, disorganized vasculature, elevated interstitial pressure, and lactate production through glycolysis, all contributing to low pH in tumor tissue.^[443,444] However, low extracellular pH also promotes invasiveness, whereas high intracellular pH provides an advantage over normal cells in terms of cell growth.^[222] The fate of DMSN after cell uptake and *in vitro* delivery of TNF- α was tracked with three different dye-labeled DMSN (DMSN-R, DMSN-B and DMSN-F). A431 cells and human dendritic cells (DC) were stained, and uptake of the DMSN was observed using confocal microscopy. Images were obtained after up to 4 h of treatment with dye-labeled DMSN. Accumulations of DMSN were found inside (white arrows) A431 cells and in DC following treatment (**Figure 3.12**). No significant accumulation of DMSN inside cells was found for the 4 °C control.

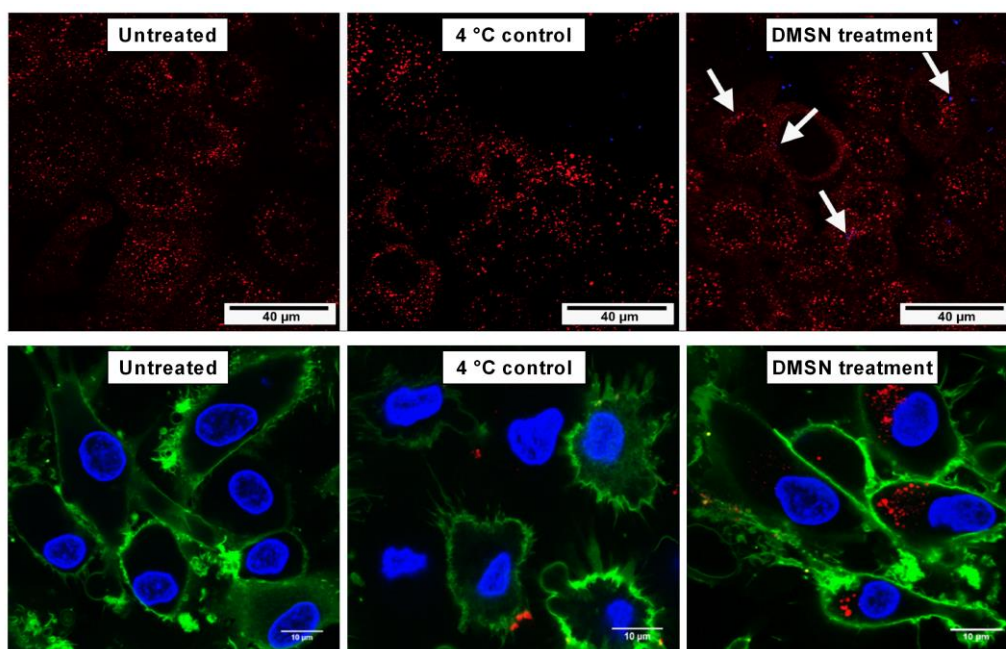


Figure 3.12. Cellular uptake of DMSN. Cells were stained and treated with dye-labeled DMSN. Accumulations of DMSN-B were found inside (white arrows) A431 cells (top) and in DC (DMSN red, nucleus blue, cell membrane green, bottom) following treatment. All experiments were performed in triplicate and means \pm 1 standard deviation are shown.

TNF- α release and particle stability. PEI-PEG-coated DMSN have to hold and shield off their cargo for a period of time, and then release their cargo once the coating disintegrates. Previous research employed TNF- α bound to gold nanoparticles to enhance nanoparticle delivery to the tumor site.^[429] However, the use of TNF- α was restricted by its toxicity, since it was coated onto the outer surface of the particles. Protection of the cargo is critical since free TNF- α has a relatively short half-life of 18.2 min *in vivo*.^[445] After up to 24 h of incubation of TNF- α -loaded DMSN in culture media, enzyme-linked immunosorbent assay (ELISA) was used to determine the TNF- α release, calculated as the percentage of TNF- α in the supernatant.

TNF- α release was calculated as the percentage of TNF- α in the supernatant compared to original drug load. Complete release was observed after 6 h, with an almost linear increase in release prior to this time point (**Figure 3.13A**). TNF- α release was greatly delayed when DMSN were coated with PEI-PEG-copolymer after drug loading: drug release was below 25% for up to 3 d. Thereafter, TNF- α was released rapidly from the DMSN, with almost complete release after 5 d (**Figure 3.13B**). We assume the open structure of the DMSN and its biodegradation is responsible for the full release of the cytokine. The observed delay of the therapeutic effect of TNF- α on tumor cells suggests successful encapsulation and preservation of the drug.

Encapsulation Efficiency. Since we observed uptake and acidification of DMSN by tumor cells, we hypothesized that TNF- α release increases when cells are treated with TNF- α -loaded DMSN. To test this hypothesis, WeHi-164 cells were incubated with decreasing concentrations of closed and pH-opened DMSN, and cell viability was assessed at 12, 24, and 48 h (**Figure 3.13C**). Fold TNF- α half maximal effective concentration (EC_{50}) was calculated for each time point (**Figure 3.13D**). After 12 h of treatment with TNF- α -loaded DMSN, TNF- α EC_{50} was 1264.74 $\mu\text{g/ml}$, while EC_{50} for pH-opened TNF- α -loaded DMSN was 4.68 $\mu\text{g/ml}$. EC_{50} for closed DMSN was 270.67 times than EC_{50} for opened DMSN at 12 h. The difference between EC_{50} values of closed and opened DMSN diminished over time: fold DMSN TNF- α concentration decreased to 30.88 and 1.02 at 24 and 48 h, respectively, indicating slow-release of TNF- α is aggravated through cellular uptake in a time-dependent manner. The observed cytotoxicity delay of encapsulated TNF- α may make DMSN drug delivery superior compared to normal drug administration. Through slow-release, local TNF- α concentration may remain at non-toxic levels for a period of time, increasing tumor vessel permeability.^[446] The observed full-on TNF- α release at later time points *in vitro* can potentially induce severe necrosis in tumor tissue and damage tumor endothelia *in vivo*, overcoming the obstacle of insufficient solid tumor drug penetration.^[447]

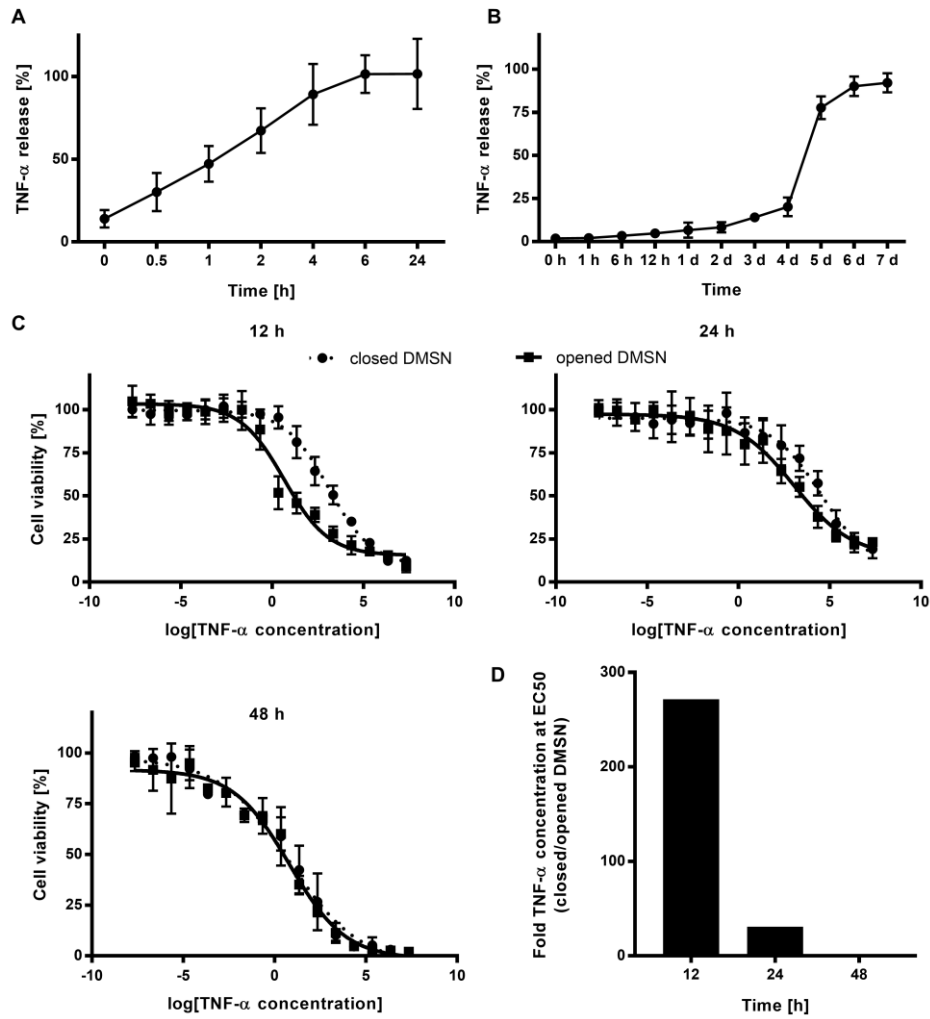


Figure 3.13. Encapsulation of TNF- α in DMSN. (A) TNF- α release was measured using ELISA and calculated as the percentage of the originally loaded amount. TNF- α -loaded, uncoated DMSN were kept in cell media for up to 24 h. (B) TNF- α release from TNF- α -loaded PEI-PEG coated DMSN cultured in DMEM with 10% fetal calf serum for up to 7 d. WeHi-164 tumor cells were treated with (C) closed and (D) pH-opened TNF- α -loaded DMSN. Cell viability was assessed 12 h, 24 h and 48 h after treatment using MTT assay. (D) Fold DMSN TNF- α concentration at EC₅₀ was calculated for different time points. All experiments were performed in triplicate and means \pm 1 standard deviation are shown.

TNF- α -loaded DMSN mature DC. TNF- α is targeting tumor not only through its toxic effects on tumor cells but also through stimulation and activation of the immune system. To test whether TNF- α -loaded DMSN are able to stimulate the immune system we investigated their impact on DC maturation. DC maturation is characterized by upregulation of the costimulatory molecules CD80 and CD83. Inducers of maturation include danger signals like pathogen-associated molecular patterns or cytokines derived from other cells. TNF- α plays an important role in inducing DC maturation.^[448,449] To display the immunostimulatory effect of TNF- α , we used a cytokine cocktail insufficient for inducing full DC maturation. While immature DC displayed low expression of CD80 (9%) and CD83 (11%), expression of CD80 (36%) and CD83 (53%) was increased on DC matured with cytokines and TNF- α . DC matured with cytokines only and cytokines with empty DMSN displayed comparably weak upregulation of CD80 (14% and 12%, respectively) and CD83 (18% and 21%, respectively) (**Figure A.7A**). TNF- α -loaded DMSN were able to cause upregulation of CD80 (24%) and CD83 (30%) as well. However, Upregulation of the two maturation markers was not as evident as for the free TNF- α group, confirming our previous findings that DMSN are capable of delaying the effects of TNF- α while maintaining its biological function. Increased expression of costimulatory molecules is often associated with a higher capacity to stimulate T cells. To test whether DC matured by TNF- α -loaded DMSN are able to stimulate T cells we performed a mixed lymphocyte reaction. While increased stimulatory ability of DC matured with cytokines and TNF- α -loaded DMSN in comparison to immature DC was found, stimulatory ability was lower compared to DC matured with free TNF- α at a DC:CD4⁺ T cell ratio of 1:20 and 1:40 but equal at a 1:10 ratio (**Figure A.7B**). These findings show that the immunostimulatory capacity of TNF- α is maintained when encapsulated in DMSN.

3D Melanoma Spheroids: DMSN Distribution, Cell Death and Cell Cycle. To address the potential issue of insufficient solid tumor drug penetration we investigated tumor penetration, uptake, and distribution of DMSN into 3D tumor spheroids, an *in vitro* model of *in vivo* tumor environment with advantages over classic *in vitro* techniques.^[450-452] The use of the FUCCI system allowed real-time cell cycle analysis: FUCCI cells in G1 phase express Kusabira Orange, while cells in S/G2/M phase express Azami Green.^[453] Cell death was analyzed using real-time DRAQ7 staining. Using this 3D real-time system, we were able to determine the influence of TNF- α -loaded DMSN on the cell cycle and cell death in a time-dependent manner. FUCCI-C8161 melanoma cells^[454] were grown as 3D spheroids for 3 d and subsequently treated up to 24 h with free TNF- α , empty DMSN-B, low-dose TNF- α -loaded DMSN-B, and high-dose

TNF- α -loaded DMSN-B. Spheroid sections were imaged by confocal microscopy. Accumulation of DMSN was mainly observed in the spheroid periphery after 6 h, whereas DMSN were found throughout the spheroids after 24 h (**Figure 3.14**). The small particle size allows rapid penetration of the tumor spheroids. In contrast to a previously described lipid-based carrier with a size of up to 20 μm , DMSN are less likely to be delivered to the liver, an organ especially sensitive to TNF- α .^[69,418] No significant changes in the cell cycle compared to control were observed (**Figure 3.14A**, **Figure A.8**). After 1 h of treatment with free TNF- α or high dose TNF- α -loaded DMSN, tumor spheroids mainly displayed cells in G1. As C8161 cells spend 10 to 13 h in S/G2/M phase, in which they are more sensitive to cytotoxic impacts.^[454,455] TNF- α appeared to preferentially affect cells in S/G2/M phase with a subsequent increase of cell death after 6 and 24 h (**Figure 3.14B-C**). However, cell death after 6 h was greater for the free TNF- α group compared to the high-dose TNF- α -loaded DMSN-B group. Late onset DRAQ7-positivity of up to 4 h from morphological cell death signs to DRAQ7-positivity has been observed (data not published yet). When treated with low-dose TNF- α -loaded DMSN-B, cytotoxicity was delayed (**Figure 3.14D**). No significant changes were observed after 1 h, the number of cells in S/G2/M phase was significantly reduced after 6 h, and cell death was induced after 24 h. Interestingly, for the low-dose TNF- α -loaded DMSN-B group, occurrence of green S/G2/M phase cells indicated a small number of cells in the spheroid corona were able to recover and re-enter the cell cycle. As previously described,^[456] we observed TNF- α induced depletion of cells in S/G2/M phase. Cell-cycle mediated drug resistance attenuating treatment efficiency is an important issue in cancer treatment,^[457] and will have to be addressed in further research. However, the inflammatory and immune system activating potential of TNF- α may be able to prevent the emergence of resistance mechanisms.”

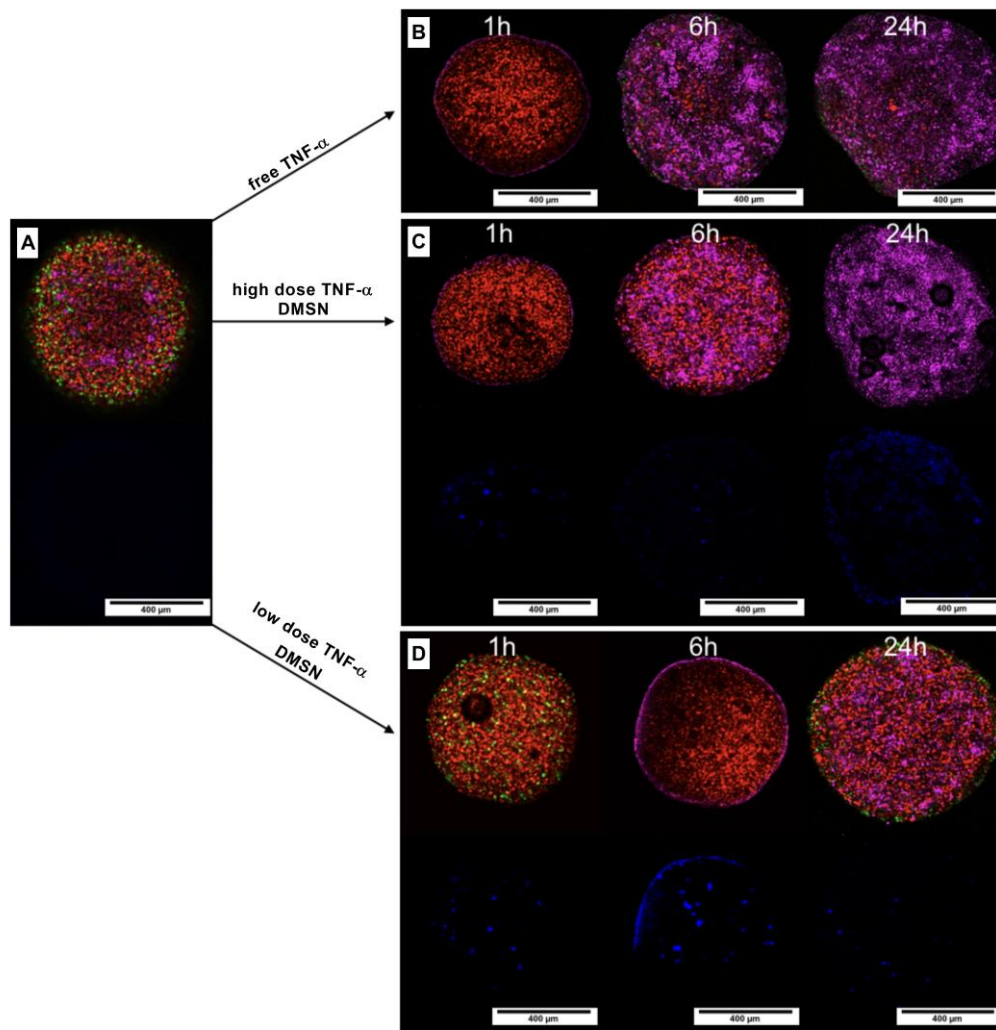


Figure 3.14. Impact on cell cycle and cell death of TNF- α -loaded DMSN in 3D melanoma spheroids. “FUCCI (red: G1, green: S/G2/M phase) C8161 melanoma cells were grown as 3D spheroids and dead cells stained using DRAQ7 (pink). (A) Untreated spheroid. Spheroids were treated with (B) free TNF- α , (C) high- and (D) low-dose TNF- α -loaded, DMSN-B (blue). Images were obtained with confocal microscopy at the indicated time points. All experiments were performed in triplicate.”

***In vivo* imaging: Cargo release and DMSN tracking.** After confirmation of sufficient solid tumor drug penetration of the DDS, we investigated uptake, release and distribution of TNF- α loaded DMSN into NOD-scid.HLA-A2.1 transgenic mice via a non-invasive optical imaging technique. *In vivo* NIR fluorescence imaging of NIR labeled TNF- α and Cy5- labeled DMSN was performed to track the fluorescent dye of the loaded drug and to locate the nanoparticle after subcutaneous injection (**Figure 3.16**). The previously shown *in vitro* shielding effect of the gatekeeper system and the time-delayed release of TNF- α could be confirmed in the *in vivo* experiment. We monitored the fluorescent signal decay over time of the Cy5 labeled DMSN (**Figure 3.16A**) and CW800 labeled TNF- α (**Figure 3.16B**). The particle signal is localized on the injection side and slowly decreasing over time, showing the subsequent

disintegration of the particle. A combination of calcium and magnesium silicates formation and hydrolysis of the silicon-oxygen bond by nucleophilic addition of hydroxyl ions leads to disintegration of silica-based nanoparticles after several days.^[70] The fluorescent signal of the free TNF- α shows distribution throughout the whole body with fast degradation over 72h. In contrast, TNF- α loaded into DMSN is clearly located at the injection side, slowly degrading over 10d. This time-delayed release capacity is an important property of the DDS, restricting interaction of the drug with healthy cells until the nanoparticle reached the TMI. The slightly acid pH triggers drug release at tumor site, reducing side effects and damage of healthy tissue. Additionally, we compared the total radiant efficiency of the DMSN and TNF-DMSN experiment (**Figure 3.16C**). Despite drug loading, similar degradation rate in comparison to unloaded DMSN can be observed. In **Figure 3.16D**, an overview of the fluorescent signal decay over time of the free TNF- α and TNF-DMSN is shown. The prolonged life time of loaded TNF- α due to the polymer coating leads to a three-fold increase in TNF- α bioavailability.

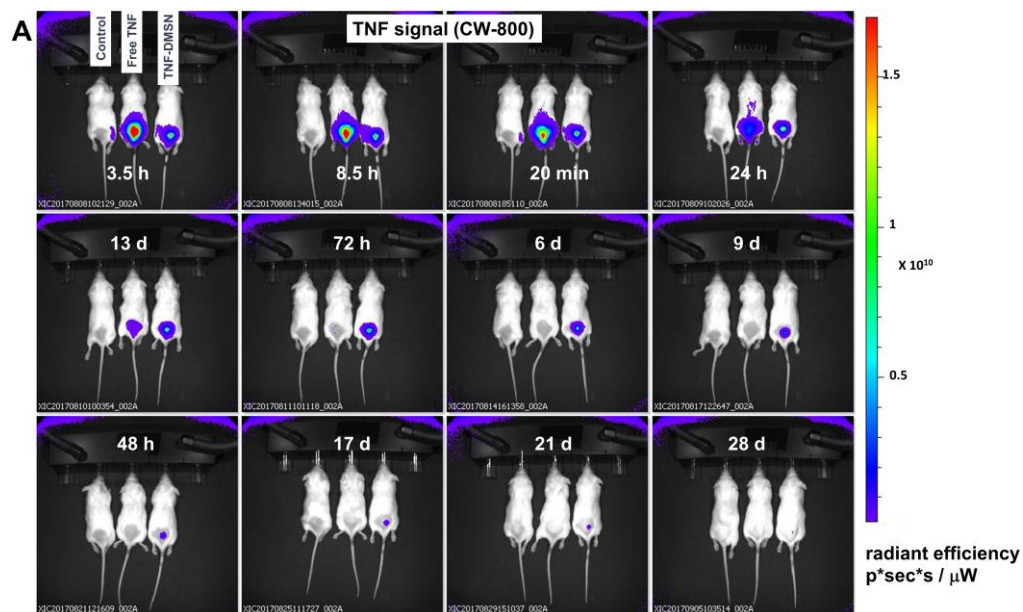


Figure 3.15. CLSM data of Cy5-DMSN and CW800-TNF- α over 28 days in transgenic mice. A) CW800 labeled TNF- α is quickly cleared over 72h with distribution over the complete body. In comparison, the protected drug is stable up to 10 days and is spatially restricted.

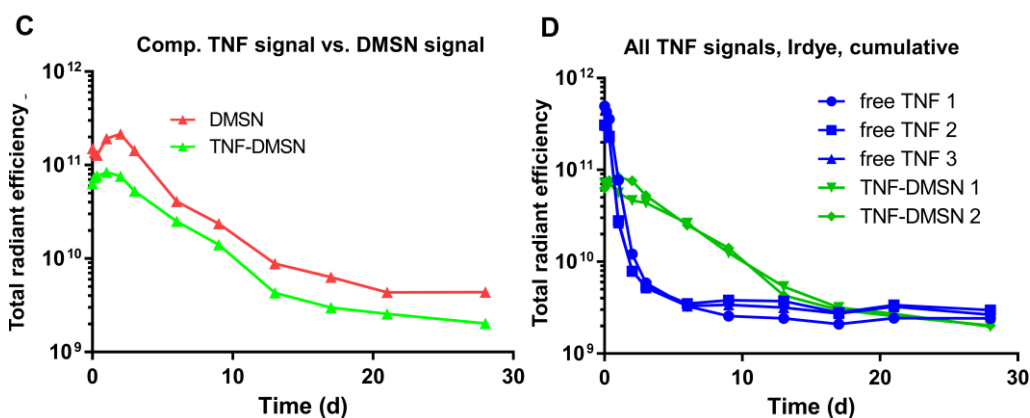
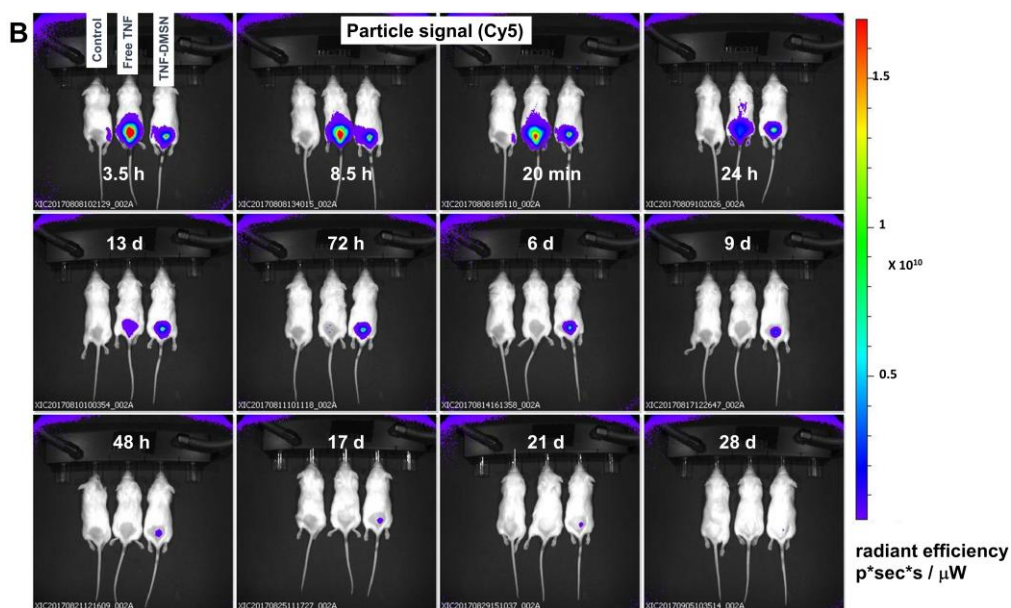


Figure 3.16. CLSM data of Cy5-DMSN and CW800-TNF- α over 28 days in transgenic mice. B) The decay of the fluorescent signal of the Cy5 labeled DMSN. The particles were applied subcutaneously next to the tumor and disintegrated over time. C) No difference in the degradation process of unloaded and loaded DMSN is visible. D) Total radiant efficiency over time of the free drug and encapsulated drug. In comparison to the free drug, the retention of the protein inside the DMSN-TNF can be monitored, leading to a three-fold increase in lifetime.

Conclusion

“We demonstrated that pH-sensitive PEI-PEG DMSN are a promising tool to encapsulate and shield TNF- α , a highly toxic drug used in cancer therapy. DMSN can attenuate the systemic toxicity of TNF- α while maintaining its pleiotropic anti-tumor activity. Complete regression of 3D melanoma spheroids *in vitro* was dose-dependent, highlighting the need for sufficient TNF- α release at the tumor site.” Additionally, first *in vivo* experiment showed the applicability of the DDS in complex biological environment. “The good monodispersity, pore volume, biodegradability, loading capacity and pH-triggered release properties of the DMSN are key factors for the further usage of systemic toxic drugs for *in vivo* applications. Our results show for the first time

that DMSN are capable of efficiently shielding highly toxic TNF- α , potentially leading to a novel systemic use of TNF- α in cancer treatment. Nanoparticle encapsulation is a promising approach to enhance the efficacy of anti-tumor drugs, while minimizing adverse side effects.”

Part IV

4. Controlled Surface Functionalization of Dendritic Mesoporous Silica Nanoparticle for Drug Delivery of Small Molecule Drugs

This project was developed in collaboration with the Chemistry Department Bielefeld University (Bielefeld, Germany) and the University Medical Center of the Johannes Gutenberg-University Mainz, (Mainz, Germany). Details to the individual contribution of each author are listed in the Appendix.

4.1 Introduction

Chemotherapy with transition metal complexes is an established method for fighting cancer. Cis-platin and second generation platinum-based anticancer drug enabling the treatment of cancer patients for almost 40 years. Despite significant improvement of the original cis-platin complex (carboplatin, oxaliplatin), side effects like nephrotoxicity and neurotoxicity are still severe safety issues. Transition metal complexes bind preferentially at the nucleobases of the DNA or they intercalate into the base pairs. The family of cytotoxic Cu(II) dinuclear complexes are related to metalloenzymes that catalyze the hydrolytic cleavage of the phosphoester bonds.^[458] Their mechanism of action is connected to cis-platin, targeting the cell replication system and inducing apoptosis in cancer cells. For cisplatin, the activation of the drug is an intracellular event. Upon administration to the bloodstream as an intravenous injection, cisplatin maintains a relatively stable neutral state due to high concentration of chloride ion (100 mM). Inside the cell, the lower ambient chloride ion concentration (4-12 mM) facilitates cisplatin aquation to form the cationic aqua complexes.^[459] A well-known problem of transition metal complexes lies in the interaction with the intracellular matrix. For cisplatin, the mono-aquated form is recognized as a highly reactive species, but its formation rate is limited by the interaction with many endogenous nucleophiles, such as glutathione (GSH), methionine, metallothionein, and protein. Thus, when cisplatin enters cells, it is potentially vulnerable to cytoplasmic inactivation by these and other intracellular components^[460] The highly toxic Cu(II)-based anticancer drug (CuOAc) shows a ten-fold increased killing potential in comparison to cis-platin, but the positive charge of the complex needs to be shielded from the interaction with extra cellular components to take effect. To enable the transport of CuOAc, we tried to solve different problems. Can the killing potential of the free drug be maintained during slow release

from a nanoparticle formula? Is the complex stable in cytoplasmic environment or is the inactivation with endogenous nucleophiles and other intracellular components hindering cell toxicity? Can the positive charge of the complex be shielded to avoid interaction with extracellular components? The encapsulation and transport of cytostatic drugs is a highly researched topic, aiming for a reduced systemic side effects and damage of healthy tissue.

Improved tumor delivery strategies of transition metal complexes for circumventing platin-resistance mechanisms might provide future clinical benefits. Gatekeeper systems must release the cargo through tumor cell specific mechanisms and triggers by utilizing the tumor microenvironment (TMI) and intrinsic features of the tumor phenotype. These intrinsic properties of the TMI like pH increase, oxygen deficit, reactive oxygen species (ROS) level and intracellular GSH concentration are utilized for an intracellularly triggered release of the drug. pH-triggered release systems depend on the low pH value within the lysosome and endosomal compartment inside tumor cells and the evaluated pH value outside the cell. Endosomal fusing with lysosomal vesicles after endocytose exposed the delivery system to pH values up to 4.5.

We utilized dendritic mesoporous silica nanoparticles (DMSN) coated with a pH/redox responsive ferrocene carboxaldehyde (ferrocene-CA) / β -cyclodextrin (β -CD) gatekeeper for drug delivery of Doxorubicin and CuOAc in a squamous cell carcinoma (SCC) tumor model. The gatekeeper system combines a pH labile imine bond between the nanoparticle and ferrocene-CA and the redox-labile hydrophobic interaction of ferrocene-CA with β -CD for drug retention. β -CD is a cyclic oligosaccharide consisting of 7 glucopyranosyl units linked by α -(1,4) bonds. It has a unique structure with a hydrophobic cavity to form inclusion complex with various hydrophobic guests. For improved water solubility, randomly methylated β -CD with degree of substitution of < 2 is utilized for pharmaceutical applications.^[461] Firstly, the ferrocene stalk is bridged through a pH-labile imine bond on the DMSN surface. Next, the interior cavity of the cyclic β -CD interacts with the organic moiety of the ferrocene stalk through hydrophobic-hydrophobic interaction, trapping the cargo inside the pores. Release of the cargo was possible through cleavage of the nanoparticle-stalk bridge due to protonation of the imine bond at low pH values, leading to dissociation of the stalk/cap from the DMSN. Additionally, high ROS level inside cancer cells can lead to reduction of the ferrocene subunit, adding an additionally gatekeeper trigger mechanism during drug delivery inside cancer cells (**Figure 4.1**).

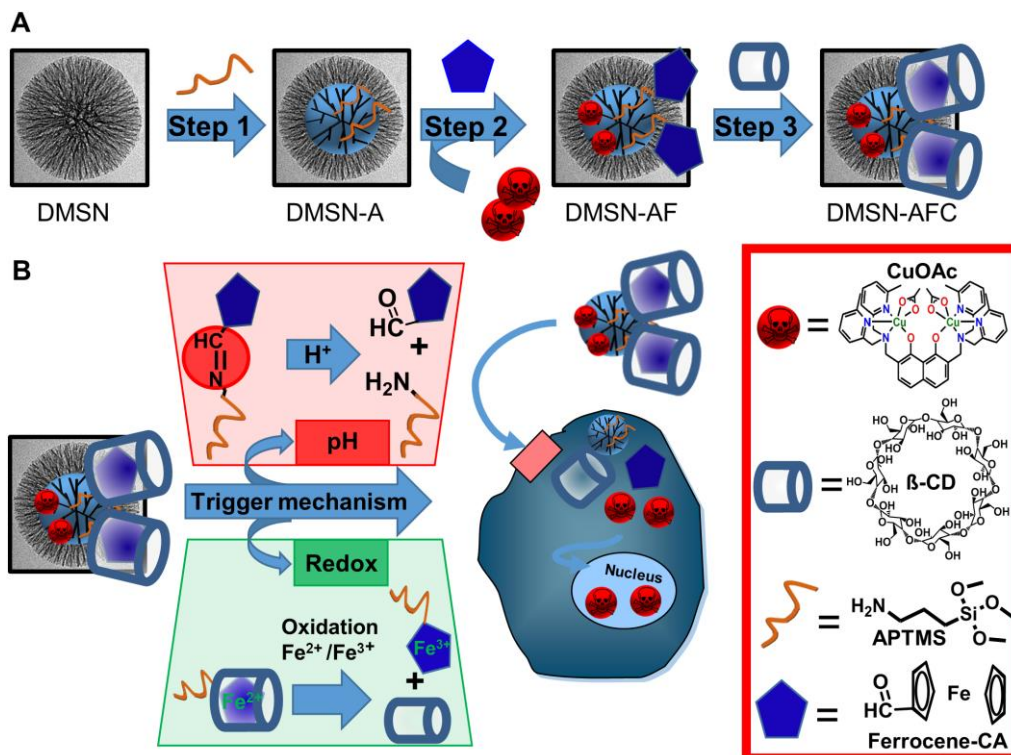


Figure 4.1. Gatekeeper system for encapsulation and transport of a potent Cu^{II}-based anticancer drug. A) Stepwise functionalization of the DMSN surface for pore sealing. After covalent attachment of the amine anchor through base-catalyzed condensation of (3-aminopropyl)trimethoxysilane (APTMS) (Step 1), the nanoparticles were loaded with the drug. After incubation overnight, the addition of ferrocene-CA leads to imine bond formation between the aldehyde group of the ferrocene and the primary amine group on the DMSN surface (Step 2). Final pore sealing was achieved through the interaction of the hydrophobic cyclopentadienyl ring of the ferrocene with the hydrophobic cavity of the cyclic sugar β -CD (Step 3). B) Trigger mechanism for the intracellular release of the Cu^{II}-based anticancer drug (CuOAc). Protonation of the imine bond between the ferrocene/ β -CD stalk and the DMSN releases the drug inside the lysosome. Additionally, high concentration of ROS level inside cancer cells can oxidize the Fe^{II} center of the gatekeeper subunit, leading to the removal of the physical obstacle blocking the pore.

A pH/redox responsive gatekeeper was utilized to encapsulate and deliver CuOAc and doxorubicin into a soft cell carcinoma (SCC) tumor cell line. We quantified the pore coverage of the DDS through all three functionalization steps and consequently optimize the encapsulation process. Detailed knowledge of surface chemistry, ligand distribution and amount of gatekeeper enabled complete pore sealing. Intracellular release of Doxorubicin was confirmed through cell metabolic activity measurements and a DNA damage assay. The reduced intracellular effect of CuOAc could be linked to cytoplasmic inactivation by endogenous nucleophiles and low intracellular release from the DDS.

4.2 Results and Discussion

Carrier system: DMSN synthesis, gatekeeper coverage and characterization. For the shielding and transport of small molecule drugs (CuOAc, doxorubicin) the pore size of the carrier system is a crucial factor. The ferrocene stalk / β -CD inclusion complex anchored onto the particle need to physical block pore entrance to restrict or significant slowdown drug diffusion. For effective encapsulation, we adjusted the pore size of the DDS in the range of 6 to 9 nm. Loading experiment with pore size > 9 nm led to significant drug leakage during storage. We synthesized fluorescent dye-labeled DMSN (Cyanine 5), based on our previous work.² Surface modification of the DMSN with 3-aminopropyltrimethoxysilane (DMSN-A) provides a suitable anchor for the ferrocene-CA stalk. **Table A.3** summarize the physicochemical properties of the DMSN-A and its functionalization with ferrocene-CA (DMSN-AF) and β -CD (DMSN-AFC). DMSN-A had particle diameters of 130 nm as confirmed by transmission electron microscopy (TEM) (**Figure 4.2A, Figure A.9**). Surface areas (Brunauer-Emmett-Teller, BET), pore volumes and pore sizes (non-linear density functional theory, NLDFT) of DMSN were determined by N_2 -sorption measurements (**Figure 4.2B, Figure 4.2C**) and showed pore diameters in the range from 6 nm to 9 nm, pore volumes of up to $1.02 \text{ cm}^3/\text{g}$ and surface areas of approx. $582 \text{ m}^2/\text{g}$. The *in situ* dye labeling during synthesis led to incorporation of fluorescent dye into the silica network, sparing the necessity of post-functionalizing the DMSN after drug loading, avoiding blocking of accessible pore volume and maximize the accessible surface area for functionalization. Wide Angle X-ray Scattering (WAXS) measurements showed the amorphous character of the DMSN (**Figure A.10**). The broad scattering signal indicates that the sample structure has no long range correlation repetition distance. Information on the pore structure of the particles is obtained from Small Angle X-ray Scattering (SAXS). **Figure 4.2D** shows SAXS patterns of silica nanoparticle at subsequent functionalization stages. For all samples, a diffuse scattering peak of comparable width is found around $q_0 = 0.7 \text{ nm}^{-1}$. This indicates, that the DMSN pore structure is maintained during the functionalization process. The peak position corresponds to a real space periodicity of $\frac{2\pi}{q_0} = 9 \text{ nm}$.

The peak is assumed to originate from the structure factor of the nanopore arrangement. Using the experimentally obtained specific surface area and assuming a local hexagonal short range ordered arrangement of cylindrical pores we estimate a pore diameter of 9nm. This value is in good agreement with the pore size distribution obtained by NLDFT analysis (**Figure 4.2C**).

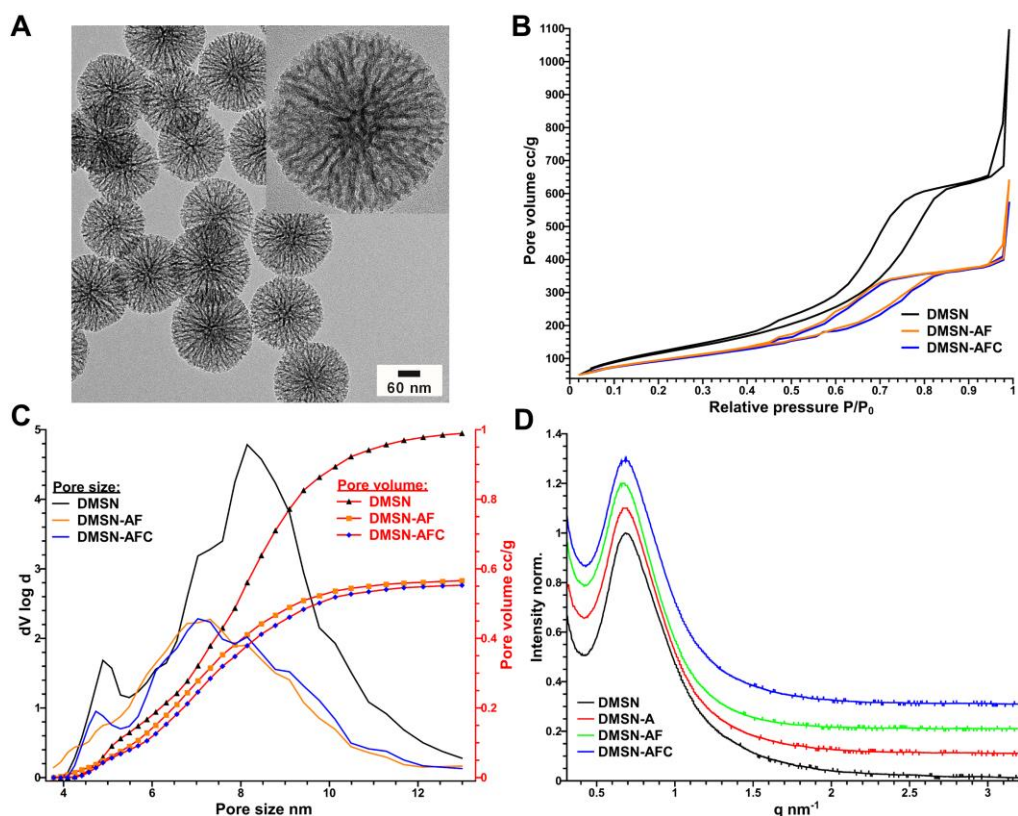


Figure 4.2. Physicochemical characterization of the carrier system. A) TEM images of DMSN-A. Inset shows the pore structure of the nanoparticle. B) Nitrogen sorption isotherm and C) pore size distribution and pore volume of the DMSN, DMSN-AF, and DMSN-AFC respectively. After functionalization with the gatekeeper, a shift in the hysteresis region of the sorption isotherm to lower relative pressure was observed. Gatekeeper attachment diminishes pore size and pore volume slightly. D) SAXS data of each functionalization step. The scattering patterns show broad peaks at $q_0 = 0.7 \text{ nm}^{-1}$. This indicates the presence of ordered mesostructures with a periodicity of approximately 9 nm. Additionally, the periodic arrangement of the nanopores is maintained after each functionalization step.

Knowledge of gatekeeper arrangement and local surface concentration ensures efficient drug loading. Before quantitative analysis of the surface coating, we confirmed the imine bond formation of APTMS with the aldehyde group of the ferrocene via solution ^1H NMR spectrum (**Figure A.11**). Further, the anchoring of the primary amine group to the DMSN surface was detected by the formation of carbon-silicon bonds (8.9 ppm) compared to free APTMS by ^{13}C ssNMR (**Figure 4.3A**) as well as the significant signal broadening (two order of magnitude compared to the solution NMR spectrum (not shown)). Appearance of the imino-group signal in the ^{13}C CP NMR spectrum at 163.4 ppm confirms the functionalization with ferrocene-CA (**Figure 4.3B**). Direct-polarization ^{29}Si magic-angle spinning nuclear magnetic resonance spectra (DPMAS NMR) confirmed the successful amine functionalization of the DMSN (**Figure 4.3D**) compared to non-functionalized DMSN (**Figure 4.3C**) through the presence of T units $[\text{R-Si}(\text{OSi})_n(\text{OCH}_2)_{3-n}]$ ($n = 2, 3$). The ^{29}Si resonances characteristic for the newly formed carbon-silicon bonds (T_2, T_3 ; -50 ppm to -70 ppm) are clearly detected in the

spectra. Surface coverage of the DMSN ^{29}Si resonances recorded by a direct polarization ^{29}Si DPMAS NMR is a powerful tool to quantify and analyze local silicon environments. A long recycle delay ensures complete relaxation. In general, the silanol groups are present at the surface of the NPs, on the walls of the pore channels and in cavities not accessible for larger organic moieties. We must distinguish between core sites connected to four Si neighbors via siloxane bridges ($\text{Si}(\text{OSi})_4$ (Q_4) and surface sites terminated by hydroxyl groups. For the calculation we assume the presence of the former two types of silanols ($(\text{HO})\text{Si}(\text{OSi})_3$ (Q_3) and $(\text{HO})_2\text{Si}(\text{OSi})_2$ (Q_2))³ (**Figure 4.3C, left**) ignoring the latter. We determine the populations of these silicon environments through signal deconvolution of the ^{29}Si DPMAS NMR spectrum. The change in relative ratio of partially to fully condensed silicon sites ($(\text{Q}_2+\text{Q}_3)/\text{Q}_4$) indicates alkoxy silane crafting. We observed decreased of the Q_2 and Q_3 peak areas with a simultaneous increase in Q_4 intensity during functionalization. Consequently, DMSN functionalization consumed 50% of the theoretically available surface silanol groups (**Calculation I, Appendix**). Additionally, ^{29}Si DPMAS NMR is a powerful tool to determine the relative surface coverage of the DMSN with aminosilanes. The grafting with APTMS results in 39.9% surface coverage (**Calculation II, Appendix**).

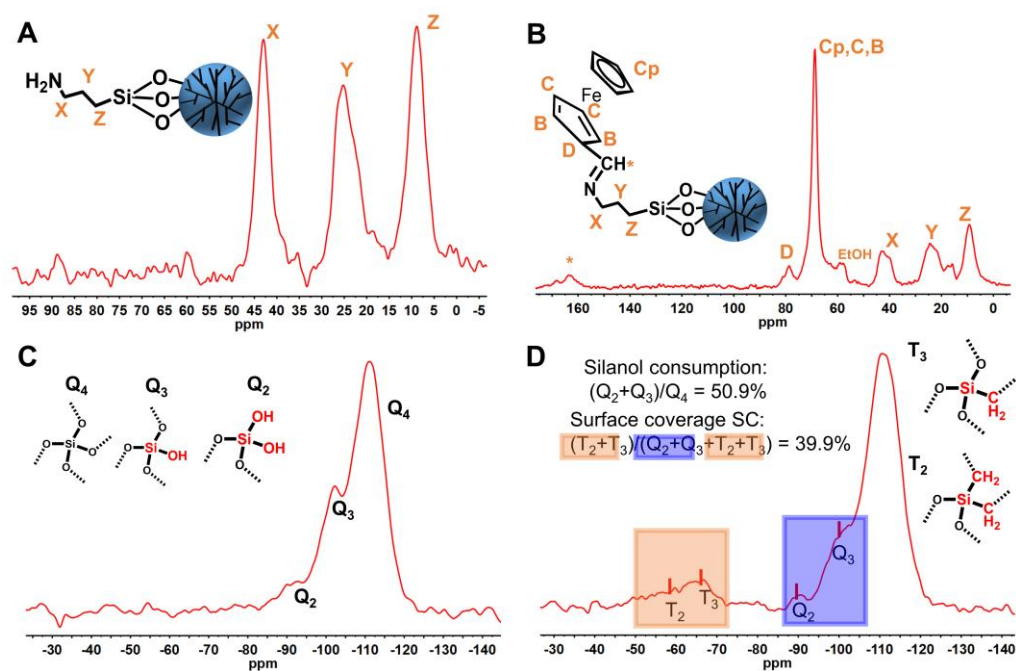


Figure 4.3. ^{13}C ssNMR of the stepwise functionalization process of the carrier system and ^{29}Si ssNMR for quantification of the surface coverage. A) Successful surface functionalization of the DMSN is proven by the change of the ^{13}C shift of the Z resonance as well as by the signal broadening more than 700 Hz. B) ^{13}C CP MAS ssNMR spectrum of the DMSN-AF. The signal at 163.4 ppm for the newly formed imino-group shows the functionalization of the free NH_2 group with the reacting ferrocenyl aldehyde. ^{29}Si DPMAS NMR of the C) DMSN and D) DMSN-A. The consumption of the surface silanols during functionalization is clearly visible through reduction of the $((Q_2+Q_3)/Q_4)$ ratio. Additionally, the C-Si Signals (T_3 , T_2) shows the presence of amine moieties on the DMSN surface. Quantitative determination of the surface coverage SC was possible with **Calculation II, Appendix**. The area under the individual signals was determined by deconvolution (Software 1D WinNMR version 6.2.0.0.).

Surface chemistry: Quantification of accessible anchor groups for pore coverage.

The quantification of binding sites on top of the DMSN is necessary for precise controlling of surface functionalization and consequently drug encapsulation efficiency. We quantified the gatekeeper with a combination of potentiometric titration and UV-Vis spectroscopy and determined the amount of amine and ferrocene moieties per nm^2 (**Figure 4.4**, **Figure 4.5** and **Figure 4.6**). Additionally we quantified the host-guest complexation process of the ferrocene/sugar gatekeeper and determined stoichiometry, binding constant and thermodynamic parameters (enthalpy, entropy) (**Figure 4.7** and **Figure 4.8**). These parameters are crucial for assessing stalk/cap/nanoparticle interaction during surface coverage.

For encapsulation of CuOAc with a pH/redox responsive release mechanism, the first step consists of the surface modification with APTMS. We utilized a base catalyzed functionalization strategy at room temperature and quantified the surface density of the amine groups with potentiometric titration. 10 mg nanoparticle in 30 ml MilliQ-water with 10 mM KNO₃ were basified with 0.1 M KOH and titrated with 0.01 HCl (**Figure 4.4A**). The accessible amine groups of each sample were calculated from the time derivation of the current signal. Gaussian fit of the two points of inflection (**Figure 4.4B**) and subtraction of the two maxima lead to a time difference. The time difference results in an amount of matter of acid titrated and is equal to consumed amine groups. This direct titration of the surface amine groups (pKa 9.6) with an acid was possible after precise measurement of the carbonate background signal, emerging from the acid-base reaction of carbon dioxide with the 0.1M KOH. We could conclude that 0.85 μmol APTMS per mg particle is conjugated on the nanoparticle surface which is equal to 0.98 NH_2/nm^2 . Consequently, we achieved around 33-59% surface silanol functionalization under consideration of two/three binding site of APTMS to the silanols (**Calculation III, Appendix**). This value is in good agreement with the surface coverage calculated through ²⁹Si MAS NMR (**Calculation I, Appendix**). To determine the accessible amine groups on the DMSN surface for larger molecules, we functionalized DMSN-A with phenyl isothiocyanate (Phenyl-SCN) to form a covalent thiourea bond (**Figure 4.5**). After back titration, 69% of the surface amine groups (1:1 molar ratio Phenyl-SCN to amine) and 89% (2:1 molar ratio) were consumed. Consequently, the amount of accessible amine groups for conjugation of larger molecules on the nanoparticle surface and in the pore cavities is in the range of 0.59-0.76 μmol per mg particle.

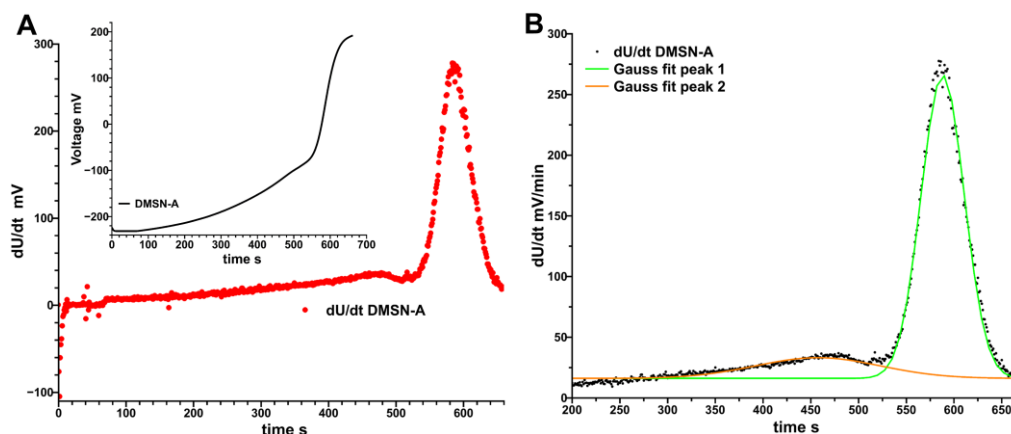


Figure 4.4. Potentiometric titration of the DMSN-A to quantify primary amine groups on the nanoparticle surface. A) Time derivative of the current signal for the potentiometric titration of DMSN-A. The resulting data were fitted with a gaussian distribution to determine a time difference, equal to molar masse acid consumed. Inlet: Current vs time plot of the titration experiment. B) Gauss fit of the potentiometric titration experiment. The first maximum can be associated with the primary amine group on the DMSN surface together with the carbonate background signal. The second maximum arises from the acid-base reaction of KOH with HCl.

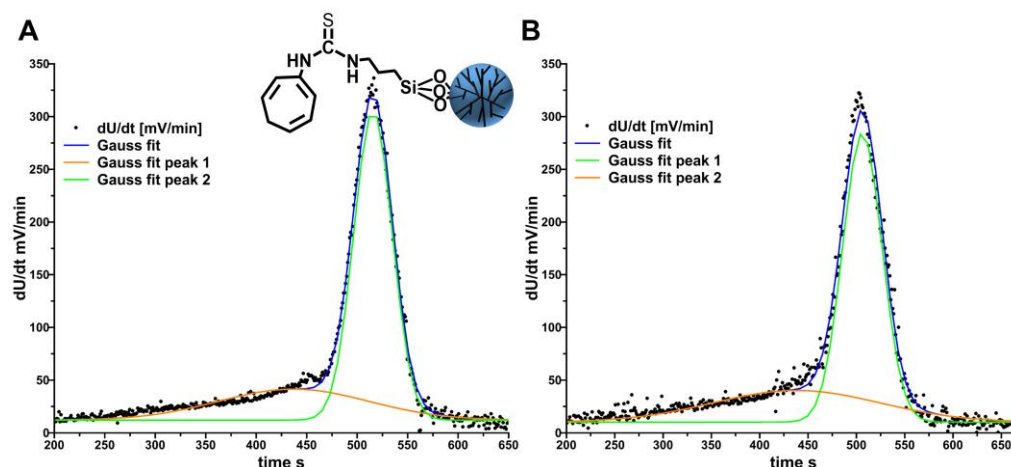


Figure 4.5. Time derivation of the current signal and resulting gauss fit for the potentiometric titration of the covalent functionalized amine groups. A) To quantify accessible functionality, DMSN were functionalized with an amine reactive compound (Phenyl-SCN) and the resulting coverage was determined by potentiometric titration. A 1:1 molar ratio Phenyl-SCN to amine results in 69% occupied amine groups. B) A 2:1 molar ratio Phenyl-SCN to amine results in 89% occupied amine groups.

Next step in quantification of the gatekeeper was the covalent attachment of the ferrocene derivate through the imine bond. We quantify the amount of ferrocene on top of the particle with UV-Vis spectroscopy. **(Figure 4.6B)** shows the external calibration of the ferrocene-CA (292 nm cyclopentadienyl ligand) and **(Figure 4.6C)** shows the consumption of ferrocene-CA after incubation with the DMSN-A. The maximum coating on top of the particle was 85% of the available amine groups. These results are in good agreement with the covalent conjugation of Phenyl-SCN, resulting in 0.59-0.76 μmol surface amine groups (equal to 60-78% surface coverage) available for functionalization.

Drug loading: Encapsulation efficiency and pH triggered release.

To assess the drug encapsulation capacities of the DDS, we correlated the consumption of the ferrocene-CA / β -CD gatekeeper with the loaded amount of the cytotoxic CuOAc complex and a small fluorescent dye Rhodamine B in PBS pH 7.4 (**Figure 4.6C**). It is important to determine the minimal needed gate keeper concentration to ensure complete pore sealing. CuOAc concentrations before and after loading were calculated through atom absorption spectroscopy (AAS) measurements of the Cu^{2+} concentration in the supernatant and Rhodamine B concentrations were measured and calculated based on UV-Vis spectroscopy measurements (**Figure 4.6A**). The loading capacity of the DMSN after incubation in PBS pH 7.4 drug solution for 24h reaches its maximum (30%) for both substances after $\geq 50\%$ ferrocene-CA consumption.

The pH triggered drug release of CuOAc from the gated DMSN-AFC is shown in (**Figure 4.6D**). The release of Cu^{2+} in $\mu\text{g/ml}$ at pH 4.5 is significant increased over 48h in comparison to the incubation at pH 7.4. The leakage of the gatekeeper system over 48h at pH 7.4 is less than 8% of the initial CuOAc concentration.

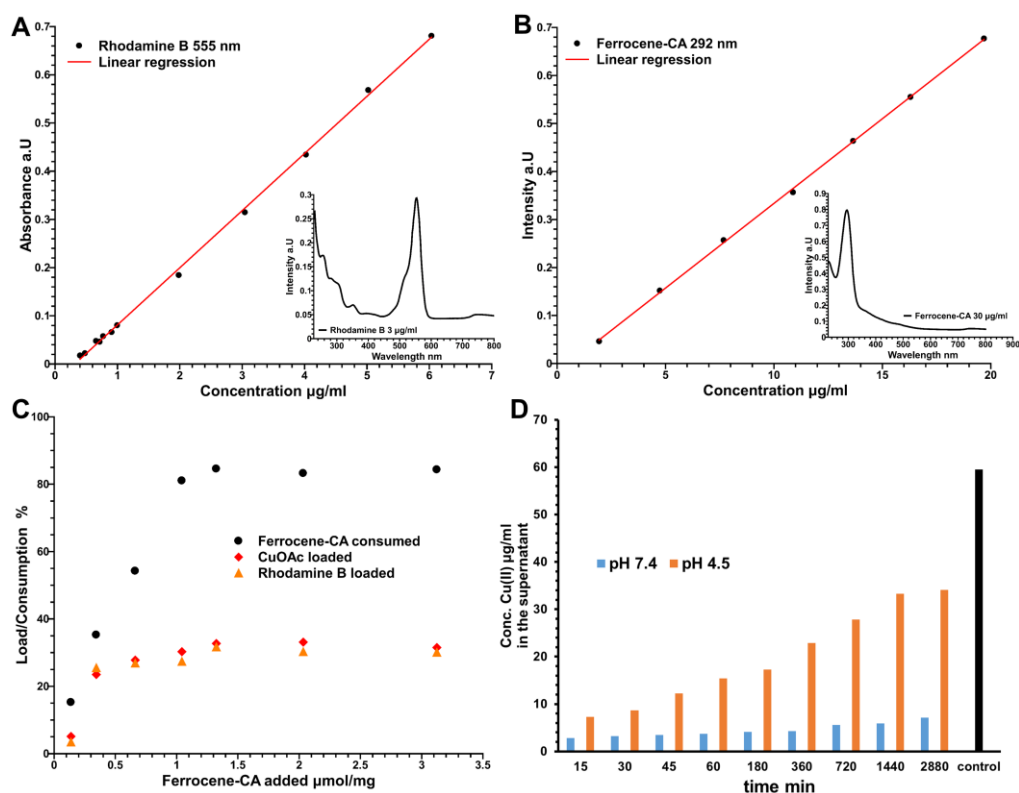


Figure 4.6. Quantification of the gate keeper/stalk and drugload/release of CuOAc/Rhodamine B. A) Linear calibration of the Rhodamine B stock solution in PBS pH 7.4 at 555 nm over the concentration range 0.4-6 $\mu\text{g/ml}$ (coefficient of determination $R^2 = 0.9991$). Inlet: UV-Vis spectrum of 3 $\mu\text{g/ml}$ Rhodamine B in PBS buffer. B) Linear calibration of the ferrocene-CA stock solution in PBS pH 7.4 at 292 nm over the concentration range 2-20 $\mu\text{g/ml}$ (coefficient of determination $R^2 = 0.9996$). Inlet: UV-Vis spectrum of 30 $\mu\text{g/ml}$ ferrocene-CA in PBS buffer. C) Plot of added amount of gatekeeper vs. loading percentage of rhodamine B and CuOAc. After consumption of $\geq 50\%$ ferrocene-CA the loaded amount of drug reaches its maximum. D) Time dependent release of CuOAc at pH 7.4 and pH 4.5 PBS buffer from the DMSN-AFC. Leakage of the nanoparticle is $< 4\%$ over 6h during drugload conditions at pH 7.4 in PBS. The release of CuOAc at pH 4.5 over 48h reaches 56% of the initial loaded content.

Binding model and association constant of the inclusion complex. Last step for complete surface coverage of the DDS is the interaction of the hydrophobic cyclopentadienyl ring of the ferrocene-CA with the hydrophobic cavity of the cyclic sugar β -CD. To prove successful β -CD-ferrocene complex formation on the DMSN surface, we investigate the binding model and determine the association constant of the inclusion complex with isothermal titration calorimetry (ITC) and ^1H NMR spectroscopy (**Figure 4.7** and **Figure 4.8**). The association constant for the ferrocene-CA/ β -CD interaction without DMSN was determined as $K_a 1190 \pm 110 \text{ M}^{-1}$ with the ITC experiment (**Figure 4.8A**). In agreement with the literature for unmodified ferrocene, a 1:1 binding model ($n = 0.82$) can be assumed.^[462-464] Additionally, ^1H NMR shift titration experiment^[465-468] was performed to determine the association constant. Shift of the proton signals of the host species (β -CD) during addition of increasing amounts

of guest (ferrocene) molecules (**Figure 4.7**) can be analyzed through non-linear curve fitting.

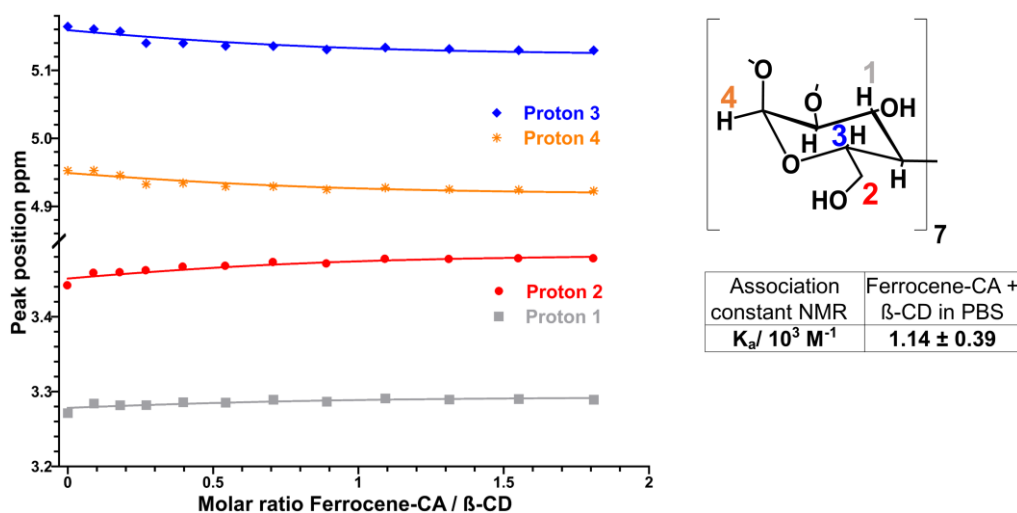


Figure 4.7. ^1H NMR shift titration experiment to quantify the strength of the ferrocene-CA/ β -CD inclusion complex. Fixed amount of the host species (β -CD) was mixed with increasing amounts of guest (ferrocene) molecules and the resulting shift in the peak position was measured. Determination of the association constant was possible through non-linear curve fitting of the peak shift.^[467,468] We analyzed four protons of the cyclic sugar simultaneously, three directly bound to the glucopyranosyl backbone and one proton next to the hydroxyl group in the six position of the ring.

We analyzed the shifts of three protons directly bound to the glucopyranosyl backbone and one proton next to the hydroxyl^[469–471] group in the six position of the ring (proton 2). After non-linear curve fitting to a 1:1 binding model (**Figure 4.7** and **Figure A.12**) a K_a value of $1140 \pm 390 \text{ M}^{-1}$ can be determined, affirming the value of the ITC experiment. Strong interaction and formation of a 1:1 inclusion complex between ferrocene-CA and β -CD is a prerequisite for drug encapsulation. The questions arise whether this inclusion complex formation also works with surface bound ferrocene and if the sugar interacts uncontrolled with the nanoparticle surface and cavities. ITC measurements of the DMSN-A with increasing concentration of β -CD exclude non-specific interaction of the cyclic sugar with the nanoparticle. Heat evolution was insignificant during the titration of DMSN-A with β -CD (**Figure A.13**) in comparison to the experiment with DMSN-AF. The interaction of DMSN-AF with β -CD is shown in **Figure 4.8B**. The association constant of $K_a = 980 \pm 140 \text{ M}^{-1}$ shows the almost unaffected interaction of β -CD to surface bound ferrocene, making the gating process of the DDS controllable and effective. Additionally, we could show that about 8000 ± 1300 β -CD molecules are interacting with one nanoparticle. Considering the amount of available surface amine and the maximal amount of ferrocene coverage (**Calculation III, Appendix** and **Figure 4.6C**) the amount of β -CD consumed during the ITC experiment is 14% (**Calculation V, Appendix**).

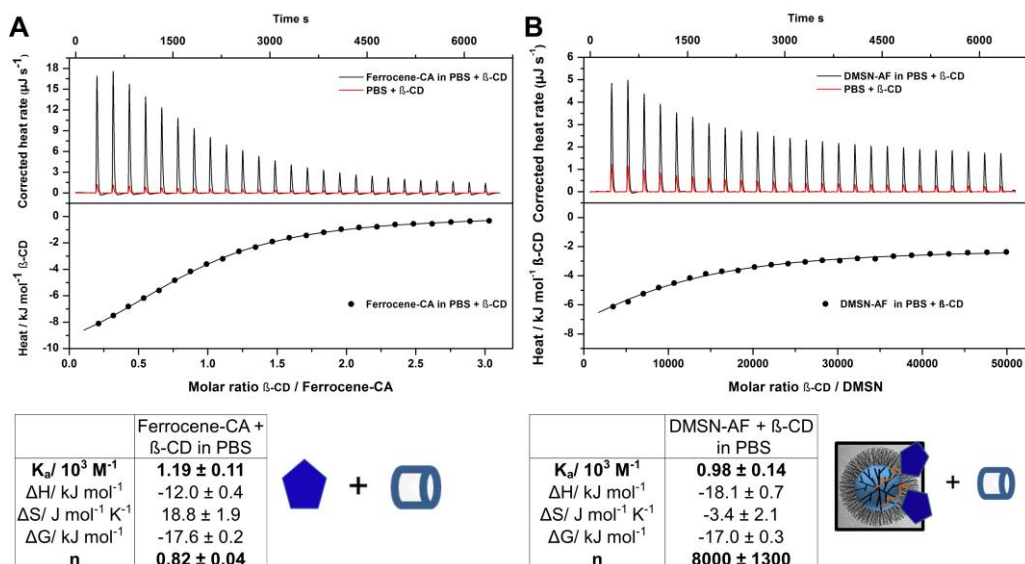


Figure 4.8. ITC measurement for the quantification of binding strength and binding model for the ferrocene-CA/β-CD inclusion complex. A) Increasing amount of β-CD was added to ferrocene-CA and the released heat was detected. The association constant for the ferrocene-CA/β-CD interaction without DMSN was determined as K_a $1190 \pm 110 \text{ M}^{-1}$ and 1:1 binding model ($n = 0.82$) can be assumed. B) Increasing amount of β-CD was added to DMSN-AF, resulting in an association constant of K_a $980 \pm 140 \text{ M}^{-1}$. It could be concluded that 8000 ± 1300 β-CD molecules are interacting with one nanoparticle.

The dual color fluorescence cross correlation spectroscopy (dcFCCS) experiment of fluorescein-5-isothiocyanate functionalized β-CD (FITC-CD) coated onto cyanine5-labeled DMSN-AF (Figure 4.9) shows a cross correlation of the fluorescent signal of the two components. The appearance of a cross correlation signal for FITC-CD and cyanine 5 labeled DMSN-AF can only occur if the β-CD is bound to the nanoparticle surface, resulting in similar diffusion coefficient. Temporal and spatial varying diffusions of the two species in the small measuring volume would preclude a correlation signal. Both methods are in situ prove of the effective gating strategy to physical block the pore entrance of the mesoporous system.

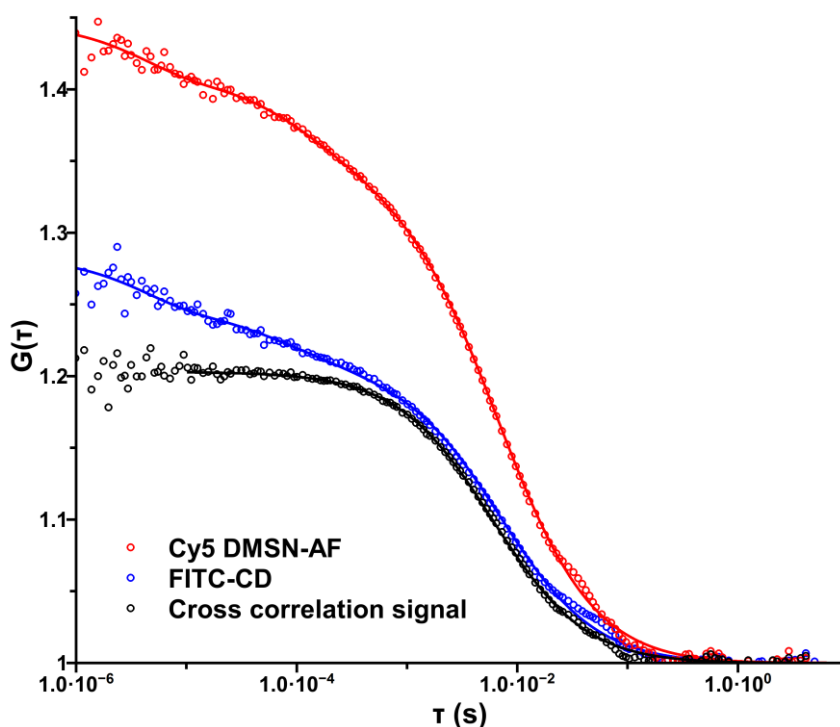


Figure 4.9. Dual color fluorescence cross correlation spectroscopy (dcFCCS) experiment of the interaction of fluorescent labeled β -CD -and DMSN-AF. Fluorescein labelled β -CD (FITC-CD, blue symbols) was combined with cyanine 5 labelled DMSN-AF (Cy5 DMSN-AF, black symbols) and the fluorescent fluctuations from these two spectrally distinct chromophores was simultaneously monitored and cross-correlated.^[472] Identical diffusion of the two species results in a cross correlation signal (red symbols) and proves *in situ* coordination of the sugar to the ferrocene moieties. Solid lines represent the corresponding fits.

Colloidal stability of DMSN-A was evaluated in phosphate-buffered saline (PBS) buffer (150 mM, pH 7.4) before and after functionalization with the ferrocene/CD gatekeeper by dynamic light scattering (DLS) (**Figure 4.10A**). Effective surface charge in terms of the ζ -potential increased from -19 mV to +12 mV after functionalization of DMSN-A with ferrocene/CD. Additionally, thermogravimetric analysis (TGA), attenuated total reflection infrared spectroscopy (ATR-IR) and negative staining TEM shows the step-by-step functionalization process of the DMSM with the gatekeeper (**Figure 4.10B**, **Figure A.15** and **Figure A.16**).

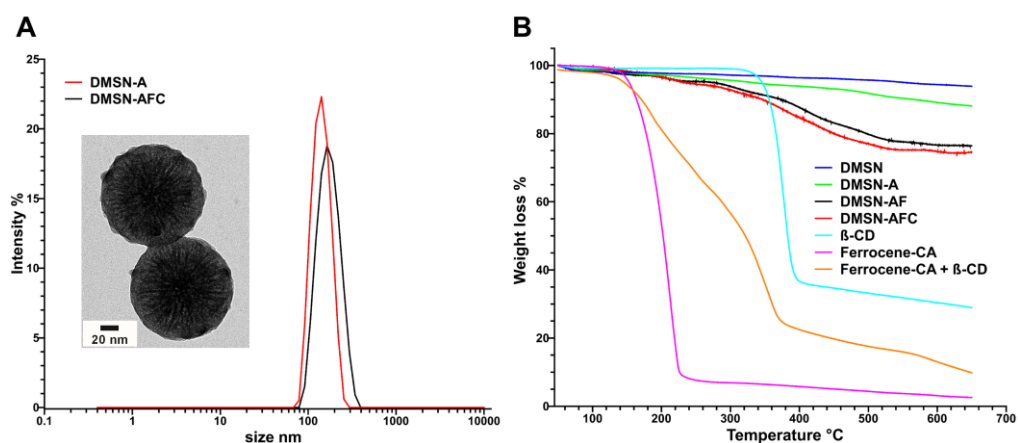


Figure 4.10. Dynamic light scattering and thermogravimetric analysis of the DMSN before and after gatekeeper attachment. A) A small increase of the DMSN diameter was visible after coating with the gatekeeper. Inlet: Staining of the organic shell reveals full pore coverage in the TEM picture. B) Mass loss for each functionalization step of the DMSN. With increasing amount of organic coverage, the mass loss increases. Additionally, the decomposition of the separate components and their inclusion complex is shown. Both decomposition steps are visible, with inflection points at 210 °C and 400 °C.

Last step in characterization of the DDS was the biodegradation of the DDS in Dulbecco's Modified Eagle Media (DMEM) with 10% fetal calf serum at 37 °C over time, monitored via TEM (**Figure A.14**). After 12h, partial degradation is observed. After 30h, complete collapse of the dendritic pore structure is visible. MSN are biodegradable in medium due to high concentrations of divalent ions, which form calcium and magnesium silicates and intercalate into DMSN. Additionally, hydrolysis of the silicon-oxygen bond by nucleophilic addition of hydroxyl ions and protonation leads to disintegration of silica-based nanoparticles and the pore structure.

Drug release and *in vitro* studies.

To investigate the *in vitro* drug delivery capabilities of the DDS, we analyzed the time delayed release of small molecule drugs in SCC tumor model. We confirmed the cellular toxicity of free and encapsulated Doxorubicin over 96h from the DDS (**Figure 4.11**). Metabolic activity was measured at indicated time points and decreased over time for Dox-DMSN. Gatekeeper detachment and drug release from the pore system results in a time delayed effect in comparison to the free drug. (**Figure 4.11A-B**) To confirm intracellular release of the drug and nanoparticle uptake, we monitored the metabolic cell activity after 24h nanoparticle exposure. and incubation for 72 hours without nanoparticles (**Figure 4.11C**). Despite the removal of the DDS, cell toxicity was detected.

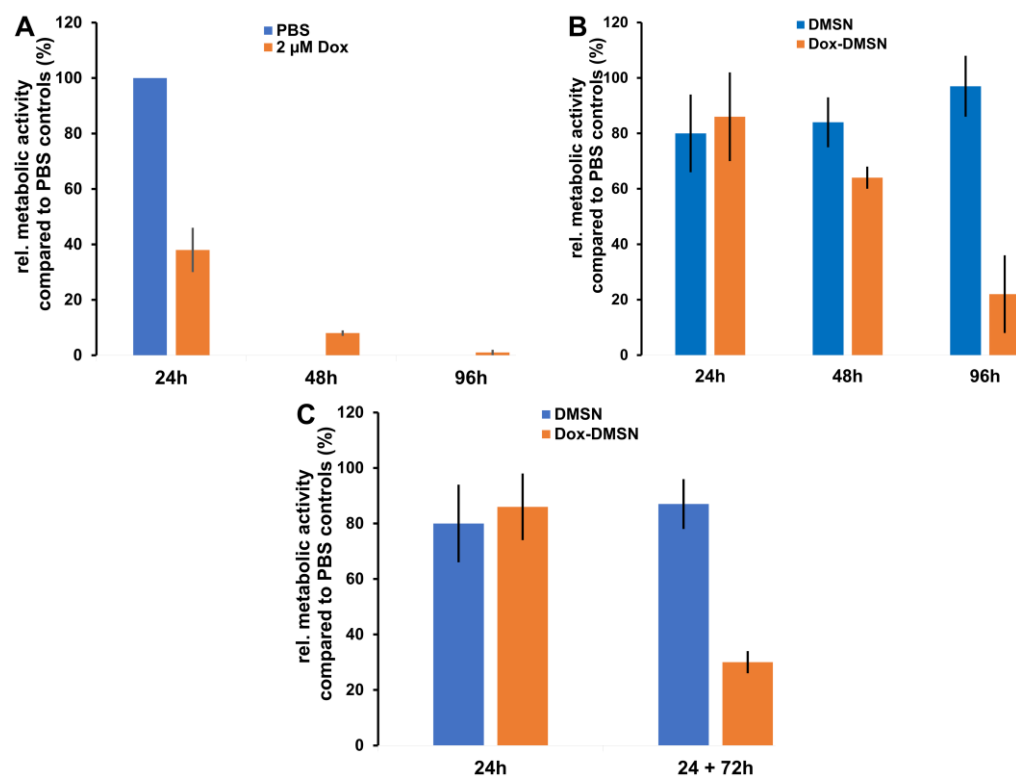


Figure 4.11. Cell viability of HNSCCUM-02T treated with Dox-DMSN over 96h. HNSCCUM-02T were treated with A) 2 μ M Doxorubicin, B) Dox-DMSN and control DMSN for 24, 48, and 96 hours, respectively. Metabolic activity was measured at indicated time points and decreased over time for Dox-DMSN. C) After 24 hours nanoparticle exposure cells were incubated further for 72 hours without nanoparticles and an effect of Doxorubicin was observed. n=3; mean \pm S.D.

The effect of CuOAc with the established DDS could not be shown. In **Figure 4.12** the effect of Cu(II) Chloride, DMSN and CuOAc loaded DMSN on the cell viability is shown. The free complex shows high cell toxicity and the control DMSN did not influence the cell viability. Free Cu(II) chloride shows no effect in the concentration range of the applied complex, excluding Cu(II) induced toxicity. Despite high killing potential of the free drug, the encapsulated CuOAc did not show significant toxicity over 96h.

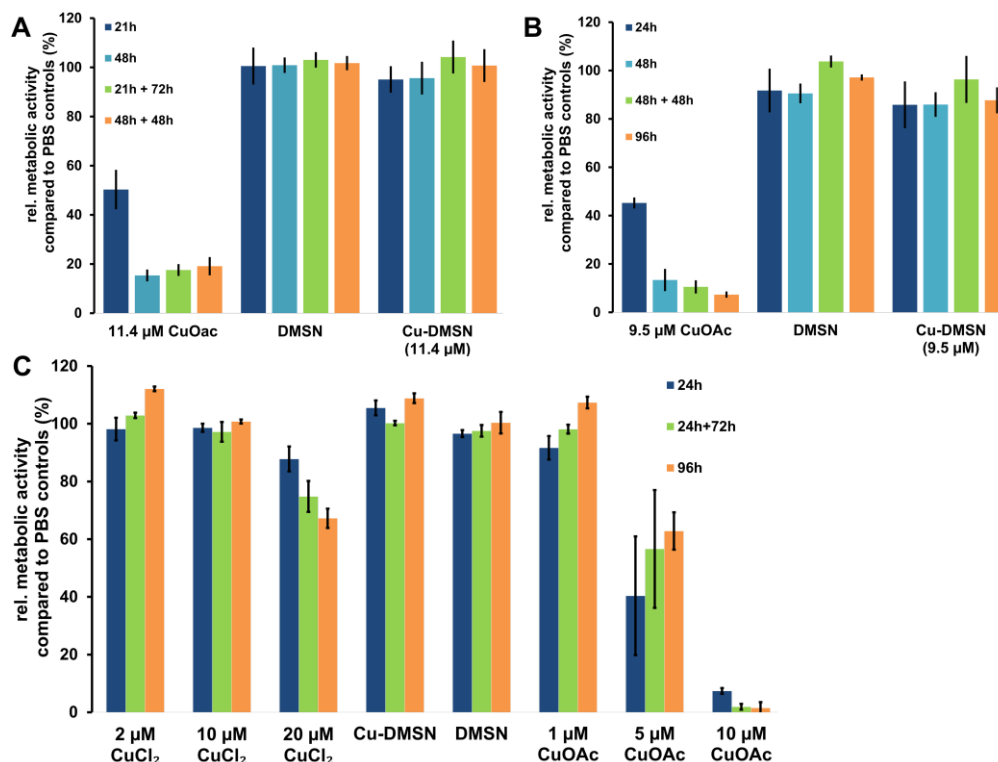


Figure 4.12. Cell viability of HNSCCUM-02T treated with Cu-DMSN over 96h. HNSCCUM-02T were treated with A) 11.4 μM CuOAc, Cu-DMSN and control DMSN for 21 and 48 hours respectively. Additionally, after 24/48 hours nanoparticle exposure cells were incubated further for 72/48 hours without nanoparticles. Metabolic activity was measured at indicated time points and didn't decreased over time for Cu-DMSN. HNSCCUM-02T were treated with B) 9.5 μM CuOAc, Cu-DMSN and control DMSN for 24, 48 and 96 hours, respectively. Additionally, after 48 hours nanoparticle exposure cells were incubated further for 48 hours without nanoparticles. Metabolic activity was measured at indicated time points and didn't decreased over time for Cu-DMSN. To analyze the influence of free Cu(II) on the cancer cell line, C) 2-20 μM CuCl₂ was added as control. No significant cell toxicity is visible after 24, 24+72 and 96 hours.

To analyze the intracellular mode of action of both drugs after encapsulation, we monitored the DNA damage via γ -H2A.X foci staining. The histone-subunits (H2A.X) of the DNA nucleosome is phosphorylated at Serine 139 upon DNA damage (γ -H2A.X) by members of the Phosphoinositol-3-kinase-like kinases (PIKK). This phosphorylation promotes a cascade of further H2A-X phosphorylation which finally leads to a cell cycle arrest and DNA repair or apoptosis if the damage is too severe. Hence, the more γ -H2A.X foci are detected the more DNA damage is present in the cell. This method is a sensitive tool to detect even small effects of DNA damaging agents because the foci appear already after a short amount of time and viability is not yet affected. We treated HNSCCUM-02T with 1 μ M drug, Cy5 labeled Dox-DMSN and control DMSN. DNA damage was measured through γ -H2A.X foci staining at indicated time points (**Figure 4.13** and **Figure 4.14**). Doxorubicin and Dox-DMSN showed DNA damage and the nanoparticle are accumulated inside the cells after 2h incubation. Subsequent release of the drug over time results in increased DNA damage for the DOX-DMSN after 24h (**Figure 4.13**).

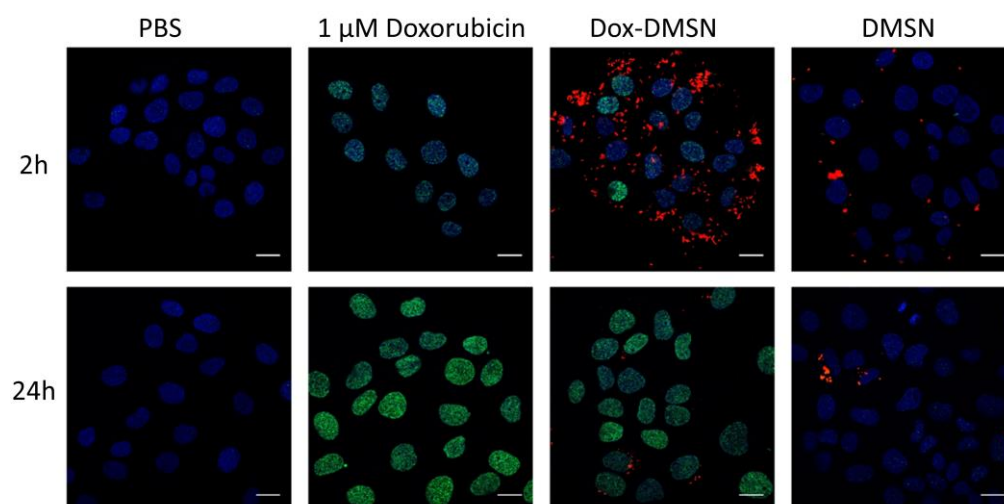


Figure 4.13. DNA damage detection of Doxorubicin via γ -H2A.X foci staining. HNSCCUM-02T were treated with 1 μ M Doxorubicin, Dox-DMSN and control DMSN for 2 hours and 24 hours, respectively. DNA damage was measured through γ -H2A.X foci staining at indicated time points. DNA damage is shown in green, as well as the nanoparticle in red and the cell nucleus in blue. The free drug and Dox-DMSN showed low DNA damage after 2h and increased damage after 24h in comparison to the PBS control. Scalebar 20 μ m.

In **Figure 4.14**, the γ -H2A.X foci staining of CuOAc and Cu-DMSN is shown. No DNA damage is visible after 2h and 24h incubation and the Cy5 labeled DMSN are clearly visible inside the cells after 2h. It is possible that the release of the CuOAc is too slow to reach toxic concentration and induces DNA damage. Another way of diminishing cellular toxicity and reduction of intracellular concentration is the cytoplasmic inactivation by endogenous nucleophiles and other intracellular components.

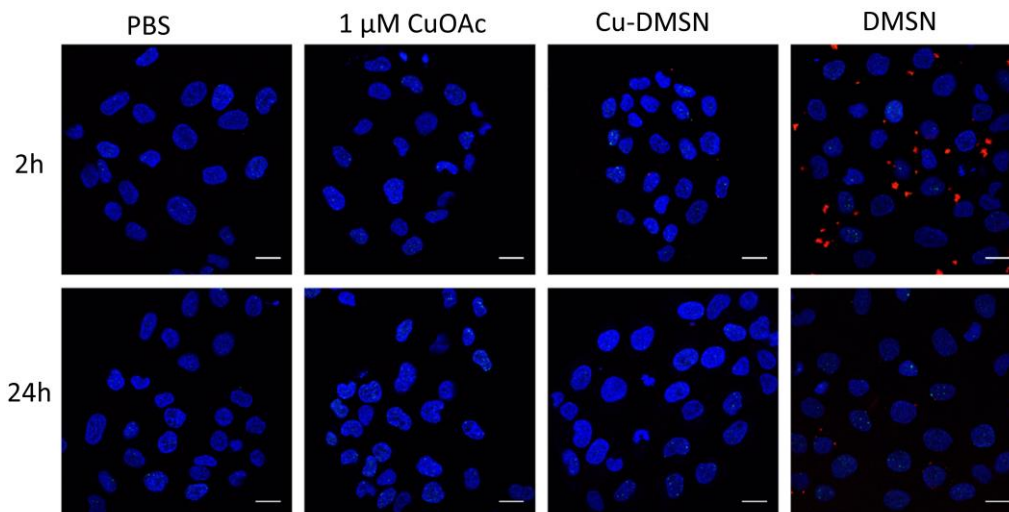


Figure 4.14. DNA damage detection of CuOAc via γ -H2A.X foci staining. DHNSCCUM-02T were treated with 1 μ M CuOAc, Cu-DMSN and control DMSN for 2 hours and 24 hours, respectively. DNA damage was measured through γ -H2A.X foci staining at indicated time points. DNA damage is shown in green, as well as the nanoparticle in red and the cell nucleus in blue. The free drug and Cu-DMSN showed no increased DNA damage in comparison to the PBS control. Scalebar 20 μ m.

Conclusion

We demonstrated that pH/redox-sensitive DMSN-AFC gatekeeper is a well-quantified tool to encapsulate and shield small molecular drugs. The three functionalization steps of the DMSN surface for drug encapsulation were analyzed with various techniques and we were able to correlate the drug loading efficiency with the consumption of gatekeeper. A critical surface density is necessary to physical block the pore entrance and restrict drug diffusion. The *in vitro* release and effect of Doxorubicin was proven with cell metabolic activity test and γ -H2A.X foci staining. The reduced effectiveness of CuOAc with the DDS can be explained through low intracellular concentration and cytoplasmic inactivation by endogenous nucleophiles.

5. Summary and Outlook

The synthesis and modification of the mesoporous carrier enables adjustment of pore size and particle diameter over a broad range. Influence through reaction parameters like pH value, temperature, stirring rate or additional surfactant makes the DDS a highly versatile tool for drug delivery of anti-cancer drugs. The incorporation of fluorescent dyes and redox responsive organosilica bridging enables intracellular tracking and biodegradation. Especially *in vitro* tracking of the DDS is an important property to monitor drug release and degradation processes. Magnetic core shell particles help for the *ex vivo* analysis of protein corona formation during incubation in the blood stream. The application of the DMSN could be shown in two different drug delivery setups, tailored to the specific drug properties. The pH-sensitive PEI-PEG DMSN can attenuate the systemic toxicity of TNF- α while maintaining its pleiotropic anti-tumor activity. Complete regression of 3D melanoma spheroids *in vitro* was dose-dependent, highlighting the need for sufficient TNF- α release at the tumor site. Additionally, first *in vivo* experiment showed the applicability of the DDS in complex biological environment. The developed DDS is capable of efficiently shielding highly toxic TNF- α , potentially leading to a novel systemic use of TNF- α in cancer treatment. The good monodispersity, pore volume, biodegradability, loading capacity and pH-triggered release properties of the DMSN are key factors for the further usage of systemic toxic drugs for *in vivo* applications. For the transport and encapsulation of small molecule drugs, pore size and particle diameter were adjusted and combined with a stimuli-responsive gater system. DMSN coated with a pH/redox responsive ferrocene carboxaldehyde (ferrocene-CA) / β -cyclodextrin (β -CD) gatekeeper were synthesized for drug delivery of Doxorubicin and CuOAc in a squamous cell carcinoma tumor model. The gatekeeper system combines a pH labile imine bond between the nanoparticle and ferrocene-CA and the redox-labile hydrophobic interaction of ferrocene-CA with β -CD for drug retention. The three functionalization steps of the DMSN surface for drug encapsulation were analyzed with various techniques and showed a correlation of the drug loading efficiency with surface coverage. A critical surface density of the gatekeeper is necessary to physical block the pore entrance and restrict drug diffusion. The *in vitro* release and effect of Doxorubicin for the established DDS was proven with cell metabolic activity test and γ -H2A.X foci staining. A reduced effectiveness of encapsulated CuOAc could be explained through a combination of low intracellular concentration to reach a toxic level and a cytoplasmic inactivation by endogenous nucleophiles during intracellular release.

Appendix

A.1 Material and Methods Chapter 2

If not explicitly described, all chemicals were purchased from Sigma Aldrich, USA. All reagents and solvents were of analytical grade and used as received. All syntheses were carried out with Milli-Q water (18.2 M Ω cm, 25 °C). The Fe₃O₄ nanoparticle were supplied by Eugen Schechtel. Magnetic separation columns were purchased from Miltenyi Biotec.

Preparation of DMSN. DMSN were synthesized via inverse biphasic stratification after a modified experimental setup.^[397] A standard synthesis is described in the following passage. 6 ml cetyltrimethylammonium chloride (CTAC) solution (25 wt. % in H₂O) and 150 μ l triethanolamine (TEA) were added to 54 ml Milli-Q water (18.2 M Ω cm) and stirred at 70 °C for 1 h in a 100 ml 3-neck round-bottomed flask with a KPG stirrer. The heated water-CTAC-TEA solution was under-laid with 20 ml tetraethyl orthosilicate (TEOS) in 1,2-dichlorobenzene (20 v/v %) without stirring. The stirrer was adjusted right above the boundary layer in the water phase, and the stirring rate was set to 155 rpm to avoid mixing phases. After the reaction was kept at 70 °C for 16 h, the organic phase was removed. The resulting products were collected by centrifugation (9.000 rpm / 20 min) and washed several times with ethanol to remove residual reactants. Stirring rate was monitored between 0-310 rpm. Base concentration was doubled and quintupled, and temperature was adjusted between 60 °C-90 °C.

Dye functionalization. Rhodamine B isothiocyanate (mixed isomers), Fluorescein-5-isothiocyanate (FITC), Pacific Blue (Thermo Fisher Scientific) and Cyanine5 N-hydroxysuccinimide (NHS) (Cy5 NHS, Lumiprobe), were encapsulated in DMSN. 0.5 mg dye was dissolved in 1 ml anhydrous dimethyl sulfoxide (DMSO), mixed with 15 μ l (3-aminopropyl)-trimethoxysilane (APTMS, >99%) and stirred for 12 under argon atmosphere and light exclusion. 500 μ l of the prepared dye solution was added after 5 min to the organic phase of the above described reaction.

Dual surfactant reaction. For the preparation of the dual surfactant reactions, a mixture of 6 ml (CTAC) solution (25 wt. % in H₂O) and 150 μ l triethanolamine (TEA) were added to 54 ml Milli-Q water (18.2 M Ω cm). Additionally, the second surfactant was added in the respective molar ratio (for example 3:1 equals to 4.71 mmol CTAC and 1.55 mmol sodium salicylate (NaSal)) and stirred at 70 °C for 1 h in a 100 ml 3-neck

round-bottomed flask with a KPG stirrer. The heated water-CTAC-TEA solution was under-laid with 20 ml tetraethyl orthosilicate (TEOS) in 1,2-dichlorobenzene (20 v/v %) without stirring. The stirrer was adjusted right above the boundary layer in the water phase, and the stirring rate was set to 155 rpm to avoid mixing phases. After the reaction was kept at 70 °C for 16 h, the organic phase was removed. The resulting products were collected by centrifugation (9.000 rpm / 20 min) and washed several times with ethanol to remove residual reactants. For anthracene-9-carboxylic acid (AC), 6-hydroxynaphthoic acid (HNA) and 2,3-naphthalenedicarboxylic acid (NDCA) a molar ratio of 1:1, 2:1 and 1:2 was analyzed. The organic acids were prior to the synthesis dissolved in MQ water with subsequent addition of 5M NH₄OH until complete deprotonation. The pH value of the surfactant stock solution was pH 7. For NaSal, the salt was directly added into the CTAC/TEA/Water solution.

Template extraction. DMSN (2.5 mg/ml in ethanol) with encapsulated dye were extracted three times with 1 wt. % ammonium nitrate (NH₄NO₃) at 80 °C under light exclusion to remove the surfactant template.

Organosilanes incorporation. The reaction was carried out as aforementioned. Bis[3-(triethoxysilyl)propyl] tetrasulfide (BTEPTS) and Bis[3-(triethoxysilyl)propyl] disulfide (top, BTEPS) were added with up to 5 wt. % in relation to TEOS After formation of the boundary layer into the organic phase. The time difference between layering and organosilanes addition was 30 sec.

Fe₃O₄ core shell system. For the incorporation of Fe₃O₄ into the DMSN, the reaction solution was prepared as before. The metal oxide nanoparticles were stored in hexane and prior to the addition centrifuged and redispersed in a small amount ethanol. The nanoparticles were added 5 min after TEOS addition into the water phase. Magnetic separation of the nanoparticle from free silica was possible by a MS column purchased from Miltenyi Biotec. The nanoparticle suspension in ethanol was added to the magnetic activated column and intensively flushed with ethanol. After removal of the column from the magnet, the core-shell nanoparticle could be flushed out with ethanol and were collected by centrifugation.

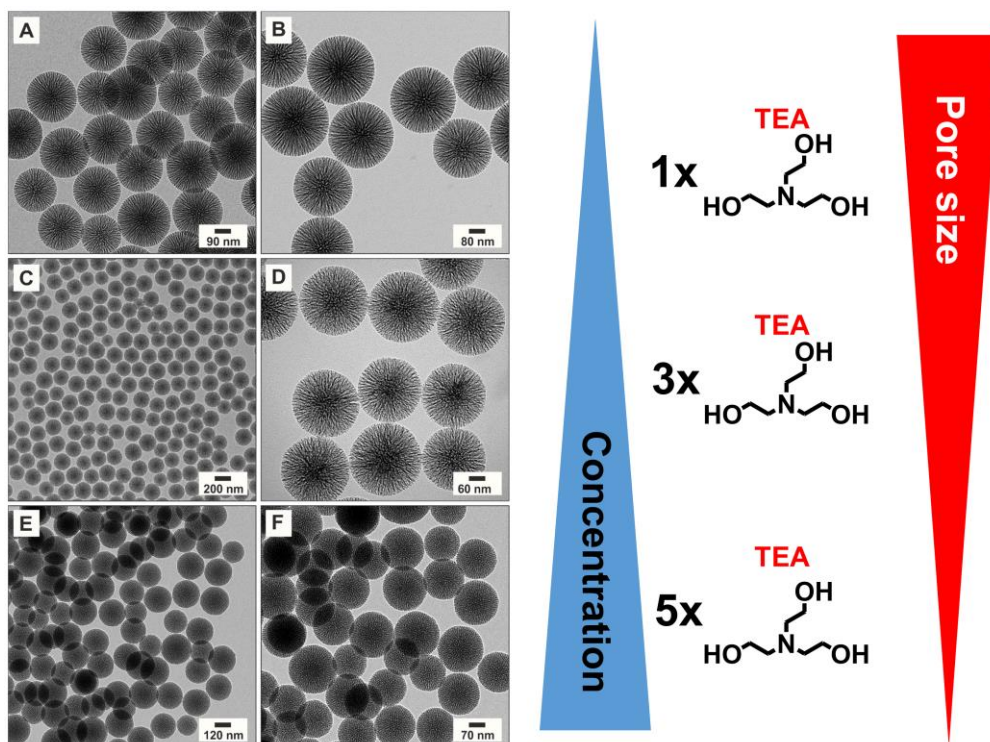


Figure A.1. Influence of organic base concentration on the pore size. (A-F) Pore size of the DMSN decreases with increasing base concentration.

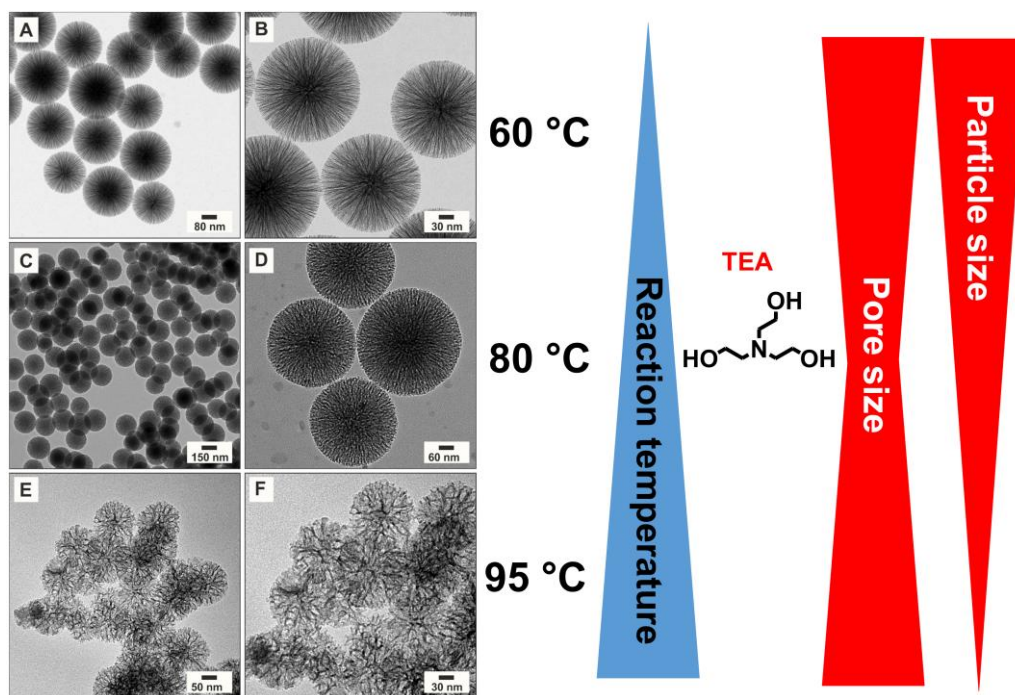


Figure A.2. Influence of the temperature on the pore size and particle diameter. (A-F) Particle size of the DMSN decreases with increasing temperature. Micelle template formation is disturbed with increasing temperature, resulting in large disordered pore channel. Lower temperature promotes regular pore wall growth but increases particle size.

A.2 Material and Methods Chapter 3

Preparation of DMSN. DMSN with diameters of 120 to 205 nm and pore size of 6.7 to 12.7 nm were synthesized via inverse biphasic stratification after a modified experimental setup.^[397] 6 ml cetyltrimethylammonium chloride (CTAC) solution (25 wt. % in H₂O) and 150 μ l triethanolamine (TEA) were added to 54 ml Milli-Q water (18.2 M Ω) and stirred at 70 °C for 1 h in a 100 ml 3-neck round-bottomed flask with a KPG stirrer. The heated water-CTAC-TEA solution was under-laid with 20 ml tetraethyl orthosilicate (TEOS) in 1,2-dichlorobenzene (20 v/v %) without stirring. The stirrer was adjusted right above the boundary layer in the water phase, and the stirring rate was set to 155 rpm to avoid mixing phases. After the reaction was kept at 70 °C for 8-16 h, the organic phase was removed. The resulting products were collected by centrifugation (9.000 rpm / 20 min) and washed several times with ethanol to remove residual reactants. Rhodamine B isothiocyanate (mixed isomers), Fluorescein-5-isothiocyanate (FITC), or Pacific Blue (Thermo Fisher Scientific) was encapsulated in DMSN: 0.5 mg dye was dissolved in 1 ml anhydrous dimethyl sulfoxide (DMSO), mixed with 150 μ l (3-aminopropyl)-triethoxysilane (APTES, >99%) and stirred for 12 h under argon atmosphere and light exclusion. 100 μ l of the prepared dye solution was added after 15 min to the organic phase containing DMSN.

Template extraction. DMSN (2.5 mg/ml in ethanol) with encapsulated dye were extracted three times with 1 wt. % ammonium nitrate (NH₄NO₃) at 80 °C under light exclusion to remove the surfactant template.

Copolymer Synthesis. Synthesis and characterization of the copolymer was adapted from Petersen et al.^[437] adjusting the molecular weights of the polymers. Briefly, 4 g dried methoxypolyethylene glycol (PEG, M.W. 1.000) were dissolved in 10 ml anhydrous dichloromethane (DCM) and activated for the reaction with amino groups of polyethyleneimine branched (PEI, M.W. 600, 99%). Hexamethylene diisocyanate (HMDI) was added in 3.4-fold excess to the PEG solution at 60 °C for 8 h under an argon atmosphere. For extraction, the resulting liquid was precipitated in ice cold petrol ether and dissolved in DCM. The resulting, solid product was collected and dried under vacuum. This process was repeated 5 times to obtain 2.4 g activated PEG (HMDI linked with a urethane bond to the PEG chain). PEI (2.1 g) was dissolved in 40 ml DCM in a 3-neck round-bottomed flask with a Dimroth condenser, bubble counter and dropping funnel. The activated PEG (2.1 g) was dissolved in DCM and added to the PEI solution under constant stirring and heating for 12 h under reflux. The resulting yellowish liquid was repetitively extracted with diethyl ether and dried in vacuum. Polymers were characterized by ¹H- and ¹³C-NMR spectroscopy, verifying the structure of the

copolymers and allowing calculation of the ethylene imine and ethylene glycol unit composition.

TNF- α and DMSN loading. Beromun (Boehringer Ingelheim, Germany) is a recombinant TNF- α drug that has been approved for clinical use.^[428] To stress the potential clinical relevance of this work, Beromun was used for all conducted experiments and is referred to as TNF- α . For DMSN loading, TNF- α and DMSN were mixed at a ratio of 1:10 and kept under constant shaking for 24 h at 4 °C. For PEI-PEG coating, copolymer was added to the solution at a ratio of 1:3 (DMSN:PEI-PEG) and kept shaking under constant shaking for another 24 h. To remove free TNF- α , samples were centrifuged at 15.000 rpm, supernatant discarded and DMSN re-suspended in PBS using sonication, twice. For every individual experiment the exact loading degree was measured by ELISA and the employed TNF-DMSN concentration adjusted accordingly. Samples were used within 7 d after preparation.

Cell cultures. WeHi-164 (mouse fibrosarcoma), L-929 (mouse fibroblast), HeLa (human adenocarcinoma), UKRV Mel15a (human melanoma), and A431 (human epidermoid carcinoma) were cultured in DMEM (Invitrogen, USA) with 10% fetal calf serum. The human melanoma cell line C8161 (kindly provided by Mary Hendrix, Chicago, IL, USA) was genotypically characterized,^[473] grown as described^[474] (using 4% fetal bovine serum instead of 2%), and authenticated by STR fingerprinting (QIMR Berghofer Medical Research Institute, Herston, QLD, Australia). Cells were maintained in a 5% CO₂ humidified incubator at 37 °C and split when confluent using trypsin-ethylenediaminetetraacetic acid (EDTA) (Gibco, USA).

Generation of human DC. Human DC were generated from buffy coats or cord blood of healthy volunteers as described previously.^[448,449] In brief, peripheral blood mononuclear cells were isolated by Ficoll density gradient centrifugation and monocytes were isolated by plastic adherence and cultured in X-VIVO-15 supplemented with 1% heat-inactivated autologous plasma, 800 IU/ml granulocyte-macrophage colony-stimulating factor (GM-CSF) (Leukine, Berlex) and 100 IU/ml interleukin (IL)-4 (CellGenix). Fresh media with GM-CSF (800 U/ml) and IL-4 (100 IU/ml) was added at day 2 and day 4. Immature DC were harvested at day 6, transferred to new culture plates, and stimulated with 400 IU/ml GM-CSF, 100 IU/ml IL-4, 0.5 ng/ml IL-1 β , 1000 U/ml IL-6, 50 ng/ml prostaglandin E2 and 10 ng/ml TNF- α for 24-72 h at 37 °C, 5% CO₂. For the DMSN group, TNF- α was replaced with equal amounts of TNF- α -loaded DMSN. For flow cytometry, DC were stained with primary antibody mouse anti-human CD80 (clone 37711, R&D Systems), mouse anti-human CD83 (clone HB15a, Beckman Coulter) and rat anti-human HLA-DR (clone YD1/63.4.10,

Thermo Scientific) followed by secondary staining with donkey anti-mouse PE (Abcam) and goat anti-rat FITC (Abcam) antibodies.

Cellular Uptake. For confocal microscopy analysis, A431 cells were seeded on coverslips and grown to ~70% confluence. A431 cells were treated with 10 µg/ml DMSN-B and kept in a 5% CO₂ humidified incubator at 37 °C. At 5, 15 and 30 min the cells were washed twice. Untreated cells and cells incubated with 10 µg/ml DMSN-B for 30 min at 4 °C were used as controls to determine background signal and amount of unspecific cell surface binding. Early endosomes were stained using rabbit anti-hEEA1 (Abcam, UK) and red fluorescent protein anti-rabbit antibody (Abcam, UK). Images were obtained using a Leica TCS SP5 confocal microscope. To determine whether DMSN were acidified within the cells, A431 or HeLa cells were seeded into 6-well plates and grown to ~70% confluence. Cells were treated with 10 µg/ml DMSN-F or DMSN-B and kept in a 5% CO₂ humidified incubator at 37 °C. At 1, 3, 6, 24, 48, and 72 h the cells were harvested using trypsin-EDTA and washed with medium twice. Cellular DMSN uptake was determined using BD Accuri C6 (BD Biosciences, Heidelberg Germany) for flow cytometry. Immature human dendritic cells (DC) were generated as described,^[448,449] harvested at day 6-8, seeded on 8-well chambered polymer coverslips (ibidi, Germany) and incubated with 10 µg/mL Cy3-labeled DMSN at 37 °C or 4 °C or left untreated for up to 4 h. After particle incubation, the cells were washed and fixed with 2% paraformaldehyde (Carl Roth, Germany) in PBS (Sigma Aldrich, Germany). 10 µM Hoechst 33258 dye solution (PromoCell, Germany) was used for nuclei staining and Green-fluorescent Cytoplasmic Membrane Staining Kit (PromoCell, Germany) for cell membrane staining of fixed cells as indicated by the manufacturer. Images were acquired on a Leica TCS SP8 and analyzed using Fiji.^[475] For flow cytometry, DC were harvested after particle treatment by incubation on ice in PBS (Sigma Aldrich, Germany) supplemented with 1 mM EDTA (AppliChem, Germany) for 15 min and subsequently analyzed with a Accuri C6 flow cytometer.

TNF-α release from DMSN. After TNF-α loading, DMSN were kept in DMEM with 10% fetal calf serum. At 0, 0.5, 1, 2, 4, 6, and 24 h the samples were centrifuged at 15.000 rpm and supernatants were collected. Moreover, TNF-α loaded DMSN were coated with PEI-PEG, washed twice with PBS, and kept in DMEM with 10% fetal calf serum at 37 °C for up to 7 d. At 0, 1, 6, and 12 h and at 1 (24 h), 2, 3, 4, 5, 6, and 7 d, samples were centrifuged at 15.000 rpm and supernatants collected. Recombinant human TNF-α ELISA (ELISA MAXTM Deluxe Sets, Biolegend, USA) was performed according to manufacturer instructions to determine the amount of free TNF-α in the supernatant.

Mixed leukocyte reaction. Naive CD4⁺ T cells isolated from cord blood were stimulated with allogenic DC. Cells were cultured in flat-bottom 96-well plates in a final volume of 200 µl/well X-VIVO-15 (Lonza, Belgium) for 4 d and an additional 16 h [³H] Thymidine pulse. [³H] Thymidine incorporation was measured using a liquid scintillation counter (Perkin Elmer, Walluf, Germany).

MTT assay. Cell viability of A431, WeHi-164, and L-929 cells was examined using the MTT colorimetric assay. Cells were plated in 96-well plates in DMEM with 10% fetal calf serum, grown to 60% to 70% confluence and treated with different concentrations of empty non-coated, empty PEI-PEG-coated, TNF- α -loaded and PEI-PEG-coated and dye-loaded and PEI-PEG-coated DMSN for 12, 24, and 48 h. Untreated cells were used as live control and cells treated with 100 µl DMSO were used as dead control. To determine cell viability, 50 µl/well MTT solution was added and cells were kept in a 5% CO₂ humidified incubator at 37 °C for 4 h. In viable cells, NAD(P)H-dependent cellular oxidoreductase enzymes can catalyze the reduction of MTT to its insoluble formazan. To stop this reaction and to dissolve the formazan crystals, 200 µl of isopropanol with Triton-X 100 (10%) and 0.1 M HCl was added to each well. Dye absorbance was measured at 570 nm, with 630 nm as a reference wavelength using an ELx808 (BioTek, USA). Cell viability was calculated as a percentage compared to live control.

Fluorescent ubiquitination-based cell cycle indicator (FUCCI). To generate stable melanoma cell lines expressing the FUCCI constructs, mKO2-hCdt1 (30-120) and mAG-hGem (1-110)^[453] were subcloned into a replication-defective, self-inactivating lentiviral expression vector system as previously described.^[474] The lentivirus was produced by co-transfection of human embryonic kidney 293T cells. High-titer viral solutions for mKO2-hCdt1 (30/120) and mAG-hGem (1/110) were prepared and used for co-transduction into a biologically and genetically well-characterized melanoma cell line (see above) and subclones were generated by single cell sorting.^[454]

Melanoma 3D-spheroid assays. The melanoma spheroid model mimics *in vivo* tumor architecture and microenvironment and is used for investigating growth, cell cycle, and viability of melanoma cells.^[450] Spheroids were prepared as described.^[431] Briefly, 100 µl agarose gel (1.5%) was added to each well of a 96-well plate and cooled down for at least 2 min. 200 µl medium (DMEM with 2% fetal bovine serum) containing 5.000 C8161 human melanoma cells was added and cells were grown for 3 d in a 5% CO₂ humidified incubator at 37 °C. Spheroids were treated with unloaded and TNF- α -loaded PEI-PEG DMSN-B (1 and 50 µg/ml TNF- α , respectively) for up to 24 h. To

stain dead cells, 2 μ l DRAQ7 (BioStatus Ltd., UK) was added 12 h before spheroid sectioning. At 3, 6 and 24 h spheroids were transferred into 5% agarose gel and sectioned into 100 μ m sections in cold PBS using a Leica Vibratome (Leica, Germany). Only sections of the middle of spheroids were imaged to exclude DMSN adhering to the outside of the spheroids. Sections were mounted onto glass slides and imaged using confocal microscopy.

Distribution of TNF- α after subcutaneous administration in a transgenic mice model. TNF- α was labeled with IRDye 800CW Protein Labeling Kits (LI-COR). Six NOD/LtSz-scid/scid tg(HLA-A2.1) mice were treated as following. 10 μ g TNF- α (< 50 μ l solution) were subcutaneous injected into 3 mice. 10 μ g TNF- α (< 50 μ l solution) encapsulated into DMS was injected into 2 mice and 1 mice was left untreated. After 20 min, 3.5, 8.5, 24, 48, 72 hours and 6, 9, 13, 17, 21 and 28 days, mice were monitored for distribution of TNF- α via fluorescence (see Instruments Chapter 3). All animal experiments were authorized by the Research Animal Care Committees, in agreement with local state and federal regulations.

Transmission electron microscopy (TEM). Low-resolution TEM images were obtained using a LEO 906E Transmission Electron Microscope (ZEISS, Germany) and a Tecnai T12 Cryo-electron microscope (FEI, USA). LEO 906E TEM was equipped with a Tungsten cathode with an acceleration voltage of 20-120 kV and a slow-scan charge-coupled device (CCD) camera (1k by 1k). Tecnai T12 Cryo-electron microscope was equipped with a LaB6 cathode with an acceleration voltage of 20-120 kV and a Gatan 4 mega pixel CCD (2k by 2k) with a point-point resolution of 0.34 nm. DMSN in the appropriate solvent (hexane, ethanol, or water) were plated onto a carbon coated 300 mesh copper grid (Electron Microscopy Sciences, Germany) for TEM imaging. 3D surface plot TEM images of DMSN (format .dm3) were analyzed with ImageJ3D.

Small angle X-ray spectroscopy (SAXS). SAXS measurements were performed in transmission geometry using CuK α radiation (wavelength 1.54 \AA) from a rotating anode X-ray generator (Rigaku MicroMax007). The beam was monochromized by a curved multilayer optic (Osmic Confocal Max-Flux) and collimated by three 4-jaw slit sets (0.7 mrad divergence). Samples were placed in 1 mm glass capillaries. Scattered intensities were recorded on a 2D online image plate detector (MAR 345) with 3 min exposure time. The sample-detector distance of 2.1 m was calibrated by a silverbehenic-acid reference sample. Scattering patterns $I(q)$ vs. momentum transfer $q=4\pi/\lambda \sin(\theta)$ were determined by radial averaging of the 2D scattering data.

Powder-X-ray diffraction patterns (XRD). X-ray diffractograms of samples were obtained with a step size of 0.0078° on a Siemens D5000 powder diffractometer equipped with a Braun M50 position-sensitive detector, Ge (220) monochromator, and using Cu-K α ($\lambda = 1.5405 \text{ \AA}$) radiation. XRD patterns were recorded in 2Θ range of 10-90° at ambient temperature.

Nitrogen sorption measurements. DMSN were transferred into a piston measuring cell. Before testing, samples were degassed at 273 K overnight in a vacuum line. Sorption measurements were performed at 77.4 K using nitrogen (28.0134 g·mol⁻¹). Total pore volume was calculated using the gas amount adsorbed at a maximum relative pressure (P/P_0) of 0.97. Pore sizes of samples from adsorption branches of isotherms were calculated using the Barrett, Joyner und Halenda (BJH) formula.^[116] Specific surface areas were calculated using the Brunauer Emmett-Teller (BET) formula.^[116] Quantachrome ASiQwin 3.0 software was used to analyze obtained data.

Nuclear magnetic resonance spectra (NMR). NMR experiments were performed on a Bruker ARX 400 spectrometer using a ¹H frequency of 399.83 MHz and a ¹³C frequency of 100.54 MHz. Samples (40 mg) were dissolved in d⁶ DMSO or D₂O and obtained data analyzed using Mnova NMR software.

Solid-state nuclear magnetic resonance spectra (ssNMR). ssNMR experiments were performed on a Bruker Avance DSX 400 NMR spectrometer using a ¹H frequency of 399.83 MHz and a ¹³C frequency of 100.54 MHz. A Bruker double resonance probe, equipped with supporting rotors of 4.0 mm outer diameter, was used. ²⁹Si MAS-NMR spectra were corrected using an exponential apodization of 100 Hz. ¹³C MAS-NMR spectra were corrected using an exponential apodization of 50 Hz.

Ultraviolet–visible spectroscopy (UV-Vis). UV-VIS spectra (300 to 800 nm) were measured on Agilent Varian Cary 500 UV-VIS/NIR-spectrometer using 1 ml QS-suprasil quartz absorption cuvettes with a thickness of 10 mm (Hellma, Germany).

Zetasizer surface charge and dynamic light scattering (DLS). Hydrodynamic particle size and net surface charge in terms of ζ -potential of DMSN were determined by DLS (Malvern Zetasizer Nano ZS).

Attenuated total reflection infrared spectroscopy (ATR-IR). ATR-IR spectroscopy was performed on a Nicolet iS10 (Thermo Scientific, USA). Spectra were recorded for $\omega = 650\text{-}3500 \text{ cm}^{-1}$ with a resolution of 1.4 cm⁻¹ per data point.

Differential scanning calorimetry/thermogravimetric analysis (DSC/TGA). DSC/TGA was performed on a Netzsch STA 449 F3 Jupiter device. DMSN (10 mg)

were heated in an alumina cup under argon atmosphere from 50 to 800 °C at a heating rate of 10 K/min and a flow rate of 10 ml/min.

Fluorescence correlation spectroscopy (FCS). FCS experiments were performed on LSM 880 (Carl Zeiss, Jena, Germany). Excitation laser light was focused on samples using Zeiss C-Apochromat 40×/1.2 W water immersion objective. Emission was collected with the same objective and, after passing through a confocal pinhole, directed to a spectral detection unit (Quasar, Carl Zeiss). In this unit emission is spectrally separated by a grating element on a 32 channel array of GaAsP detectors operating in a single photon counting mode. A HeNe laser ($\lambda = 543$ nm) was used for excitation of Rhodamine B and emission in the range from 593 to 696 nm was detected with a QUASAR detection unit. An eight-well polystyrene, chambered cover glass (Laboratory-Tek, Nalge Nunc International) was used as a sample cell. For each sample, 10 measurements (30 seconds each) were performed. Obtained experimental autocorrelation curves were fitted with a theoretical model function for an ensemble of either 1 (in free Rhodamine B solutions and coated DMSN-F dispersions) or 2 (in Rhodamine B-labeled PEI-PEG solutions) different types of freely diffusing fluorescence species.^[476] The fits yielded the diffusion coefficients of fluorescent species. Using the Stokes-Einstein relation, hydrodynamic radii R_h were calculated assuming spherical species.

Dynamic light scattering (DLS). Light scattering measurements were performed at 20 °C. Solutions were prepared in a dust-free flow box. Cylindrical quartz cuvettes (Hellma, Germany) were cleaned using dust-free distilled acetone. DLS measurements were performed on a HeNe Laser (25 mW output power at $\lambda = 632.8$ nm) and on an ALV-CGS 8F SLS/DLS 5022F goniometer with eight simultaneously working ALV 7004 correlators and eight QEAPD avalanche photodiode detectors. The correlation functions of the particles were fitted using one exponential or a sum of two exponentials from which the initial slope, i.e. the first cumulant Γ , was calculated. The z-average diffusion coefficient D_z was calculated by extrapolating Γ/q^2 for $q = 0$. By formal application of Stokes law, the inverse z-average hydrodynamic radius is $R_h = \langle R_h^{-1} \rangle_z^{-1}$. Experimental uncertainties were estimated to be $\pm 2\%$ for R_h .

To investigate the aggregation behavior of DMSN-F + PEI-PEG in human plasma, EDTA-plasma pooled from 6 donors was used. The following mixtures have been prepared:

- 1) plasma : PBS 9:1
- 2) PBS : DMSN-F + PEI-PEG (c = 300 mg·l⁻¹) 9:1
- 3) plasma : DMSN-F + PEI-PEG (c = 300 mg·l⁻¹) 9:1
- 4) PBS : DMSN-F + PEI-PEG (c = 30 mg·l⁻¹) 9:1
- 5) plasma: DMSN-F + PEI-PEG (c = 30 mg·l⁻¹) 9:1

The plasma was filtered through a Millex GS 0.22 µm filter and PBS was filtered through a Pall GHP 0.2 µm filter. Cuvettes were incubated for 20 min at room temperature before measurement.

With no aggregate formation, the determined autocorrelation function of solutions 3 and 5 ($g_1(t)_{mix}$) should be well-fitted by the weighted sum of the fit functions of the autocorrelation functions of the two single components (**Equation A.1**). To fit the plasma autocorrelation function (ACF) three exponentials are needed, reflecting the large size differences of the plasma proteins, whereas for the silica particles one exponential was sufficient due to narrow size distribution.

$$g_1(t)_{mix} = a_p \cdot g_1(t)_p + a_s \cdot g_1(t)_s \quad \text{Equation A.1}$$

$g_1(t)_p$ = fit function that describes the measured ACF of the particles in buffer

$g_1(t)_s$ = fit function that describes the measured ACF of the plasma in buffer

a_i = amplitudes

The only variable fit parameters of the correlation function fit of the mixture are the amplitudes a_i whereas all other parameters were kept constant to the values obtained by the fit of the ACF of plasma and particles. In case of aggregate formation, a third fit function ($g_1(t)_a$) needs to be added to adequately fit the autocorrelation function of the mixture (**Equation A.2**).

$$g_1(t)_{mix} = a_p \cdot g_1(t)_p + a_s \cdot g_1(t)_s + a_A \cdot g_1(t)_A \quad \text{Equation A.2}$$

Isothermal titration calorimetry (ITC). ITC experiments were performed on a NanoITC Low Volume (TA Instruments, Germany). An effective cell volume of 170 μ l, a stirring rate of 350 rpm, and a temperature of 25 °C were maintained for all experiments. To correct the data for the heat of dilution, the titrant was titrated into water and resulting heats were subtracted from each titration of DMSN. An aqueous dispersion of DMSN (0.1 wt. %) was titrated with 50 μ l of PEI (2.0 g/l, 3.3 mM), PEG (3.3 g/l, 3.3 mM), or PEI-PEG (2.3 g/l, 0.64 mM) in aqueous solution.

Confocal imaging. Confocal imaging of 3D spheroids was performed as previously described.^[454] A Leica TCS SP5 confocal microscope equipped with eight laser lines and five filter-free PMT detectors with individually tunable spectral bands to image multiple colors simultaneously with minimal spectral bleed-through was used to image stained tumor cells and FUCCI-expressing melanoma cells in adherent culture, as spheroids or as sections from spheroids.

***In vivo* imaging of NIR labeled TNF- α and DMSN.** *In vivo* NIR fluorescence imaging of NIR labeled TNF- α and Cy5- labeled DMSN was performed with the IVIS Lumina Spectrum Imaging system (Caliper LifeSciences, Hopkinton, US). After injection at predetermined time points, mice were transferred into the machine's image chamber and anesthetized temporarily with isoflurane. A picture integration time of 3 s was set for the fluorescence source. Filters were adjusted with excitation at 740 nm and emission at 790 nm to visualize CW800 labeled TNF- α and for Cy5- labeled DMSN it was set to excitation at 640 nm and emission at 700 nm.

A.3 Figures, Tables and Equations Chapter 3

Table A.1. Characterization of dye-labeled nanocarrier DMSN-F by DLS.

Sample	Hydrodyn. radius ^{a)}	Hydrodyn. radius ^{b)}	ζ-potential ^{c)}
	[nm]	[nm]	[mV]
DMSN-F	112	/	-19
PEI-PEG DMSN-F	113	115	+23

^{a)} DLS in PBS; ^{b)} FCS ; ^{c)} Zetasizer in PBS (10 mM, pH 7.4)

Calculation for molecular weight of DMSN-B.

(i) Density of amorphous silica $\rho_{\text{SiO}_2} = 2.2 \text{ (g/cm}^3\text{)}$

(ii) Avogadro constant $N_a = 6.022 \times 10^{23} \text{ (1/mol)}$

(iii) Pore volume = $1.42 \text{ (g/cm}^3\text{)}$

The volume of each NP $(V/\text{NP}) = 4/3 \times \pi \times (62.5 \times 10^{-7})^3 = 1.02 \times 10^{-15} \text{ (cm}^3/\text{NP})$

Mass of each NP $(m/\text{NP}) = (V/\text{NP}) \times \rho_{\text{SiO}_2} = 1.02 \times 10^{-15} \times 2.2 = 2.25 \times 10^{-15} \text{ (g/NP)}$

Molar masse of the NP $(M) = (m/\text{NP}) \times N_a \text{ (M)} = 2.25 \times 10^{-15} \times 6.022 \times 10^{23} = 1.4 \times 10^9 \text{ (g/mol)}$

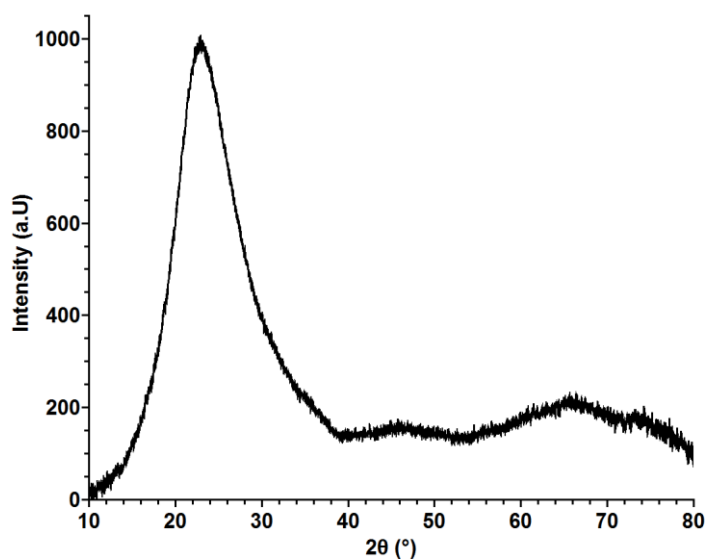


Figure A.3. Powder x-ray diffraction measurements of DMSN. The peak at $2\Theta = 22^\circ$ ($\text{Cu-K}\alpha$) in the X-ray diffractogram is characteristic for the amorphous character of synthesized silica nanoparticles.

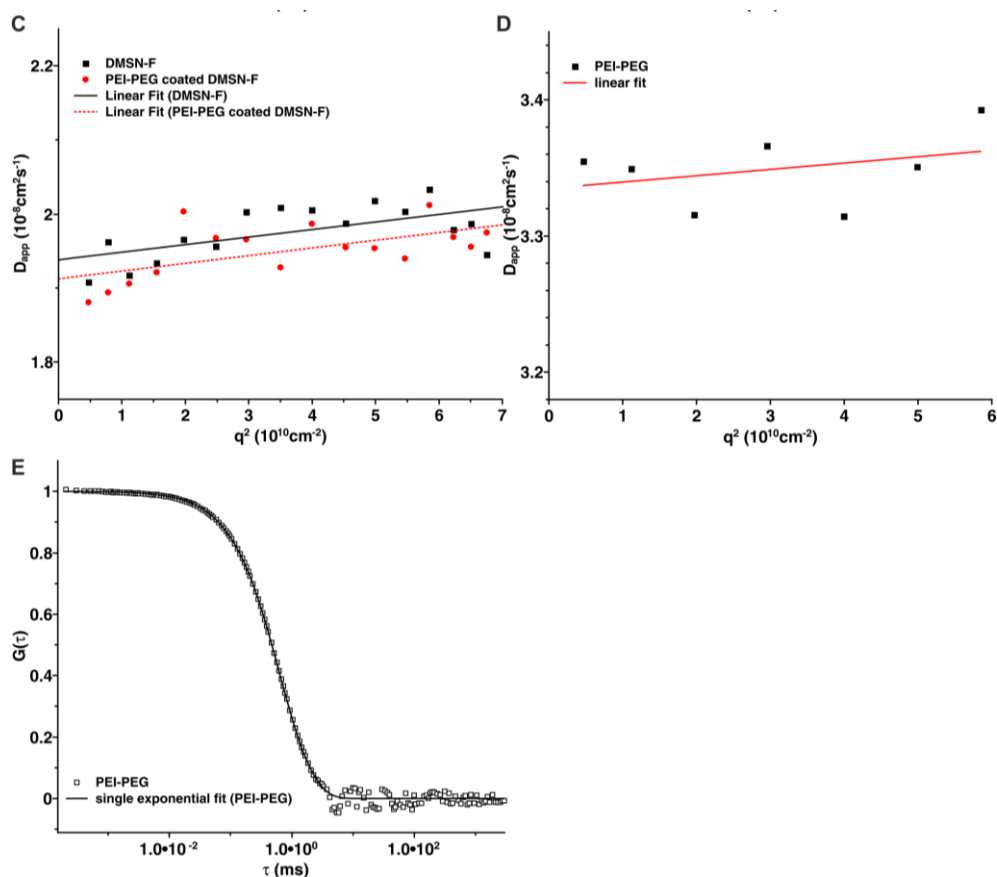


Figure A.4. Light scattering of the copolymer and apparent diffusion coefficient. (C) Apparent diffusion coefficient D_{app} of the drug-carrier system and (D) unbound PEI-PEG polymer in PBS buffer (150 mM, pH 7.3). Determination of D_{app} was possible through extrapolating the quadratic scattering vector q^2 to zero. (E) Autocorrelation function of the single PEI-PEG polymer in PBS (150 mM, pH 7.3) with resulting hydrodynamic radius R_h of 6.5 nm; scattering angle 30° .

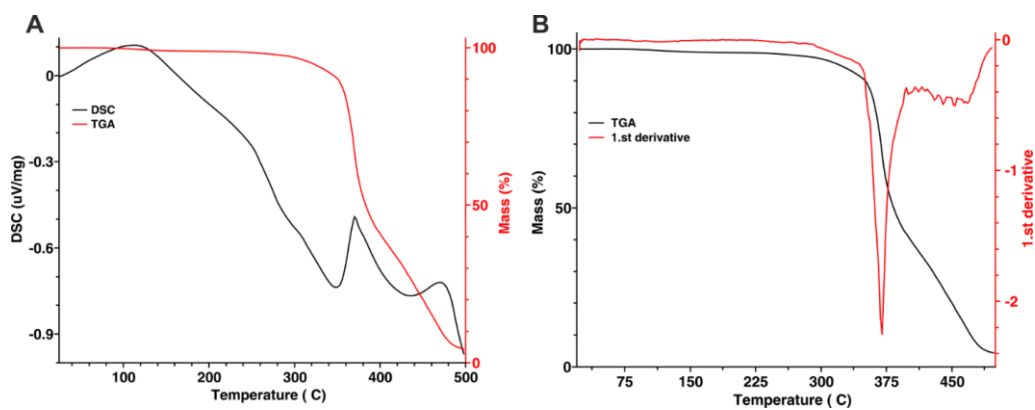


Figure A.5. Thermal decomposition of the copolymer. (A) TGA/DSC measurements of gatekeeper-coated DMSN-B. The exothermic signal at 370 °C indicates decarboxylation of the two polymers. Due to similar decomposition temperatures of the two homopolymers, their individual decomposition signals could not be resolved. (B) Weight loss and first derivative of the degradation plot indicates a maximum degradation temperature of 370 °C.

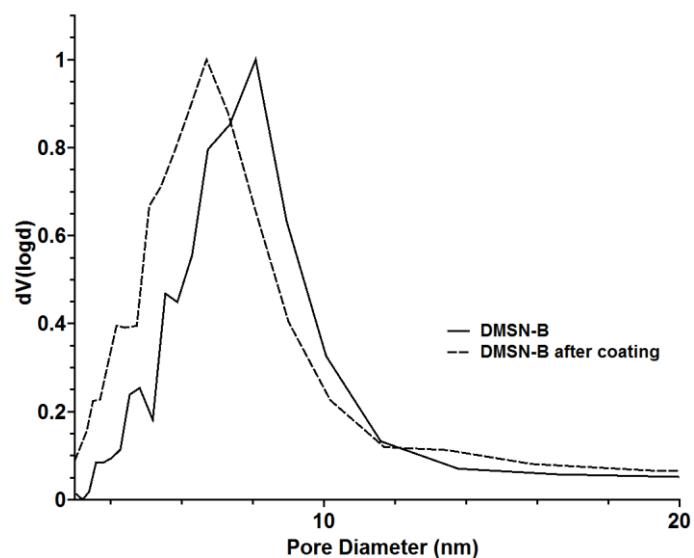


Figure A.6. Pore size distribution of DMSN-B before and after PEI-PEG coating. A slightly shift in the pore size distribution to smaller pores is visible after coating with the copolymer.

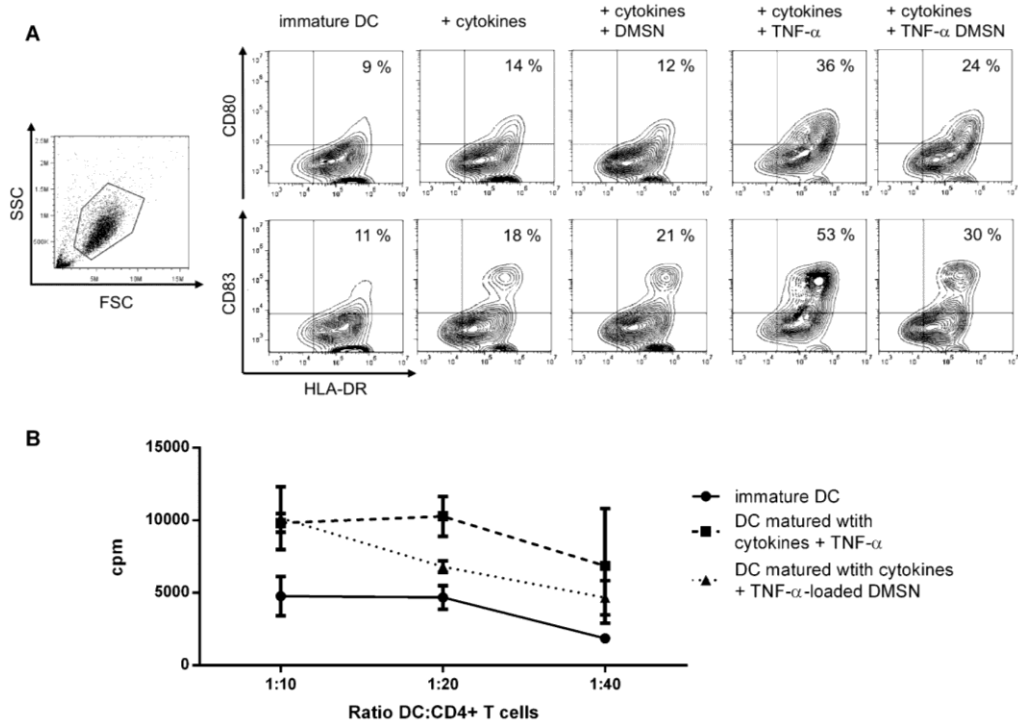


Figure A.7. TNF- α -loaded DMSN induce DC maturation. Human DC were cultured for 6 d in the presence of granulocyte-macrophage colony-stimulating factor (GM-CSF) and interleukin (IL)-4 and matured for 24 h using a cytokine cocktail +/- TNF- α , DMSN or TNF- α -loaded DMSN, respectively. (A) Expression of costimulatory molecules CD80 and CD83 was determined via flow cytometry. While TNF- α -loaded DMSN caused upregulation of the two molecules, the effect was not as strong as for free TNF- α , supporting the hypothesized encapsulation of TNF- α while maintaining its biological activity upon release. Cytokines only and cytokines with empty DMSN caused a comparably low upregulation of CD80 and CD83. (B) Differences in maturation were functionally verified using MLR. Matured DC were co-cultured with allogenic naive CD4⁺ T cells for 4 d followed by a [³H] thymidine pulse. Thymidine incorporation was determined as measurement for proliferation. While stimulatory ability of DC matured with cytokines and TNF- α -loaded DMSN was increased in comparison to immature DC, stimulatory ability was lower compared to DC matured with free TNF- α at a DC:CD4⁺ T cell ratio of 1:20 and 1:40 but equal at a 1:10 ratio. One representative experiment out of three is shown.

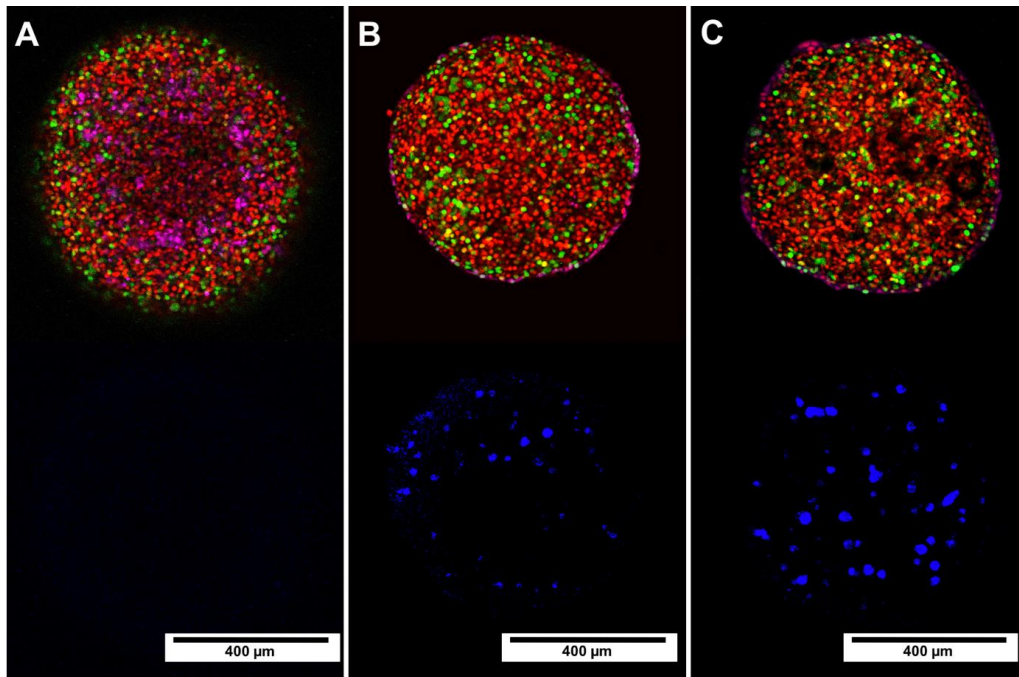


Figure A.8. DMSN distribution in 3D Melanoma Spheroids. Fucci (red: G1, green: S/G2/M phase) C8161 melanoma cells were grown as 3D spheroids and dead cells stained using DRAQ7 (pink). Images of spheroid sections were obtained using confocal microscopy. (A) Untreated spheroid. Spheroids were treated with DMSN-B (blue) for (B) 6 h or (C) 24 h.

A.4 Material and Methods Chapter 4

If not explicitly described, all chemicals were purchased from Sigma Aldrich, USA. All reagents and solvents were of analytical grade and used as received. All syntheses were carried out with Milli-Q water (18.2 M Ω ·cm, 25 °C). The copper complex CuOAc was supplied by the working group of Prof. Glaser (Bielefeld). Random methylated β -CD was purchased from TCI. Molecular weight of the β -CD and degree of substitution was determined by ESI-MS measurement (data not shown).

Preparation of DMSN. DMSN were synthesized via inverse biphasic stratification after a modified experimental setup.^[397] 12 ml cetyltrimethylammonium chloride (CTAC) solution (25 wt. % in H₂O) and 150 μ l triethanolamine (TEA) were added to 54 ml Milli-Q water (18.2 M Ω) and stirred at 75 °C for 1 h in a 100 ml 3-neck round-bottomed flask with a KPG stirrer. The heated water-CTAC-TEA solution was underlaid with 20 ml tetraethyl orthosilicate (TEOS) in 1,2-dichlorobenzene (15 v/v %) without stirring. The stirrer was adjusted right above the boundary layer in the water phase, and the stirring rate was set to 130 rpm to avoid mixing phases. Additionally, a stirring rate of 150 rpm was chosen to synthesize DMSN with bigger pores. After the reaction was kept at 70 °C for 14 h, the organic phase was removed. The resulting products were collected by centrifugation (9.000 rpm / 20 min) and re-suspended in ethanol using sonication. This procedure was repeated several times to remove residual reactants. Cyanine5 N-hydroxysuccinimide (NHS) (Cy5 NHS, Lumiprobe), was encapsulated in DMSN during the nanoparticle synthesis: 0.1 mg dye was dissolved in 200 μ l anhydrous dimethyl sulfoxide (DMSO), mixed with 1 μ l (3-aminopropyl)-trimethoxysilane (APTMS, >99%), stock solution freshly prepared from anhydrous DMSO) and stirred for 4h under argon atmosphere and light exclusion. 175 μ l of the prepared dye solution was added after 15 min reaction time to the TEOS/1,2-dichlorobenzene mixture.

Template extraction. DMSN (2.5 mg/ml in ethanol) with encapsulated dye were extracted three times with 1 wt. % ammonium nitrate (NH₄NO₃) at 80 °C under light exclusion to remove the surfactant template. The resulting DMSN were collected by centrifugation (9.000 rpm / 20 min) and washed several times with ethanol to remove NH₄NO₃.

Attachment of APTMS to surface of DMSN. The template extracted DMSN were dispersed in absolute EtOH and stirred at 1000 rpm in a polypropylene centrifuge tube. After addition of 15 μ l NH₄OH (30-32%), 3 μ l APTMS (stock solution 0.1 freshly prepared from anhydrous DMSO) was added each hour. After 3 h, the DMSN were

stirred for another 12h, collected by centrifugation (9.000 rpm / 20 min) and washed several times with ethanol to remove excess NH_4OH and APTMS.

Gatekeeper functionalization and drug loading. Functionalization of Cy5 labeled DMSN with the gatekeeper system was as follows. DMSN were dispersed in PBS buffer (pH 7.4 10 mM). A 1:1 molar mixture of ferrocene-CA and β -CD was prepared in Milli-Q water. To ensure formation of the inclusion complex, ferrocene-CA was dissolved in DMSO and added to a β -CD stock solution in Milli-Q water and kept under constant shaking for 3 h at room temperature. Afterwards, 0.438 μg ferrocene-CA / μg DMSN was added to the DMSN and incubated overnight. The closed DMSN were centrifuged at 15.000 rpm, supernatant discarded and DMSN re-suspended in PBS using sonication. Quantification of the ferrocene-CA amount in the supernatant was possible through UV-vis calibration (Beer's law) at 292 nm in the concentration range of 0-20 $\mu\text{g}/\text{ml}$. For drug loading of the DMSN, a stock solution of the drug was prepared in MQ water, added in various concentrations to the nanoparticle and kept under constant shaking for 12 h at room temperature. After gatekeeper functionalization (analogous to previously described), the wash supernatants were collected and analyzed for remaining drug. Samples were used within 1d after preparation.

Drug load quantification. A Rhodamine B ($\geq 95\%$ (HPLC)) RhoB (0.096 g, 0.2 mM) solution (10 mL) was prepared using volumetric equipment. Quantification of the RhoB amount in the supernatant was possible through UV-vis calibration (Beer's law) at 554 nm in the concentration range of 0-7 $\mu\text{g}/\text{ml}$. The amount of unloaded RhoB was calculated as follows. Loading capacity (%) = $[(C_{\text{Stock solution}} - C_{\text{RhoB after loading}})/C_{\text{Stock solution}}] * 100\%$. Determination of the copper amount was possible through atom absorption spectroscopy (AAS) measurement of the drug load supernatants and stock solution of CuOAc. 200 μl of the supernatant was acidified with 1 ml concentrated HNO_3 . After 3h stirring at 500 rpm, 9 ml Milli-Q water was added and the samples were analyzed in triplicate. Considering two copper atoms per complex, known concentration of the complex (mg/L) during drug load and the molecular weight of the complex (1140 g/mol), maximum amount of copper in the supernatant (g/L) can be calculated. After analysis of the drug load supernatant and the CuOAc stock solution, the difference in copper concentration was used to calculate the remaining amount of CuOAc in the nanoparticle.

β -CD labeling. Fluorescein-5-isothiocyanate (FITC), (Thermo Fisher Scientific) stock solution (1 mg/ml) was prepared in anhydrous ethanol and 400 μl was added to 11.9 mg 3A-Amino-3A-deoxy-(2AS,3AS)- β -cyclodextrin Hydrate (TCI chemicals) in 3 ml

ether. Excess fluorescent dye was extracted three times with methanol/THF and the dye labeled β -CD was used for gatekeeper functionalization of Cy5 labeled DMSN-AF.

CuOAc release from DMSN. After CuOAc loading, closed DMSN were kept in PBS buffer (pH 7.4 10 mM) and PBS/Citrate buffer (pH 4.5 10 mM). At 15, 30, 45, 60, 180, 360, 720, 1440 and 2880 min the samples were centrifuged at 15.000 rpm and washed three times. The supernatants were collected and analyzed by AAS. For the control experiment, closed DMSN were dissolved in 5M NaOH over 24h. After acidification with concentrated HNO₃, AAS was performed.

Cell cultures. HNSCCUM-02T base of tongue squamous cell carcinoma cell line was established in our laboratory^[477] and cultivated in DMEM/Ham-F12 with 10% FCS and 2% antibiotics.

Release of Doxorubicin. Release of Doxorubicin was measured by changes in metabolic activity of HNSCCUM-02T. DMSN were loaded with Doxorubicin (2 mg/mL = 3.45 mM, 290 μ L for 200 μ g DMSN used, Loading efficiency could not be determined, differences between supernatants and loading solutions were too low) (Dox-DMSN) overnight at 4 °C and then sealed with ferrocene-CA and 3A-Amino-3A-deoxy-(2AS,3AS)- β -cyclodextrin for 6 hours at 4 °C. Control DMSN (DMSN) were incubated with PBS and sealed the same way. Cells were incubated with 2 μ M free Doxorubicin (Dox), 10 μ g/mL Dox-DMSN (10 μ M) or DMSN, respectively for 24, 48 and 96 hours. Then, AlamarBlue® Assay^[478] was performed. Afterwards, cells were incubated further for 72 hours in medium without nanoparticles, respectively, and metabolic activity was measured again.

FOCI staining for detecting DNA damage

HNSCCUM-02T cells were seeded in a μ -Slide 8 Well, ibiTreat (Ibidi®) and treated with Dulbecco's Phosphate Buffered Saline (PBS), 1 μ M Doxorubicin (Dox), 10 μ g/mL Dox-DMSN or 10 μ g/mL DMSN, respectively. After 2 or 24 hours cells were washed with PBS (3 times 5 min), fixed with 4% paraformaldehyde in PBS (15 min at room temperature) and washed again (3 times 5 min). Right before immunofluorescence labeling cells were fixed with ice-cold methanol (10 min at room temperature) and washed with PBS (3 times at room temperature). Next, samples were blocked with 5% bovine serum albumin in 0.3% TritonX100 in PBS (1 hour at room temperature) and stained with anti-phospho-Histone H2A.X (Ser139), clone JBW301 anti-body (Millipore) 1:500 in 0.3% TritonX100/PBS for 1 hour at room temperature under gentle shaking. Samples were washed two times with PBS, briefly with tris-buffered saline (TBS, pH 7.6) containing 400 mM NaCl and again with PBS. Fluorescence labeling was conducted with anti-mouse AlexaFlour®488 anti-body (Molecular Probes (Life Technology)) 1:500 in 0.5% BSA in 0.3% TritonX100/PBS with 450 nM 2-(4-carbamimidoylphenyl)-1H-indol-6-carboximidamid (DAPI) for 1 hour at room temperature under gentle shaking. Finally, samples were washed with PBS and TBS with 400 mM NaCl as before, briefly rinsed with water and embedded in Fluorescence Mounting Medium (Vectashield). Imaging was performed with DMi8 confocal laser scanning microscope (Leica) with a 63x objective using the settings shown in **Table A.2**.

Table A.2. Settings of the confocal laser scanning microscope (Leica)

Laser	Laserpower (%)	Gain (V)	Photomultipliertube range	Color in image
405 nm	5.52	700	408-496 nm	Blue
488 nm	8.12	720	505-535 nm	Green
638 nm	8.04	720	640-737 nm	Red

A.5 Instruments Chapter 4

Transmission electron microscopy (TEM). See Instruments Chapter 3 for reference. Staining of the coated DMSN was possible with ammonium molybdate.^[479]

Small angle X-ray scattering (SAXS). SAXS measurements were performed in transmission geometry at a self-constructed instrument using a rotating Cu anode X-ray generator (Rigaku MicroMax 007). The beam was monochromatized (1.54 Å wavelength) and collimated by a multilayer optics (Osmic Confocal Max-Flux, Cu K α) and three 4-jaw slit sets (700 \times 700 μm^2 slit gap) with 150 cm collimation length. An incident X-ray flux of 1×10^7 photons/s at the sample position was measured by an inversion layer silicon photodiode (XUV-100, OSI Optoelectronics). Samples were contained in 1 mm diameter borosilicate glass capillaries. 2D diffraction patterns were recorded on an online image plate detector (Mar345). The sample–detector distance of 210 cm was calibrated with silver behenate.^[480] SAXS data, collected during four independent measurements with 120 s exposure time each, were averaged and corrected by dark images. Artifacts, originating from high energy radiation, were removed by Laplace filtering. 2D data sets were converted to $I(q)$ versus momentum transfer $q = 4\pi/\lambda \sin(\theta)$ by azimuthal integration.

Nitrogen sorption measurements. See Instruments Chapter 3 for reference.

Nuclear magnetic resonance spectra (NMR). NMR experiments were performed on a Bruker ARX 400 spectrometer using a ^1H frequency of 400.31 MHz equipped with a 5 mm commercial Bruker inverse probe head. The ^1H experiments were conducted by averaging 32 transient with a recycle delay of 1 s. Samples (10 mg) were dissolved in d^6 DMSO or D_2O and obtained data analyzed using Mnova NMR software. For the titration experiment, a fixed concentration of β -CD in a D_2O :DMSO mixture (10:1) was placed in a NMR tube. Subsequently ferrocene-CA (in steps of 0.2 mole fraction) was added and measured after thoroughly mixing. Concentration range of the host complex and non-linear curve fitting was performed according to the literature.^[468,481,482]

Solid-state nuclear magnetic resonance spectra (ssNMR). All ssNMR experiments were performed on a Bruker Avance DSX 400 NMR spectrometer using a ^1H frequency of 399.83 MHz, ^{13}C frequency of 100.54 MHz and ^{29}Si frequency of 79.44 MHz. A commercial 3 channel 4 mm Bruker probe head was used at magic angle spinning (MAS) of 5 kHz for the ^{29}Si and 10 kHz for the ^{13}C experiments. The ^{29}Si single pulse (DP) direct polarization experiment was carried out by a 90° pulse with a length of 4 μs and repetition time of 300 s averaging 1024 transients. The ^1H - ^{29}Si cross-polarization (CP) experiments were recorded with a duration of the variable amplitude (64-100%)

CP contact time of 8000 μs collecting 10 k transients with 6 s recycle delay. The ^{13}C CP measurements were performed using variable amplitude (64-100%) CP contact time of 2000 μs collecting either 1k or 30 k scans with a repetition times varying from 3 to 5 s. For all heteronuclear NMR experiments a two pulse phase modulation (TPPM) decoupling scheme was used. A broadening of 100 Hz was used when processing the ^{29}Si MAS-NMR spectra and 50 Hz for the ^{13}C MAS-NMR spectra. The ^{13}C chemical shifts were referenced to external adamantane as a secondary standard at 38.48 ppm while for the ^{29}Si chemical shifts external tetra-kis-trimethylsilylsilane at -9.7 ppm was used as a reference.

Ultraviolet–visible spectroscopy (UV-Vis). See Instruments Chapter 3 for reference.

Potentiometric titration. Potentiometric measurements were performed using a computer-controlled system from Metrohm (Filderstadt, Germany), operated with the custom-designed software Tiamo (v2.4). The setup consists of a titration device (Titrando 905) that controls two dosing units (Dosino 800). The system is supplemented by a pH module (Metrohm, pH module 867). The pH in the sample was monitored in real time with a glass iUnitrode electrode (Metrohm, No. 6.0278.300) All experiments were carried out in a lab-built PTFE titration vessel. The vessel was closed and protected from the atmosphere to minimize potential artifacts that may arise from diffusion of atmospheric CO_2 or evaporation of the solution. Additionally, all used solutions except the base were purged for 15 min with nitrogen gas before each use. The room temperature was controlled at $T = 293.15\text{ K}$. For example, 10 mg nanoparticle in 30 ml MilliQ-water with 10 mM KNO_3 were basified with 0.1 M KOH and titrated with 0.01 HCl. Titration rate was set to 0.5 ml/min and each experiment was conducted 600 seconds. To determine the background signal, arising from carbonate species solved inside the base and the titration matrix, all experimental series were monitored by blank titrations before and after each set. All samples were analyzed in triplicate and the mean value was calculated.

For the functionalization of the DMSN-A with Phenyl-SCN, 10 mg of the DMSN-A were dispersed in dry DMSO and 1.4 mg (8.5 μmol) (1:1 ratio amine:Phenyl-SCN) and 2.8 mg (17 μmol) (1:2 ratio amine:Phenyl-SCN) were added. After 6h incubation under argon and light exclusion, the nanoparticles were extensively washed with MeOH/THF and ethanol.

Zetasizer surface charge and dynamic light scattering (DLS). See Instruments Chapter 3 for reference.

Attenuated total reflection infrared spectroscopy (ATR-IR). See Instruments Chapter 3 for reference.

Thermogravimetric analysis (TGA). See Instruments Chapter 3 for reference.

Fluorescence correlation spectroscopy (FCS Dual color fluorescence cross correlation spectroscopy (dcFCCS)) dcFCCS experiments were performed on an LSM 880 (Carl Zeiss, Jena, Germany) setup. Excitation laser light was focused on the samples using a Zeiss C-Apochromat 40 \times /1.2 W water immersion objective. Emission was collected with the same objective and, after passing through a confocal pinhole, directed to a spectral detection unit (Quasar, Carl Zeiss). In this unit emission is spectrally separated by a grating element on a 32 channel array of GaAsP detectors operating in a single photon counting mode. An eight-well polystyrene, chambered cover glass (Laboratory-Tek, Nalge Nunc International) was used as a sample cell. For each sample, 5 measurements (30 seconds each) were performed. An argon ion laser ($\lambda = 488 \text{ nm}$) was used for excitation of FITC-labeled species and a HeNe laser ($\lambda = 633 \text{ nm}$) was used for excitation of Cy5-labeled compound. Emission in the range from 500 to 553 nm for the “blue” channel and from 642 to 696 nm for “red” channel was detected with a QUASAR detection unit. These arrangements resulted in two overlapping confocal observation volumes V_b and V_r that superimpose to a common observation volume V_{br} . The temporal fluctuations of the fluorescence intensities $\delta F_b(t)$ and $\delta F_r(t)$, caused by the diffusion of the FITC-labeled species through V_b and Cy5-labeled species through V_r were independently recorded and evaluated through the corresponding auto- and cross-correlation functions:

$$G_{bb}(\tau) = 1 + \frac{\langle \delta F_b(t) \cdot \delta F_b(t+\tau) \rangle}{\langle F_b(t) \rangle^2} \quad \text{Equation A.3}$$

$$G_{rr}(\tau) = 1 + \frac{\langle \delta F_r(t) \cdot \delta F_r(t+\tau) \rangle}{\langle F_r(t) \rangle^2} \quad \text{Equation A.4}$$

$$G_{br}(\tau) = 1 + \frac{\langle \delta F_b(t) \cdot \delta F_r(t+\tau) \rangle}{\langle F_b(t) \rangle \cdot \langle F_r(t) \rangle} \quad \text{Equation A.5}$$

For an ensemble of identical, freely diffusing fluorescent species, the correlation functions have the following analytical form:

$$G_D(\tau) = 1 + \frac{1}{N} \frac{1}{\left(1 + \frac{\tau}{\tau_D}\right)} \frac{1}{\sqrt{1 + \frac{\tau}{S^2 \tau_D}}} \quad \text{Equation A.6}$$

Here, N represents the number of fluorescent species in the confocal volume V and τ_D is the average lateral diffusion time. The structural parameter S considers the ratio of axial to lateral dimensions of the confocal volume V . The dimensions of V_b and V_r were determined by performing calibration measurements with reference standards (Alexa Fluor 488 and Alexa Fluor 647) with known diffusion coefficients. The experimental autocorrelation curves (**Equation A.4** and **Equation A.5**) were fitted with (**Equation A.6**), yielding the corresponding values of N and τ_D . Consequently, the concentration $c = \frac{N}{V}$, the diffusion coefficient $D = \frac{r_0^2}{4\tau_D}$ and through the Stokes-Einstein relation the hydrodynamic radius R_H of the FITC-labeled and Cy5-labeled species were evaluated.

Isothermal titration calorimetry (ITC). ITC experiments were performed on a NanoITC Low Volume (TA Instruments, Germany). An effective cell volume of 170 μl , a stirring rate of 350 rpm, and a temperature of 25 $^\circ\text{C}$ were maintained for all experiments. To correct the data for the heat of dilution, the titrant was titrated into water and resulting heats were subtracted from each titration of DMSN. The resulting data were analyzed with an independent binding model^[483] using the software NanoAnalyze (version 3.5.0) by TA Instruments.

A.6 Figures, Tables and Equations Chapter 4

Table A.3. Characterization of the dye-labeled nanocarrier DMSN-A and its functionalization steps DMSN-AF and DMSN-AFC.

Sample	Dye	Diameter ^{a)}	Pore size ^{b)}	Surface area ^{c)}	Pore volume ^{d)}
		[nm]	[nm]	[m ² /g]	[cm ³ /g]
DMSN-A	Cyanine 5	130 ± 9.9	8.2	522	1.02
DMSN-AF	Cyanine 5	133 ± 11.9	7.3	327	0.56
DMSN-AFC	Cyanine 5	138 ± 9.8	7.3	304	0.55

^{a)}Average diameter by TEM; ^{b)}Calculated by NLDFT method; ^{c)}Calculated by BET method; ^{d)}Value at P/P₀ = 0.972 by N₂-sorption isotherm.

Calculation Part I:

Consumption silanol groups during APTMS functionalization through ²⁹Si DPMAS NMR .

Peak areas for the single silanol (Q₃) and germinal silanol (Q₂) before and after functionalization. The peak areas are normalized to the siloxane network (Q₄).

$$S_{N,DMSN} = \frac{Q_2 \times Q_3}{Q_4} = 0.57 \qquad S_{N,DMSN-A} = \frac{Q_2 \times Q_3}{Q_4} = 0.29$$

➤ Ratio of the normalized peak areas results in consumed silanol groups

$$\text{Silanol groups consumed} = \frac{S_{N,DMSN-A}}{S_{N,DMSN}} \times 100 = 50.9\%$$

Calculation Part II:

Surface coverage determination through ^{29}Si DPMAS NMR .

- Peak areas for the single silanol (Q_3) and germinal silanol (Q_2) are correlated with the peak areas of the single organosiloxane (T_3) and germinal organosiloxane (T_2). Ratio of the peak areas results in surface coverage of the DMSN.

$$SC_{DMSN-A} = \frac{(T_2 + T_3)}{(Q_2 + Q_3 + T_2 + T_3)} \times 100 = 39.9\%$$

Calculation Part III:

Potentiometric titration for determination of the amount amine groups $\times nm^{-2}$.

- Mass particle in the experiment $m_{particle} = 6.55 \text{ mg}$
- Avogadro constant $N_a = 6.022 \times 10^{23} \text{ mol}^{-1}$
- Surface area DMSN $SA_{DMSN} = 522 \frac{m^2}{g}$
- Concentration acid for titration $c_{acid} = 0.01 \frac{mol}{l}$
- Volume acid consumed during experiment $V_{acid} = 0.54 \text{ ml}$
- Molar amount acid consumed during experiment

$$n_{acid} = c_{acid} \times V_{acid} \times 10^{-3} = 5.35 \times 10^{-6} \text{ mol}$$

- Molar amount amine per particle mass $n_{Amine} = \frac{n_{acid}}{m_{particle}} = 0.85 \frac{\mu mol}{mg}$
- **Monolayer on the nanoparticle surface**^[484]
- **Amount amine groups $\times nm^{-2}$** $\frac{n_{Amine}}{SA_{DMSN}} \times N_a \times 10^{15} = 0.98 \text{ nm}^{-2}$
- 5 silanols $\times nm^{-2}$ on the DMSN surface / pore channels^[485,486]
- 50% consumption of surface silanols during APTMS functionalization (DPMAS NMR)
- 2-3 anchor groups of APTMS to the surface equals 2.5–1.66 amine groups $\times nm^{-2}$

➔ **59-39% of the accessible surface silanols are consumed**

Calculation Part IV:

Potentiometric titration for determination of the surface area coverage after functionalization.

➤ Mass particle in the experiment $m_{particle} = 6.55 \text{ mg}$

➤ Avogadro constant $N_a = 6.022 \times 10^{23} \text{ mol}^{-1}$

➤ Surface area DMSN $SA_{DMSN} = 522 \frac{\text{m}^2}{\text{g}}$

➤ Concentration acid for titration $c_{acid} = 0.01 \frac{\text{mol}}{\text{l}}$

➤ Volume acid consumed during experiment $V_{acid} = 0.54 \text{ ml}$

➤ Molar amount acid consumed during experiment

$$n_{acid} = c_{acid} \times V_{acid} \times 10^{-3} = 5.35 \times 10^{-6} \text{ mol}$$

➤ Molar amount amine per particle mass $n_{Amine} = \frac{n_{acid}}{m_{particle}} = 0.85 \frac{\mu\text{mol}}{\text{mg}}$

➤ Surface area covered by one amine group $SC_{amine} = 5 \text{ nm}^2$

➤ Surface area covered by organic layer

$$SC_{organic} = SC_{amine} \times n_{particle} \times 10 \times N_a = 256 \frac{\text{m}^2}{\text{g}}$$

➔ **49% surface area coverage in comparison to the initial DMSN surface**

Calculation Part V:

Determination of the concentration DMSN-AF in the isothermal titration experiment.

➤ Density of amorphous silica $\delta_{amorph. silica} = 2 \frac{g}{cm^3}$

➤ Avogadro constant $N_a = 6.022 \times 10^{23} mol^{-1}$

➤ pi $\pi = 3.141$

➤ Particle diameter $d_{DMSN} = 130 \text{ nm}$

➤ DMSN concentration $c_{DMSN} = 6282 \frac{\mu g}{ml}$

➤ Conversion factor $b = 6 \times 10^{15}$

➤ Concentration DMSN amount per ml

$$\chi = (c_{DMSN} \times b) \frac{c_{DMSN} \times b}{\delta_{amorph. silica} \times \pi \times d_{DMSN}^3} = 4.62 \times 10^{16} ml^{-1}$$

➤ Concentration DMSN mmol per ml

$$\chi \times N_a = 7.66 \frac{mmol}{ml}$$

➤ Volume ITC measuring cell $V_{ITC} = 300 \mu l$

➤ Amount particle in the ITC experiment $A_{NP} = \chi \times V_{ITC} \times 10^{-3} = 1.39 \times 10^{16}$

Calculation Part VI:

Total amount of β -CD on DMSN in the isothermal titration experiment.

- Amount β -CD per DMSN consumed (ITC) $A_{CD} = 8000$
- Amount particle in the ITC experiment $A_{NP} = \chi \times V_{ITC} \times 10^{-3} = 1.39 \times 10^{16}$
- Total quantity β -CD consumed $A_{NP} \times A_{CD} = 1.12 \times 10^{20}$
- Molar amount amine per particle mass $n_{Amine} = 0.85 \frac{\mu mol}{mg}$

- Amount amine groups in the ITC experiment

$$A_{Amine} = n_{Amine} \times N_a \times c_{DMSN} \times V_{ITC} = 9.65 \times 10^{20}$$

- Maximal 85% amine groups accessible for gatekeeper functionalization (**Figure 4.6C**)

$$A_{accessible} = A_{Amine} \times 0.85 = 8.19 \times 10^{20}$$

- Ratio of the total amounts amine and β -CD defines surface coverage of the DMSN $\frac{A_{\beta-CD}}{A_{Amine}}$

➔ **14% of the nanoparticle surface is covered with β -CD moieties.**

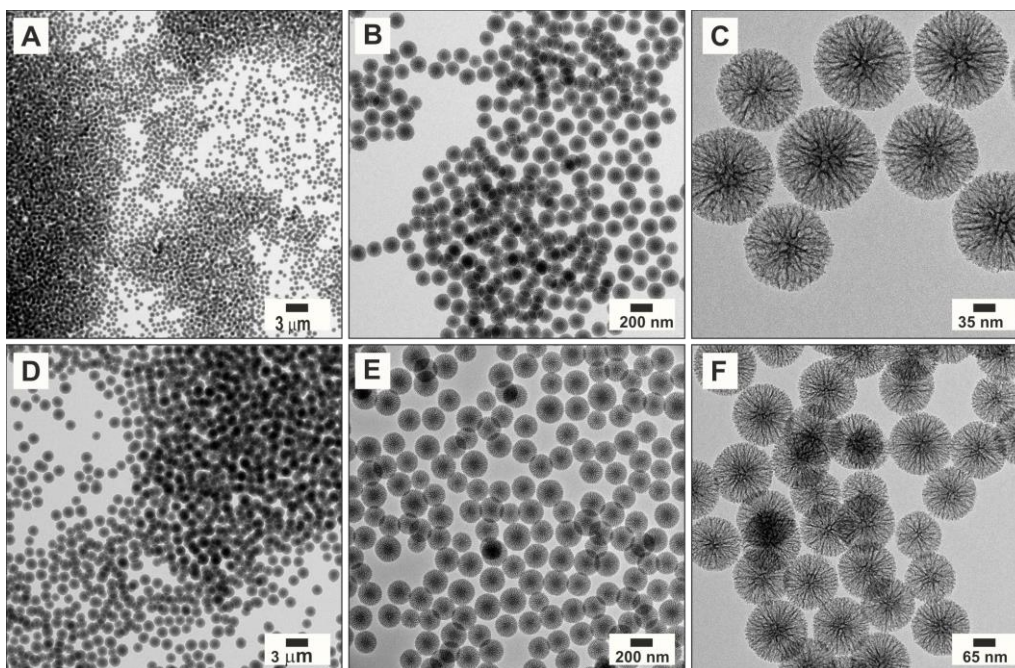


Figure A.9. Overview of the utilized DMSN with two different pore sizes. A)-C) small pores (4-5 nm) and D)-F) medium pores (7-8 nm). Pore size > 11 nm were excluded in this study due to limited drug retention/ increased drug leakage over time.

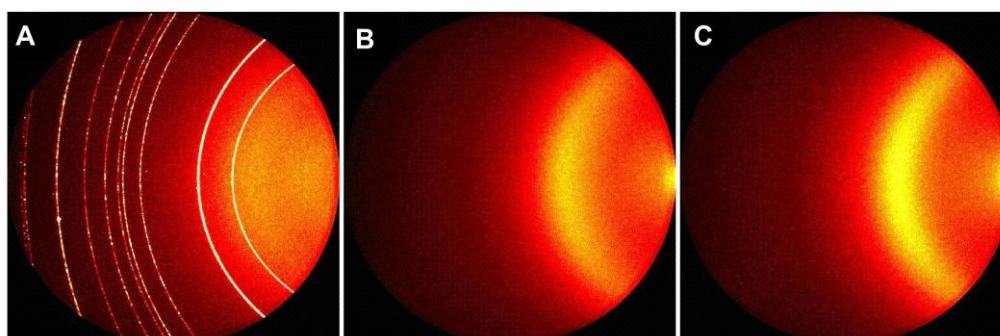


Figure A.10. Wide Angle X-Ray Scattering (WAXS) measurements of silica (SiO_2) (20 minutes exposure time each). A) shows crystalline silica with sharp signals visible. Detector range was from 10 to 60 degree scattering angle. B) shows amorphous silica and C) shows the unfunctionalized sample of dendritic mesoporous silica nanoparticle (DMSN). It is well visible that the sample structure compares to the amorphous reference measurement and has an amorphous structure.

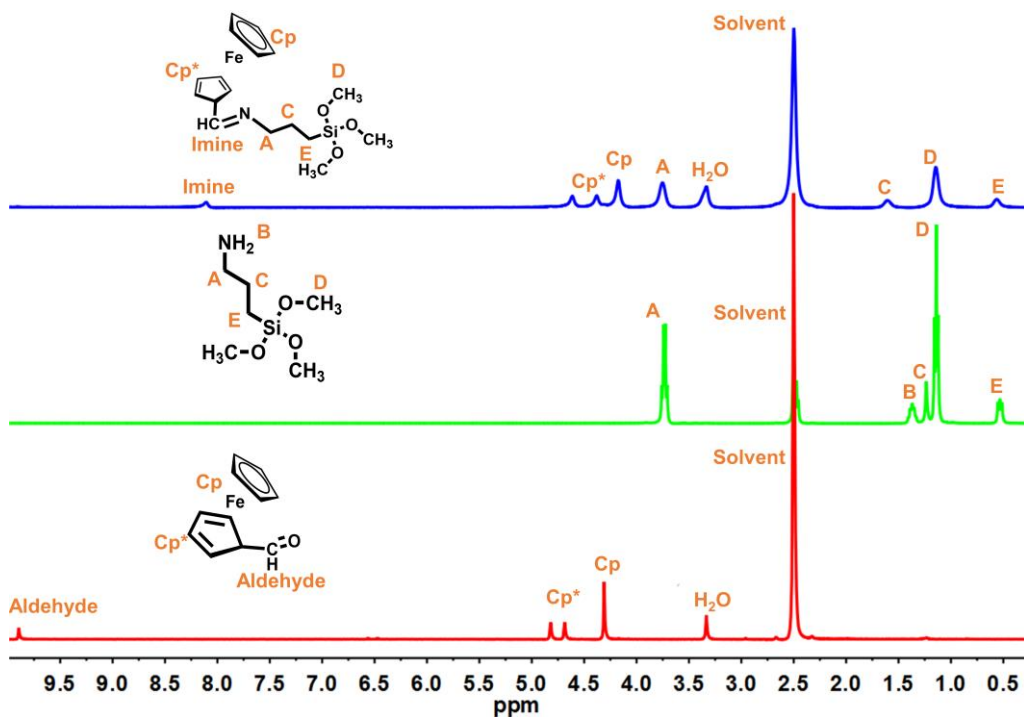


Figure A.11. ^1H NMR spectroscopy of the reaction of ferrocene-CA with APTMS. The disappearance of the aldehyde signal at 9.7 ppm for ferrocene-CA, the consumption of the primary amine signal at 1.45 ppm and the appearance of the imine signal at 8.1 ppm^[487] shows the successful coupling of the silica anchor group to the aromatic aldehyde.

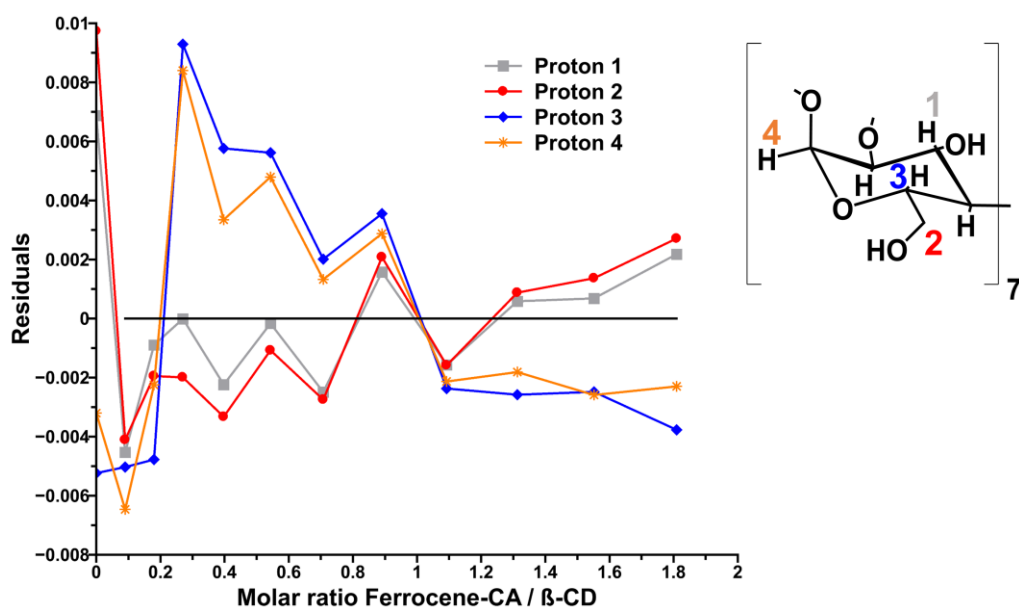


Figure A.12. Residuals of the non-linear curve fit of the ^1H NMR titration experiment. The variance of the experimental peak positions of the titration experiment from the peak position of the non-linear curve fit is shown.

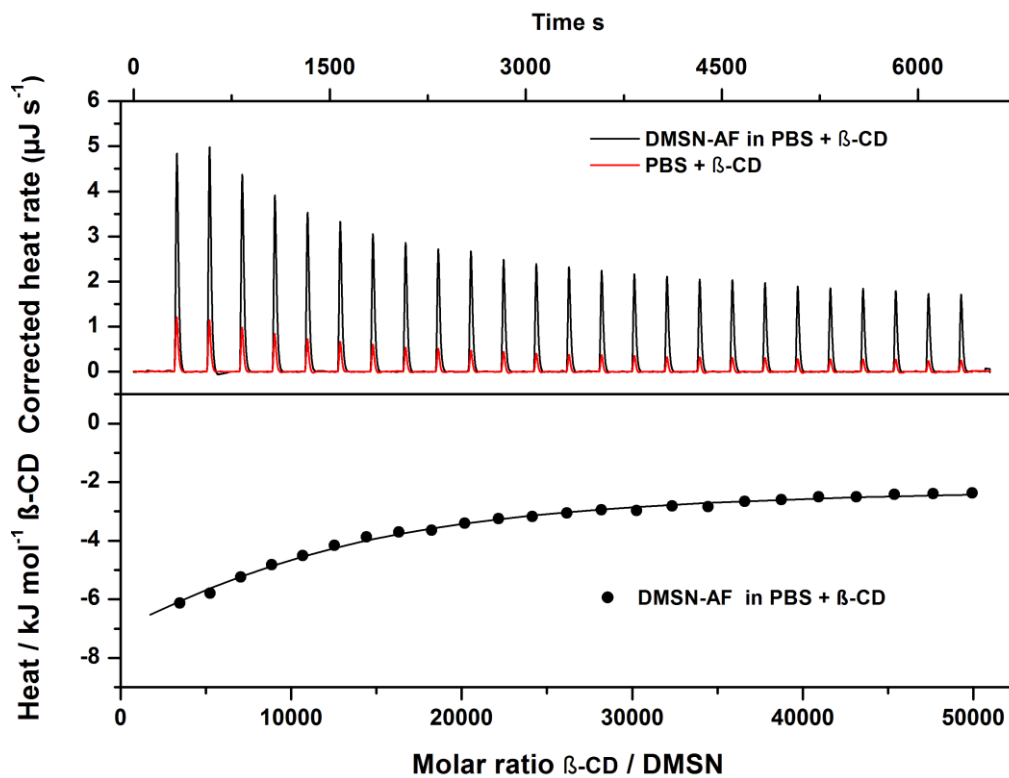


Figure A.13. ITC Titration experiment of the interaction of β -CD with DMSN-A. No interaction of the sugar with the DMSN-A over the whole concentration range is visible. Non-specific interaction of the β -CD with the nanoparticle during drug load can be excluded.

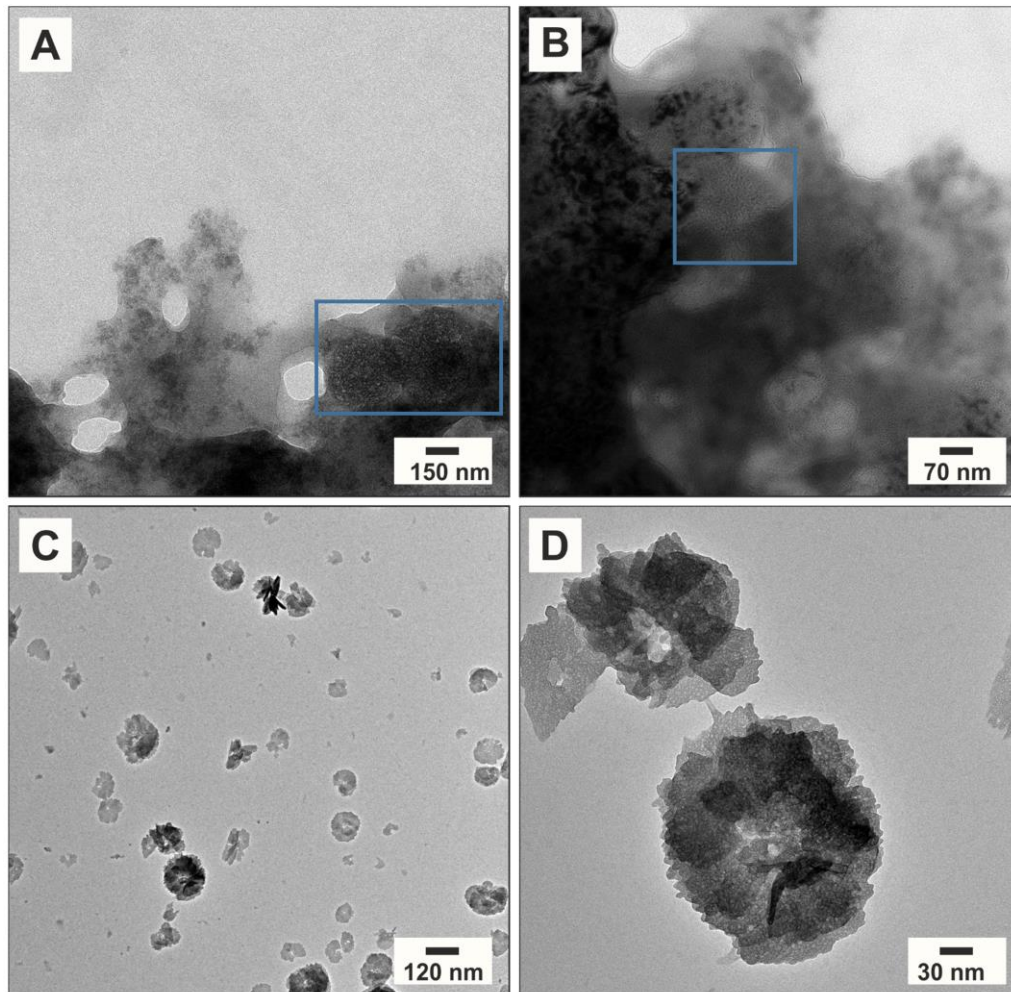


Figure A.14. Biodegradation of the coated DMSN. Degradation of the drug delivery system after 12h (A,B) and 30h (C,D) in DMEM + 10% fetal calf serum at 37 °C. After 12h, some partial disintegrates particle are visible (blue arrows). After 30h, complete degradation of the pore structure has occurred, leaving only the core silica structure behind.

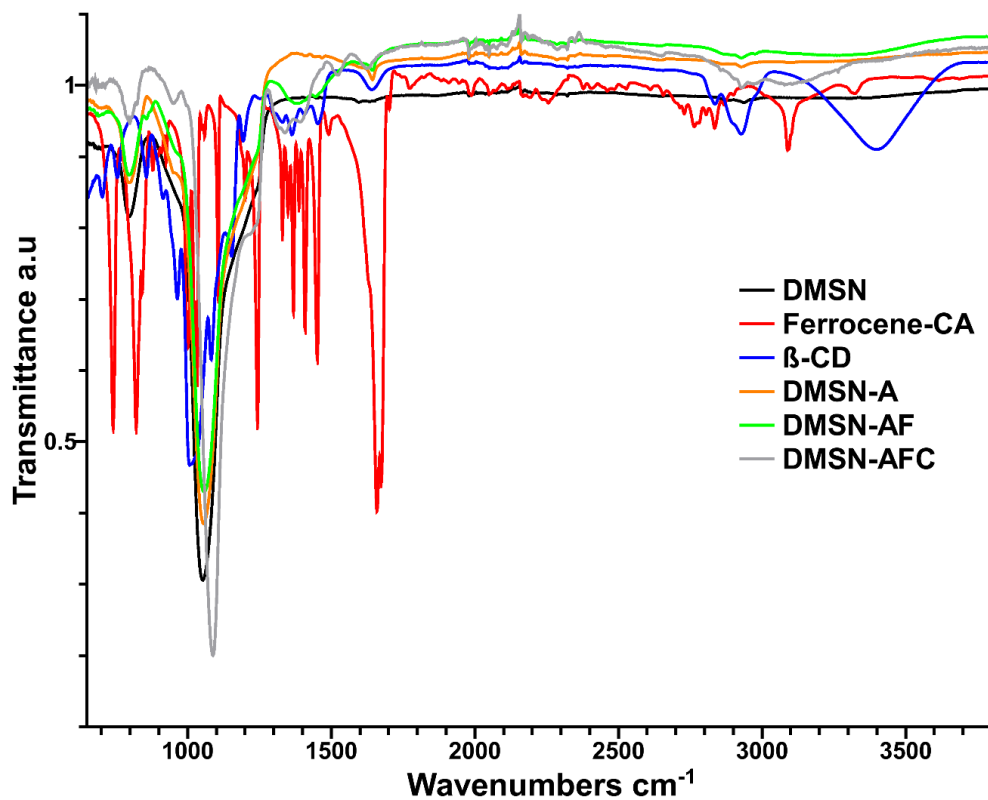


Figure A.15. ATR-IR spectra of the functionalization process. Signals for the amine bending mode at $1650\text{-}1590\text{ cm}^{-1}$ of the DMSN-A, imine group at $1650\text{-}1690\text{ cm}^{-1}$ for the DMSN-AF and C-O signals for the glucopyranosyl framework at 900 cm^{-1} for DMSN-AFC indicated successful functionalization steps.^[437] Spectra are vertical shifted for better visualization.

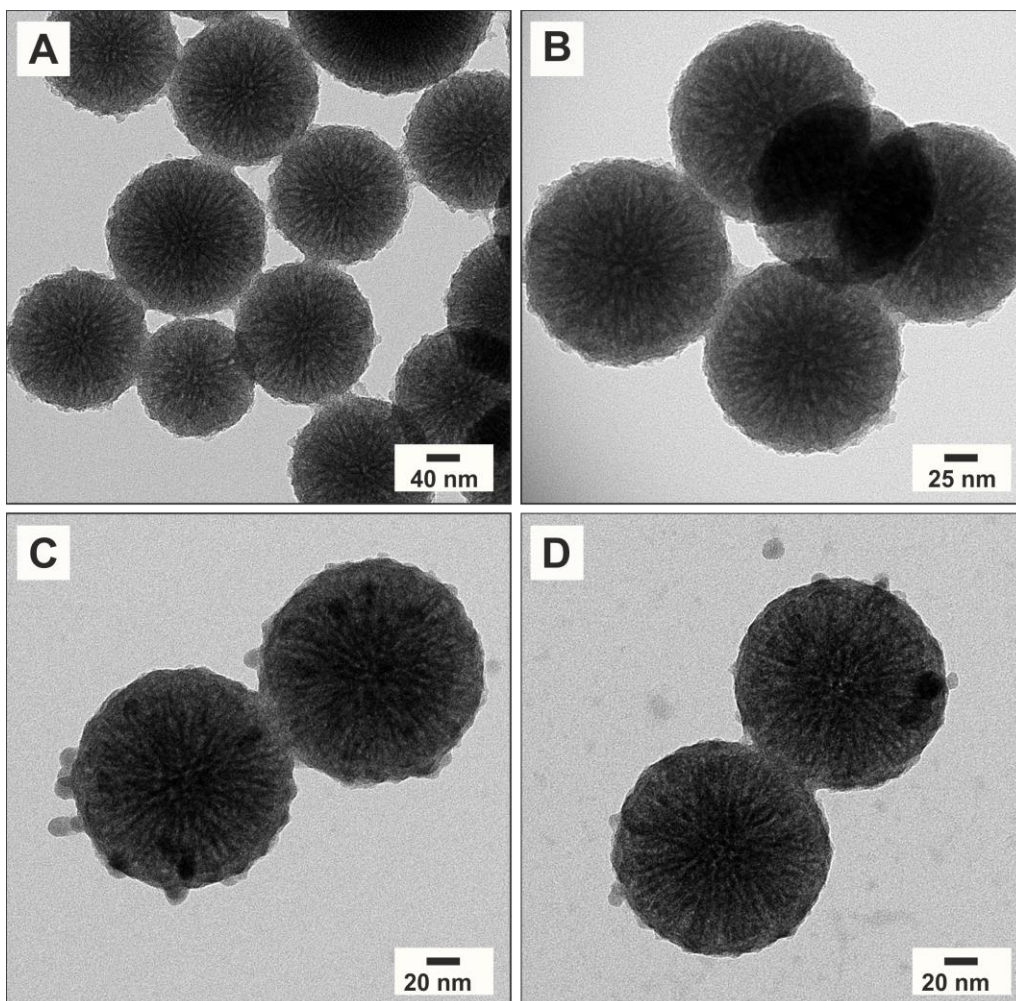


Figure A.16. Staining of the gatekeeper functionalized DMSN with ammonium molybdate. Coverage of the surface/pores with the gatekeeper is visible due to increased contrast after staining.

A.7 Authorship Contributions

Chapter 1: Introduction and scope

The content of chapter 1 is partially taken and adapted from the book chapter “Bio-Nano: Theranostic At Cellular Level” written by S. Kurch, M. Klunker, M. N. Tahir, W. Tremel which is part of the book “The Role of Particles in Pharmaceutical Products” by Henk G. Merkus, Gabrie M.H. Meesters, Wim Oostra. The book is intended to be published under the imprint Springer. The work may be published in the book series “Advances in the Pharmaceutical Sciences”. (Status May 2018)

Chapter 3: Dendritic Mesoporous Silica Nanoparticles for pH-Stimuli-Responsive Drug Delivery of TNF-Alpha

The content of the following chapter is partially taken and adapted from Adv. Healthcare Mater. 2017, 6, 1700012. S.K. and A.K. contributed equally to this work. This project was developed in collaboration with the Translational Research Institute of the University of Queensland, (Brisbane, Australia) and the University Medical Center of the Johannes Gutenberg-University Mainz, (Mainz, Germany). Details to the individual contribution of each author are listed below.

Category 1

Conception and design of study:

S. Kurch, A. Kienzle, H. Jonuleit, W. Tremel

Acquisition of data:

S. Kurch	Nanoparticle/copolymer synthesis, ATR-IR, ^1H , ^{13}C -NMR, Gasadsorption TEM; DLS/Zeta (Zetasizer), TGA/DSC, TNF dye labeling
A. Kienzle	MTT) assay, ELISA, Cellular uptake and cytokine release, EC_{50} values, 3D Melanoma Spheroids
J. Schlöder	DC maturation, mixed lymphocyte reaction
C. Berges	DC maturation, mixed lymphocyte reaction
R. Ose	DC maturation, mixed lymphocyte reaction
J. Schupp	CLSM images DC, mixed lymphocyte reaction
J. Müller	ITC and fitting procedure
H. Weiss	SAXS
J. Schultze	FCS and fitting procedure
M. Schinnerer	Dynamic light scattering in human plasma/fitting procedure/multi-angle DLS
M. Mondeshki	^{13}C , ^{29}Si ssNMR

Analysis and/or interpretation of data:

S. Kurch Nanoparticle/copolymer synthesis, ATR-IR, ^1H , ^{13}C -NMR, Gasadsorption TEM; DLS/Zeta (Zetasizer), TGA/DSC, TNF dye labeling, ^{13}C , ^{29}Si ssNMR

A. Kienzle	MTT) assay, ELISA, Cellular uptake and cytokine release, EC ₅₀ values,
	3D Melanoma Spheroids
J. Schlöder	DC maturation, mixed lymphocyte reaction
C. Berges	DC maturation, mixed lymphocyte reaction
R. Ose	DC maturation, mixed lymphocyte reaction
J. Schupp	CLSM images DC
J. Müller	ITC and fitting procedure
H. Weiss	SAXS
J. Schultze	FCS and fitting procedure
M. Schinnerer	Dynamic light scattering in human plasma/fitting procedure/multi-angle DLS
A. Tüttenberg,	Supervisor J. Schupp, CLSM images DC
S. Winzen,	Supervisor J. Müller, ITC
M. Mezger	Supervisor H. Weiss, SAXS
K. Koynov,	Supervisor J. Schultze, FCS
N. K. Haas.	Supervisor (Australia) A. Kienzle, 3D Melanoma Spheroids

Category 2

Drafting the manuscript:

S. Kurch, A. Kienzle,

Revising the manuscript critically for important intellectual content:

S. Kurch, A. Kienzle, J. Schlöder, C. Berges, R. Ose, J. Schupp, H. Weiss, J. Schultze, M. Schinnerer, A. Tüttenberg, S. Winzen, M. Mezger, K. Koynov, N. K. Haas, H. Jonuleit, W. Tremel.

Category 3

Approval of the version of the manuscript to be published:

S. Kurch, A. Kienzle, J. Schlöder, C. Berges, R. Ose, J. Schupp, H. Weiss, J. Schultze, M. Schinnerer, A. Tüttenberg, M. Mezger, K. Koynov, N. K. Haas, H. Jonuleit, W. Tremel.

All figures, tables and schema used were prepared by S. Kurch, exceptions are listed below:

Figures 3.11, 3.12, 3.13, 3.14, A5, A6: Prepared by A. Kienzle J. Schlöder, C. Berges, R. Ose

Figure 3.15: Prepared by M. Diken, J. Schlöder

- Copolymer synthesis was conducted under supervision of S. Kurch from P. Opitz (Bachelor thesis 2015).
- Section: *in vivo* experiment: Cargo release and DMSN tracking were conducted by M. Diken and J. Schlöder.

Chapter 4: Controlled surface functionalization of dendritic mesoporous silica nanoparticle for pH responsive drug delivery of a cytotoxic dinuclear Cu₂ complex

The content of the chapter is thought to be published in 2018. S.K., A. Watermann and J. Schupp. contributed equally to this work This project was developed in collaboration with the Chemistry Department Bielefeld University (Bielefeld, Germany) and the University Medical Center of the Johannes Gutenberg-University Mainz, (Mainz, Germany). Details to the individual contribution of each author are listed below.

Category 1

Conception and design of study:

S. Kurch, A. Watermann, J. Schupp, T. Glaser, A. Tüttenberg, J. Brieger, W. Tremel

Acquisition of data:

S. Kurch	Nanoparticle synthesis/functionalization, β -CD modification, ATR-IR, ^1H , ^{13}C -NMR, UV-Vis, Quantification drugload AAS, Gasadsorption TEM; DLS/Zeta (Zetasizer), TGA, Titrimetric Titration
A. Watermann	<i>in vitro</i> experiments
J. Schupp	<i>in vitro</i> experiments
D. Prozeller	ITC and fitting procedure
H. Weiss	SAXS and WAXS
S. Schwarzbich	Cu-Complex Synthesis
M. Mondeshki	^{13}C ssNMR, ^{29}Si DPMAS NMR
J. Schultze	FCS/cross correlation and fitting procedure

Analysis and/or interpretation of data:

S. Kurch	Nanoparticle synthesis/functionalization, β -CD modification, ATR-IR, ^1H , ^{13}C -NMR, UV-Vis, Quantification drugload AAS, Gasadsorption TEM; DLS/Zeta (Zetasizer), TGA, TNF dye labeling, Titrimetric Titration
A. Watermann	<i>in vitro</i> experiments, FOCI staining
J. Schupp	<i>in vitro</i> experiments, FOCI staining
D. Prozeller	ITC and fitting procedure
H. Weiss	SAXS and WAXS
M. Mondeshki	^{13}C ssNMR, ^{29}Si DPMAS NMR
J. Schultze	FCS/cross correlation and fitting procedure
A. Tüttenberg,	Supervisor J. Schupp, <i>in vitro</i> experiments
S. Winzen,	Supervisor J. Müller, ITC
M. Mezger	Supervisor H. Weiss, SAXS
K. Koynov,	Supervisor J. Schultze, FCS
T. Glaser	Supervisor J. Schupp, <i>in vitro</i> experiments, FOCI staining
J. Brieger	Supervisor A. Watermann, <i>in vitro</i> experiments, FOCI staining

All figures, tables and schema used were prepared by S. Kurch, exceptions are listed below:

Figures 4.11, 4.12, 4.13, 4.14: Original plotted by A. Watermann, modified by S. Kurch

Cu-Complex synthesis was conducted at the Chemistry Department Bielefeld University (S. Schwarzbich, T. Glaser).

Titrimetric titration experiment were partially conducted by A. Schüll (Bachelor thesis 2017) under supervision of S.K.

A.8 List of Figures

Figure 1.1. Historical timeline of major developments in the field of cancer nanomedicine.	18
Figure 1.2. Endocytose of particles and solutes.	21
Figure 1.3. Effects of protein corona surrounding a nanoparticle.	24
Figure 1.4. Physical characteristics of nanoparticles determine <i>in vivo</i> biocompatibility.	25
Figure 1.5. The nanoparticle–corona complex in a biological environment.	27
Figure 1.6. Vessel density and hypoxic/necrotic areas in developing tumors and the impact of antiangiogenic treatment onto tumor blood vessels.	30
Figure 1.7. Physical characteristics of nanoparticles determine <i>in vivo</i> biocompatibility.	34
Figure 1.8. Ideal versus actual nanoparticle-tumor targeting strategies.	41
Figure 2.1. Important properties of mesoporous silica nanoparticle for drug delivery applications.	48
Figure 2.2. Reaction mechanism of the inverse biphasic stratification process of the DMSN.	49
Figure 2.3. An example for the N ₂ gas adsorption measurement for mesoporous silica nanoparticles.	51
Figure 2.4. Influence of the stirring rate on the particle size and pore diameter of the DMSN.	52
Figure 2.5. Chelation and basicity of the organic base and its influence on the particle size and pore diameter of the DMSN.	53
Figure 2.6. Micelle swelling and CTAC interaction capabilities of the four structure-directing agents.	55
Figure 2.7. Dual surfactant synthesis of CTAC with anthracene-9-carboxylic acid (AC) and 6-hydroxy-napthoic acid (HNA), respectively.	56
Figure 2.8. Dual surfactant synthesis with 2,3-naphthalenedicarboxylic acid (NDCA).	57

Figure 2.9. Dual surfactant synthesis with sodium salicylate (NaSal) at different molar ratio.	58
Figure 2.10. TEM height profile and gas adsorption for the ordered shell like pore structure.	59
Figure 2.11. Model of the multicomponent system.	59
Figure 2.12. Fluorescent dyes and the silica core functionalization strategy.	61
Figure 2.13. Organosilica hybrid nanoparticles for increased intracellular degradation.	63
Figure 2.14. Mesoporous DMSN with magnetic core.	64
Figure 3.1. Transmission electron microscopy of the DMSN.	71
Figure 3.2. Nitrogen physisorption measurement of the mesoporous carrier.	72
Figure 3.3. SAXS data of DMSN-F and DMSN-B.	72
Figure 3.4. Solid-state NMR of the dye labeled DMSN.	73
Figure 3.5. Physicochemical characterization, of DMSN.	74
Figure 3.6. Dynamic light scattering in human plasma.	75
Figure 3.7. Gatekeeper synthesis and physicochemical characterization.	76
Figure 3.8. Interaction of the gatekeeper with DMSN.	78
Figure 3.9. Analysis of the DMSN after surfactant extraction.	79
Figure 3.10. Biodegradation of the DMSN in fetal calf serum.	80
Figure 3.11. Toxicity and Uptake of DMSN.	81
Figure 3.12. Cellular uptake of DMSN.	82
Figure 3.13. Encapsulation of TNF- α in DMSN.	84
Figure 3.14. Impact on cell cycle and cell death of TNF- α -loaded DMSN in 3D melanoma spheroids.	87
Figure 3.15. CLSM data of Cy5-DMSN and CW800-TNF- α over 28 days in transgenic mice.	89

Figure 4.1. Gatekeeper system for encapsulation and transport of a potent Cu ^{II} -based anticancer drug.	93
Figure 4.2. Physicochemical characterization of the carrier system.	95
Figure 4.3. ¹³ C ssNMR of the stepwise functionalization process of the carrier system and ²⁹ Si ssNMR for quantification of the surface coverage.	97
Figure 4.4. Potentiometric titration of the DMSN-A to quantify primary amine groups on the nanoparticle surface.	99
Figure 4.5. Time derivation of the current signal and resulting gauss fit for the potentiometric titration of the covalent functionalized amine groups.	99
Figure 4.6. Quantification of the gate keeper/stalk and drugload/release of CuOAc/Rhodamine B.	101
Figure 4.7. ¹ H NMR shift titration experiment to quantify the strength of the ferrocene-CA/ β -CD inclusion complex.	102
Figure 4.8. ITC measurement for the quantification of binding strength and binding model for the ferrocene-CA/ β -CD inclusion complex.	103
Figure 4.9. Dual color fluorescence cross correlation spectroscopy (dcFCCS) experiment of the interaction of fluorescent labeled β -CD -and DMSN-AF.	104
Figure 4.10. Dynamic light scattering and thermogravimetric analysis of the DMSN before and after gatekeeper attachment.	105
Figure 4.11. Cell viability of HNSCCUM-02T treated with Dox-DMSN over 96h.	106
Figure 4.12. Cell viability of HNSCCUM-02T treated with Cu-DMSN over 96h.	107
Figure 4.13. DNA damage detection of Doxorubicin via γ -H2A.X foci staining.	108
Figure 4.14. DNA damage detection of CuOAc via γ -H2A.X foci staining.	109
Figure A.1. Influence of organic base concentration on the pore size.	116
Figure A.2. Influence of the temperature on the pore size and particle diameter.	117
Figure A.3. Powder x-ray diffraction measurements of DMSN.	128
Figure A.4. Light scattering of the copolymer and apparent diffusion coefficient.	128
Figure A.5. Thermal decomposition of the copolymer.	129

Figure A.6. Pore size distribution of DMSN-B before and after PEI-PEG coating.	129
Figure A.7. TNF- α -loaded DMSN induce DC maturation.	130
Figure A.8. DMSN distribution in 3D Melanoma Spheroids.	131
Figure A.9. Overview of the utilized DMSN with two different pore sizes.	145
Figure A.10. Wide Angle X-Ray Scattering (WAXS) measurements of silica (SiO ₂) (20 minutes exposure time each).	145
Figure A.11. ¹ H NMR spectroscopy of the reaction of ferrocene-CA with APTMS.	146
Figure A.12. Residuals of the non-linear curve fit of the ¹ H NMR titration experiment.	146
Figure A.13. ITC Titration experiment of the interaction of β -CD with DMSN-A.	147
Figure A.14. Biodegradation of the coated DMSN.	148
Figure A.15. ATR-IR spectra of the functionalization process.	149
Figure A.16. Staining of the gatekeeper functionalized DMSN with ammonium molybdate.	150

A.9 List of Tables

Table 3.1. Characterization of the dye-labeled nanocarriers DMSN-R, DMSN-B, and DMSN-F.	54
Table A.1. Characterization of dye-labeled nanocarrier DMSN-F by DLS.	110
Table A.2. Settings of the confocal laser scanning microscope (Leica)	118
Table A.3. Characterization of the dye-labeled nanocarrier DMSN-A and its functionalization steps DMSN-AF and DMSN-AFC.	123

A.10 List of Abbreviations

APTMS	(3-Aminopropyl)trimethoxysilane
ATR-IR	Attenuated total reflection infrared spectroscopy
BET	Brunauer-Emmett-Teller
β -CD	beta-cyclodextrin
BJH	Barrett-Joyner-Halenda
CPMAS	Cross-polarization magic-angle spinning
CTAC	cetyltrimethylammonium chloride
Cy5	cyanine 5
DC	dendritic cells
DDS	drug delivery system
DLS	dynamic light scattering
DMEM	Dulbecco's Modified Eagle Media
DMSN	dendritic mesoporous silica nanoparticle
DPMAS	direct-polarization magic-angle spinning
DSC	differential scanning calorimetry

EC₅₀ half maximal effective concentration

ECM extracellular matrix

ELISA enzyme-linked immunosorbent assay

EMDR environment-mediated drug resistance

EPR enhanced permeability and retention

FCS fluorescence correlation spectroscopy

FDA Food and Drug Administration (USA)

FITC fluorescein-5-isothiocyanate

FUCCI fluorescence ubiquitination cell cycle indicator

GSH glutathione

HMDI hexamethylene di-isocyanate

IFP interstitial fluid pressure

ILP isolated limb perfusion

ITC isothermal titration calorimetry

IUPAC International Union of Pure and Applied Chemistry

MCM mobile crystalline material

MDR multidrug resistance

MPS mononuclear phagocyte system

MRI magneto-resonance imaging

MSN mesoporous silica nanoparticle

MTT 3-(4,5-dimethylthiazol-2-yl)-2,5-diphenyltetrazolium bromide

NIR near infrared

NLDFT non-linear density functional theory

NMR nuclear magnetic resonance

NOD non-obese diabetic

NP nanoparticle

OFDI optical frequency domain imaging
PBS phosphate-buffered saline
PEG polyethylene glycol
PEI polyethylenimine
PET positron emission tomography
Phenyl-SCN phenyl isothiocyanate
QD quantum dot
ROS reactive oxygen species
SAXS small-angle x-ray diffraction
SCID severe combined immunodeficiency
si-RNA small interfering ribonucleic acid
ssNMR solid-state nuclear magnetic resonance spectra
SWNT single-walled carbon nanotube
TAM tumor-associated macrophage
TEM transmission electron microscopy
TEOS tetraethyl orthosilicate
TGA thermogravimetric analysis
TMI tumor microenvironment
TNF- α tumor necrosis factor-alpha
UV ultra-violet
VB valence band
VDW van der Waals
VEGFR vascular epidermal growth factor receptor

6. References

- [1] S. McGuire, *Adv. Nutr.* **2016**, 7, 418.
- [2] I. A. for R. on C. W. C. R. W. Geneva, 2014 Switzerland, **n.d.**
- [3] M. Martínez-Carmona, M. Colilla, M. Vallet-Regí, *Nanomater. (Basel, Switzerland)* **2015**, 5, 1906.
- [4] W. (2014) W. C. R. 2014 Stewart, B. and Wild, C.P. (eds.), International Agency for Research on Cancer, “World Cancer Report 2014,” can be found under <http://www.thehealthwell.info/node/725845>, **n.d.**
- [5] S. FARBER, L. K. DIAMOND, *N. Engl. J. Med.* **1948**, 238, 787.
- [6] D. Peer, J. M. Karp, S. Hong, O. C. Farokhzad, R. Margalit, R. Langer, *Nat. Nanotechnol.* **2007**, 2, 751.
- [7] Y. Barenholz, *J. Control. Release* **2012**, 160, 117.
- [8] C. T. Kresge, M. E. Leonowicz, W. J. Roth, J. C. Vartuli, J. S. Beck, *Nature* **1992**, 359, 710.
- [9] J. S. Beck, J. C. Vartuli, W. J. Roth, M. E. Leonowicz, C. T. Kresge, K. D. Schmitt, C. T. W. Chu, D. H. Olson, E. W. Sheppard, *J. Am. Chem. Soc.* **1992**, 114, 10834.
- [10] M. Vallet-Regí, A. Rámila, R. P. del Real, J. Pérez-Pariente, *Chem. Mater.* **2001**, 13, 308.
- [11] A. Baeza, M. Colilla, M. Vallet-Regí, *Expert Opin. Drug Deliv.* **2015**, 12, 319.
- [12] C. Caltagirone, A. Bettoschi, A. Garau, R. Montis, *Chem. Soc. Rev.* **2014**, 44, 4645.
- [13] X. Du, X. Li, L. Xiong, X. Zhang, F. Kleitz, S. Z. Qiao, *Biomaterials* **2016**, 91, 90.
- [14] H. Mekaru, J. Lu, F. Tamanoi, *Adv. Drug Deliv. Rev.* **2015**, 95, 40.
- [15] A. Nouredine, L. Lichon, M. Maynadier, M. Garcia, M. Gary-Bobo, J. I. Zink, M. Wong Chi Man, X. Cattoën, *Nanoscale* **2015**, 7, 11444.
- [16] M. Xie, H. Shi, K. Ma, H. Shen, B. Li, S. Shen, X. Wang, Y. Jin, *J. Colloid Interface Sci.* **2013**, 395, 306.
- [17] E. Soto-Cantu, R. Cueto, J. Koch, P. S. Russo, *Langmuir* **2012**, 28, 5562.
- [18] B. Malvi, B. R. Sarkar, D. Pati, R. Mathew, T. G. Ajithkumar, S. Sen Gupta, *J. Mater. Chem.* **2009**, 19, 1409.
- [19] C.-L. Chang, H. S. Fogler, *AIChE J.* **1996**, 42, 3153.
- [20] C.-L. Chang, H. S. Fogler, *Langmuir* **1997**, 13, 3295.
- [21] K. Osseo-Asare, F. J. Arriagada, *Colloids and Surfaces* **1990**, 50, 321.
- [22] W. Stöber, A. Fink, E. Bohn, *J. Colloid Interface Sci.* **1968**, 26, 62.
- [23] M. Yanagi, Y. Asano, K. Kandori, K. Kon-on, *Chem. Soc. Japan* **1986**, Abs. 39th, 396.
- [24] H. Yamauchi, T. Ishikawa, S. Kondo, *Colloids and Surfaces* **1989**, 37, 71.
- [25] X. Du, J. He, *Langmuir* **2010**, 26, 10057.

- [26] D. Shen, L. Chen, J. Yang, R. Zhang, Y. Wei, X. Li, W. Li, Z. Sun, H. Zhu, A. M. Abdullah, et al., *ACS Appl. Mater. Interfaces* **2015**, *7*, 17450.
- [27] J. Wang, Y. Wang, Q. Liu, L. Yang, R. Zhu, C. Yu, S. Wang, *ACS Appl. Mater. Interfaces* **2016**, *8*, 26511.
- [28] C. Xu, M. Yu, O. Noonan, J. Zhang, H. Song, H. Zhang, C. Lei, Y. Niu, X. Huang, Y. Yang, et al., *Small* **2015**, *25*, 5949.
- [29] H. Yamada, H. Ujiie, C. Urata, E. Yamamoto, Y. Yamauchi, K. Kuroda, *Nanoscale* **2015**, *7*, 19557.
- [30] J. Yang, W. Chen, D. Shen, Y. Wei, X. Ran, W. Teng, J. Fan, W. Zhang, D. Zhao, *J. Mater. Chem. A* **2014**, *2*, 11045.
- [31] Y. Yang, Y. Niu, J. Zhang, A. K. Meka, H. Zhang, C. Xu, C. X. C. Lin, M. Yu, C. Yu, *Small* **2015**, *11*, 2743.
- [32] W. H. Fu, Y. Guan, Y. M. Wang, M.-Y. He, *Microporous Mesoporous Mater.* **2016**, *220*, 168.
- [33] L. Dai, Q. Zhang, H. Gu, K. Cai, *J. Mater. Chem. B* **2015**, *3*, 8303.
- [34] J. Liu, S. Z. Qiao, S. Budi Hartono, G. Q. M. Lu, *Angew. Chem. Int. Ed. Engl.* **2010**, *49*, 4981.
- [35] T. S. Atabaev, J. H. Lee, J. J. Lee, D.-W. Han, Y.-H. Hwang, H.-K. Kim, N. H. Hong, *Nanotechnology* **2013**, *24*, 345603/1.
- [36] S. Gai, P. Yang, P. Ma, D. Wang, C. Li, X. Li, N. Niu, J. Lin, *J. Mater. Chem.* **2011**, *21*, 16420.
- [37] J. Pang, G. Zhou, R. Liu, T. Li, *Mater. Sci. Eng. C* **2016**, *59*, 35.
- [38] A. K. Meka, Y. Niu, S. Karmakar, S. B. Hartono, J. Zhang, C. X. C. Lin, H. Zhang, A. Whittaker, K. Jack, M. Yu, et al., *ChemNanoMat* **2016**, *2*, 220.
- [39] J. Croissant, X. Cattoën, M. W. C. Man, A. Gallud, L. Raehm, P. Trens, M. Maynadier, J.-O. Durand, *Adv. Mater.* **2014**, *26*, 6174.
- [40] J. G. Croissant, Y. Fatieiev, H. Omar, D. H. Anjum, A. Gurinov, J. Lu, F. Tamanoi, J. I. Zink, N. M. Khashab, *Chemistry (Easton)*. **2016**, *22*, 9607.
- [41] J. G. Croissant, S. Picard, D. Aggad, M. Klausen, C. Mauriello Jimenez, M. Maynadier, O. Mongin, G. Clermont, E. Genin, X. Cattoën, et al., *J. Mater. Chem. B* **2016**, *4*, 5567.
- [42] N. Lu, Y. Tian, W. Tian, P. Huang, Y. Liu, Y. Tang, C. Wang, S. Wang, Y. Su, Y. Zhang, et al., *ACS Appl. Mater. Interfaces* **2016**, *8*, 2985.
- [43] Y. Lee, D. H. Thompson, *Wiley Interdiscip. Rev. Nanomed. Nanobiotechnol.* **2017**, *e1450*, 1.
- [44] V. P. Torchilin, *Nat. Rev. Drug Discov.* **2005**, *4*, 145.
- [45] T. S. Zimmermann, A. C. H. Lee, A. Akinc, B. Bramlage, D. Bumcrot, M. N. Fedoruk, J. Harborth, J. A. Heyes, L. B. Jeffs, M. John, et al., *Nature* **2006**, *441*, 111.
- [46] J. Shi, P. W. Kantoff, R. Wooster, O. C. Farokhzad, *Nat. Rev. Cancer* **2017**, *17*, 20.
- [47] A. Burns, H. Ow, U. Wiesner, *Chem. Soc. Rev.* **2006**, *35*, 1028.
- [48] F. Hoffmann, M. Cornelius, J. Morell, M. Fröba, *Angew. Chem. Int. Ed. Engl.* **2006**, *45*, 3216.

- [49] R. G. Chaudhuri, S. Paria, *Chem. Rev.* **2012**, *112*, 2373.
- [50] D. Knopp, D. Tang, R. Niessner, *Anal. Chim. Acta* **2009**, *647*, 14.
- [51] C. Graf, D. L. J. Vossen, A. Imhof, A. van Blaaderen, *Langmuir* **2003**, *19*, 6693.
- [52] N. Jana, C. Earhart, J. Ying, *Chem. Mater.* **2007**, *5*, 5074.
- [53] F. Di Renzo, F. Testa, J. Chen, H. Cambon, A. Galarneau, D. Plee, F. Fajula, *Microporous Mesoporous Mater.* **1999**, *28*, 437.
- [54] C. Brinker, W. Scherer, *The Physics and Chemistry of Sol-Gel Processing*, Academic Press, San Diego, **1990**.
- [55] S.-H. Wu, C.-Y. Mou, H.-P. Lin, *Chem. Soc. Rev.* **2013**, *42*, 3862.
- [56] R. Hong, N. Fischer, *Chem. Mater.* **2005**, 4617.
- [57] B. P. Lee, J. L. Dalsin, P. B. Messersmith, *Biomacromolecules* **2002**, *3*, 1038.
- [58] A. Thomas, H. Bauer, A. M. Schilman, K. Fischer, W. Tremel, H. Frey, *Macromolecules* **2014**, *47*, 4557.
- [59] V. S. Wilms, H. Bauer, C. Tonhauser, A. M. Schilman, M. C. Müller, W. Tremel, H. Frey, *Biomacromolecules* **2013**, *14*, 193.
- [60] C. C. Berry, S. Wells, S. Charles, A. S. G. Curtis, *Biomaterials* **2003**, *24*, 4551.
- [61] M. Ballauff, Y. Lu, *Polymer (Guildf)*. **2007**, *48*, 1815.
- [62] J. Qin, S. Laurent, Y. S. Jo, A. Roch, M. Mikhaylova, Z. M. Bhujwala, R. N. Müller, M. Muhammed, *Adv. Mater.* **2007**, *19*, 1874.
- [63] R. De Palma, S. Peeters, M. J. Van Bael, H. Van den Rul, K. Bonroy, W. Laureyn, J. Mullens, G. Borghs, G. Maes, *Chem. Mater.* **2007**, *19*, 1821.
- [64] T. Sun, Y. S. Zhang, B. Pang, D. C. Hyun, M. Yang, Y. Xia, *Angew. Chem. Int. Ed. Engl.* **2014**, *53*, 12320.
- [65] M. Bruchez Jr., M. Moronne, P. Gin, S. Weiss, A. P. Alivisatos, *Science (80-.)*. **1998**, *281*, 2013.
- [66] W. C. W. Chan, S. Nie, *Science (80-.)*. **1998**, *281*, 2016.
- [67] X. Michalet, F. F. Pinaud, L. A. Bentolila, J. M. Tsay, S. Doose, J. J. Li, G. Sundaresan, A. M. Wu, S. S. Gambhir, S. Weiss, *Science (80-.)*. **2008**, *538*, 538.
- [68] H. S. Choi, W. Liu, P. Misra, E. Tanaka, J. P. Zimmer, B. Itty Ipe, M. G. Bawendi, J. V. Frangioni, *Nat. Biotechnol.* **2007**, *25*, 1165.
- [69] J. Liu, M. Yu, C. Zhou, J. Zheng, *Mater. Today* **2013**, *16*, 477.
- [70] E. B. Ehlerding, F. Chen, W. Cai, *Adv. Sci.* **2016**, *3*, 1500223/1.
- [71] A. Nel, T. Xia, L. Mädler, N. Li, *Science* **2006**, *311*, 622.
- [72] N. Bertrand, J.-C. Leroux, *J. Control. Release* **2012**, *161*, 152.
- [73] K. M. Tsoi, S. A. MacParland, X.-Z. Ma, V. N. Spetzler, J. Echeverri, B. Ouyang, S. M. Fadel, E. A. Sykes, N. Goldaracena, J. M. Kathas, et al., *Nat. Mater.* **2016**, *15*, 1212.
- [74] D. E. Owens, N. A. Peppas, *Int. J. Pharm.* **2006**, *307*, 93.
- [75] R. Gref, Y. Minamitake, M. T. Peracchia, V. Trubetskoy, V. Torchilin, R. Langer, *Science* **1994**, *263*, 1600.

- [76] K. Knop, R. Hoogenboom, D. Fischer, U. S. Schubert, *Angew. Chemie - Int. Ed.* **2010**, *49*, 6288.
- [77] N. J. Butcher, G. M. Mortimer, R. F. Minchin, *Nat. Nanotechnol.* **2016**, *11*, 310.
- [78] S. Schöttler, G. Becker, S. Winzen, T. Steinbach, K. Mohr, K. Landfester, V. Mailänder, F. R. Wurm, *Nat. Nanotechnol.* **2016**, *11*, 372.
- [79] R. Kumar, I. Roy, T. Y. Ohulchanskyy, L. N. Goswami, A. C. Bonoiu, E. J. Bergey, K. M. Tramposch, A. Maitra, P. N. Prasad, *ACS Nano* **2008**, *2*, 449.
- [80] V. Cauda, C. Argyo, T. Bein, *J. Mater. Chem.* **2010**, *20*, 8693.
- [81] V. Cauda, A. Schlossbauer, T. Bein, *Microporous Mesoporous Mater.* **2010**, *132*, 60.
- [82] C.-M. J. Hu, L. Zhang, S. Aryal, C. Cheung, R. H. Fang, L. Zhang, *Proc. Natl. Acad. Sci. U. S. A.* **2011**, *108*, 10980.
- [83] A. Parodi, N. Quattrocchi, A. L. van de Ven, C. Chiappini, M. Evangelopoulos, J. O. Martinez, B. S. Brown, S. Z. Khaled, I. K. Yazdi, M. V. Enzo, et al., *Nat. Nanotechnol.* **2013**, *8*, 61.
- [84] C.-M. J. Hu, R. H. Fang, K.-C. Wang, B. T. Luk, S. Thamphiwatana, D. Dehaini, P. Nguyen, P. Angsantikul, C. H. Wen, A. V Kroll, et al., *Nature* **2015**, *526*, 118.
- [85] P. L. Rodriguez, T. Harada, D. A. Christian, D. A. Pantano, R. K. Tsai, D. E. Discher, *Science* **2013**, *339*, 971.
- [86] G. J. Doherty, H. T. McMahon, *Annu. Rev. Biochem.* **2009**, *78*, 857.
- [87] G. Sahay, D. Y. Alakhova, A. V Kabanov, *J. Control. Release* **2010**, *145*, 182.
- [88] S. Zhang, H. Gao, G. Bao, *ACS Nano* **2015**, *9*, 8655.
- [89] H. Yuan, S. Zhang, *Appl. Phys. Lett.* **2010**, *96*, 33704/1.
- [90] B. D. Chithrani, W. C. W. Chan, *Nano Lett.* **2007**, *7*, 1542.
- [91] C. Tekle, B. van Deurs, K. Sandvig, T.-G. Iversen, *Nano Lett.* **2008**, *8*, 1858.
- [92] L. W. Zhang, N. A. Monteiro-Riviere, *Toxicol. Sci.* **2009**, *110*, 138.
- [93] I. Slowing, B. G. Trewyn, V. S.-Y. Lin, *J. Am. Chem. Soc.* **2006**, *128*, 14792.
- [94] E. T. Ahrens, M. Feili-Hariri, H. Xu, G. Genove, P. A. Morel, *Magn. Reson. Med.* **2003**, *49*, 1006.
- [95] A. Jordan, R. Scholz, P. Wust, H. Schirra, T. Schiestel, H. Schmidt, R. Felix, *J. Magn. Mater.* **1999**, *194*, 185.
- [96] I.-L. Hsiao, Y.-K. Hsieh, C.-Y. Chuang, C.-F. Wang, Y.-J. Huang, *Environ. Toxicol.* **2017**, DOI 10.1002/tox.22397.
- [97] A. E. Nel, L. Mädler, D. Velegol, T. Xia, E. M. V Hoek, P. Somasundaran, F. Klaessig, V. Castranova, M. Thompson, *Nat. Mater.* **2009**, *8*, 543.
- [98] Y. Min, M. Akbulut, K. Kristiansen, Y. Golan, J. Israelachvili, *Nat. Mater.* **2008**, *7*, 527.
- [99] G. Oberdörster, A. Maynard, K. Donaldson, V. Castranova, J. Fitzpatrick, K. Ausman, J. Carter, B. Karn, W. Kreyling, D. Lai, et al., *Part. Fibre Toxicol.* **2005**, *2*, 8/1.
- [100] A. A. Vertegel, R. W. Siegel, J. S. Dordick, *Langmuir* **2004**, *20*, 6800.

- [101] M. Zhu, G. Nie, H. Meng, T. Xia, A. Nel, Y. Zhao, *Acc. Chem. Res.* **2013**, *46*, 622.
- [102] L. Bergman, J. Rosenholm, A.-B. Öst, A. Duchanoy, P. Kankaanpää, J. Heino, M. Lindén, *J. Nanomater.* **2008**, *2008*, 1.
- [103] J. M. Rosenholm, C. Sahlgren, M. Lindén, *Nanoscale* **2010**, *2*, 1870.
- [104] B. D. Chithrani, A. A. Ghazani, W. C. W. Chan, *Nano Lett.* **2006**, *6*, 662.
- [105] L. J. Mortensen, G. Oberdörster, A. P. Pentland, L. A. Delouise, *Nano Lett.* **2008**, *8*, 2779.
- [106] H. Cabral, Y. Matsumoto, K. Mizuno, Q. Chen, M. Murakami, M. Kimura, Y. Terada, M. R. Kano, K. Miyazono, M. Uesaka, et al., *Nat. Nanotechnol.* **2011**, *6*, 815.
- [107] V. P. Chauhan, Z. Popović, O. Chen, J. Cui, D. Fukumura, M. G. Bawendi, R. K. Jain, *Angew. Chem. Int. Ed. Engl.* **2011**, *50*, 11417.
- [108] P. Kolhar, A. C. Anselmo, V. Gupta, K. Pant, B. Prabhakarandian, E. Ruoslahti, S. Mitragotri, *Proc. Natl. Acad. Sci. U. S. A.* **2013**, *110*, 10753.
- [109] B. R. Smith, P. Kempen, D. Bouley, A. Xu, Z. Liu, N. Melosh, H. Dai, R. Sinclair, S. S. Gambhir, *Nano Lett.* **2012**, *12*, 3369.
- [110] E. Tasciotti, X. Liu, R. Bhavane, K. Plant, A. D. Leonard, B. K. Price, M. M.-C. Cheng, P. Decuzzi, J. M. Tour, F. Robertson, et al., *Nat. Nanotechnol.* **2008**, *3*, 151.
- [111] H.-J. Li, J.-Z. Du, X.-J. Du, C.-F. Xu, C.-Y. Sun, H.-X. Wang, Z.-T. Cao, X.-Z. Yang, Y.-H. Zhu, S. Nie, et al., *Proc. Natl. Acad. Sci. U. S. A.* **2016**, *113*, 4164.
- [112] R. Xu, G. Zhang, J. Mai, X. Deng, V. Segura-Ibarra, S. Wu, J. Shen, H. Liu, Z. Hu, L. Chen, et al., *Nat. Biotechnol.* **2016**, *34*, 414.
- [113] S. E. McNeil, *Wiley Interdiscip. Rev. Nanomed. Nanobiotechnol.* **2009**, *1*, 264.
- [114] V. P. Chauhan, R. K. Jain, *Nat. Mater.* **2013**, *12*, 958.
- [115] M. Mahmoudi, I. Lynch, M. R. Ejtehadi, M. P. Monopoli, F. B. Bombelli, S. Laurent, *Chem. Rev.* **2011**, *111*, 5610.
- [116] A. M. Clemments, P. Botella, C. C. Landry, *ACS Appl. Mater. Interfaces* **2015**, *7*, 21682.
- [117] C. D. Walkey, J. B. Olsen, H. Guo, A. Emili, W. C. W. Chan, *J. Am. Chem. Soc.* **2012**, *134*, 2139.
- [118] M. P. Monopoli, C. Aberg, A. Salvati, K. A. Dawson, *Nat. Nanotechnol.* **2012**, *7*, 779.
- [119] S. Rana, Y.-C. Yeh, V. M. Rotello, *Curr. Opin. Chem. Biol.* **2010**, *14*, 828.
- [120] J. Wolfram, Y. Yang, J. Shen, A. Moten, C. Chen, H. Shen, M. Ferrari, Y. Zhao, *Colloids Surf. B. Biointerfaces* **2014**, *124*, 17.
- [121] K. Ogawara, K. Furumoto, S. Nagayama, K. Minato, K. Higaki, T. Kai, T. Kimura, *J. Control. Release* **2004**, *100*, 451.
- [122] S. Ritz, S. Schöttler, N. Kotman, G. Baier, A. Musyanovych, J. Kuharev, K. Landfester, H. Schild, O. Jahn, S. Tenzer, et al., *Biomacromolecules* **2015**, *16*, 1311.
- [123] M. J. Hajipour, S. Laurent, A. Aghaie, F. Rezaee, M. Mahmoudi, *Biomater. Sci.* **2014**, *2*, 1210.
- [124] E. Casals, T. Pfaller, A. Duschl, G. J. Oostingh, V. F. Puentes, *Small* **2011**, *7*, 3479.

- [125] D. F. Moyano, K. Saha, G. Prakash, B. Yan, H. Kong, M. Yazdani, V. M. Rotello, *ACS Nano* **2014**, *8*, 6748.
- [126] A. Salvati, A. S. Pitek, M. P. Monopoli, K. Prapainop, F. B. Bombelli, D. R. Hristov, P. M. Kelly, C. Åberg, E. Mahon, K. A. Dawson, *Nat. Nanotechnol.* **2013**, *8*, 137.
- [127] T. Cedervall, I. Lynch, S. Lindman, T. Berggård, E. Thulin, H. Nilsson, K. A. Dawson, S. Linse, *Proc. Natl. Acad. Sci. U. S. A.* **2007**, *104*, 2050.
- [128] S. Tenzer, D. Docter, J. J. J. Kuharev, A. Musyanovych, V. Fetz, R. Hecht, F. Schlenk, D. Fischer, K. Kiouptsi, C. Reinhardt, et al., *Nat Nano* **2013**, *8*, 772.
- [129] C. D. Walkey, J. B. Olsen, F. Song, R. Liu, H. Guo, D. W. H. Olsen, Y. Cohen, A. Emili, W. C. W. Chan, *ACS Nano* **2014**, *8*, 2439.
- [130] S. Winzen, S. Schoettler, G. Baier, C. Rosenauer, V. Mailaender, K. Landfester, K. Mohr, *Nanoscale* **2015**, *7*, 2992.
- [131] U. Sakulku, L. Maurizi, M. Mahmoudi, M. Motazacker, M. Vries, A. Gramoun, M.-G. Ollivier Beuzelin, J.-P. Vallée, F. Rezaee, H. Hofmann, *Nanoscale* **2014**, *6*, 11439.
- [132] B. S. Kuszyk, F. M. Corl, F. N. Franano, D. A. Bluemke, L. V Hofmann, B. J. Fortman, E. K. Fishman, *AJR. Am. J. Roentgenol.* **2001**, *177*, 747.
- [133] W. C. Aird, *Circ. Res.* **2007**, *100*, 158.
- [134] B. Hobson, J. Denekamp, *Br. J. Cancer* **1984**, *49*, 405.
- [135] T. P. Padera, B. R. Stoll, J. B. Tooredman, D. Capen, E. Di Tomaso, R. K. Jain, *Nature* **2004**, *427*, 695.
- [136] P. S. Ward, C. B. Thompson, *Cancer Cell* **2012**, *21*, 297.
- [137] H. K. Awwad, M. El Aggar, N. Mocktar, M. Barsoum, *Int. J. Radiat. Oncol.* **1986**, *12*, 1329.
- [138] Y. Yoshii, K. Sugiyama, *Cancer Res.* **1988**, *48*, 2938.
- [139] P. L. Olive, C. Vikse, M. J. Trotter, *Int. J. Radiat. Oncol.* **1992**, *22*, 397.
- [140] C. M. West, R. A. Cooper, J. A. Loncaster, D. P. Wilks, M. Bromley, *Cancer Res.* **2001**, *61*, 2907.
- [141] C. J. Eskey, A. P. Koretsky, M. M. Domach, R. K. Jain, *Proc. Natl. Acad. Sci. U. S. A.* **1993**, *90*, 2646.
- [142] A. Facciabene, X. Peng, I. S. Hagemann, K. Balint, A. Barchetti, L.-P. Wang, P. A. Gimotty, C. B. Gilks, P. Lal, L. Zhang, et al., *Nature* **2011**, *475*, 226.
- [143] S. V Karakashev, M. J. Reginato, *Cancer Manag. Res.* **2015**, *7*, 253.
- [144] B. Keith, R. S. Johnson, M. C. Simon, *Nat. Rev. Cancer* **2011**, *12*, 9.
- [145] R. K. Jain, *J. Clin. Oncol.* **2013**, *31*, 2205.
- [146] B. J. Vakoc, R. M. Lanning, J. A. Tyrrell, T. P. Padera, L. A. Bartlett, T. Stylianopoulos, L. L. Munn, G. J. Tearney, D. Fukumura, R. K. Jain, et al., *Nat. Med.* **2009**, *15*, 1219.
- [147] Y. Boucher, J. M. Kirkwood, D. Opacic, M. Desantis, R. K. Jain, *Cancer Res.* **1991**, *51*, 6691.
- [148] P. P. Adiseshiaiah, J. B. Hall, S. E. McNeil, *Wiley Interdiscip. Rev. Nanomedicine Nanobiotechnology* **2010**, *2*, 99.

- [149] R. K. Jain, L. T. Baxter, *Cancer Res.* **1988**, *48*, 7022.
- [150] Y. Boucher, L. T. Baxter, R. K. Jain, *Cancer Res.* **1990**, *50*, 4478.
- [151] M. Stohrer, Y. Boucher, M. Stangassinger, R. K. Jain, *Cancer Res.* **2000**, *60*, 4251.
- [152] S. Ramanujan, A. Pluen, T. D. McKee, E. B. Brown, Y. Boucher, R. K. Jain, *Biophys. J.* **2002**, *83*, 1650.
- [153] P. A. Netti, D. A. Berk, M. A. Swartz, A. J. Grodzinsky, R. K. Jain, *Cancer Res.* **2000**, *60*, 2497.
- [154] T. Stylianopoulos, M.-Z. Poh, N. Insin, M. G. Bawendi, D. Fukumura, L. L. Munn, R. K. Jain, *Biophys. J.* **2010**, *99*, 1342.
- [155] T. P. Szatrowski, C. F. Nathan, *Cancer Res.* **1991**, *51*, 794.
- [156] P. P. Fu, Q. Xia, H.-M. Hwang, P. C. Ray, H. Yu, *Nanomater. - Toxicol. Med. Appl.* **2014**, *22*, 64.
- [157] P. Storz, *Front. Biosci.* **2005**, *10*, 1881.
- [158] D. Trachootham, J. Alexandre, P. Huang, *Nat. Rev. Drug Discov.* **2009**, *8*, 579.
- [159] G.-Y. Liou, P. Storz, *Free Radic. Res.* **2010**, *44*, 479.
- [160] D. Magda, R. A. Miller, *Semin. Cancer Biol.* **2006**, *16*, 466.
- [161] C. E. Myers, W. P. McGuire, R. H. Liss, I. Ifrim, K. Grotzinger, R. C. Young, *Science* **1977**, *197*, 165.
- [162] G. T. Wondrak, *Free Radic. Biol. Med.* **2007**, *43*, 178.
- [163] T. Dragovich, M. Gordon, D. Mendelson, L. Wong, M. Modiano, H.-H. S. Chow, B. Samulitis, S. O'Day, K. Grenier, E. Hersh, et al., *J. Clin. Oncol.* **2007**, *25*, 1779.
- [164] J. C. Juarez, M. Manuia, M. E. Burnett, O. Betancourt, B. Boivin, D. E. Shaw, N. K. Tonks, A. P. Mazar, F. Doñate, *Proc. Natl. Acad. Sci. U. S. A.* **2008**, *105*, 7147.
- [165] K. Matsumoto, T. Yamamoto, R. Kamata, H. Maeda, *Adv. Exp. Med. Biol.* **1986**, *198*, 71.
- [166] Y. Matsumura, H. Maeda, *Cancer Res.* **1986**, *46*, 6387.
- [167] L. E. Gerlowski, R. K. Jain, *Microvasc. Res.* **1986**, *31*, 288.
- [168] C. V Pecot, G. A. Calin, R. L. Coleman, G. Lopez-Berestein, A. K. Sood, *Nat. Rev. Cancer* **2011**, *11*, 59.
- [169] R. de la Rica, D. Aili, M. M. Stevens, *Adv. Drug Deliv. Rev.* **2012**, *64*, 967.
- [170] C. M. Dawidczyk, C. Kim, J. H. Park, L. M. Russell, K. H. Lee, M. G. Pomper, P. C. Searson, *J. Control. Release* **2014**, *187*, 133.
- [171] J. Folkman, *JNCI J. Natl. Cancer Inst.* **1990**, *82*, 4.
- [172] Y. Matsumoto, J. W. Nichols, K. Toh, T. Nomoto, H. Cabral, Y. Miura, R. J. Christie, N. Yamada, T. Ogura, M. R. Kano, et al., *Nat. Nanotechnol.* **2016**, *11*, 533.
- [173] H. Maeda, K. Tsukigawa, J. Fang, *Microcirculation* **2016**, *23*, 173.
- [174] K. J. Harrington, S. Mohammadtaghi, P. S. Uster, D. Glass, A. M. Peters, R. G. Vile, J. S. Stewart, *Clin. Cancer Res.* **2001**, *7*, 243.
- [175] M. I. Koukourakis, S. Koukouraki, A. Giatromanolaki, S. C. Archimandritis, J.

- Skarlatos, K. Beroukas, J. G. Bizakis, G. Retalis, N. Karkavitsas, E. S. Helidonis, *J. Clin. Oncol.* **1999**, *17*, 3512.
- [176] S. Eliasof, D. Lazarus, C. G. Peters, R. I. Case, R. O. Cole, J. Hwang, T. Schluep, J. Chao, J. Lin, Y. Yen, et al., *Proc. Natl. Acad. Sci. U. S. A.* **2013**, *110*, 15127.
- [177] G. J. Weiss, J. Chao, J. D. Neidhart, R. K. Ramanathan, D. Bassett, J. A. Neidhart, C. H. J. Choi, W. Chow, V. Chung, S. J. Forman, et al., *Invest. New Drugs* **2013**, *31*, 986.
- [178] A. J. Clark, D. T. Wiley, J. E. Zuckerman, P. Webster, J. Chao, J. Lin, Y. Yen, M. E. Davis, *Proc. Natl. Acad. Sci. U. S. A.* **2016**, *113*, 3850.
- [179] D. Brevet, M. Gary-Bobo, L. Raehm, S. Richeter, O. Hocine, K. Amro, B. Loock, P. Couleaud, C. Frochot, A. Morère, et al., *Chem. Commun. (Camb)*. **2009**, 1475.
- [180] V. Mamaeva, J. M. Rosenholm, L. T. Bate-Eya, L. Bergman, E. Peuhu, A. Duchanoy, L. E. Fortelius, S. Landor, D. M. Toivola, M. Lindén, et al., *Mol. Ther.* **2011**, *19*, 1538.
- [181] J. Sun, D.-H. Kim, Y. Guo, Z. Teng, Y. Li, L. Zheng, Z. Zhang, A. C. Larson, G. Lu, *J. Mater. Chem. B* **2015**, *3*, 1049.
- [182] Z.-Y. Li, J.-J. Hu, Q. Xu, S. Chen, H.-Z. Jia, Y.-X. Sun, R.-X. Zhuo, X.-Z. Zhang, *J. Mater. Chem. B* **2015**, *3*, 39.
- [183] Z. Deng, Z. Zhen, X. Hu, S. Wu, Z. Xu, P. K. Chu, *Biomaterials* **2011**, *32*, 4976.
- [184] L. Pan, Q. He, J. Liu, Y. Chen, M. Ma, L. Zhang, J. Shi, *J. Am. Chem. Soc.* **2012**, *134*, 5722.
- [185] S. A. Mackowiak, A. Schmidt, V. Weiss, C. Argyo, C. Schirnding, T. Bein, C. Bräuchle, *Nano Lett.* **2013**, *13*, 2576.
- [186] L. Gao, Y. Cui, Q. He, Y. Yang, J. Fei, J. Li, *Chemistry* **2011**, *17*, 13170.
- [187] C.-L. Zhu, X.-Y. Song, W.-H. Zhou, H.-H. Yang, Y.-H. Wen, X.-R. Wang, *J. Mater. Chem.* **2009**, *19*, 7765.
- [188] B. Borisch, I. Semac, A. Soltermann, C. Palomba, D. C. Hoessli, *Verh. Dtsch. Ges. Pathol.* **2001**, *85*, 161.
- [189] J. Baselga, *Oncology* **2001**, *61 Suppl 2*, 14.
- [190] N. Ferrara, K. J. Hillan, W. Novotny, *Biochem. Biophys. Res. Commun.* **2005**, *333*, 328.
- [191] L. D. Leserman, J. Barbet, F. Kourilsky, J. N. Weinstein, *Nature* **1980**, *288*, 602.
- [192] J. C. Reubi, *Endocr. Rev.* **2003**, *24*, 389.
- [193] D. E. Lopes de Menezes, L. M. Pilarski, T. M. Allen, *Cancer Res.* **1998**, *58*, 3320.
- [194] J. Folkman, *N. Engl. J. Med.* **1971**, *285*, 1182.
- [195] Z. Cheng, A. Al Zaki, J. Z. Hui, V. R. Muzykantov, A. Tsourkas, *Science* **2012**, *338*, 903.
- [196] T. M. Allen, *Nat. Rev. Cancer* **2002**, *2*, 750.
- [197] E. A. Sykes, J. Chen, G. Zheng, W. C. W. Chan, *ACS Nano* **2014**, *8*, 5696.
- [198] S. Hong, P. R. Leroueil, I. J. Majoros, B. G. Orr, J. R. Baker, M. M. Banaszak Holl, *Chem. Biol.* **2007**, *14*, 107.
- [199] A. M. Scott, J. P. Allison, J. D. Wolchok, *Cancer Immun.* **2012**, *12*, 14/1.

- [200] D. B. Kirpotin, D. C. Drummond, Y. Shao, M. R. Shalaby, K. Hong, U. B. Nielsen, J. D. Marks, C. C. Benz, J. W. Park, *Cancer Res.* **2006**, *66*, 6732.
- [201] F. Danhier, O. Feron, V. Préat, *J. Control. Release* **2010**, *148*, 135.
- [202] J. A. Joyce, *Cancer Cell* **2005**, *7*, 513.
- [203] D. F. Quail, J. A. Joyce, *Nat. Med.* **2013**, *19*, 1423.
- [204] M. M. Mueller, N. E. Fusenig, *Nat. Rev. Cancer* **2004**, *4*, 839.
- [205] D. Neri, R. Bicknell, *Nat. Rev. Cancer* **2005**, *5*, 436.
- [206] R. K. Jain, T. Stylianopoulos, *Nat. Rev. Clin. Oncol.* **2010**, *7*, 653.
- [207] T. J. Anchordoquy, Y. Barenholz, D. Boraschi, M. Chorny, P. Decuzzi, M. A. Dobrovolskaia, Z. S. Farhangrazi, D. Farrell, A. Gabizon, H. Ghandehari, et al., *ACS Nano* **2017**, *11*, 12.
- [208] R. K. Jain, *Science* **2005**, *307*, 58.
- [209] M. Kato, Y. Hattori, M. Kubo, Y. Maitani, *Int. J. Pharm.* **2012**, *423*, 428.
- [210] J. D. Byrne, T. Betancourt, L. Brannon-Peppas, *Adv. Drug Deliv. Rev.* **2008**, *60*, 1615.
- [211] E. A. Murphy, B. K. Majeti, L. A. Barnes, M. Makale, S. M. Weis, K. Lutu-Fuga, W. Wrasidlo, D. A. Cheresch, *Proc. Natl. Acad. Sci. U. S. A.* **2008**, *105*, 9343.
- [212] C. G. Willett, Y. Boucher, E. Di Tomaso, D. G. Duda, L. L. Munn, R. T. Tong, D. C. Chung, D. V Sahani, S. P. Kalva, S. V Kozin, et al., *Nat. Med.* **2004**, *10*, 145.
- [213] V. P. Chauhan, T. Stylianopoulos, J. D. Martin, Z. Popović, O. Chen, W. S. Kamoun, M. G. Bawendi, D. Fukumura, R. K. Jain, *Nat. Nanotechnol.* **2012**, *7*, 383.
- [214] M. E. Davis, J. E. Zuckerman, C. H. J. Choi, D. Seligson, A. Tolcher, C. A. Alabi, Y. Yen, J. D. Heidel, A. Ribas, *Nature* **2010**, *464*, 1067.
- [215] C. A. Smith, T. Farrah, R. G. Goodwin, *Cell* **1994**, *76*, 959.
- [216] R. van Horssen, T. L. M. Ten Hagen, A. M. M. Eggermont, *Oncologist* **2006**, *11*, 397.
- [217] H. J. Hoekstra, R. J. van Ginkel, *Curr. Opin. Oncol.* **2003**, *15*, 300.
- [218] A. Kienzle, S. Kurch, J. Schlöder, C. Berges, R. Ose, J. Schupp, A. Tuettenberg, H. Weiss, J. Schultze, S. Winzen, et al., *Adv. Healthc. Mater.* **2017**, *6*, DOI 10.1002/adhm.201700012.
- [219] C.-Y. Lai, B. G. Trewyn, D. M. Jęftinija, K. Jęftinija, S. Xu, S. Jęftinija, V. S.-Y. Lin, *J. Am. Chem. Soc.* **2003**, *125*, 4451.
- [220] O. Warburg, *J. Cancer Res.* **1925**, *9*, 148.
- [221] G. Helmlinger, A. Sckell, M. Dellian, N. S. Forbes, R. K. Jain, *Clin. Cancer Res.* **2002**, *8*, 1284.
- [222] M. Stubbs, P. M. J. McSheehy, J. R. Griffiths, C. L. Bashford, *Mol. Med. Today* **2000**, *6*, 15.
- [223] S. Ohkuma, B. Poole, *Proc. Natl. Acad. Sci.* **1978**, *75*, 3327.
- [224] R. Casasús, M. D. Marcos, R. Martínez-Máñez, J. V Ros-Lis, J. Soto, L. A. Villaescusa, P. Amorós, D. Beltrán, C. Guillem, J. Latorre, *J. Am. Chem. Soc.* **2004**, *126*, 8612.

- [225] S. Heidegger, D. Gößl, A. Schmidt, S. Niedermayer, C. Argyo, S. Endres, T. Bein, C. Bourquin, *Nanoscale* **2015**, *8*, 938.
- [226] S. Niedermayer, V. Weiss, A. Herrmann, A. Schmidt, S. Datz, K. Müller, E. Wagner, T. Bein, C. Bräuchle, *Nanoscale* **2015**, *7*, 7953.
- [227] D. Desai, N. Prabhakar, V. Mamaeva, D. Ş. Karaman, I. A. K. Lähdeniemi, C. Sahlgren, J. M. Rosenholm, D. M. Toivola, *Int. J. Nanomedicine* **2016**, *11*, 299.
- [228] J. Finlay, C. M. Roberts, J. Dong, J. I. Zink, F. Tamanoi, C. A. Glackin, *Nanomedicine* **2015**, *11*, 1657.
- [229] M. Y. Hanafi-Bojd, M. R. Jaafari, N. Ramezani, M. Xue, M. Amin, N. Shahtahmassebi, B. Malaekheh-Nikouei, *Eur. J. Pharm. Biopharm.* **2015**, *89*, 248.
- [230] H. Hu, Y. You, L. He, T. Chen, *J. Mater. Chem. B* **2015**, *3*, 6368.
- [231] A. A. Hwang, B.-Y. Lee, D. L. Clemens, B. J. Dillon, J. I. Zink, M. A. Horwitz, *Small* **2015**, *11*, 5066.
- [232] X. Li, Y. Chen, M. Wang, Y. Ma, W. Xia, H. Gu, *Biomaterials* **2013**, *34*, 1391.
- [233] X. Li, Q. R. Xie, J. Zhang, W. Xia, H. Gu, *Biomaterials* **2011**, *32*, 9546.
- [234] X. Ma, Y. Zhao, K. W. Ng, Y. Zhao, *Chemistry* **2013**, *19*, 15593.
- [235] H. Meng, M. Xue, T. Xia, Z. Ji, D. Y. Tarn, J. I. Zink, A. E. Nel, *ACS Nano* **2011**, *5*, 4131.
- [236] E. Niemelä, D. Desai, Y. Nkizinkiko, J. E. Eriksson, J. M. Rosenholm, *Eur. J. Pharm. Biopharm.* **2015**, *96*, 11.
- [237] N. Prabhakar, J. Zhang, D. Desai, E. Casals, T. Gulin-Sarfraz, T. Näreoja, J. Westermarck, J. M. Rosenholm, *Int. J. Nanomedicine* **2016**, *11*, 6591.
- [238] J. M. Rosenholm, A. Meinander, E. Peuhu, R. Niemi, J. E. Eriksson, C. Sahlgren, M. Lindén, *ACS Nano* **2009**, *3*, 197.
- [239] D. Şen Karaman, T. Gulin-Sarfraz, G. Hedström, A. Duchanoy, P. Eklund, J. M. Rosenholm, *J. Colloid Interface Sci.* **2014**, *418*, 300.
- [240] L. Sun, Y.-J. Liu, Z.-Z. Yang, X.-R. Qi, *RSC Adv* **2015**, *5*, 55566.
- [241] T. Xia, M. Kovichich, M. Liang, H. Meng, S. Kabehie, S. George, J. I. Zink, A. E. Nel, *ACS Nano* **2009**, *3*, 3273.
- [242] J. Zhang, D. Desai, J. M. Rosenholm, *Adv. Funct. Mater.* **2014**, *24*, 2352.
- [243] H. Cheng, J.-L. Zhu, X. Zeng, Y. Jing, X.-Z. Zhang, R.-X. Zhuo, *Bioconjug. Chem.* **2009**, *20*, 481.
- [244] R. Satchi-Fainaro, R. Duncan, *Advances in Polymer Science*, Springer, Berlin/Heidelberg, **2006**.
- [245] E. Wagner, J. Kloeckner, *Gene Delivery Using Polymer Therapeutics*, Springer-Verlag, Berlin/Heidelberg, **2006**.
- [246] J.-P. Behr, *Chim. Int. J. Chem.* **1997**, *51*, 34.
- [247] R. V Benjaminsen, M. A. Matthebjerg, J. R. Henriksen, S. M. Moghimi, T. L. Andresen, *Mol. Ther.* **2013**, *21*, 149.
- [248] Y. Yue, F. Jin, R. Deng, J. Cai, Z. Dai, M. C. M. Lin, H.-F. Kung, M. A. Matthebjerg, T. L. Andresen, C. Wu, *J. Control. Release* **2011**, *152*, 143.

- [249] A. M. Chen, M. Zhang, D. Wei, D. Stueber, O. Taratula, T. Minko, H. He, *Small* **2009**, *5*, 2673.
- [250] H. Meng, M. Liong, T. Xia, Z. Li, Z. Ji, J. I. Zink, A. E. Nel, *ACS Nano* **2010**, *4*, 4539.
- [251] H. Meng, W. X. Mai, H. Zhang, M. Xue, T. Xia, S. Lin, X. Wang, Y. Zhao, Z. Ji, J. I. Zink, et al., *ACS Nano* **2013**, *7*, 994.
- [252] Y.-J. Chang, X.-Z. Liu, Q. Zhao, X.-H. Yang, K.-M. Wang, Q. Wang, M. Lin, M. Yang, *Chinese Chem. Lett.* **2015**, *26*, 1203.
- [253] T. Chen, W. Wu, H. Xiao, Y. Chen, M. Chen, J. Li, *ACS Macro Lett.* **2016**, *5*, 55.
- [254] H.-Y. Chiu, W. Deng, H. Engelke, J. Helma, H. Leonhardt, T. Bein, *Sci. Rep.* **2016**, *6*, 25019/1.
- [255] J. G. Croissant, D. Zhang, S. Alsaiani, J. Lu, L. Deng, F. Tamanoi, A. M. AlMalik, J. I. Zink, N. M. Khashab, *J. Control. Release* **2016**, *229*, 183.
- [256] K. Yang, H. Luo, M. Zeng, Y. Jiang, J. Li, X. Fu, *ACS Appl. Mater. Interfaces* **2015**, *7*, 17399.
- [257] G. Saito, J. A. Swanson, K.-D. Lee, *Adv. Drug Deliv. Rev.* **2003**, *55*, 199.
- [258] R. Cheng, F. Feng, F. Meng, C. Deng, J. Feijen, Z. Zhong, *J. Control. Release* **2011**, *152*, 2.
- [259] P. Maher, *Ageing Res. Rev.* **2005**, *4*, 288.
- [260] L. Palanikumar, H. Y. Kim, J. Y. Oh, A. P. Thomas, E. S. Choi, M. T. Jeena, S. H. Joo, J.-H. Ryu, *Biomacromolecules* **2015**, *16*, 2701.
- [261] R. Dong, Y. Su, S. Yu, Y. Zhou, Y. Lu, X. Zhu, *Chem. Commun. (Camb)*. **2013**, *49*, 9845.
- [262] Y. Wang, H.-Y. Huang, L. Yang, Z. Zhang, H. Ji, *Sci. Rep.* **2016**, *6*, 25468.
- [263] L. Maggini, I. Cabrera, A. Ruiz-Carretero, E. A. Prasetyanto, E. Robinet, L. Cola, *Nanoscale* **2016**, *8*, 7240.
- [264] E. Guisasola, A. Baeza, M. Talelli, D. Arcos, M. Vallet-Regí, *RSC Adv* **2016**, *6*, 42510.
- [265] M. Karesoja, J. McKee, E. Karjalainen, S. Hietala, L. Bergman, M. Linden, H. Tenhu, *J. Polym. Sci. Part A Polym. Chem.* **2013**, *51*, 5012.
- [266] Q. He, D. O. Kiesewetter, Y. Qu, X. Fu, J. Fan, P. Huang, Y. Liu, G. Zhu, Y. Liu, Z. Qian, et al., *Adv. Mater.* **2015**, *27*, 6741.
- [267] J. Zhang, J. M. Rosenholm, *Ther. Deliv.* **2015**, *6*, 891.
- [268] Y. Zhang, Z. Hou, Y. Ge, K. Deng, B. Liu, X. Li, Q. Li, Z. Cheng, P. Ma, C. Li, et al., *ACS Appl. Mater. Interfaces* **2015**, *7*, 20696.
- [269] A. Nouredine, M. Gary-Bobo, L. Lichon, M. Garcia, J. I. Zink, M. Wong Chi Man, X. Cattoën, *Chem. - A Eur. J.* **2016**, *22*, 9624.
- [270] S. Chai, Y. Guo, Z. Zhang, Z. Chai, Y. Ma, L. Qi, *Nanotechnology* **2017**, *28*, 145101/1.
- [271] A. Bernardos, L. Mondragon, E. Aznar, M. D. Marcos, R. Martinez-Mañez, F. Sancenon, J. Soto, J. M. Barat, E. Perez-Paya, C. Guillem, et al., *ACS Nano* **2010**, *4*, 6353.
- [272] C. Yang, W. Guo, N. An, L. Cui, T. Zhang, R. Tong, Y. Chen, H. Lin, F. Qu, *RSC Adv* **2015**, *5*, 80728.

- [273] C. Wong, T. Stylianopoulos, J. Cui, J. Martin, V. P. Chauhan, W. Jiang, Z. Popovic, R. K. Jain, M. G. Bawendi, D. Fukumura, *Proc. Natl. Acad. Sci. U. S. A.* **2011**, *108*, 2426.
- [274] W.-H. Chen, G.-F. Luo, Q. Lei, H.-Z. Jia, S. Hong, Q.-R. Wang, R.-X. Zhuo, X.-Z. Zhang, *Chem. Commun. (Camb)*. **2015**, *51*, 465.
- [275] Z. Zou, X. He, D. He, K. Wang, Z. Qing, X. Yang, L. Wen, J. Xiong, L. Li, L. Cai, *Biomaterials* **2015**, *58*, 35.
- [276] A. Holmberg, A. Blomstergren, O. Nord, M. Lukacs, J. Lundeberg, M. Uhlén, *Electrophoresis* **2005**, *26*, 501.
- [277] N. M. Green, *Methods Enzymol.* **1990**, *184*, 51.
- [278] M. Martinez-Carmona, A. Baeza, M. A. Rodriguez-Milla, J. García-Castro, M. Vallet, *J. Mater. Chem. B* **2015**, *3*, 5746.
- [279] A. D. Keefe, S. Pai, A. Ellington, *Nat. Rev. Drug Discov.* **2010**, *9*, 537.
- [280] A. D. Ellington, J. W. Szostak, *Nature* **1990**, *346*, 818.
- [281] J. Cheng, B. A. Teply, I. Sherifi, J. Sung, G. Luther, F. X. Gu, E. Levy-Nissenbaum, A. F. Radovic-Moreno, R. Langer, O. C. Farokhzad, *Biomaterials* **2007**, *28*, 869.
- [282] O. C. Farokhzad, J. Cheng, B. A. Teply, I. Sherifi, S. Jon, P. W. Kantoff, J. P. Richie, R. Langer, *Proc. Natl. Acad. Sci. U. S. A.* **2006**, *103*, 6315.
- [283] M. Kavruk, O. Celikbicak, V. C. Ozalp, B. A. Borsa, F. J. Hernandez, G. Bayramoglu, B. Salih, M. Y. Arica, *Chem. Commun. (Camb)*. **2015**, *51*, 8492.
- [284] Z. Li, Z. Liu, M. Yin, X. Yang, Q. Yuan, J. Ren, X. Qu, *Biomacromolecules* **2012**, *13*, 4257.
- [285] C. E. Ashley, E. C. Carnes, G. K. Phillips, D. Padilla, P. N. Durfee, P. A. Brown, T. N. Hanna, J. Liu, B. Phillips, M. B. Carter, et al., *Nat. Mater.* **2011**, *10*, 389.
- [286] P. N. Durfee, Y.-S. Lin, D. R. Dunphy, A. J. Muñoz, K. S. Butler, K. R. Humphrey, A. J. Lokke, J. O. Agola, S. S. Chou, I.-M. Chen, et al., *ACS Nano* **2016**, *10*, 8325.
- [287] M. A. Gonzalez Porras, P. N. Durfee, A. M. Gregory, G. C. Sieck, C. J. Brinker, C. B. Mantilla, *J. Neurosci. Methods* **2016**, *273*, 160.
- [288] Dolmans, Dennis E J G J, D. Fukumura, R. K. Jain, *Nat. Rev. Cancer* **2003**, *3*, 380.
- [289] L. Han, C. Tang, C. Yin, *Biomaterials* **2015**, *60*, 42.
- [290] Y. Wang, Y. Cui, J. Huang, D. Di, Y. Dong, X. Zhang, Q. Zhao, N. Han, Y. Gao, T. Jiang, et al., *Appl. Surf. Sci.* **2015**, *356*, 1282.
- [291] N. M. Khashab, A. Trabolsi, Y. A. Lau, M. W. Ambrogio, D. C. Friedman, H. A. Khatib, J. I. Zink, J. F. Stoddart, *European J. Org. Chem.* **2009**, *2009*, 1669.
- [292] Q.-L. Li, S.-H. Xu, H. Zhou, X. Wang, B. Dong, H. Gao, J. Tang, Y.-W. Yang, *ACS Appl. Mater. Interfaces* **2015**, *7*, 28656.
- [293] Y. Tian, Y. Kong, X. Li, J. Wu, A. C.-T. Ko, M. Xing, *Colloids Surfaces B Biointerfaces* **2015**, *134*, 147.
- [294] X. Yao, X. Chen, C. He, L. Chen, X. Chen, *J. Mater. Chem. B* **2015**, *3*, 4707.
- [295] M. Vert, Y. Doi, K.-H. Hellwich, M. Hess, P. Hodge, P. Kubisa, M. Rinaudo, F. Schué, *Pure Appl. Chem.* **2012**, *84*, 377.
- [296] J. G. Croissant, Y. Fatieiev, N. M. Khashab, *Adv. Mater.* **2017**, *29*, 1604634/1.

- [297] F. Alexis, E. Pridgen, L. K. Molnar, O. C. Farokhzad, *Mol. Pharm.* **2008**, *5*, 505.
- [298] X. Hao, X. Hu, C. Zhang, S. Chen, Z. Li, X. Yang, H. Liu, G. Jia, D. Liu, K. Ge, et al., *ACS Nano* **2015**, *9*, 9614.
- [299] G. Chen, Z. Teng, X. Su, Y. Liu, G. Lu, *J. Biomed. Nanotechnol.* **2015**, *11*, 722.
- [300] L. Lartigue, D. Alloyeau, J. Kolosnjaj-Tabi, Y. Javed, P. Guardia, A. Riedinger, C. Péchoux, T. Pellegrino, C. Wilhelm, F. Gazeau, *ACS Nano* **2013**, *7*, 3939.
- [301] M. Levy, N. Luciani, D. Alloyeau, D. Elgrabli, V. Deveaux, C. Pechoux, S. Chat, G. Wang, N. Vats, F. Gendron, et al., *Biomaterials* **2011**, *32*, 3988.
- [302] E. Sadauskas, G. Danscher, M. Stoltenberg, U. Vogel, A. Larsen, H. Wallin, *Nanomedicine* **2009**, *5*, 162.
- [303] A. K. Rengan, A. B. Bukhari, A. Pradhan, R. Malhotra, R. Banerjee, R. Srivastava, A. De, *Nano Lett.* **2015**, *15*, 842.
- [304] K. Zhang, S. L. E. Loong, S. Connor, S. W. K. Yu, S.-Y. Tan, R. T. H. Ng, K. M. Lee, L. Canham, P. K. H. Chow, *Clin. Cancer Res.* **2005**, *11*, 7532.
- [305] G. S. Korotchenkov, *Porous Silicon: From Formation to Application*, CRC Press, Boca Raton, **2015**.
- [306] Y.-S. Lin, C. L. Haynes, *J. Am. Chem. Soc.* **2010**, *132*, 4834.
- [307] A. Tzur-Balter, Z. Shatsberg, M. Beckerman, E. Segal, N. Artzi, *Nat. Commun.* **2015**, *6*, 6208/1.
- [308] Y. Choi, J.-E. Lee, J. H. Lee, J. H. Jeong, J. Kim, *Langmuir* **2015**, *31*, 6457.
- [309] K. Braun, A. Pochert, M. Beck, R. Fiedler, J. Gruber, M. Lindén, *J. Sol-Gel Sci. Technol.* **2016**, *79*, 319.
- [310] R. Kumar, I. Roy, T. Y. Ohulchanskyy, L. A. Vathy, E. J. Bergey, M. Sajjad, P. N. Prasad, *ACS Nano* **2010**, *4*, 699.
- [311] Q. He, J. Shi, M. Zhu, Y. Chen, F. Chen, *Microporous Mesoporous Mater.* **2010**, *131*, 314.
- [312] E. Haartman, D. Lindberg, N. Prabhakar, J. M. Rosenholm, *Eur. J. Pharm. Sci.* **2016**, *95*, 17.
- [313] A. T. Florence, *J. Control. Release* **2012**, *164*, 115.
- [314] A. S. Abu Lila, H. Kiwada, T. Ishida, *J. Control. Release* **2013**, *172*, 38.
- [315] S. Wilhelm, A. J. Tavares, Q. Dai, S. Ohta, J. Audet, H. F. Dvorak, W. C. W. Chan, *Nat. Rev. Mater.* **2016**, *1*, 16014/1.
- [316] J. W. Nichols, Y. H. Bae, *Nano Today* **2012**, *7*, 606.
- [317] R. A. Weinberg, *The Biology of Cancer*, Garland Science, New York, **2007**.
- [318] C. L. Carter, C. Allen, D. E. Henson, *Cancer* **1989**, *63*, 181.
- [319] R. K. Jain, *Ann. Biomed. Eng.* **1996**, *24*, 457.
- [320] J. Zhou, *Multi-Drug Resistance in Cancer*, Humana Press, Totowa, **2010**.
- [321] M. B. Meads, R. A. Gatenby, W. S. Dalton, *Nat. Rev. Cancer* **2009**, *9*, 665.
- [322] A. Persidis, *Nat. Biotechnol.* **1999**, *17*, 94.

- [323] C. Holohan, S. van Schaeybroeck, D. B. Longley, P. G. Johnston, *Nat. Rev. Cancer* **2013**, *13*, 714.
- [324] G. Szakács, J. K. Paterson, J. A. Ludwig, C. Booth-Genthe, M. M. Gottesman, *Nat. Rev. Drug Discov.* **2006**, *5*, 219.
- [325] M. M. Gottesman, T. Fojo, S. E. Bates, *Nat. Rev. Cancer* **2002**, *2*, 48.
- [326] D. Peer, R. Margalit, *Cancer Lett.* **2006**, *237*, 180.
- [327] J.-P. Gillet, M. M. Gottesman, *Methods Mol. Biol.* **2010**, *596*, 47.
- [328] P. D. W. Eckford, F. J. Sharom, *Chem. Rev.* **2009**, *109*, 2989.
- [329] F. Leonessa, *Endocr. Relat. Cancer* **2003**, *10*, 43.
- [330] K. W. Yip, J. C. Reed, *Oncogene* **2008**, *27*, 6398.
- [331] R. I. Pakunlu, T. J. Cook, T. Minko, *Pharm. Res.* **2003**, *20*, 351.
- [332] R. I. Pakunlu, Y. Wang, W. Tsao, V. Pozharov, T. J. Cook, T. Minko, *Cancer Res.* **2004**, *64*, 6214.
- [333] R. T. Lima, L. M. Martins, J. E. Guimarães, C. Sambade, M. H. Vasconcelos, *Cancer Gene Ther.* **2004**, *11*, 309.
- [334] Y. Li, X. Xu, X. Zhang, Y. Li, Z. Zhang, Z. Gu, *ACS Nano* **2017**, *11*, 416.
- [335] J. Liu, Q. Li, J. Zhang, L. Huang, C. Qi, L. Xu, X. Liu, G. Wang, L. Wang, Z. Wang, *Small* **2017**, *13*, 1602567/1.
- [336] F. Wang, Y.-C. Wang, S. Dou, M.-H. Xiong, T.-M. Sun, J. Wang, *ACS Nano* **2011**, *5*, 3679.
- [337] R.-H. Wang, J. Bai, J. Deng, C.-J. Fang, X. Chen, *ACS Appl. Mater. Interfaces* **2017**, *9*, 5828.
- [338] S. A. Love, M. A. Maurer-Jones, J. W. Thompson, Y.-S. Lin, C. L. Haynes, *Annu. Rev. Anal. Chem. (Palo Alto, Calif.)* **2012**, *5*, 181.
- [339] B. Fadeel, A. E. Garcia-Bennett, *Adv. Drug Deliv. Rev.* **2010**, *62*, 362.
- [340] B. S. Zolnik, A. González-Fernández, N. Sadrieh, M. A. Dobrovolskaia, *Endocrinology* **2010**, *151*, 458.
- [341] Y. Zhao, X. Sun, G. Zhang, B. G. Trewyn, I. I. Slowing, V. S.-Y. Lin, *ACS Nano* **2011**, *5*, 1366.
- [342] Z. Tao, M. P. Morrow, T. Asefa, K. K. Sharma, C. Duncan, A. Anan, H. S. Penefsky, J. Goodisman, A.-K. Souid, *Nano Lett.* **2008**, *8*, 1517.
- [343] H. Shinto, T. Fukasawa, K. Yoshisue, M. Tezuka, M. Orita, *Adv. Powder Technol.* **2014**, *25*, 1872.
- [344] B. Ballou, B. C. Lagerholm, L. A. Ernst, M. P. Bruchez, A. S. Waggoner, *Bioconjug. Chem.* **2004**, *15*, 79.
- [345] A. M. Derfus, W. C. W. Chan, S. N. Bhatia, *Nano Lett.* **2004**, *4*, 11.
- [346] Z. Liu, C. Davis, W. Cai, L. He, X. Chen, H. Dai, *Proc. Natl. Acad. Sci. U. S. A.* **2008**, *105*, 1410.
- [347] D. Kim, S. Park, J. H. Lee, Y. Y. Jeong, S. Jon, *J. Am. Chem. Soc.* **2007**, *129*, 7661.

- [348] J.-H. Park, L. Gu, G. Maltzahn, E. Ruoslahti, S. N. Bhatia, M. J. Sailor, *Nat. Mater.* **2009**, *8*, 331.
- [349] T. Wang, X. Jiang, *ACS Appl. Mater. Interfaces* **2015**, *7*, 129.
- [350] T. Wang, S. Zhu, X. Jiang, *Toxicol. Res.* **2015**, *4*, 885.
- [351] Q. He, Z. Zhang, Y. Gao, J. Shi, Y. Li, *Small* **2009**, *5*, 2722.
- [352] J. Lu, M. Liong, Z. Li, J. I. Zink, F. Tamanoi, *Small* **2010**, *6*, 1794.
- [353] S. van Rijt, D. A. Boeluekbas, C. Argyo, K. Wipplinger, M. Naureen, S. Datz, O. Eickelberg, S. Meiners, T. Bein, O. Schmid, et al., *Nanoscale* **2016**, *8*, 8058.
- [354] T. Laaksonen, H. Santos, H. Vihola, J. Salonen, J. Riikonen, T. Heikkilä, L. Peltonen, N. Kumar, D. Y. Murzin, V.-P. Lehto, et al., *Chem. Res. Toxicol.* **2007**, *20*, 1913.
- [355] N. Lewinski, V. Colvin, R. Drezek, *Small* **2008**, *4*, 26.
- [356] B. J. Marquis, S. A. Love, K. L. Braun, C. L. Haynes, *Analyst* **2009**, *134*, 425.
- [357] N. A. Monteiro-Riviere, A. O. Inman, L. W. Zhang, *Toxicol. Appl. Pharmacol.* **2009**, *234*, 222.
- [358] J. Lazarovits, Y. Y. Chen, E. A. Sykes, W. C. W. Chan, *Chem. Commun. (Camb)*. **2015**, *51*, 2756.
- [359] H. Jiang, L. Chess, in *Adv. Immunol.*, Academic Press, **2009**, pp. 95–133.
- [360] W. Zou, *Nat. Rev. Immunol.* **2006**, *6*, 295.
- [361] S. Shukla, N. F. Steinmetz, *Exp. Biol. Med. (Maywood)*. **2016**, *241*, 1116.
- [362] C. J. M. Melief, *Immunity* **2008**, *29*, 372.
- [363] R. D. Schreiber, L. J. Old, M. J. Smyth, *Science* **2011**, *331*, 1565.
- [364] S. A. Rosenberg, J. C. Yang, N. P. Restifo, *Nat. Med.* **2004**, *10*, 909.
- [365] P. Carter, *Nat. Rev. Cancer* **2001**, *1*, 118.
- [366] D. M. Pardoll, *Nat. Rev. Cancer* **2012**, *12*, 252.
- [367] S. Sakaguchi, M. Miyara, C. M. Costantino, D. A. Hafler, *Nat. Rev. Immunol.* **2010**, *10*, 490.
- [368] C. G. Figdor, I. J. M. de Vries, W. J. Lesterhuis, C. J. M. Melief, *Nat. Med.* **2004**, *10*, 475.
- [369] Y. Luo, H. Zhou, J. Krueger, C. Kaplan, S.-H. Lee, C. Dolman, D. Markowitz, W. Wu, C. Liu, R. A. Reisfeld, et al., *J. Clin. Invest.* **2006**, *116*, 2132.
- [370] A. Mantovani, A. Sica, *Curr. Opin. Immunol.* **2010**, *22*, 231.
- [371] T. Saleh, S. A. Shojaosadati, *Hum. Vaccin. Immunother.* **2016**, *12*, 1863.
- [372] P. Tsirikis, K. Wilson, S. Xiang, W. Wei, G. Ma, C. Selomulya, M. Plebanski, *J. Immunol.* **2016**, *196*, 75.28.
- [373] T. C. van der Sluis, S. van Duikeren, S. Huppelschoten, E. S. Jordanova, E. Beyranvand Nejad, A. Sloots, L. Boon, V. T. H. B. M. Smit, M. J. P. Welters, F. Ossendorp, et al., *Clin. Cancer Res.* **2015**, *21*, 781.
- [374] L. Apetoh, F. Ghiringhelli, A. Tesniere, M. Obeid, C. Ortiz, A. Criollo, G. Mignot, M. C. Maiuri, E. Ullrich, P. Saulnier, et al., *Nat. Med.* **2007**, *13*, 1050.

- [375] M. Obeid, A. Tesniere, F. Ghiringhelli, G. M. Fimia, L. Apetoh, J.-L. Perfettini, M. Castedo, G. Mignot, T. Panaretakis, N. Casares, et al., *Nat. Med.* **2007**, *13*, 54.
- [376] N. Casares, M. O. Pequignot, A. Tesniere, F. Ghiringhelli, S. Roux, N. Chaput, E. Schmitt, A. Hamai, S. Hervas-Stubbs, M. Obeid, et al., *J. Exp. Med.* **2005**, *202*, 1691.
- [377] R. A. Lake, R. G. van der Most, *N. Engl. J. Med.* **2006**, *354*, 2503.
- [378] S. Elmore, *Toxicol. Pathol.* **2007**, *35*, 495.
- [379] J. Conde, C. Bao, Y. Tan, D. Cui, E. R. Edelman, H. S. Azevedo, H. J. Byrne, N. Artzi, F. Tian, *Adv. Funct. Mater.* **2015**, *25*, 4183.
- [380] J. P. M. Almeida, E. R. Figueroa, R. A. Drezek, *Nanomedicine* **2014**, *10*, 503.
- [381] X. Wang, X. Li, K. Yoshiyuki, Y. Watanabe, Y. Sogo, T. Ohno, N. M. Tsuji, A. Ito, *Adv. Healthc. Mater.* **2016**, *5*, 1169.
- [382] F. M. Kievit, M. Zhang, *Adv. Mater.* **2011**, *23*, H217.
- [383] H. E. Daldrup-Link, D. Golovko, B. Ruffell, D. G. Denardo, R. Castaneda, C. Ansari, J. Rao, G. A. Tikhomirov, M. F. Wendland, C. Corot, et al., *Clin. Cancer Res.* **2011**, *17*, 5695.
- [384] S. Zhu, M. Niu, H. O'Mary, Z. Cui, *Mol. Pharm.* **2013**, *10*, 3525.
- [385] M. A. Miller, Y.-R. Zheng, S. Gadde, C. Pfirschke, H. Zope, C. Engblom, R. H. Kohler, Y. Iwamoto, K. S. Yang, B. Askevold, et al., *Nat. Commun.* **2015**, *6*, 8692.
- [386] X. Zhang, W. Tian, X. Cai, X. Wang, W. Dang, H. Tang, H. Cao, L. Wang, T. Chen, *PLoS One* **2013**, *8*, e65896/1.
- [387] M. A. Curran, W. Montalvo, H. Yagita, J. P. Allison, *Proc. Natl. Acad. Sci. U. S. A.* **2010**, *107*, 4275.
- [388] J. D. Wolchok, H. Kluger, M. K. Callahan, M. A. Postow, N. A. Rizvi, A. M. Lesokhin, N. H. Segal, C. E. Ariyan, R.-A. Gordon, K. Reed, et al., *N. Engl. J. Med.* **2013**, *369*, 122.
- [389] J. R. Brahmer, S. S. Tykodi, L. Q. M. Chow, W.-J. Hwu, S. L. Topalian, P. Hwu, C. G. Drake, L. H. Camacho, J. Kauh, K. Odunsi, et al., *N. Engl. J. Med.* **2012**, *366*, 2455.
- [390] P. Sharma, J. P. Allison, *Science* **2015**, *348*, 56.
- [391] D. I. Gabrilovich, S. Nagaraj, *Nat. Rev. Immunol.* **2009**, *9*, 162.
- [392] Q. Zhang, K. G. Neoh, L. Xu, S. Lu, E. T. Kang, R. Mahendran, E. Chiong, *Langmuir* **2014**, *30*, 6151.
- [393] J. R. Cubillos-Ruiz, X. Engle, U. K. Scarlett, D. Martinez, A. Barber, R. Elgueta, L. Wang, Y. Nesbeth, Y. Durant, A. T. Gewirtz, et al., *J. Clin. Invest.* **2009**, *119*, 2231.
- [394] T. D. Schladt, K. Schneider, H. Schild, W. Tremel, *Dalt. Trans.* **2011**, *40*, 6315.
- [395] R. P. Bagwe, L. R. Hilliard, W. Tan, *Langmuir* **2006**, *22*, 4357.
- [396] X. Du, S. Z. Qiao, *Small* **2015**, *11*, 392.
- [397] D. Shen, J. Yang, X. Li, L. Zhou, R. Zhang, W. Li, L. Chen, R. Wang, F. Zhang, D. Zhao, *Nano Lett.* **2014**, *14*, 923.
- [398] Sing, K. S. W., *Pure Appl. Chem.* **1985**, *57*, DOI 10.1351/pac198557040603.
- [399] S. Lowell, *Characterization of Porous Solids and Powders: Surface Area, Pore Size*,

and Density, Kluwer Academic Publishers, Dordrecht and Boston, **2004**.

- [400] F. Rouquerol, J. Rouquerol, Sing, K. S. W., *Adsorption by Powders and Porous Solids: Principles, Methodology, and Applications*, Academic Press, San Diego, **1999**.
- [401] M. Thommes, K. A. Cychoz, *Adsorption* **2014**, *20*, 233.
- [402] M. Thommes, K. Kaneko, A. V Neimark, J. P. Olivier, F. Rodriguez-Reinoso, J. Rouquerol, K. S. W. Sing, *Pure Appl. Chem.* **2015**, *87*, DOI 10.1515/pac-2014-1117.
- [403] J. C. Groen, L. A. A. Peffer, J. Perez-Ramirez, *Microporous Mesoporous Mater.* **2003**, *60*, 1.
- [404] X. Du, B. Shi, J. Liang, J. Bi, S. Dai, S. Z. Qiao, *Adv. Mater.* **2013**, *25*, 5981.
- [405] J. Eastoe, M. H. Hatzopoulos, P. J. Dowding, *Soft Matter* **2011**, *7*, 5917.
- [406] G. Verma, S. Kumar, R. Schweins, V. K. Aswal, P. A. Hassan, *Soft Matter* **2013**, *9*, 4544.
- [407] E. Roduner, *Chem. Soc. Rev.* **2014**, *43*, 8226.
- [408] Z. W. Seh, S. Liu, M. Low, S.-Y. Zhang, Z. Liu, A. Mlayah, M.-Y. Han, *Adv. Mater.* **2012**, *24*, 2310.
- [409] H. Zeng, J. Li, J. P. Liu, Z. L. Wang, S. Sun, *Nature* **2002**, *420*, 395.
- [410] J. P. Zimmer, S. Kim, S. Ohnishi, E. Tanaka, J. V Frangioni, M. G. Bawendi, *J. Am. Chem. Soc.* **2006**, *128*, 2526.
- [411] W. U. Huynh, J. J. Dittmer, A. P. Alivisatos, *Science (80-.)*. **2002**, *295*, 2425.
- [412] H. Hosoya, A. S. Dobroff, W. H. P. Driessen, V. Cristini, L. M. Brinker, F. I. Staquicini, M. Cardó-Vila, S. D'Angelo, F. Ferrara, B. Proneth, et al., *Proc. Natl. Acad. Sci.* **2016**, *113*, 1877 LP.
- [413] J. Wu, N. Kamaly, J. Shi, L. Zhao, Z. Xiao, G. Hollett, R. John, S. Ray, X. Xu, X. Zhang, et al., *Angew. Chemie - Int. Ed.* **2014**, *53*, 8975.
- [414] X. Zhu, J. Wu, W. Shan, W. Tao, L. Zhao, J. M. Lim, M. D'Ortenzio, R. Karnik, Y. Huang, J. Shi, et al., *Angew. Chemie - Int. Ed.* **2016**, *55*, 3309.
- [415] A. Kumar, *J. Exp. Med.* **1996**, *183*, 949.
- [416] D. J. Grünhagen, J. H. W. de Wilt, T. L. M. ten Hagen, A. M. M. Eggermont, *Nat. Clin. Pract. Oncol.* **2006**, *3*, 94.
- [417] F. Balkwill, *Nat Rev Cancer* **2009**, *9*, 361.
- [418] E. Kedar, O. Palgi, G. Golod, I. Babai, Y. Barenholz, *J. Immunother.* **1997**, *20*, 180.
- [419] A. Wicovsky, F. Henkler, S. Salzmann, P. Scheurich, C. Kneitz, H. Wajant, *Oncogene* **2009**, *28*, 1769.
- [420] F. Curnis, A. Sacchi, A. Corti, *J. Clin. Invest.* **2002**, *110*, 475.
- [421] C. Brunner, J. Seiderer, A. Schlamp, M. Bidlingmaier, A. Eigler, W. Haimerl, H.-A. Lehr, A. M. Krieg, G. Hartmann, S. Endres, *J. Immunol.* **2000**, *165*, 6278.
- [422] M. Vallet-Regí, *ISRN Mater. Sci.* **2012**, *2012*, 1.
- [423] P. Yang, S. Gai, J. Lin, *Chem. Soc. Rev.* **2012**, *41*, 3679.
- [424] C. Argyo, V. Weiss, C. Bräuchle, T. Bein, *Chem. Mater.* **2014**, *26*, 435.

- [425] S. B. Hartono, W. Gu, F. Kleitz, J. Liu, L. He, Middelberg, Anton P. J., C. Yu, G. Q. Lu, S. Z. Qiao, *ACS Nano* **2012**, *6*, 2104.
- [426] J. L. Paris, M. V. Cabañas, M. Manzano, M. Vallet-Regí, *ACS Nano* **2015**, *9*, 11023.
- [427] B. Delalat, V. C. Sheppard, S. Rasi Ghaemi, S. Rao, C. A. Prestidge, G. McPhee, M. L. Rogers, J. F. Donoghue, V. Pillay, T. G. Johns, et al., *Nat. Commun.* **2015**, *6*, DOI 10.1038/ncomms9791.
- [428] E. M. Agenc, *Eur. Med. Agency* **1999**, EMEA/H/C/2.
- [429] R. Goel, N. Shah, R. Visaria, G. F. Paciotti, J. C. Bischof, *Nanomedicine (Lond)*. **2009**, *4*, 401.
- [430] F. Chen, S. Goel, H. F. Valdovinos, H. Luo, R. Hernandez, T. E. Barnhart, W. Cai, *ACS Nano* **2015**, DOI 10.1021/acsnano.5b00526.
- [431] K. S. Smalley, M. Lioni, K. Noma, N. K. Haass, M. Herlyn, *Expert Opin. Drug Discov.* **2008**, *3*, 1.
- [432] K. A. Beaumont, A. Anfosso, F. Ahmed, W. Weninger, N. K. Haass, *J. Vis. Exp.* **2015**, e53486.
- [433] Eck, Michael J and Sprang, Stephen R, *J. Biol. Chem.* **1989**, 17595.
- [434] E. Y. Jones, D. I. Stuart, N. P. Walker, *J. Cell Sci. Suppl.* **1990**, *13*, 11.
- [435] Á. Martínez, E. Fuentes-Paniagua, A. Baeza, J. Sánchez-Nieves, M. Cicuéndez, R. Gómez, de la Mata, F Javier, B. González, M. Vallet-Regí, *Chemistry* **2015**, DOI 10.1002/chem.201501966.
- [436] S. Javadian, V. Ruhi, A. Heydari, A. Asadzadeh Shahir, A. Yousefi, J. Akbari, *Ind. Eng. Chem. Res.* **2013**, *52*, 4517.
- [437] H. Petersen, P. M. Fechner, D. Fischer, T. Kissel, *Macromolecules* **2002**, *35*, 6867.
- [438] J. Pitha, J. Milecki, H. Fales, L. Pannell, K. Uekama, J. Schindelin, I. Arganda-Carreras, E. Frise, V. Kaynig, M. Longair, et al., *ACS Nano* **2015**, *7*, 60.
- [439] S. C. Junggeburth, K. Schwinghammer, K. S. Virdi, C. Scheu, B. V Lotsch, *Chemistry* **2012**, *18*, 2143.
- [440] X. Liu, W. He, Z. Fang, A. Kienzle, Q. Feng, *J. Biomed. Nanotechnol.* **2014**, *10*, 1277.
- [441] W. He, X. Liu, A. Kienzle, Müller, Werner E. G., Q. Feng, *J. Nanosci. Nanotechnol.* **2016**, *16*, 219.
- [442] W. He, A. Kienzle, X. Liu, W. E. G. Muller, T. A. Elkhooly, Q. Feng, *J. Biomed. Nanotechnol.* **2016**, *12*, 525.
- [443] Y. Feng, N. Panwar, Tng, Danny Jian Hang, S. C. Tjin, K. Wang, K.-T. Yong, *Coord. Chem. Rev.* **2016**, *319*, 86.
- [444] Y. Kato, S. Ozawa, C. Miyamoto, Y. Maehata, A. Suzuki, T. Maeda, Y. Baba, *Cancer Cell Int.* **2013**, *13*, DOI 10.1186/1475-2867-13-89.
- [445] J. C. Oliver, L. A. Bland, C. W. Oettinger, M. J. Arduino, S. K. McAllister, S. M. Agüero, M. S. Favero, *Lymphokine Cytokine Res.* **1993**, *12*, 115.
- [446] A. L. B. Seynhaeve, S. Hoving, D. Schipper, C. E. Vermeulen, G. A. De Wiel-Ambagtsheer, S. T. Van Tiel, A. M. M. Eggermont, T. L. M. Ten Hagen, *Cancer Res.* **2007**, *67*, 9455.
- [447] A. I. Minchinton, I. F. Tannock, *Nat. Rev. Cancer* **2006**, *6*, 583.

- [448] H. Jonuleit, U. Kühn, G. Müller, K. Steinbrink, L. Paragnik, E. Schmitt, J. Knop, A. H. Enk, *Eur. J. Immunol.* **1997**, *27*, 3135.
- [449] M. Hubo, B. Trinschek, F. Kryczanowsky, A. Tuettenberg, K. Steinbrink, H. Jonuleit, *Front. Immunol.* **2013**, *4*, DOI 10.3389/fimmu.2013.00082.
- [450] A. Santiago-Walker, L. Li, N. K. Haass, M. Herlyn, *Skin Pharmacol. Physiol.* **2009**, *22*, 114.
- [451] W. He, A. Kienzle, X. Liu, Müller, Werner E. G., Q. Feng, *RSC Adv* **2015**, *5*, 49809.
- [452] R. M. Sutherland, *Science* **1988**, *240*, 177.
- [453] A. Sakaue-Sawano, H. Kurokawa, T. Morimura, A. Hanyu, H. Hama, H. Osawa, S. Kashiwagi, K. Fukami, T. Miyata, H. Miyoshi, et al., *Cell* **2008**, *132*, 487.
- [454] N. K. Haass, K. A. Beaumont, D. S. Hill, A. Anfosso, P. Mrass, M. A. Munoz, I. Kinjyo, W. Weninger, *Pigment Cell Melanoma Res.* **2014**, *27*, 764.
- [455] K. A. Beaumont, D. S. Hill, S. M. Daignault, G. Y. L. Lui, D. M. Sharp, B. Gabrielli, W. Weninger, N. K. Haass, *J. Invest. Dermatol.* **2016**, *136*, 1479.
- [456] L. Pusztai, C. E. Lewis, J. O. McGee, *Br. J. Cancer* **1993**, *67*, 290.
- [457] M. A. Shah, G. K. Schwartz, *Clin. Cancer Res.* **2001**, *7*, 2168.
- [458] T. Glaser, Fischer von Mollard, Gabriele, D. Anselmetti, *Inorganica Chim. Acta* **2016**, *452*, 62.
- [459] Y. Jung, S. J. Lippard, *Chem. Rev.* **2007**, *107*, 1387.
- [460] Z. H. Siddik, *Oncogene* **2003**, *22*, 7265.
- [461] V. J. Stella, Q. He, *Toxicol. Pathol.* **2008**, *36*, 30.
- [462] K. Hirose, *J. Incl. Phenom. Macrocycl. Chem.* **2001**, *39*, 193.
- [463] L. Fielding, *Tetrahedron* **2000**, *56*, 6151.
- [464] D. Osella, A. Carretta, C. Nervi, M. Ravera, R. Gobetto, *Organometallics* **2000**, *19*, 2791.
- [465] M. Poorghorban, A. H. Karoyo, P. Grochulski, R. E. Verrall, L. D. Wilson, I. Badea, *Mol. Pharm.* **2015**, *12*, 2993.
- [466] M. Rouchal, A. Matelová, F. P. de Carvalho, R. Bernat, D. Grbić, I. Kuřitka, M. Babinský, R. Marek, R. Čmelík, R. Vícha, *Supramol. Chem.* **2013**, *25*, 349.
- [467] J. W. Steed, J. L. Atwood, *Supramolecular Chemistry*, John Wiley & Sons, Ltd, Chichester, UK, **2009**.
- [468] P. Thordarson, *Chem. Soc. Rev.* **2011**, *40*, 1305.
- [469] S. Gibaud, S. Ben Zirar, P. Mutzenhardt, I. Fries, A. Astier, *Int. J. Pharm.* **2005**, *306*, 107.
- [470] J. Pitha, J. Milecki, H. Fales, L. Pannell, K. Uekama, *Int. J. Pharm.* **1986**, *29*, 73.
- [471] Y. Cui, C. Wang, J. Mao, Y. Yu, *J. Chem. Technol. Biotechnol.* **2010**, *85*, 248.
- [472] K. Koynov, H.-J. Butt, *Curr. Opin. Colloid Interface Sci.* **2012**, *17*, 377.
- [473] Smalley, K S M, R. Contractor, N. K. Haass, J. T. Lee, K. L. Nathanson, C. A. Medina, K. T. Flaherty, M. Herlyn, *Br. J. Cancer* **2007**, *96*, 445.

- [474] Smalley, Keiran S M, P. Brafford, N. K. Haass, J. M. Brandner, E. Brown, M. Herlyn, *Am. J. Pathol.* **2005**, *166*, 1541.
- [475] J. Schindelin, I. Arganda-Carreras, E. Frise, V. Kaynig, M. Longair, T. Pietzsch, S. Preibisch, C. Rueden, S. Saalfeld, B. Schmid, et al., *Nat. Methods* **2012**, *9*, 676.
- [476] R. Rigler, E. S. Elson, *Fluorescence Correlation Spectroscopy: Theory and Applications*, Springer Berlin Heidelberg, Berlin, Heidelberg, **2001**.
- [477] H.-J. Welkoborsky, R. Jacob, S. H. Riazimand, H. S. Bernauer, W. J. Mann, *Oncology* **2003**, *65*, 60.
- [478] A. Schreer, C. Tinson, J. P. Sherry, K. Schirmer, *Anal. Biochem.* **2005**, *344*, 76.
- [479] S. de Carlo, J. R. Harris, *Micron* **2011**, *42*, 117.
- [480] R. Gilles, U. Keiderling, A. Wiedenmann, *J. Appl. Crystallogr.* **1998**, *31*, 957.
- [481] A. M. Brown, *Comput. Methods Programs Biomed.* **2001**, *65*, 191.
- [482] "Curve fitting Homepage," can be found under www.supramolecular.org, **n.d.**
- [483] E. Freire, O. L. Mayorga, M. Straume, *Anal. Chem.* **2008**, *62*, 950A.
- [484] M. Etienne, *Talanta* **2003**, *59*, 1173.
- [485] L. T. Zhuravlev, *Langmuir* **1987**, *3*, 316.
- [486] L. T. Zhuravlev, *Colloids Surfaces A Physicochem. Eng. Asp.* **2000**, *173*, 1.
- [487] Y. Wei, J. Wang, Y. Zhang, L. Wang, X. Zhang, *RSC Adv* **2015**, *5*, 91407.

Curriculum Vitae

Sven Andreas Kurch

[REDACTED]
[REDACTED]
[REDACTED]
[REDACTED]



KURZPROFIL

- Promotion im Fach Chemie Juni 2018
- Interdisziplinäre Doktorarbeit Immunologie/Chemie
- Nanodimensionale Transportsysteme für die Krebstherapie
- Mitglied Sonderforschungsbereich 1066-„Nanodimensionale polymere Therapeutika für die Tumorthherapie“
- Zertifikat und Fortbildung Projektmanagement/GMP

Promotion

[REDACTED]
Johannes Gutenberg-Universität Mainz, Anorganische Chemie

Universitätsmedizin Mainz, HNO-Klinik und Hautklinik

Thema der Dissertation: Entwicklung von nanodimensionalen Transportsystemen für die Krebstherapie und Immunmodulation

- **Mitglied Sonderforschungsbereich 1066** „Nanodimensionale polymere Therapeutika für die Tumorthherapie“ und Förderung durch das zugehörige Graduiertenkolleg.
- Kooperationen mit [REDACTED] [REDACTED] der Universitätsmedizin Mainz für biologische Fragestellungen.
- Internationale Zusammenarbeit mit [REDACTED] [REDACTED] für wissenschaftliche Publikationen.

- **Betreuung** der Abschlussarbeit von Bachelorkandidaten und Modulanten.
 - Anleitung von wissenschaftlichen Hilfskräften zur Qualitätssicherung.
 - Betreuung des Grundpraktikums Chemie für Mediziner (Tutorium und Klausurbetreuung für 140 Studenten, Austausch zwischen Lehrkräften, wissenschaftlichen Mitarbeitern und Studenten).
- **Buchkapitel** „Bio-Nano: Theranostic at a cellular level“ in der Springer „Advances in the Pharmaceutical Sciences“ (AAPS) Buchserie.
 - Zwei wissenschaftliche Publikationen im Bereich Wirkstofftransport für die Krebstherapie.
 - Besuch der CIMT Konferenz (Cancer Immunotherapy) in Mainz mit Poster Präsentation.

STUDIUM

- | | |
|--|--|
| 05/2015 – 05/2018 | <div style="background-color: black; width: 100%; height: 1.2em; margin-bottom: 5px;"></div> Johannes Gutenberg-Universität Mainz
Promotion im Fachbereich Anorganische Chemie
Titel der Dissertation: Mesoporous silica nanoparticle for drug delivery of cancer therapeutics |
| 10/2008 – 05/2018 | Johannes-Gutenberg Universität Mainz,
Studium der Chemie
Abschluss: Diplom Chemiker (Abschlussnote: 2.4) |
| 07/2014 – 10/2014 &
07/2013 – 10/2013 | Wissenschaftliche Hilfskraft
Abteilung physikalische Chemie von Polymeren,
Max-Planck Institute für Polymere, Mainz |

WEHRDIENSTZEIT

- | | |
|-------------------|---|
| 07/2007 – 05/2008 | ABC Abwehrregiment 750 Baden in Bruchsal
Einsatz in der Verwaltung/Truppenversorgung
Koordination Übungsplatzaufenthalt |
|-------------------|---|

SCHULE UND AUSBILDUNG

- | | |
|----------------|---|
| 1999 – 06/2007 | Überwald Gymnasium, Wald-Michelbach
Abschluss: Allgemeine Hochschulreife |
| 1997 – 1999 | Grundschule, Locherhof |